

DISS. ETH NO. 21101

QUANTIFYING AND MODELING SEDIMENT TRANSFER THROUGH THE ILLGRABEN

A dissertation submitted to
ETH ZURICH

for the degree of
Doctor of Sciences

presented by
GEORGINA LUCY BENNETT
MSc, Durham University

29.06.1986

citizen of Great Britain

accepted on the recommendation of

Professor Paolo Burlando
Dr. Peter Molnar
Dr. Brian McArdell
Professor Stuart Lane

2013

Abstract

Quantification of sediment yield from mountain basins is an key component in the study of the evolution of mountain ranges and is important to the population living downstream to which sediment can be both a vital resource and hazard. Mountain basins are particularly susceptible to climate change due to their sensitivity to snow and ice melt processes and rapid rainfall-runoff response. Understanding the interactions of earth surface processes with climate is important to be able to model and predict mountain basin sediment yield under a changing climate. In this thesis I aimed to quantify processes of sediment production, transport and yield; identify their interactions, climatic and seismic controls, and finally to model sediment transfer in the Illgraben, a small but highly active mountain basin in the Swiss Alps prone to large slope failures and debris flows.

I quantified sediment production, transfer and yield over a 42-year period from 1963 – 2005, split into 4 sub-periods, from aerial photographs using digital photogrammetry. The hillslopes were eroded at an extremely high mean annual rate of $0.39 \pm 0.03 \text{ m yr}^{-1}$ by slope failures. I extracted an inventory of more than 2000 failures spanning 6 orders of magnitude in volume and analyzed their statistics. The failures follow a characteristic magnitude-frequency distribution with a roll-over and power-law tail. The results support the hypothesis that the shape of the distribution arises from 2 different failure types: shallow slides within the upper weathered layer of the slope that have a restricted depth and therefore volume, and deep-seated bedrock failures that occur along failure surfaces in the slope and have a wide range of volumes. The latter account for more than 98% of sediment supply and limit the relief of the slopes, providing empirical support for the concept of threshold slopes. The results also demonstrate the importance of constraining the scaling exponent between landslide area and volume for different geological settings.

I analyzed climate and seismic data over the study period with the aim of explaining the observed patterns of hillslope erosion (production), channel erosion (transfer) and sediment yield. A marked increase in hillslope erosion rate in the 1980s was most likely related to a significant increase in air temperature and related decrease in snow cover depth and duration. However, analysis of the potential triggers of an individual failure event in the Illgraben illustrates that multiple triggering mechanisms may exist such that slope failure is highly stochastic phenomenon. Channel erosion rate is more clearly related to the frequency of intense summer rainfall events. Hillslope erosion rate exceeded channel erosion rate over the study period, indicative of a downslope-directed coupling relationship in which hillslopes erode independently of channel incision. This implies that hillslope erosion is the first-order control on the high sediment yield in the Illgraben, which averaged $2.3 \times 10^5 \text{ m}^3 \text{ yr}^{-1}$ over the study period.

I developed a probabilistic model of sediment transfer in the Illgraben with the overall aim of explaining the observed non-linear and stochastic sediment discharge. The model is based on the concept of a sediment cascade, in which, following erosion sediment goes through multiple cycles of storage and remobilization. Sediment input is drawn from the probability distribution of slope failures and the model is driven by observed climate. The model consists of two sediment storage reservoirs representing hillslopes and channels and a basin-wide water reservoir, through which sediment and water are routed at a daily resolution according to simple but physically meaningful rules. Despite its simplicity, the model reproduces remarkably complex sediment discharge dynamics, which can be explained only by considering jointly the availability of sediment and the triggering potential, quantifying the role of history (system memory) and climate (triggering events) on sediment discharge in the Illgraben. Although the model was developed for the Illgraben, the findings have general implications for fluvial systems that can be schematized into sediment cascades and where the supply of sediment and triggering of events is largely stochastic. The model may be used in future research to investigate uncertainty in erosion rates back-calculated from sediment yield and to predict sediment yield under a changing climate in the Illgraben.

Zusammenfassung

Die Quantifizierung von Sedimentfracht von Einzugsgebieten im Gebirge ist eine Schlüsselkomponente in der Studie über die Entwicklung von Gebirgsketten, und sie ist wichtig für die talwärts lebende Bevölkerung, für welche Sedimente sowohl eine lebenswichtige Ressource als auch eine Gefahr sein können. Einzugsgebiete im Gebirge sind besonders anfällig für den Klimawandel aufgrund ihrer Empfindlichkeit gegenüber Schnee- und Eisschmelzprozessen und ihrer schnellen Niederschlag-Abfluss-Reaktion. Das Verständnis der Wechselwirkungen zwischen Prozessen der Erdoberfläche und dem Klima ist wichtig, um im Stande zu sein die Sedimentfracht von Gebirgsbecken unter einem sich ändernden Klima modellieren und vorherzusagen zu können. Ziel dieser Doktorarbeit ist es die Prozesse der Sedimentproduktion, des Sedimenttransports und der Sedimentfracht zu quantifizieren; ihre Interaktionen sowie die klimatischen und seismischen Steuerungen zu erkennen und schliesslich den Sedimenttransport im Illgraben zu modellieren. Der Illgraben ist ein kleines, aber sehr aktives Gebirgsbecken in den Schweizer Alpen anfällig für große Rutschungen und Murgänge.

Anhand von Luftbildern mittels digitaler Photogrammetrie konnten die Sedimentproduktion, der Sedimenttransport und die Sedimentfracht über einen Zeitraum von 42 Jahren von 1963 bis 2005 quantifiziert und in 4 Subperioden eingeteilt werden. Durch Rutschungen wurden die Berghänge mit einer extrem hohen durchschnittlichen jährlichen Rate von $0,39 \pm 0,03 \text{ m yr}^{-1}$ erodiert. Ich wählte einen Bestand von mehr als 2000 Rutschungen aus, deren Volumina sich über 6 Größenordnungen erstrecken und analysierte ihre Statistiken. Die Rutschungen folgen einer charakteristischen Größenhäufigkeitsverteilung mit einem roll-over und power-law tail. Die Ergebnisse belegen die Hypothese, dass die Form der Verteilung durch 2 verschiedenen Rutschungstypen entsteht: flache Rutschungen innerhalb der oberen verwitterten Schicht des Hanges, die eine eingeschränkte Tiefe sowie Volumen haben und tief sitzende Felsgesteinausbrüche, die entlang der Bruchflächen am Hang auftreten und einen grossen Volumenbereich aufweisen. Letztere machen mehr als 98% der Sedimentversorgung aus und begrenzen das Relief des Hanges, und liefern somit empirischen Nachweis für das Konzept des Schwellenabhangs. Die Ergebnisse demonstrieren auch die Bedeutung der Einschränkung des Skalenexponents zwischen Erdrutschgebieten und Volumen für verschiedene geologische Einstellungen.

Im Verlauf der Studie analysierte ich Klimadaten und seismische Daten mit dem Ziel die beobachteten Muster der Hangerosion (Produktion), Erosion im Flussbett (Übertragung) und Sedimentfracht erklären zu können. Ein deutlicher Anstieg der Hangerosionsrate in den 1980er Jahren ist vermutlich mit einem deutlichen Anstieg der Lufttemperatur und dem daraus resultierenden Rückgang der Schneedecke und Schneedauer verbunden. Allerdings verdeutlicht

die Analyse der potentiellen Auslöser einer einzelnen Rutschung im Illgraben, dass mehrere auslösende Mechanismen bestehen, so dass Rutschungen ein sehr stochastisches Phänomen darstellen. Die Erosionsrate im Flussbett ist eindeutig auf die Häufigkeit der intensiven Niederschlagsereignisse im Sommer zurückzuführen. Die Hangerosionsraten überschritten die Erosionsrate im Flussbett im beobachteten Zeitraum, was auf eine hangabwärts gerichtete gekoppelte Beziehung hinweist in welcher Berghänge unabhängig vom Flussbett erodieren. Dies impliziert, dass die Hangerosion der wichtigste kontrollierende Faktor der hohen Sedimentproduktion im Illgraben ist, welche im beobachteten Zeitraum im Mittel $2.3 \times 10^5 \text{ m}^3 \text{ yr}^{-1}$ beträgt.

Ich entwickelte ein probabilistisches Modell für den Sedimenttransfer im Illgraben mit dem übergeordneten Ziel den beobachteten nichtlinearen und stochastischen Feststoffaustrag zu erklären. Das Modell basiert auf dem Konzept einer Sedimentkaskade, in welcher das folgende Erosionssediment mehrere Zyklen einer Speicherung und Remobilisation durchläuft. Der Sedimenteintrag ist aus der Wahrscheinlichkeitsverteilung der Rutschungen herangezogen worden und das Modell wird durch die beobachteten Klimadaten angetrieben. Das Modell besteht aus zwei Sedimentspeichern, welche die Berghänge und das Flussbett repräsentieren und ein Wasserreservoir, durch das Sedimente und Wasser in einer täglichen Auflösung nach einfachen, aber physikalisch sinnvollen Regeln geleitet werden. Trotz seiner Einfachheit gibt das Modell eine bemerkenswert komplexe Feststoffaustragdynamik wieder, die nur durch die gemeinsame Betrachtung der verfügbaren Sedimente und des auslösenden Potentials erklärt werden kann, und quantifiziert die Rolle der Vorgeschichte (Speicher) und des Klimas (Triggerereignisse) auf den Feststoffaustrag im Illgraben. Obwohl das Modell für den Illgraben entwickelt wurde, haben die Ergebnisse allgemeine Implikationen für fluviale Systeme, die in Sedimentkaskaden schematisiert werden können und in denen die Versorgung von Sedimenten und das Auslösen von Ereignissen weitgehend stochastisch ist. Das Modell kann für zukünftige Studien verwendet werden, um die Unsicherheit von aus Sedimentfracht berechneten Erosionsraten zu untersuchen und um die Sedimentfracht in einem sich ändernden Klima im Illgraben vorherzusagen.

Acknowledgements

The last three and a half years have been a very steep but extremely enjoyable and rewarding learning curve, much of which I owe to my main supervisor and collaborator, Peter Molnar. He has helped me continuously over the years to formulate and constrain my ideas, analyze and interpret my data, and finally to present the results to the scientific community. I will miss our thought-provoking discussions. I am also very grateful to Brian McArdell at the Swiss Federal Institute for Forest, Snow and Landscape Research (WSL) for coming on board as my second supervisor. He has been a continual source of knowledge and inspiration, particularly on the Illgraben, my research catchment. I have spent many enjoyable hours in the Illgraben with Brian both in the channel and up on the channel crest observing earth-surface processes and landforms first-hand (though never a debris flow, unfortunately!). I am also very thankful to Professor Paolo Burlando for giving me the opportunity to do my PhD in his group and for helping to manage and facilitate my research. It was a pleasure to collaborate with you all.

Outside my direct circle of supervisors and Professor, I would like to thank Henri Eisenbeiss of the Institute of Geodesy and Photogrammetry at ETH for helping me to generate the digital elevation models, which form the basis of data that I worked with in my PhD and for his collaboration on my first research paper. I would also like to thank Professor Fritz Schlunegger of the University of Bern and the head of the SedyMONT project, which my PhD was part of, for many interesting discussions and for his collaboration on my second research paper.

Thanks to all my Hydrology group colleagues for all the stimulating lunch-time discussions on a diverse range of topics (I am now much more informed about European politics, in particular!). Bettina Schächli, Maurizio Savina, Nicola Pasquale, Marco Carenzo, Roger Bordoy, Illaria Clemenzi, Stefan Rimkus, Thanos Paschalis, Grigoris Anagnostopolous, Christoforos Pappas, Silvan Ragettli, Simoni Fatichi, Alvaro Ayala and Matteo Saletti; I have learnt a lot from you and have had a lot of fun with you both in and out of the office over the years. We made a great Sola 2012 team! Thanks particularly to Bettina Schächli, who has been a fantastic and helpful office mate, particularly when it comes to Matlab! Thanks also to Juliane Kneisler and Bettina for helping to translate my thesis abstract into German.

I have not just been a member of the Hydrology group, but also a member of SedyMONT, part of the European Science Foundation's TOPOEUROPE. This consisted of several other PhD projects, students and their supervisors: Sara Savi and Fritz Schlunegger close by in Bern; Martin Geilhausen, Jan-Christoph Otto and Lothar Schrott in Salzburg, Austria; Susan Liermann, Katya Laute and Achim Beylich in Trondheim, Norway; Daniel Franke, Jens Hornung and Mattias Hinderer in Damstaadt, Germany; Tanja Vicovac and Alexander Reiterer in Vienna, Austria; Vincenzo Picotti, Sandro Simoni and Francesco Brardinoni in Italy and Peter Schürch and Alex Densmore in Durham, UK. We had some amazing times together, at annual meetings and

workshops in exciting locations such as the Alps in Switzerland and Austria, in Bologna, Italy, and on the glaciers of Norway, as well as at EGU in Vienna. It was a pleasure to get to know you all and to share our ideas and these experiences together.

I would like to offer extra gratitude to Peter Schürch, who I first met at Durham while doing my MSc. He was a friend and mentor for me then and was in fact the one to show me the advertisement for my PhD and encourage me to apply, already being a SedyMONT PhD himself. He continued to be a mentor for me throughout my PhD with his efficient and clever approach to research being an inspiration to me. Sara Savi has also been a good friend, room-mate at conferences, as well as SedyMONT colleague of mine since starting my PhD.

I also feel as though I have been a part-time member of the Earth Surface Dynamics Group of Sean Willet at ETH. I attended several courses and field trips with this group, including great field trips to the Apennines in Italy and to the Pyrenees in Spain. It was on this last fieldtrip where I got to know Rebecca Reverman and Stefan Nagel, who have become good friends.

This research would not have been possible without funding from the Swiss National Science Foundation Grant 20T021-120467. This funding has also enabled me to attend several international conferences and workshops that were a particularly enjoyable aspect of my PhD. Several sources of data to which I am very grateful for are acknowledged in the individual research papers (Chapters 2-4) of this thesis.

The last three and a half years have not only been about sediment! I have had huge amount of fun in the mountains and great outdoors with many good friends, who are not all mentioned here. Roger Bordoy was a great climbing partner for the Bishorn and Nadelhorn as well as a number of smaller peaks. I have had some great ski tours, hikes, cycle tours and various other adventures with James Glover, Käthi Lichti, Erin Gleeson, Becci Blum and Nans Addor. James Glover, a friend from my BSc years in Durham, was a big inspiration for me to accept the PhD and embrace life in Switzerland, having moved over here to work with all-things-rock a year earlier than me. I will always be grateful to him for picking me up at the airport on first arriving in Switzerland and for introducing me to many people, especially Nans, who later would become my boyfriend.

I would especially like to thank Nans for constant encouragement and support with my PhD and for many fun and special times. Going back to my English roots, I'd like to thank my Mum, Janie, and my Dad, Jeff, for their unconditional love and support and for introducing me to the great outdoors. Regular family walking holidays with them and my brother, Tom, in Dorset, Cornwall and the Lake District in England and in the valleys around St. Martin de Belleville in the French Alps were formative for me and ignited my passion for the earth's landscape.

Contents

Abstract	i
Acknowledgements	v
1. Introduction	1
1.1. Motivation and aim	1
1.2. Background	2
1.2.1. Quantifying sediment production transfer and yield	2
1.2.2. Identifying controls on sediment production, transfer and yield	5
1.2.3. Modeling sediment yield	7
1.3. Study catchment	10
1.3.1. Sediment production in the Illgraben	12
1.3.2. Sediment transfer in the Illgraben	13
1.3.3. Sediment yield in the Illgraben	13
1.4. Summary of research papers	14
2. Erosional power in the Swiss Alps: characterizing slope failure at the head of the Illgraben	17
2.1. Introduction	18
2.2. Study site	19
2.3. Methods	22
2.3.1. DEM preparation	22
2.3.2. Uncertainty analysis	24
2.3.3. Slope failure analysis	25
2.3.3.1. Analysis of erosion rates	25
2.3.3.2. Extraction of areas and volumes of slope failures	26
2.3.3.3. Magnitude-Frequency analysis	26
2.3.3.4. Volume-Area and Depth-Gradient relations	29
2.4. Results	29
2.4.1. Erosion rates	29
2.4.2. Magnitude-Frequency distributions	30
2.4.3. Volume-Area relation	33
2.4.4. Pre-failure slope gradient of failures	34
2.5. Discussion	35
2.5.1. Methodological discussion	35
2.5.2. Physical interpretation of our dataset	36
2.6. Conclusions	39

3. Patterns and controls of sediment production, transfer and yield in the Illgraben	41
3.1. Introduction	42
3.2. Study site	44
3.3. Datasets	47
3.3.1. Sediment fluxes	47
3.3.2. Climatic variables	48
3.3.3. Seismic activity	49
3.4. Methods	49
3.5. Results	51
3.5.1. Sediment production and transport	51
3.5.2. Relation of changes to climate and earthquakes	56
3.5.3. Triggering of the 1961 rock avalanche	59
3.6. Discussion	60
3.6.1. Patterns and influences of hillslope erosion	60
3.6.2. Patterns and influences of channel sediment transfer	62
3.6.3. Hillslope-channel coupling and implications for landscape evolution and sediment yield	63
3.7. Conclusions	64
4. A probabilistic sediment cascade model of sediment transfer in the Illgraben	66
4.1. Introduction	67
4.2. Slope failures and debris flows in the Illgraben	69
4.3. Model structure and calibration	71
4.3.1. Hydrological model	73
4.3.1.1. Snow	73
4.3.1.2. Water balance	74
4.3.2. Sediment model	76
4.3.2.1. Sediment supply by slope failure	76
4.3.2.2. Sediment storage accounting	77
4.3.2.3. Debris flow generation	79
4.4. Results	80
4.4.1. Probability distribution of debris flows	80
4.4.2. Transport and sediment supply limitations	83
4.4.3. Timing of debris flows	85
4.5. Discussion	89
4.6. Conclusions	90

5. Conclusions and Outlook	92
5.1. Conclusions	92
5.2. Findings relevant to the Illgraben	95
5.3. Outlook	96
Bibliography	100
Appendices	112
A. Supplementary material for Chapter 2	112
A.1. Aerial photographs and camera calibration certificates	112
A.2. Details of Ground Control Points used in the photogrammetric procedure	130
A.3. Additional figures of slope change	133
B. Supplementary material for Chapter 3	134
B.1. Recorded debris flow volumes	134
B.2. Suspended sediment sampling	136
C. Supplementary material for Chapter 4	138
C.1. Independent calibration of hydrological model parameters	138
C.2. Estimation of channel sediment residence time	139
D. Photo documentation	140

List of Figures

Figure 1.1 – Simplified sediment cascade, modified from Ballantyne (2002).	3
Figure 1.2 – Figure from Guzzetti et al. (2008) showing a comparison between global ID thresholds both defined in their study (6 and 7) and in other studies (for details see Guzzetti et al., 2008). Dashed line shows 0.25 mm h^{-1} rainfall intensity.	6
Figure 1.3 – Typical plot of the magnitude-frequency relation observed in landslide inventories. Magnitude is usually expressed in area but may also be expressed in volume. Frequency is usually expressed in probability density, but may also be expressed as cumulative probability or non-exceedence probability.	9
Figure 1.4 – Location of the Illgraben within Switzerland (inset map) and the Rhone Valley.	11
Figure 1.5 – (a) the Illgraben basin showing the location of the study channel (b) and slope (c).	12
Figure 2.1 – Location of the study slope in relation to the Illgraben catchment, the Rhône Valley and Switzerland. Ground control points used in the photogrammetric process are also shown.	21
Figure 2.2 – Geology of a part of the study slope in the Illgraben catchment (photograph) in relation to the geology of the Illgraben and Illbach catchments. Geological map adapted from Gabus et al. (2008).	22
Figure 2.3 – Probability distribution of erosion depth for (a): periods A (1963 – 1986) and B (1986 – 2005); (b): sub-periods B1 (1986-1992), B2 (1992-1998) and B3 (1998-2005). Only statistically significant erosion of over 3 m, the mean σ_{diff} , is shown in each plot.	25
Figure 2.4 a,b – Spatial distribution of elevation change, including deposition, in the study slope and at the channel head for (a): sub-period B1 (1986-1992); (b) sub-period B2 (1992-1998), and location of the largest slope failures (SF1 and SF2).	26
Figure 2.5 a,b – (a): Empirical frequency-volume distribution for logarithmically transformed datasets (1) and (2). Uncertainty in the volume of individual landslides is shown for dataset (1) as the grey range. The uncertainty is similar for dataset (2). (b): Distributions for temporal sub-periods B1-B3 within dataset (1).	32
Figure 2.6 a,b – Complementary cumulative empirical distributions for (a) dataset (1) and (b) dataset (2), fit with theoretical power law model by the maximum likelihood method.	32
Figure 2.7 a-c – Volume-Area distribution of log transformed dataset (1) split into the three periods of analysis (a) B1: 1986-1992, (b) B2: 1992-1998, (c) B3: 1998-2005. Uncertainty in volumes is shown by the small dashed lines. Power-law fits are shown along with 95% prediction bounds. For model exponents see Table 2.7.	33
Figure 2.8 – Relationship between mean failure depth and slope gradient of the pre-failure surface for failures $> 233\text{m}^3$ (grey circles) and failures $< 233\text{m}^3$ (black circles) on the right-hand axes along with their probability distributions (grey and black lines respectively), plotted against the probability distributions of slope gradient of the study slope and Illgraben catchment (Figure 2.1).	34
Figure 2.9 – Example of the environment of type (1) failures: the upper 5m of weathered rock and unconsolidated sediment. A = loose sediment cover; B= fold in the quartzites cropping out at the surface; C= imminent failure of $\sim 5\text{m}$ depth.	37

- Figure 2.10 a-c** – Example of a type (2) failure, SF2 in Figure 2.4b. (a): 1992 orthophoto overlaid with the 1992-1998 elevation change map. (b): 1998 orthophoto overlaid with the same elevation change map. (c): Oblique photograph taken in July 2011 overlaid with the elevation change map. The relation of SF2 to the thrust fault is clear. We observed water originating from this boundary at point X. 39
- Figure 3.1** – Location map of the Illgraben in relation to the Rhône Valley and Switzerland (inset map). The locations of Sion and Grimentz, from which we obtained time series of temperature and snow depth are also shown. The study area delineated by the white box is shown in detail in Figure 3.2. 44
- Figure 3.2** – The Illgraben and Illbach catchments and Illgraben channel; (a) map of the study slope and channel within the Illgraben catchment and channel and in relation to the surrounding topography and hydrogeography; (b) view of the base of the study slope and upper part of the study channel from the catchment crest; (c) view of the upper part of the study slope from the catchment crest. Viewing directions of photographs (b) and (c) are shown in panel (a) with black arrows. 46
- Figure 3.3** – Estimated annual average debris flow output constructed from unpublished WSL project reports. Where debris flow volume was unknown prior to 2000, an average volume of $\sim 30,000\text{m}^3$ per event was used. The black arrow indicates the construction date of CD1. 48
- Figure 3.4** – Schematic of the sediment routing system with equations used to calculate rates of hillslope erosion, hillslope output, channel storage change and catchment output of sediment referred to in the text and displayed in Figure 3.5. T refers to the length of the period (years) between the relevant DEMs. Variables highlighted in bold are shown in Figure 3.5. 50
- Figure 3.5 a-c** – (a) Comparison of DEM-derived total catchment output rate with debris flow output rate. Output rate from debris flow data is obtained by normalizing the debris flow output, for 1963-2000 from unpublished WSL reports and for 2000-2005 from McARDell et al. (2009), by the total study area. This is only a rough estimation for periods A, B1 and B2 due to the fact that the debris flow output was only roughly estimated until 2000. (b) DEM-derived rates of hillslope erosion and output (erosion – deposition), channel sediment storage change for c1 and c2 (see also Figure 3.7) and total catchment output with associated uncertainty bars. (c) DEM-derived rate and depth of hillslope erosion for periods A to B3 and statistics of slope failures from Bennett et al. (2012) for sub-periods B1-B3. 52
- Figure 3.6** – Depositional zone at the base of the study slope and channel head. For values of σ_{diff} , see Figure 3.7. Data from Bennett et al. (2012). 54
- Figure 3.7** – Channel elevation change for periods A and B1–B3 (see also Figure 3.5). σ_{diff} values are the elevation uncertainties specific to each period. Only elevation changes above $\pm \sigma_{\text{diff}}$ are considered statistically significant (Bennett et al., 2012). 55
- Figure 3.8 a-d** – Empirical cumulative distribution functions of the main climatic variables in Table 3.2 for the different study periods. 57
- Figure 3.9** – Mean monthly temperatures for periods A and B adjusted for the mean elevation of the study slope. 59

Figure 3.10 – Seismic activity and meteorological conditions leading up to the rock avalanche on 26th March (red arrow).	60
Figure 4.1 – Location of the Illgraben in the Rhone Valley and Switzerland.	70
Figure 4.2 – SedCas model structure. The probability distribution of slope failures is from Bennett et al. (2012a). The distribution of sediment discharge events (debris flows) are those measured at the catchment outlet from 2000 through 2009.	72
Figure 4.3 – (a) Example of time series of modeled daily snow depth, rainfall, snowmelt and measured snow depth (in SWE) at Grimentz. (b) Cumulative distribution of modeled and measured daily snow depth for the period 2000-2009.	74
Figure 4.4 – Seasonal distribution of modeled hydrological variables. Plotted are the monthly means over the simulation period 2000-2009.	76
Figure 4.5 – Non-exceedence probability distribution of modeled debris flows, potential debris flows and observed debris flows, based on model runs with sediment input procedure (1). The black line is the mean of 1000 runs of the model and the red lines are the 5% and 95% percentiles. Potential debris flows are events with the maximum potential sediment concentration c_{max} in the hypothetical case of an abundant sediment supply.	81
Figure 4.6 – Mean actual debris flow volumes of 1000 runs versus potential debris flow. The black line is the one-to-one line in the case of an abundant sediment supply, i.e. represents transport limited events. The model was run with sediment input procedure (1) and the event data are binned to compute the mean.	83
Figure 4.7 – Relationship between sediment discharge and water discharge according to Equation (7). Sediment concentration c is calculated as the volume of sediment in the total volume of water and sediment in an event, assuming a material porosity $p = 0.52$, and where water is the excess discharge $Q - Q_{df}$. The Illgraben monitoring system only records “large events” (horizontal line in figure) which exceed a sediment discharge of 2900 m ³ .	84
Figure 4.8 – Cumulative distribution of the actual volumetric sediment concentration c of modeled debris flows, shown for procedure (1).	85
Figure 4.9 – (a) Time series of water discharge Q , modeled debris flows and supply limited debris flows and floods, and observed debris flows. Grey bars denote snow cover. (b) Evolution of channel sediment storage during one example model run, shown for procedure (1).	86
Figure 4.10 – (a) Seasonal distribution of mean sediment input and output depth in (mm) (modeled and observed); and (b) active sediment storage, both shown for procedure (1).	87
Figure 4.11 – Modeled and observed (36 events) probability of debris flow occurrence as a function of daily rainfall intensity. Simulations are for sediment input procedure (1).	88
Figure A.1 – One of each aerial photograph stereopair used in the photogrammetric procedure to extract DEMs as detailed in Chapter 2.	112
Figure A.2 – Next 17 pages – Camera calibration certificates for cameras used to acquire the photographs in Figure A.1.	113
Figure A.3 – GCP 30 – taken from documentation by MSc students of the University of Bern.	131

Figure A.4 – GCP 31 – taken from documentation by MSc students of the University of Bern.	131
Figure A.5 – GCP 35 – taken from documentation by MSc student of the University of Bern.	132
Figure A.6 – Collection of GCP 35 by a MSc student of the University of Bern. Photo taken by an MSc student of the University of Bern.	132
Figure A.7 – Part of the study slope, the South face of the Illhorn in 1921 and from roughly the same location 90 years on in 2011. Significant erosion is evident from comparison of the two photos.	133
Figure A.8 – Slope failure (SF) 1 in Figure 2.4 shown by the 1986-1992 elevation change overlaid on the orthophotos from these periods. The removal of the cliff between 1986 and 1992 by slope failure is clear from comparison of the orthophotos, providing some validation of the elevation change calculated from the DEMs.* The value of 3.1 is calculated from uncertainty analysis presented in Chapter 2.	133
Figure B.1 – Preliminary sediment rating curve for suspended sediment transport in the Illgraben. The sample point highlighted by the red circle was taken about 1 day following a debris flow and is starred in Table B.3.	137
Figure C.1 – Modified from Figure 7 in Badoux et al. (2009) showing the selection of the critical discharge for debris flow generation (Q_{df}) in the model in Chapter 4.	138
Figure D.1 – Rain/Temperature gauge 1, 2200m, from which I obtained time series of rainfall with which to validate Rhires-D modeled precipitation and time series of temperature with which to calculate a lapse rate from Sion in Chapter 3.	140
Figure D.2 – Rafael Caduff and a Masters student observing the study slope in summer 2011.	140
Figure D.3 – Brian McArdell (left) and Peter Molnar at CD29 in Spring 2012.	141
Figure D.4 – Me (Georgie Bennett) in the channel just below CD28 collecting a suspended sediment sample.	141
Figure D.5 – Rockfall in the Illgraben in December 2012.	142
Figure D.6 – Suspended sediment transport and deposition of boulders along the channel, February 2012.	142

List of Tables

Table 2.1 – Aerial photograph parameters.	23
Table 2.2 – DEM and georeferencing parameters.	23
Table 2.3 – Results of registration and error analysis. σ_{reg} is the standard deviation of registration error. σ_{diff} is the standard deviation of the combined error in elevation between two DEMs.	24
Table 2.4 – Next page – Comparison of values of the exponents of the power law tails (β and ρ) obtained for landslide and rockfall inventories, including this study, ordered from low to high β . R= Rockfall, L=Landslide, V= Volume, A=Area. H= Historical, E=Event-based. Values in bold are those reported in the studies.	28
Table 2.5 – Comparison of frequency-volume relationship using the methods of least squares fitting (LS) to the PDF and CCDF and maximum likelihood estimation (MLE) based on the method of Clauset et al. (2009). p – values over 0.1 indicate a good fit to the power law distribution. ‘Tail’ refers to the power law tail, i.e. where $x \geq x_{min}$.	30
Table 2.6 – Comparison of frequency-volume relationship using different methods for different periods within dataset (1) (B1 – B3). p – values over 0.1 indicate a good fit to the power law distribution. The p – value is not reported for B2 as the number of landslides is too small for an accurate estimation of β . ‘Tail’ refers to the power law tail, i.e. where $x \geq x_{min}$.	31
Table 2.7 – Comparison of volume-area relationship for projected and plan area and different periods using dataset (1). A is the projected area and A^* is the real surface area of the slope failure.	33
Table 3.1 – Rates of hillslope erosion (Eh) and output (Oh), channel storage change ($\Delta Sc1$ and $\Delta Sc2$) and catchment output (Ot) and uncertainties. Positive ΔSc means erosion.	54
Table 3.2 – Analysis of climatic variables for sub-periods within 1963-2005. Statistically significant changes in statistics are marked X. All p -values for statistically significant changes in variables marked in Table 3.3 are less than 0.04.	58
Table 4.1 – Model parameters. Parameters estimated independently are indicated with X.	73
Table 4.2 – Results of 1000 model runs for different sediment input procedures compared to observations (df = debris flow; * indicates the procedures that were closest to the observation for each measure). The percentage of supply-limited debris flows is calculated as the % of actual debris flows with lower than maximum sediment concentration. The percentage of supply-prohibited debris flows is calculated as the % of potential debris flows that did not occur due to the absence of any stored sediment along the channel.	82
Table 4.3 – Comparison of the predictive skill of variations of our model with variations of a more simple precipitation exceedence model based on accuracy statistics. We consider the prediction of all debris flows ($> 0 \text{ m}^3$) in the analysis.	88

Table A.1 – Ground Control Points (GCPs) used for each set of aerial photographs. For GCPs from Berger (2010) please see Appendix in Berger (2010). GCPs from the University of Bern (Uni Bern) were collected by MSc students during a field course and are given in more detail in figures below.	130
Table B.1 – Sediment volumes of observed debris flow events in the Illgraben in the period of 1963 to 1999 (modified after Rhyner et al., 2005).	134
Table B.2 – Debris flow volumes from 2000 through 2009 (McArdell et al., 2009). Debris flows from 2000 through 2005 were used along with debris flows from 1998 and 1999 shown in Table B.1 to calculate the annual sediment yield in period B3 shown in Figure 3.5a.	135
Table B.3 – Details of the Illgraben suspended sediment samples.	137
Table C.1 – Table modified from Nydegger (2008) showing the calibration of catchment water storage (S_{wcap}). The first 5 columns are values reported in Nydegger (2008) for the analyzed events and last 2 columns are my calculations of catchment water storage. The value highlighted in bold is a minimum estimate of catchment water storage based on the greatest difference between rainfall and runoff of the analyzed events. This reasoning is explained in more detail in Chapter 4.	138
Table C.2 – Calculation of residence time of sediment in channel storage.	139

1. Introduction

1.1. Motivation and aim

Quantifying sediment yield from mountain basins is an important component in the study of the evolution of mountain ranges, which includes the role of tectonics, climate and erosion history. It is also of considerable societal significance because of its influence on downstream regions. It has been estimated that close to 60% of global sediment delivery to the coastal zone is derived from basins draining high mountains (Syvitski et al., 2005). A lack of sediment supply to coastal regions due to upstream damming is resulting in the sinking of river deltas around the world, threatening millions of lives (Syvitski et al., 2009). Along Alpine rivers, communities suffer both from a lack of sediment in heavily regulated rivers and from an excess of sediment during extreme floods and debris flows (Jakob and Hungr, 2005). Furthermore, mountain basins are particularly susceptible to climate change because of their sensitivity to snow and ice melt processes and rapid rainfall-runoff response (e.g. Scherrer et al., 2004; Birsan et al., 2005). Ultimately, we would like to predict future mountain basin sediment yield under a changing climate. A first step to achieving this goal is to quantify and model past mountain sediment yield. However, quantification of the response of sediment yield to climate forcing is still a developing field, lacking good field datasets and a solid conceptual framework in which to interpret the data.

Mountain basin sediment transfer has been conceptualized as a sediment cascade (Burt and Allison, 2010 and references therein), in which, following erosion, sediment travels through multiple cycles of storage and remobilization before exiting the basin. Related to this concept is that of the sediment budget, which aims to account for all of the sediment in the sediment cascade (e.g. Slaymaker, 1991). However, difficulties in measuring sediment supply and transfer processes as well as short record lengths hinder the construction of sediment budgets of sufficient length and detail with which to corroborate the sediment cascade concept and to analyze the impact of climate forcing on sediment yield. In particular there is a lack of measurements of sediment production, via landslide and rockfall processes, and sediment storage times (Rosser, 2010). Further research efforts are needed that should focus on (i) quantifying sediment supply, storage and transfer processes (ii) identifying controls on these processes, and (iii) addressing the lack of models with which to extend the concept of the sediment cascade beyond the identification and quantification of individual processes and sediment storages to the investigation of thresholds and feedbacks within the system. These are the main aims of this thesis.

The thesis is structured as follows. In the remainder of this chapter I introduce the state of the art for the research themes identified above, the research catchment and give a summary of the research papers that comprise chapters 2, 3 and 4. The conclusions and outlook are presented in Chapter 5, and additional details pertaining to methods and data presented in chapters 2-4 are given in the Appendix.

This PhD is part of the European Science Foundation TOPOEUROPE SedyMONT project that brings together 7 PhDs at universities around Europe under the common aim of understanding the timescales and controls of sediment dynamics in mountain basins.

1.2. Background

1.2.1. Quantifying sediment production, transfer and yield

Production – Sediment production in mountainous landscapes occurs by two general types of erosive processes: hillslope diffusion and landsliding. Diffusive processes are those considered to be dependent primarily on slope angle and include rainsplash, animal burrowing and tree throw (Roering et al., 1999). These processes detach and gradually diffuse sediment downslope. Landsliding can take a wide range of forms (Cruden and Varnes, 1996) from shallow soil slides to deep-seated bedrock slides that have more in common with rockfall. I therefore use the term slope failure for landsliding in this thesis. In contrast to diffusive processes, slope failures are discrete events that may have numerous triggers and thus are more stochastic in terms of their sediment delivery. Slope failures are the most important erosional process (Brardinoni and Church, 2004) and the most important to quantify. However, they are also inherently difficult to measure due to their inaccessibility and often catastrophic nature. Thus, failure volumes are usually inferred from their areas, which can be measured from aerial photographs or in the field (e.g. Brardinoni et al., 2003), using empirical relationships established in other catchments (e.g. Hovius et al., 1997). However, uncertainty in the scaling relation between volume and area used may lead to large uncertainties in failure volumes (Larsen et al., 2010). Therefore more studies are needed to constrain the scaling exponent for different geological settings. Techniques to directly measure volumes include terrestrial laser scanning (e.g. Lim et al., 2010), airborne laser scanning (e.g. Fischer et al., 2011), radar interferometry (e.g. Caduff et al. in review) and photogrammetry (e.g. Schwab et al., 2008, Berger et al., 2011b). These techniques all involve the production of sequences of digital elevation models (DEMs) that can be used to assess surface change. Photogrammetry is used to convert historical archives of aerial photographs often extending as far back as the 1940s into digital elevation models (e.g. Bennett and Evans, 2012) and therefore allows the reconstruction of surface change over the longest period of time.

Transfer – Following erosion, the transfer of sediment to catchment outlet is not always direct and can involve several cycles of storage and remobilization as illustrated by Figure 1.1. For example sediment can be eroded from a rock wall by rockfall, primarily stored in a talus cone at the base of the slope before being reworked by fluvial processes and being deposited for a second period of time in a valley fill deposit. Further fluvial reworking of this deposit will result in the eventual discharge of the sediment from the catchment and into a sedimentary sink, which is a more permanent zone of storage than a sediment store where sediment resides for considerable periods of time, such as a lake (Fryirs and Brierly, 2001). The spatial chain of sediment stores is termed the sediment cascade (Burt and Allison, 2010, and references therein). The location and size of these sediment stores is primarily determined by the available

accommodation space in the landscape (Fryirs, 2013). For example, there is less accommodation space at the base of a hillslope than along the valley such that sediment is likely to be stored for a longer period of time in the valley.

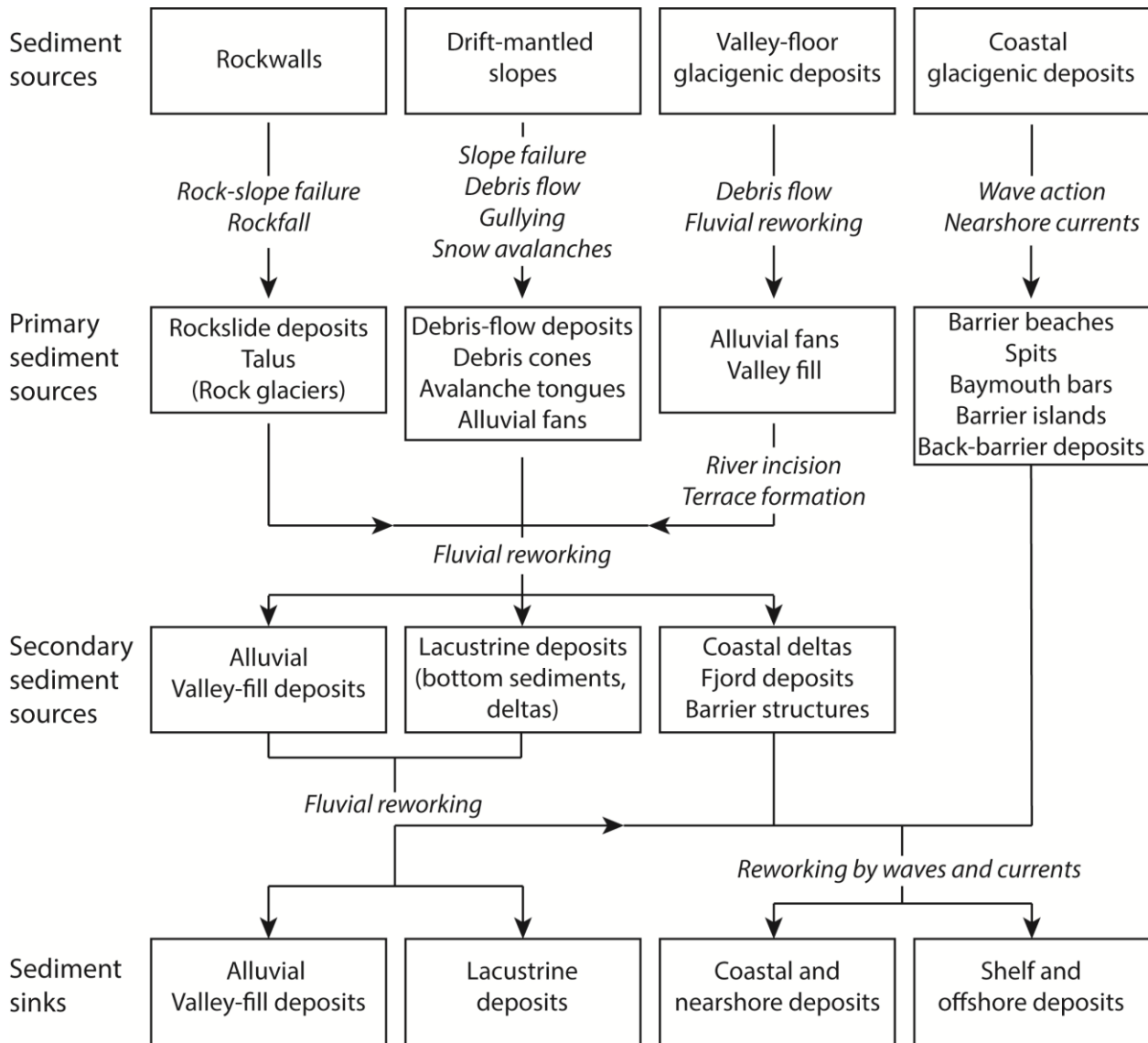


Figure 1.1 – Simplified sediment cascade, modified from Ballantyne (2002).

Sediment storage plays a crucial role in the rate of sediment transfer (Lisle and Church, 2002) making it important to identify and quantify sediment stores and to calculate their residence time. Residence time can be calculated as the mass of the reservoir divided by the flux through the reservoir (Eriksson, 1971), as used by Lancaster and Casebeer (2007) to calculate sediment flux from measurements of deposit volumes and residence times. This calculation is based on a linear storage-output relationship such that all sediment in the reservoir has an equal probability of evacuation, as hypothesized by Benda and Dunne (1997a), Lisle and Church (2002) and Malmon et al. (2003), and Lancaster and Casebeer (2007) for fluvial deposits in their study catchment. Conversely, Nakamura and Kikuchi (1996) found that a proportion of

sediment passing through a floodplain is deposited at the valley margins into long term storage that is inaccessible to the majority of fluvial events and therefore unconnected from the system (Brierley et al., 2006). In this case sediment transfer times in the valley fill have a power-law distribution (Bolin and Rodhe, 1973), with younger sediment stored along the channel having a higher probability of evacuation than older sediment along the valley margins. Lancaster and Casebeer (2007) also found a power-law distribution of transit times for debris flow deposits in their study catchment. Long term measurements of sediment storage and fluxes are needed to calculate residence times and to study the sediment storage-output relation in other catchments. Again, photogrammetry is well suited to this task.

Sediment can be reworked or remobilized from storage by various fluvial processes. In this thesis I focus on transfer of sediment originally produced from rock walls by slope failure in the upper reaches of a mountain catchment, which is dominated by debris flows. Debris flows are fast moving mixtures of water, air and sediment (Varnes, 1978) that show flow behavior intermediate between sediment-transporting floods and landslides (McArdell et al., 2007). Cycles of channel scour and aggradation in debris flow channels were described by Benda (1990), Bovis and Jakob (1999), Jakob et al. (2005) and Berger et al. (2011b), amongst others. Jakob et al. (2005) discuss the recharge time of a debris flow channel following a debris flow, which is in turn dependent on the rate of hillslope erosion. The timing and magnitude of erosion at a point along the channel may be measured in the channel using erosion sensors (e.g. Berger et al., 2011a). However, spatial patterns of erosion and deposition are best measured using repeat laser scanning or photogrammetry. Schürch et al. (2011a) used laser scanning before and after debris flows to monitor debris flow erosion and deposition. Berger et al. (2011a) used close range photogrammetry to quantify change on an event basis and aerial photogrammetry to quantify change on a seasonal basis (Berger et al., 2011b). Few studies have utilized historical archives of aerial photographs to measure spatial patterns of sediment transfer over periods of decades, as I do in this thesis.

Yield – Sediment yield can be differentiated into different size fractions: dissolved, suspended and bed loads (Waugh, 2000). The suspended and bed loads make up the mechanical load, which together are the focus of this thesis. In fluvial environments suspended sediment makes up the majority of the load and is therefore the more commonly measured (e.g. Gray et al., 2010). There are multiple methods for sampling suspended load consisting of manual and automatic samplers (Gray, 2008). Bed load is more difficult to measure due to its size and variability but has been measured using a variety of traps and sensors (Gray et al., 2010). In many cases an empirical ratio of bedload to suspended load is used to calculate bedload from measurements of suspended load (Turowski et al., 2010). However, the ratio of bedload to suspended load is highly variable and as drainage areas decrease and channel slopes increase, bedload makes up larger percentages of the total load (Turowski et al., 2010) and debris flows may occur. In contrast to fluvial transport in which there is a relatively clear stratification between the two components enabling them to be measured separately, debris flows contain a mixture of sediment size fractions throughout the flow meaning that these must be measured together. Measuring debris flows involves extensive instrumentation of the channel that

automatically records debris flow depth, velocity and density (McArdell et al., 2009), from which sediment volume can be calculated. Due to the large expense of such a measurement set-up, direct measurements of debris flow volumes are relatively rare (Marchi et al. 2002; Hürlimann et al., 2003; McArdell et al., 2009).

Sediment yield can instead be measured indirectly from reservoirs, if present in the catchment, and valley fills (Hinderer et al., 2001), and in the case of debris flows from deposits using dendrochronology (Stoffel, 2010). Another way to measure sediment yield indirectly is to quantify surface change over the catchment over a period of time (e.g. Berger et al., 2011b). While these techniques have lower temporal resolution, they have the advantage that they enable the quantification of sediment yield back in time, which is the first aim of this thesis.

In this thesis I utilize digital photogrammetry to quantify sediment production, transfer and yield in a mountain basin over periods of decades. This approach has been used to model geomorphic change related to several mountain environment processes including permafrost creep (Kaab, 2002), gully incision (Betts et al., 2003), glacier recession (e.g. Bennett and Evans, 2012) and slope failure (e.g. Schwab et al., 2008) but has rarely been used to quantify catchment sediment transfer and yield (e.g. Berger et al., 2011b), especially over periods of decades.

1.2.2. Identifying controls on sediment production, transfer and yield

Production – Sediment production in mountain basins containing steep bedrock slopes is dominated by rock-slope failure. Controls on rock-slope failure can be divided into conditioning factors, destabilizing processes and triggering factors. Conditioning factors include bedrock type, strength, and fracture density (Moore et al., 2009). Research into destabilizing processes and triggering factors of rock-slope failure is divided into instrumental approaches involving the installation of various monitoring equipment into the slope (e.g. Matsuoka and Sakai, 1999; Gruber et al., 2004; Gischig et al., 2011) and analysis of long time series of slope failures and potential triggering factors in the attempt to identify correlations between hillslope activity and these variables (e.g. Allen et al., 2011; Fischer et al. 2012). Destabilizing and triggering processes may be rainfall (e.g. Crozier, 2010; Rossi et al., 2010), freeze-thaw weathering (Matsuoka and Sakai, 1999), frost cracking/ice-segregation (Hales and Roering, 2007), permafrost degradation (Gruber et al., 2004) and seismic activity (e.g. Keefer, 1984; Korup, 2010). The combination of these processes means that in some settings it is difficult to detect the dominance of any one particular process (e.g. Allen et al., 2011; Rosser et al., 2007). Rosser et al. (2007) hypothesize that a slope accumulates damage from small failures and eventually reaches a threshold condition for large failure, which thus may have no apparent trigger. Although instrumental studies provide details pertaining to the process of failure, analysis of long time series of hillslope erosion data along with potential influencing variables can shed light on first order controls on hillslope erosion (e.g. Fischer et al., 2012) and is the approach that I take in this thesis.

Transfer – Sediment transport in mountain channels is a function of some measure of flow strength, like stream power (Whipple and Tucker, 1999), which in turn is a function of discharge and slope for a certain channel cross-section. Thus sediment transfer is primarily controlled by the variables that control discharge: rainfall and snowmelt (and glacier melt in glacierized catchments). Discharge exerts a shear stress on the channel bed and it is well known that to entrain sediment of a certain size fraction, the critical shear stress for that size must be reached (Bagnold, 1966). The amount of sediment transported is then a function of the excess shear stress. Debris flows may occur in the case of an abundant supply of loose sediment and steep slopes. The susceptibility of a catchment to debris flows is therefore primarily dependent on its morphology and lithology (Cannon, 2001). In-channel entrainment of sediment by water runoff as described above is one of the main mechanisms of debris flow entrainment (e.g. Cannon and Reneau, 2000). Debris flow activity has thus been linked with high intensity rainfall (Caine, 1980; McArdell et al., 2007; Coe et al., 2008; Guzzetti et al., 2008; Badoux et al., 2009), antecedent moisture (Wieczorek and Glade, 2005) and snow melt (Bardou et al., 2004). Figure 1.2 shows a compilation of global rainfall intensity-duration (ID) curves for shallow landslides/debris flows from Guzzetti et al. (2008). These curves all show that with increased rainfall duration, the intensity of rainfall needed to trigger debris flows decreases linearly due to the increased saturation of the catchment. Other initiation mechanisms of debris flows include water flow over loose sediment deposits at the base of a cliff (e.g. Larsen et al., 2006), catastrophic failure of landslide dammed lakes (e.g. Badoux et al., 2009) and the transformation of landslides into debris flows (e.g. Bovis and Dagg, 1992; Iverson et al., 1997; Burtin et al., 2012).

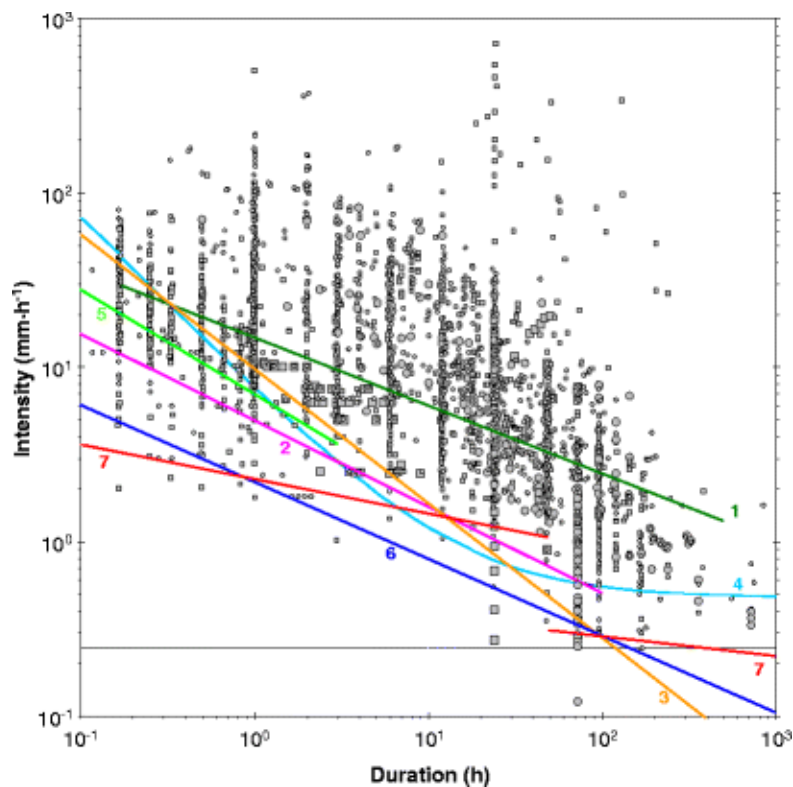


Figure 1.2 – Figure from Guzzetti et al. (2008) showing a comparison between global ID thresholds both defined in their study (6 and 7) and in other studies (for details see Guzzetti et al., 2008). Dashed line shows 0.25 mm h^{-1} rainfall intensity.

Yield – Catchments can be broadly classified into supply/weathering-limited or transport/detachment-limited with regard to sediment discharge (Bovis and Jakob, 1999). In supply-limited catchments sediment discharge is limited by sediment supply and the magnitude and frequency of sediment discharge events, for example debris flows, will depend on the recharge time of sediment in the channel (Jakob et al., 2005) and therefore on the rate of sediment production. In transport-limited catchments sediment discharge magnitude and frequency is limited by transport capacity or the magnitude and frequency of runoff events capable of entraining sediment (Bovis and Jakob, 1999). In fact these cases are two ends of a spectrum and most catchments alternate between these two conditions. We therefore need to consider both controls on the supply and transfer of sediment to effectively understand the controls on sediment yield. It is also important to consider the coupling of hillslope and channel erosion. Coupling may either be in the upslope direction, in which hillslopes respond to channel incision by landsliding, usually at the toes of the slopes (e.g. Burbank et al., 1996; Whipple, 2004), or in the downslope direction, in which hillslopes erode independently of channel incision in response to environmental controls (Schlunegger et al., in press). In the first case, which is the more commonly reported, the channel incision and its controls are the dominant control on hillslope erosion and on sediment yield. In the second case, hillslope erosion and its controls are the first-order control on sediment yield.

Despite more clear controls on sediment transfer than on hillslope production, the influence of geomorphic thresholds, storage effects and hysteresis (Phillips, 2006) can result in non-linear and unpredictable sediment discharge behavior at the event scale. A system is non-linear if the outputs are not proportional to the inputs of water and sediment across the entire range of the inputs (Phillips, 2003). An example of a geomorphic threshold is the critical shear stress needed to entrain sediment. Thus up to a certain discharge there is no or very little sediment transport. Once the critical discharge is reached to entrain sediment, the amount of sediment transported by the flow may be limited by the amount of sediment in storage. Thus discharge events of similar magnitude may have a range of different sediment concentrations (e.g. Van der Wiel and Coulthard, 2010). Sediment discharge may decrease throughout a single event or over longer timescales, due to a gradual depletion of sediment or due to other effects, such as dilution by groundwater (Andermann et al., 2012). It is important to consider these effects to understand and model sediment discharge at the event scale.

1.2.3. Modeling sediment yield

Modeling approaches

Numerical modeling is useful for understanding and developing hypotheses about mountain basin sediment transfer dynamics because it enables full control over initial conditions and parameters, which is difficult to achieve in laboratory modeling studies. The repeatability of model experiments and the ability to use the model to predict future behavior of a system (Van de Wiel et al., 2011) are further advantages. There are basically two modeling approaches to trace the flux of sediment through a fluvial system. The first is a pathway approach taken in

landscape evolution or soil erosion modeling, applying a set of conservation equations for the motion of water and sediment on a grid basis, usually fully distributed in space (e.g., Istanbuluoglu & Bras, 2005; Coulthard et al., 2000; Tucker et al., 2001; Molnar et al., 2006). These models simulate the transfer of sediment through the entire river basin; however they have to assume sediment transport laws and are heavily data-dependent. As such they are subject to uncertainties which are difficult to evaluate, leading to an over-parameterized problem where observed data are generally not sufficient to justify the model complexity.

The alternative approach is one where a systemic view of the fluvial system is taken as a cascade of sediment reservoirs (e.g. Davies & Korup, 2010) with different degrees of connectivity to each other that comes from the physical internal coupling between production (hillslopes) and transport (channels) elements of the fluvial system (e.g., Harvey, 2001). Such a modeling approach can be termed conceptual and attempts to capture the essential physics of the system (Brasington and Richards, 2007; Kirchner 2009) in contrast to the first type of models described. Furthermore, it is often probabilistic rather than deterministic, as in the case of the first type of models described, the advantage being that a distribution of possible outcomes contains the uncertainty in the model prediction. There are successful examples of this approach in the geomorphological community, most notably for processes such as landslides (Benda & Dunne, 1997a), sediment storage and routing in channels (Benda & Dunne, 1997b; Lisle & Church, 2002), catchment sediment delivery ratio (Lu et al., 2005; 2006), among others. The contribution of this thesis is an application of this concept to the interactions between sediment production by landsliding and its transfer into debris flows in an active debris-flow catchment in the Alps (Section 1.3).

Modeling sediment input

All models of sediment transfer require a sediment source. Most landscape evolution and soil erosion models of the first type of models described above incorporate diffusion in the form of a linear diffusion equation, where diffusion is a function of slope gradient (Tucker and Hancock, 2010). Some incorporate shallow landsliding in the form of a non-linear diffusion equation which enables transport rates on steep slope to increase at a greater than linear rate with slope gradient (e.g. Howard, 1994; Roering et al., 1999; Gabet, 2000). Deep-seated landsliding however is more difficult to describe in a physical manner and thus poses a significant challenge to physically-based landscape evolution and sediment yield modeling. There are examples of physically-based models that attempt to deterministically predict movement of individual failures based on geomechanical slope properties (e.g. Malet et al., 2005) but spatial and temporal variability in hillslope material properties, vegetation and triggering factors make it difficult to extrapolate these to the landscape scale. The statistical analysis of past slope failures is an alternative approach to modeling slope failure occurrence and magnitude in a probabilistic way through the construction of frequency-magnitude distributions and the fitting of distribution laws (e.g. Malamud et al., 2004). These models may be incorporated in models of sediment transfer (e.g. Fuller et al., 2003). It is this approach that I use in this thesis to model slope failure (Chapter 2), which is incorporated into a model of sediment transfer (Chapter 4).

Magnitude-frequency distribution laws exist for other natural events. For example, it is well known that earthquakes follow a power-law distribution (Gutenberg and Richter, 1949), while flood peaks generally follow one of the extreme value distributions (Stedinger et al., 1993). These laws are widely used to derive a probabilistic recurrence rate of an event of a given size. More recently the areas of landslides have been fit with various distributions. Malamud et al. (2004) fit several landslide inventories with a 3 parameter inverse Gamma distribution, and Stark and Hovius (2001) fit a double Pareto distribution to their landslide inventory. Both distributions model the frequency of medium-large landslides with a power-law. The frequency of smaller landslides drops off at a certain landslide magnitude. This part of the distribution is referred to as a 'roll-over' and is typical of landslide distributions (Figure 1.3).

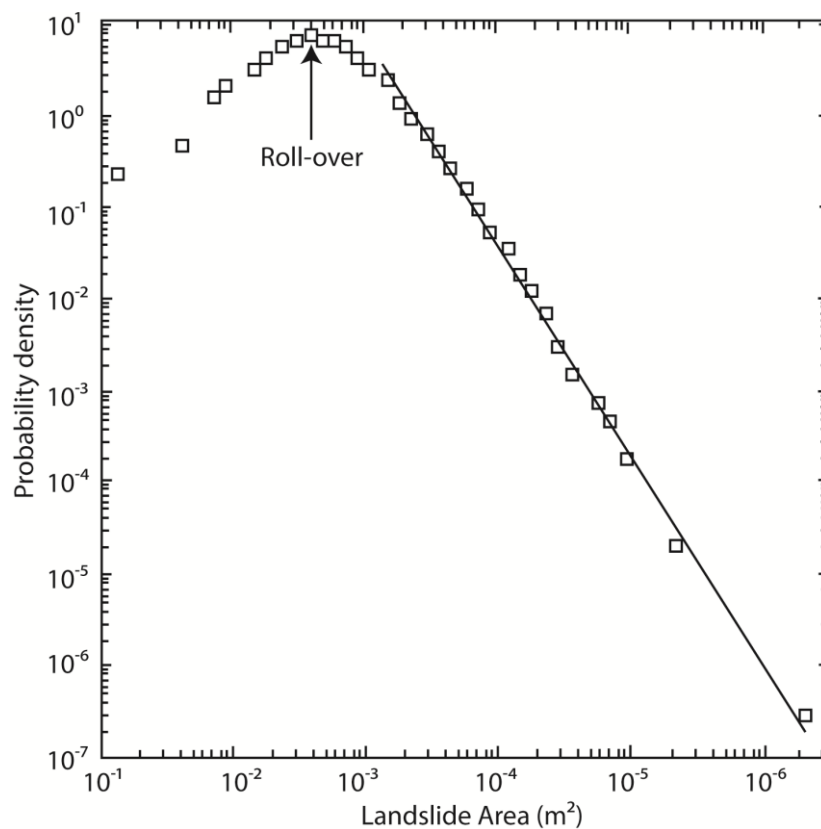


Figure 1.3 – Typical plot of the magnitude-frequency relation observed in landslide inventories. Magnitude is usually expressed in area but may also be expressed in volume. Frequency is usually expressed in probability density, but may also be expressed as cumulative probability or non-exceedence probability.

In order to better understand the physical meaning of the statistical distribution of landslides, it is interesting to consider the origin of the roll-over. In the past it was suggested that it was the result of the under-sampling of smaller landslides (Stark and Hovius, 2001). However, several recent studies have suggested a physical basis for this (e.g. Katz and Aharonov, 2006; Stark and Guzzetti, 2009). Katz and Aharonov (2006) suggest that landslide inventories contain 2 different processes. Smaller landslides in the roll-over occur by sliding and slumping in the shallow, homogenous top layer of the slope. The size of the events is controlled by the relationship

between failure depth (constrained to the depth of the layer at the time of triggering) and area. Medium to large landslides are fracturing events within the deeper, heterogeneous layer of the slope, the size of which are controlled by the location of failure planes and follow a power law distribution. More landslide inventories with directly measured volumes, like that developed in this thesis, are needed to test the validity of the proposed theoretical distributions and to test the hypothesis of Katz and Aharonov (2006).

Hydrology and sediment transfer

Models of sediment transfer also need a mechanism of generating runoff from precipitation that may subsequently entrain sediment (Section 1.2.2). The first type of sediment transfer models described above employ physically-based equations of runoff generation and flow routing (e.g. Darcy's law, Richards' equation). The problem of these models is that they assume that equations based on small scale process investigations scale up to larger scales, such as the catchment, which in fact is not likely the case (Harrison, 2001; Kirchner, 2006). An alternative approach is to try to identify a model structure and suitable equations to describe the macroscopic behavior of the system (Kirchner, 2009) or, in other words, capture the 'essential physics' of the process (Brasington and Richards, 2007). For example, Kirchner (2009) showed how runoff in two UK catchments can be modeled based on a single equation that translates time series of precipitation and evapotranspiration into stream flow. This approach is based on the premise that heterogeneity in small-scale processes does not necessarily lead to complex system behavior at large scales and that catchments can display emergent behavior (Harrison, 2001). This is the approach that I take to modeling catchment runoff in the sediment transfer model presented in this thesis (Chapter 4).

1.3. Study catchment

The study catchment in which the research aims are investigated is the Illgraben catchment in the Rhône Valley in southwest Switzerland (Figure 1.4). This highly active, alpine catchment prone to large slope failures and debris flows is ideally suited to systematically analyze the interactions between sediment production (landslides, rockfalls) on hillslopes and sediment transfer (debris flows) in the channel system. The Illgraben is of particular scientific interest due to a sediment discharge that exceeds Alpine standards by more than two orders of magnitude (Schlunegger et al., 2009).

The entire Illgraben basin is $\sim 9.5 \text{ km}^2$ in area, consisting of two tributary basins: the Illgraben ($\sim 4.6 \text{ km}^2$), which outputs several debris flows each year into the Rhône River, and the Illbach ($\sim 4.9 \text{ km}^2$), which contributes very little to sediment output due to the construction of the Illsee dam in 1923 (Berger, 2010). In this thesis the focus is on the active Illgraben sub-catchment, referred to hereafter as the Illgraben. Within the Illgraben, we focus on a single study slope and the channel until the fan apex (Figure 1.5a-c) (Chapter 2).

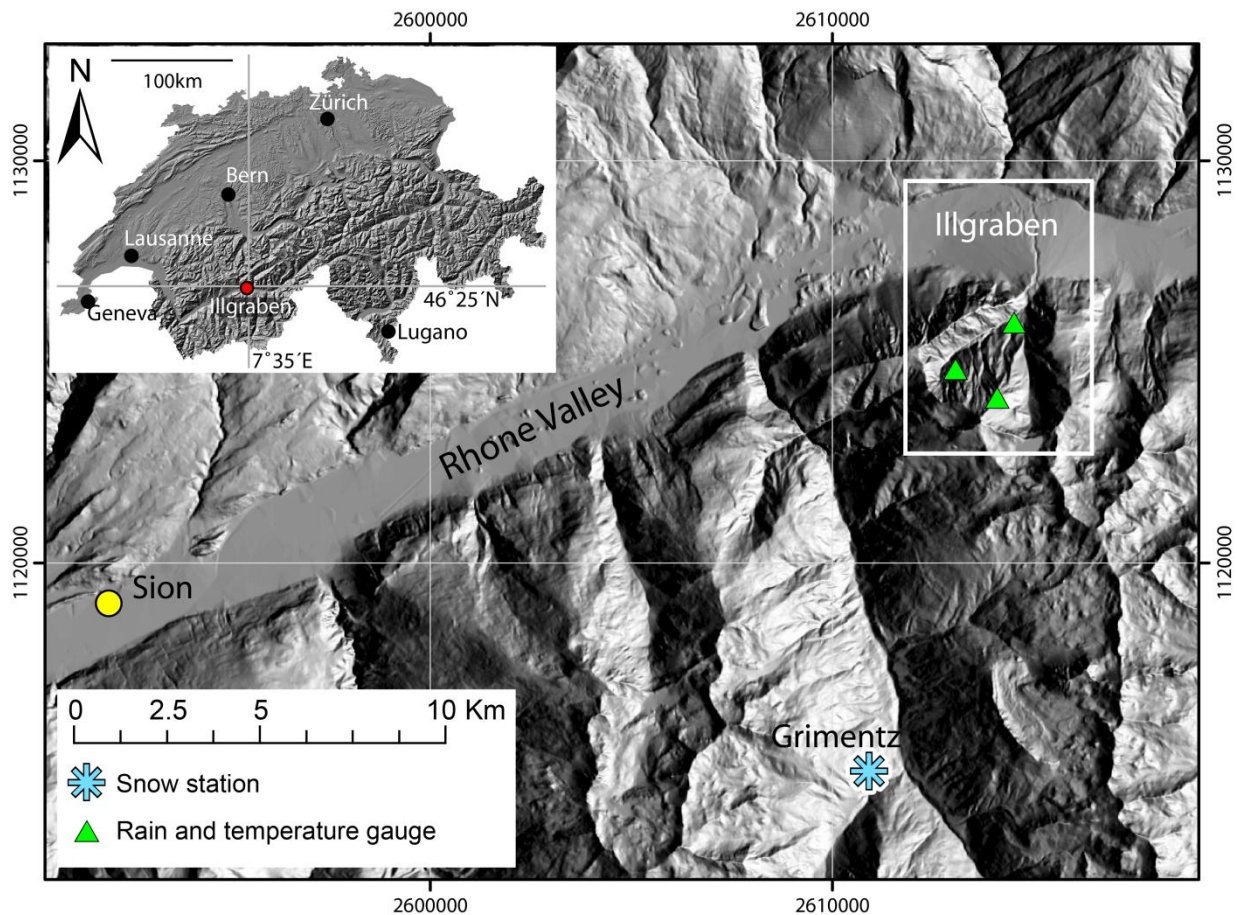


Figure 1.4 – Location of the Illgraben within Switzerland (inset map) and the Rhone Valley.

The Illgraben is underlain by Triassic metasedimentary rocks. The trunk channel follows a SW-NE striking fault that dissects the axial plane of a large anticline (Schlunegger et al., 2009). To the south and at the head of the channel and making up the study slope, slopes expose highly fractured white and light-green sericitic quartzites with interbedded dolomites and schists, all of which dip steeply to the south-east. Slopes to the north of the channel are underlain by a succession of limestones and dolomites that also dip steeply to the south east. About 44% of the Illgraben is exposed bedrock and loose sediment cover, 42% is covered by forest and 14% by grassland (Schlunegger et al., 2009). The debris fan, with a radius of ~ 2 km, area of ~ 9 km² and volume of $\sim 500 \times 10^6$ m³ (Badoux et al., 2009), is large by Alpine standards and is indicative of past high rates of sediment output (Schürch, 2011).

The Illgraben experiences a temperate-humid climate with a relatively low mean annual precipitation ranging from 700 mm in the lower part (610 m a.s.l) to 1700 mm at its summit (2716 m a.s.l). The rainfall occurs mainly during intense summer rainstorms in which rainfall intensity may reach more than 70 mm hr⁻¹ (Berger, 2010). Mean annual air temperature (MAT) is about 4°C based on temperature data at stations within the basin (Figure 1.5).

The main channel has been affected by human intervention for the purposes of erosion control and monitoring. A 49 m-high check dam (CD), henceforth referred to as CD1 (Figure 1.5), was

built in the upper channel between 1967 and 1969 in an attempt to retain sediment from the 1961 rock avalanche. An additional 28 smaller CDs were constructed along the channel between CD1 and the outlet in the following decade to further stabilize the channel.

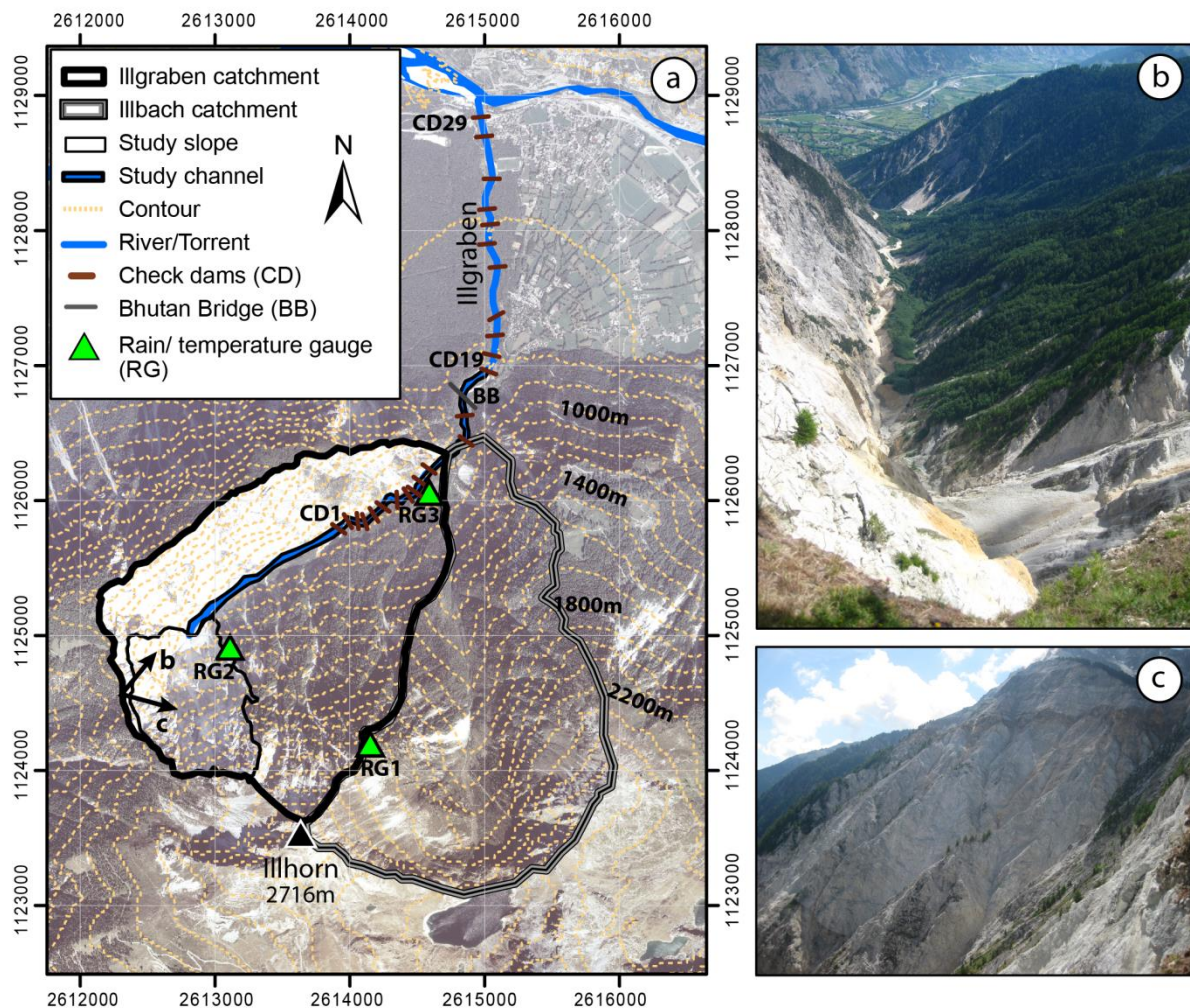


Figure 1.5 – (a) the Illgraben basin showing the location of the study channel (b) and slope (c).

Substantial research has previously been conducted on sediment production, transfer and yield in the Illgraben, which I introduce here. This thesis extends many of these observations back in time and develops a new conceptual framework with which to further understanding of sediment transfer dynamics in the Illgraben and similar mountain basins.

1.3.1. Sediment production in the Illgraben

Several extreme historical slope failures are documented in the 20th century. Major rock fall activity was reported for 1920, 1928, 1934 and 1961 by Gabus et al. (2008) and Lichtenhahn (1971). The rock avalanche of 1961 had a volume in the range of $3\text{--}5 \times 10^6 \text{ m}^3$ and had an initiation zone on the flank of the dolomite slopes to the north of the study slope and channel

(Schürch, 2011). A large rock avalanche deposit with a volume of at least $6 \times 10^6 \text{ m}^3$ near to the fan apex has recently been dated at $3,080 \pm 410 \text{ yrs.}$ (Schürch, 2011).

Schlunegger et al. (2009) quantified more recent hillslope erosion in the Illgraben and identified slopes within the study slope as the most actively eroding in the catchment between 1959 and 2004, with regions of up to 60 m of vertical erosion over the period. In contrast, the slopes to the north of the channel of predominantly dolomites experienced less than 10 m of erosion in the same period. Much of the slopes to the south of the main channel and northeast of the study slope are disconnected from the main channel due to dense vegetation cover (Schlunegger et al., 2009) and sediment supply to the main channel from these slopes is negligible. Berger et al. (2011b) made similar findings concerning catchment hillslope activity. They documented eight rockfall events and two landslides from aerial imagery in 2008 and 2009 ranging in volume from 300 to 4400 m^3 . All of these occurred from the study slope, apart from one landslide that occurred along a tributary channel of the main channel, located to the northeast of the study slope within the forested slopes.

1.3.2. Sediment transfer in the Illgraben

Recent investigations of erosion in the Illgraben make it quite clear that the processes by which sediment is generated on the hillslopes (landslides, rockfalls) and transported downstream (debris flows, floods) are stochastic with complex interactions dependent on the extent of hillslope erosion and its connectivity to the channel system downstream (Schlunegger et al., 2009; Berger et al., 2011b). In particular, Berger et al. (2011b) showed in a 2-year study period that landslides generated on hillslopes did not necessarily transform directly into debris flows, and sediment was stored on the toe of hillslopes or in the channels. The mean residence time for sediment was estimated to be less than 1 year from these data. Furthermore, in the short study period of Berger et al. (2011b) the total eroded volume was less than the export out of the catchment by debris flows measured at the distal end of the fan (McArdell et al., 2007), which suggests that sediment must have been entrained by debris flows along the lower channel. These studies suggest that entrainment by runoff in the channel (e.g. Cannon and Reneau, 2000) is an important mechanism of debris flow generation in the Illgraben. A recent study by Burtin et al. (2012) has shown that sediment transfer may be even more direct in some cases. They used a series of seismometers to capture a small landslide transforming directly into a debris flow. However, it is not known how frequently this mechanism of debris flow generation operates. A last mechanism of debris flow generation, thought to have been responsible for the largest known debris flow in the Illgraben on June 6, 1961, is that of dam-break failure (Badoux et al., 2009).

1.3.3. Sediment yield in the Illgraben

Debris-flow activity in the Illgraben has been monitored since 2000 by the Swiss Federal Research Institute WSL. A horizontal force plate together with fluid pressure sensors installed at CD29 by the outlet to the Rhône River, record total normal and shear forces and fluid pressure

ratios, and geophones, laser and radar sensors are used to calculate front velocity and flow depth (McArdell et al., 2007).

The volumes of sediment output by debris flows have been extraordinarily high by European standards, ranging from 60,000-180,000 m³ yr⁻¹ (McArdell et al., 2009; Berger et al., 2011b). In 2007 small floods were also recorded (Badoux et al., 2009), allowing an estimate of their contribution to total sediment output. There were 19 events in total in 2007; 3 of these were debris flows, contributing ~20,000 m³ of sediment, and 16 events were floods, contributing ~1,600 m³ of sediment, or 8% of that transported by debris flows. We can conclude from this that sediment discharge from the Illgraben into the Rhône River is dominated by debris flows. In between debris flows, low flow conditions and occasional floods transport suspended sediment along with small volumes of bedload.

The large sediment output has resulted in a braided pattern extending over several kilometers downstream of the Illgraben in the otherwise channelized Rhône River (Schlunegger et al., 2009) and makes up between 5 and 15% of the sediment input to the entire Rhône basin (Schlunegger et al., in press).

1.4. Summary of research aims

The main aim of the thesis is to quantify and model sediment yield from a mountain basin over periods of decades thereby corroborating and extending the sediment cascade concept and enhancing understanding of mountain basin sediment transfer. The Illgraben is considered to be representative of a mountain basin in which sediment production and transfer is dominated by rockfall and debris flow processes. In pursuing this overarching aim, I address the following research aims:

- 1) To quantify rates of sediment production, transfer and yield from the Illgraben over a period of decades and their spatial and temporal variability.
- 2) To identify the climatic and seismic controls on rates of sediment production, transfer and yield.
- 3) To identify the coupling relationship between hillslopes and channels and thereby to identify the dominant control on catchment sediment yield.
- 4) To model the magnitude-frequency distribution of slope failures.
- 5) To develop a new conceptual model of mountain basin sediment transfer applied to the Illgraben utilizing observations of the rates, interactions and controls of sediment production, transfer and yield (aims 1-4).

The chapters of the thesis are structured as research papers and I briefly outline the papers in the context of the research aims and how they address knowledge gaps in the current state of research.

The first paper (Chapter 2) describes the photogrammetric procedure used to quantify sediment production, transfer and yield back in time in the Illgraben, addressing research aim (1) of this thesis. Specifically, four 2m-resolution DEMs were extracted from aerial photographs for 1963, 1986, 1992 and 1998 and an additional DEM for 2005 obtained from Swisstopo, giving 4 periods of analysis spanning a total of 42 years. Results concerning sediment production in the catchment are presented. The main result in context of the research aims is a magnitude-frequency model of > 2000 slope failures spanning 6 orders of magnitude in volume extracted from the DEM dataset, addressing research aim (4) of this thesis. The probability distribution is typical of distributions of slope failures more generally and the results of the analysis of the characteristics of slope failures in our inventory are therefore used to test the hypothesis of Katz and Aharanov (2006) that two different types of slope failure are responsible for the characteristic landslide probability distribution (Section 1.2.3). The large inventory of slope failures also enables the testing of the little-tested hypothesis of a threshold hillslope angle for slope failure, which is important concerning our understanding of landscape evolution and in the validation of landscape evolution models. Furthermore, the inventory is used to constrain the scaling exponent in the relationship between landslide volume and area for unique geological setting, which is of relevance to other studies wanting to obtain landslide volumes and even erosion rates from landslide areas where these are not directly measured (Section 1.2.1).

The patterns and rates of sediment production, transfer and yield between 1963 and 2005 in the Illgraben obtained from the photogrammetric method described in the first paper are presented in the second paper (Chapter 3), addressing research aim (1). The differentiation of sediment yield into hillslope and channel sources for different periods of time enables an analysis of their individual controls, interactions with each other and combined impact on sediment yield, addressing research aims (2) and (3). I analyzed climatic variables of precipitation, temperature and snow, as well as seismic variables and their potential influence on rates of hillslope sediment production and channel transfer and ultimately sediment yield. The dataset enables the identification of the different sensitivities of hillslopes and channels to climate change. In particular, there was a significant increase in air temperature in the 1980s across the European Alps, which is captured in the study period and to which the response of hillslopes is investigated. This paper therefore contributes to the body of research on the sensitivity of hillslope processes to increasing air temperature. It also assesses the nature of geomorphic coupling between hillslope and channel (Section 1.2.2), thus testing the assertion that a downslope-directed coupling relationship is more prevalent in the landscape than previously thought (Schlunegger et al., in press). Finally, it discusses the dominant controls on sediment yield in light of the hillslope-channel coupling relationship.

The third paper (Chapter 4) brings together findings from research papers 1 and 2 (Chapters 2 and 3) into a new probabilistic sediment cascade model of sediment transfer through the Illgraben, addressing research aim (5) of this thesis. The aim of the modeling approach is to incorporate the minimum process representation required to reproduce the first-order properties of sediment transfer (section 1.2.3). Although the model is developed and applied in

the Illgraben, it is applicable to fluvial systems more generally that can be schematized into sediment cascades and where the supply of sediment and triggering of events is largely stochastic. The model is based on the sediment cascade concept (section 1.2.1) in the sense that sediment is routed through a series of storage reservoirs, but also extends the concept by investigating thresholds and feedbacks in the system. The magnitude-frequency model of slope failures presented in the Chapter 2 is used as sediment input into the model and findings concerning the interactions of and controls on sediment production and transfer presented in Chapter 3 were used to develop the model. The model is calibrated on a time series of 36 debris flows measured from 2000 through 2009 and is parameterized mainly on independent data. It is used to demonstrate how the interplay of sediment input, hydrological and sediment storage dynamics combine to produce a magnitude frequency distribution of debris flows out of the sediment cascade distinctly different from that of the slope failures providing the sediment input at the top of the sediment cascade. The model is also used to investigate the impact of sediment storage on simulated sediment discharge events in general and their division into transport and supply limited, floods, debris floods and debris flows. Finally, it is used to investigate the rainfall that leads to debris flows in order to understand and quantify the limitations of rainfall intensity thresholds for debris flow initiation.

2. Erosional power in the Swiss Alps: characterizing slope failure at the head of the Illgraben

Abstract

*Landslides and rockfalls are key geomorphic processes in mountain basins. Their quantification and characterization are critical for understanding the processes of slope failure and their contributions to erosion and landscape evolution. We used digital photogrammetry to produce a multi-temporal record of erosion (1963 – 2005) of a rock slope at the head of the Illgraben, a very active catchment prone to debris flows in Switzerland. Slope failures affect 70% of the study slope and erode the slope at an average rate of $0.39 \pm 0.03 \text{ m yr}^{-1}$.

The analysis of individual slope failures yielded an inventory of ~2500 failures ranging over 6 orders of magnitude in volume, despite the small slope area and short study period. The slope failures form a characteristic magnitude-frequency distribution with a rollover and a power-law tail between $\sim 200 \text{ m}^3$ and $1.6 \times 10^6 \text{ m}^3$ with an exponent of 1.65. Slope failure volume scales with area as a power law with an exponent of 1.1. Both values are low for studies of bedrock landslides and rockfall and result from the highly fractured and weathered state of the quartzitic bedrock.

Our data suggest that the magnitude-frequency distribution is the result of two separate slope failure processes. Type (1) failures are frequent, small slides and slumps within the weathered layer of highly fractured rock and loose sediment, and make up the rollover. Type (2) failures are less frequent and larger rockslides and rockfalls within the internal bedded and fractured slope along pre-determined potential failure surfaces, and make up the power-law tail.

Rockslides and rockfalls of high magnitude and relatively low frequency make up 99% of the total failure volume and are thus responsible for the high erosion rate. They are also significant in the context of landscape evolution as they occur on slopes above 45° and limit the relief of the slope.

**Bennett, G.L., Molnar, P., Eisenbeiss, H., McArdell, B.W., 2012. Erosional power in the Swiss Alps: characterizing slope failure at the head of the Illgraben. Earth Surface Processes and Landforms, Vol. 37, 1627-1640*

2.1. Introduction

Slope failure is the main erosional process in many mountainous regions and may also be the most dangerous, making it important to quantify and characterize. Slope failure may be characterized statistically by its magnitude-frequency (MF) distribution, volume-area (VA) relation, and the slope gradient on which it occurs. The MF distribution of slope failure is an important tool for assessing slope failure hazard (Hantz et al., 2003), detecting climatic and environmental change (Schlögel et al., 2011) and in models of sediment transfer (Benda and Dunne, 1997a; Fuller et al., 2003) and is thus important to accurately define and understand. In the case that slope failure volumes are unknown, empirical relationships between slope failure area and volume may be used to convert areas into volumes (Malamud et al., 2004) and associated erosion rates (Larsen et al., 2010), making it important to constrain this relationship for different geological settings. Finally, quantifying the slope gradient at which slope failures of different magnitudes occur is important in hazard assessment (Guzzetti et al., 1999) and in understanding landscape evolution (Densmore et al., 1998; Korup et al., 2010). However, the quantification and thus characterization of slope failure are restricted by the difficulty of obtaining accurate data, particularly volumetric data, from steep slopes that have often difficult access. In this study we used historical archives of aerial photographs to remotely measure the areas of past slope failures (Stark and Hovius, 2001; Brardinoni and Church, 2004; Stark and Guzzetti, 2009) and digital photogrammetry for measuring these in 3 dimensions (e.g. Schwab et al., 2008) and computing volumes of slope failures and relevant erosion rates. Our study slope is at the head of a very active, steep mountain basin, prone to debris flows. Thus quantifying and characterizing slope failures are also important for understanding debris flow sediment transfer and hazard. We investigate the patterns and controls of channel sediment transfer in relation to hillslope sediment supply in a separate paper (Bennett et al., 2013).

We use slope failure in this paper as a general term for the downslope movement of material that occurs when a slope becomes unstable. Categorization of slope failure is based on various characteristics such as the failure material (e.g. soil, debris, rock) and the mechanics of movement (e.g. slides, slumps, falls, flows). Although the term 'landslide' encompasses a range of slope movements, such as soil slips, deep-seated slides, debris flows and rockfalls (Cruden and Varnes, 1996), studies of landslides reported in this paper generally focus on slope movements of the slide, slump and flow type in soil-mantled, vegetated and often forested slopes. Studies of rockfalls focus on this particular slope movement in rock slopes and cliffs. We make a further distinction in this study between slope failures following Katz and Aharanov (2006). Rockslides and rockfalls define failures that occur in a layered sequence or in pre-fractured solid rock, whereas earth/debris-slides and slumps occur in loose sediment and soils.

It has been observed that above a certain magnitude the frequency of landslides and rockfalls decays as a power-law (Hovius et al., 1997; Hungr et al., 1999; Stark and Hovius, 2001; Dussauge-Peisser et al., 2002; 2003; Guzzetti et al., 2002; Hergarten, 2002; Malamud et al., 2004; Stark and Guzzetti, 2009; Lim et al., 2010). Below this magnitude, the frequency often drops off, resulting in a transition within the probability density function (PDF) that is

commonly referred to as the ‘rollover’. Although the general shape of the MF distribution appears to be robust across different geologic and climatic settings (Malamud et al., 2004), there is some variability in the power-law tails of the distribution. Possible causes of this variability include variability in material strength (Sugai et al., 1994), climate (Li et al., 2011), tectonics (Chen, 2009) and statistical noise (Korup et al., 2012). Additionally, the origin of the characteristic MF distribution is debated. Some studies have suggested that the rollover present in many distributions is an artifact of undersampling of small failures (Brardinoni and Church, 2004; Stark and Hovius, 2001). Conversely, recent experimental and modeling studies suggest that it may have a physical origin (Katz and Aharanov, 2006; Stark and Guzzetti, 2009). These studies suggest that the characteristic landslide MF distribution is the combination of two separate slope failure processes: small failures of the slump and slide type within loose sediment and soil make up the rollover, and larger failures of the rockslide and rockfall type make up the power-law tail. This hypothesis is supported by the observation that the rollover is often absent from rockfall MF distributions (e.g. Malamud et al., 2004). In order to be in a position to use MF distributions to detect climatic and environmental change and their effects on slope stability we need to better understand the controls on the shape of and variability in the MF distribution.

Several studies have found that landslide volume scales with area as a power law, $V \propto A^\gamma$, with an exponent γ (e.g. Simonett, 1967). Guzzetti et al. (2009) found $\gamma = 1.45$ for 677 landslides worldwide, very close to the value of 1.5, leading them to conclude that the control on the relationship is geometrical and independent of physiographic setting. Many studies have used $\gamma = 1.5$ to convert areas into volumes and to estimate erosion rates (Hovius et al., 2000; Lavé et al., 2004; Malamud et al., 2004; Gabet, 2007). However, Larsen et al., (2010) demonstrated significant variability in γ with hillslope material. They found lower γ values for soil landslides (1.1 – 1.3) than for bedrock landslides (1.3 – 1.6), which they attribute to the shallower failure depth of the former. The variability in γ is presumably the result of factors other than the soil/bedrock nature of the slope including error that is inherent to worldwide compilations that suffer from inconsistent measurement procedures. These points highlight the significance of empirically constraining γ for slopes with known geological characteristics.

In this study we aimed to (1) quantify slope failure from a mountain basin headwall over a 19 year period (1986 – 2005), (2) characterize the slope failures with regard to their MF, VA and depth-slope gradient relations, (3) explore variability in the characteristics of slope failures within the MF distribution, and (4) identify the relative importance of slope failures of different magnitudes in hillslope erosion and landscape evolution.

2.2. Study site

The focus of this study is a 0.7 km² dominantly quartzitic rock slope within the northwest facing slopes of the Illhorn (2716m a.s.l) at the head of the Illgraben catchment (Figures 2.1 and 2.2). Situated in the Rhone Valley in southwest Switzerland, this is an active, alpine, debris-flow

catchment of high scientific interest due to a sediment discharge that exceeds Alpine standards by more than 2 orders of magnitude (Schlunegger et al., 2009). Until now, the production of this sediment has been poorly quantified in comparison to the debris flow output.

The catchment has an area of 9.5 km², 4.6 km² of which is susceptible to debris flows (Figure 2.1). Debris-flow monitoring instruments were installed by the Swiss Federal Research Institute for Forest, Snow and Landscape (WSL) in 2000 and 2004 (Rickenmann et al., 2001; Hürlimann et al., 2003; McArdell et al., 2007) to capture the magnitude and frequency of sediment output. Around 3 – 5 debris flows have been measured each year, which generally occur during intense summer thunderstorms (Badoux et al., 2009) characteristic of the temperate-humid alpine climate. These make up an average annual sediment discharge of about 100,000 m³.

The complex, highly fractured geology of the catchment (Figure 2.2) undoubtedly contributes to this high sediment output. The Illgraben trunk channel follows a thrust fault within the southwest striking axial plane of a large anticline, which forms the northern steep limb of the Penninic nappe stack. To the southeast and at the head of the channel the slopes are dominantly of quartzites and have been shown to contribute more than 50% of debris flow deposits (Schlunegger et al., 2009). In the lower part of the catchment these quartzite slopes are heavily forested, whilst at the head of the channel, on the flanks of the Illhorn and including our study slope, the exposed slopes are up to 80° steep and are considered to be the dominant sediment source.

The study slope (Figure 2.2) covers an altitudinal range between 1250 m and 2370 m and spans a horizontal distance of 1250 m between the catchment crest and the head of the main debris-flow channel at its base. The perimeter was defined to be consistent with the sub-catchment scheme devised by Berger et al. (2011b) using watershed analysis in ArcGIS. There are several contacts between different lithologies that cross cut the slope. The dominant geology is massive quartzite, which is intersected by bands of other quartzites (Figure 2.2). Dolomites crop out in the northwest part of the study slope as well as in thin bands towards the upper (southern) part of the slope where they are interbanded with schist and quartzite. The thrust fault, which the main debris flow channel follows, extends up, into and across the slope between the bands of quartzite. These are folded close to the surface and as a result are highly fractured. There is a discontinuous sediment cover on the slope from the rapid weathering of the underlying bedrock.

Several large historical slope failures are documented from the study slope and surrounding slopes. The most recent and best known of these is the rock avalanche of 26th March 1961 with an estimated volume of 3.5x10⁶ m³ (Gabus et al., 2008). Other large events occurred in 1920, 1928 and 1934 (Gabus et al., 2008). The deposits of an even older rock avalanche remain on the fan apex, thought to be of late Holocene age (Schürch, 2011). Berger et al. (2011b) recorded 10 landslides of 300 – 4400 m³ in volume that occurred between 2007 and 2009, the largest of which is 5 orders of magnitude smaller than the 1961 rock avalanche. These were a mixture of

bedrock slides and debris slides (termed ‘alluvial landslides’ in Berger et al., 2011b). Erosion rates of the slopes were estimated at up to 7 cm per year (Schlunegger et al., 2009).

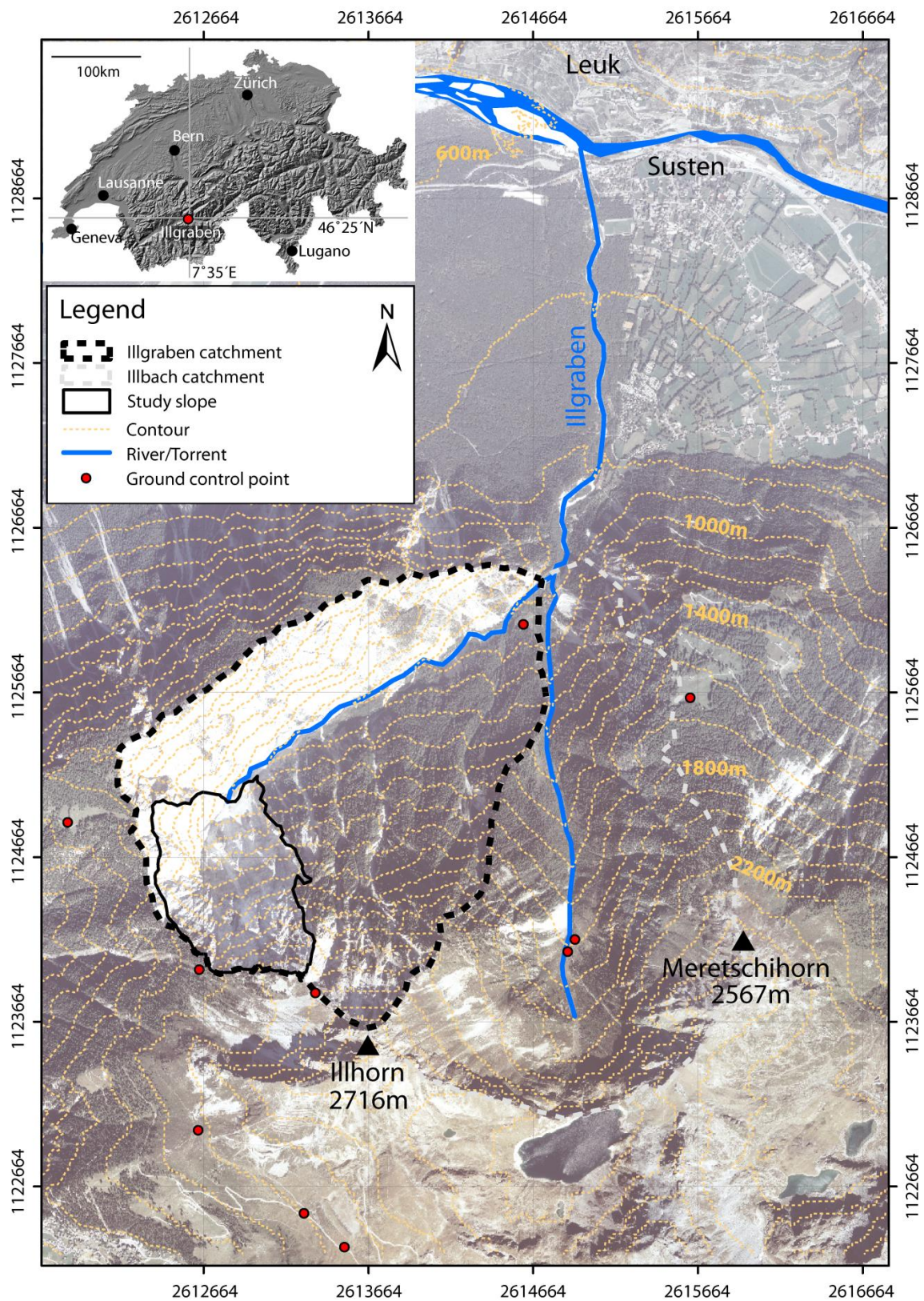


Figure 2.1 - Location of the study slope in relation to the Illgraben catchment, the Rhône Valley and Switzerland. Ground control points used in the photogrammetric process are also shown.

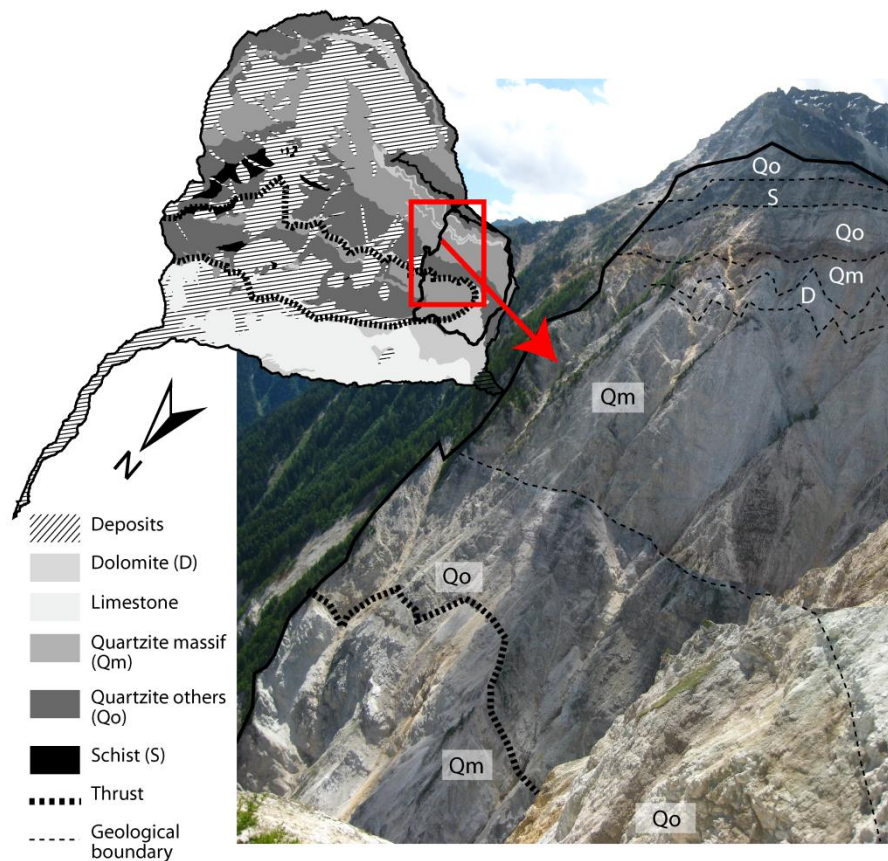


Figure 2.2 - Geology of a part of the study slope in the Illgraben catchment (photograph) in relation to the geology of the Illgraben and Illbach catchments. Geological map adapted from Gabus et al. (2008).

2.3. Methods

2.3.1 DEM preparation

Analogue aerial images of the Illgraben exist from around 1959 and have been flown repeatedly in time intervals of 1 to 17 years by the Swiss Federal Office of Topography (Swisstopo) (Appendix A.1). Additionally, Swisstopo generated a DEM in 2005 for elevations below 2000 m using airborne Lidar (Swisstopo, 2005). This has a resolution of 2 m and standard error of 0.5 m in altitude. We initially generated DEMs for 1963 and 1986 so as to produce 2 periods of analysis, 1963 – 1986 and 1986 – 2005 of comparable length. Following successful DEM generation from these aerial images and calculation of a particularly high erosion rate of $0.39 \pm 0.03 \text{ m yr}^{-1}$ for the latter period, we generated 2 additional DEMs for 1992 and 1998, giving 3 additional 6/7 year periods of analysis: 1986 – 1992, 1992 – 1998 and 1998 – 2005 in which to measure slope failure in more detail.

The aerial images were first orientated in Leica Photogrammetry Suite 9.2 (LPS). An image stereo pair was set up for each year. This procedure involves the input of the parameters of the acquisition camera obtained from the camera calibration certificates (Table 2.1; Table A.1, Appendix A.2), and the location of Ground Control Points (GCPs). GCPs used were a

combination of those collected for the study by Berger et al. (2011b) and Masters students of the University of Bern (Appendix A.2). A minimum of 6 GCPs were located along with additional tie-points. LPS uses a one-step bundle adjustment for GCPs and tie points. This resulted in a global accuracy of between 0.37 and 0.47 pixels for the different stereo pairs (Table 2.2).

Table 2.1 – Aerial photograph parameters

Year	Date	Source	Photo numbers	Camera	Focal length (mm)	Average flight height (m)	Ground resolution (m)
1963	13.09.	Swisstopo	1094, 1095	Aviogon RC5	115.29	3047	0.63
1986	10.07.	Swisstopo	7759, 7758	Wild RC10	153.37	3712	0.34
1992	18.08.	Swisstopo	0834, 0835	Wild RC20	152.92	3104	0.38
1998	8.08.	WSL	7185, 7184	Wild RC30	153.51	3377	0.38

The root mean square error (RMSE) of the GCPs in ground space ranges from 0.02 to 0.19 m in planimetry and height (Table 2.2), indicating the precision of the GCP coordinates. The accuracy of the GCPs in image space resulted in less than half a pixel, indicating the acceptable quality of the image orientation.

Table 2.2 – DEM and georeferencing parameters

DEM	GCPs	Resolution (m)	Total image RMSE (pixel)	Control point RMSE (m) x,y,z	Control point RMSE (pixels) x,y
1963	7	4	0.466	0.19, 0.17, 0.11	0.48, 0.45
1986	6	2	0.369	0.04, 0.09, 0.04	0.31, 0.40
1992	6	2	0.394	0.07, 0.09, 0.02	0.30, 0.44
1998	6	2	0.384	0.06, 0.17, 0.05	0.29, 0.28

DEM generation from the oriented aerial images was performed in ETH-developed SAT PP (Satellite image Precision Processing, ETH Zurich) following a similar procedure to Fischer et al. (2011). This software package has significant advantages over commercial packages, notably a more sophisticated image matching algorithm using a coarse-to-fine hierarchical solution that combines several image matching algorithms and automatic quality control (Zhang, 2005). For each set of images the exterior orientation parameters obtained in LPS were imported and the images pre-processed, involving noise reduction, edge enhancement and production of image pyramids. The images were then matched based on least squares matching. In-depth descriptions of these procedures are given by Gruen and Akca (2005), Zhang (2005) and Zhang and Gruen (2006). Seed points were measured manually to constrain automatic image matching. Typically 100 points were located for each set of images, with a broad coverage across the image space and with additional points on steep faces and along the channel. Finally, DEMs were extracted automatically with a resolution dictated by the resolution of the aerial images, which led to a grid size in Table 2.1 of 4 m for 1963 and 2 m for the remaining years.

We co-registered all the DEMs to the 2005 Swisstopo DEM (Swisstopo, 2005) so as to ensure a common reference, remove any systematic shift in the individual DEMs and to enable a direct comparison of the DEMs. Automatic co-registration of the DEMs on the reference DEM was performed in LS3D (Least Squares 3D Matching; Akca, 2010). Specifically, this was a local co-registration, meaning that the DEM was transformed onto the reference DEM based on a number of unchanged zones. Seven unchanged zones of at least 1000 m² were manually selected across the catchment within known stable terrain. This procedure utilizes the Generalized Gauss-Markoff model, minimizing the sum of squares of the Euclidean distances between the surfaces (Gruen and Akca, 2005). The transformation resulted in a standard deviation of registration error within these zones, which is an indication of the relative accuracy of the DEM compared to the reference DEM (Table 2.3). The relative error of the DEMs compared to the reference DEM ranged between 2 and 2.7 m.

Table 2.3 – Results of registration and error analysis. σ_{reg} is the standard deviation of registration error. σ_{diff} is the standard deviation of the combined error in elevation between two DEMs.

Year	σ_{reg} (m)	Time period	σ_{diff} (m)
1963	2.72	1963 - 1986	3.4
1986	2.05	1986 - 1992	3.1
1992	2.29	1992 - 1998	3.2
1998	2.21	1998 - 2005	2.3

2.3.2. Uncertainty analysis

In the multi-temporal comparison of the DEMs the combined error in elevation change between two DEMs has a standard deviation, which was calculated as (Taylor, 1997):

$$\sigma_{diff} = \sqrt{\sigma_1^2 + \sigma_2^2} \quad (1)$$

with σ_1^2 and σ_2^2 being the standard deviations of registration errors of the individual DEMs. The standard error σ_{diff} ranges between 2.3 and 3.4 m (Table 2.3). In the use of Equation (1) we assume that the uncertainties in the DEMs are independent (e.g. Lane et al., 2003). Each elevation difference $\Delta z = z_1 - z_2$ between two DEMs can be converted to a t statistic:

$$t = \frac{z_1 - z_2}{\sigma_{diff}} = \frac{\Delta z}{\sigma_{diff}} \quad (2)$$

We consider the elevation change to be statistically significant if $|t| > 1$, representing 68% confidence that the elevation change is significant, which is the same level of confidence used by Brasington et al. (2000) and Lane et al. (2003). Therefore in the elevation change

distributions (Figures 2.3a,b), regions with elevation change smaller than σ_{diff} were considered uncertain and were not considered in the analysis of elevation change.

In calculations of volumetric change we extended the estimation of elevation change uncertainty to volume changes following Lane et al. (2003). The volume uncertainty σ_v for the case of spatially uniform σ_{diff} is:

$$\sigma_v = d^2 \cdot \sqrt{n} \cdot \sigma_{diff} \quad (3)$$

where d is the cell size and n is the number of cells in each area of change. The measure of uncertainty σ_v was computed for individual landslides as well as for the entire areas of erosion and deposition.

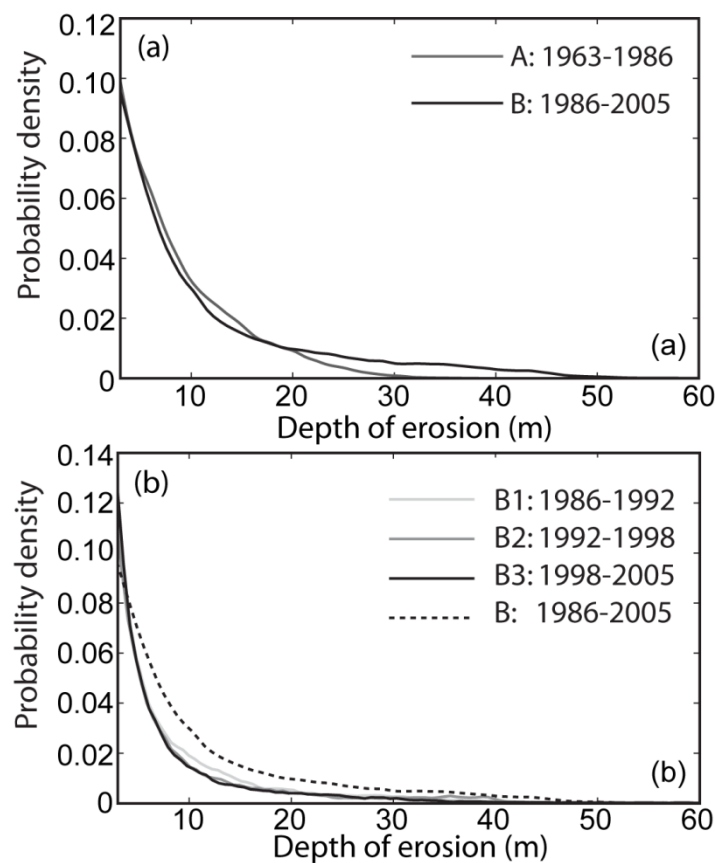


Figure 2.3 – Probability distribution of erosion depth for (a): periods A (1963 – 1986) and B (1986 – 2005); (b): sub-periods B1 (1986-1992), B2 (1992-1998) and B3 (1998-2005). Only statistically significant erosion of over 3 m, the mean σ_{diff} , is shown in each plot.

2.3.3. Slope failure analysis

2.3.3.1. Analysis of erosion rates

To calculate erosion rates we (1) delineated areas of negative elevation change (erosion) above the σ_{diff} threshold of uncertainty in the elevation change maps; (2) calculated the volume of erosion using a grid-based calculation that takes the vertical distance between the

corresponding cells in the DEMs; and finally (3) divided this volume by the area of the study slope and the period duration.

2.3.3.2. Extraction of areas and volumes of slope failures

We delineated slope failures from the areas of erosion in the elevation change maps (e.g. Figure 2.4a,b) for periods B1 – B3 using the raster to polygon tool in ArcGIS. In order to understand the sensitivity of the results to the procedure by which individual slope failures are extracted from the elevation change maps we used 2 methods. (1) We delineated all areas of negative elevation change (erosion) over the σ_{diff} threshold of error ($\Delta z > \sigma_{diff}$). In procedure (2) only areas of elevation change above 5 m were delineated ($\Delta z > 5$ m). This is a more conservative estimate of the error roughly corresponding to a 90% confidence bound and is constant between the periods. This higher threshold resulted in the division of some of the areas of erosion into more likely individual failures, although it removes a significant proportion of the eroded area. We calculated the volumes of the failures as described in point (2) in Section 3.3.1.

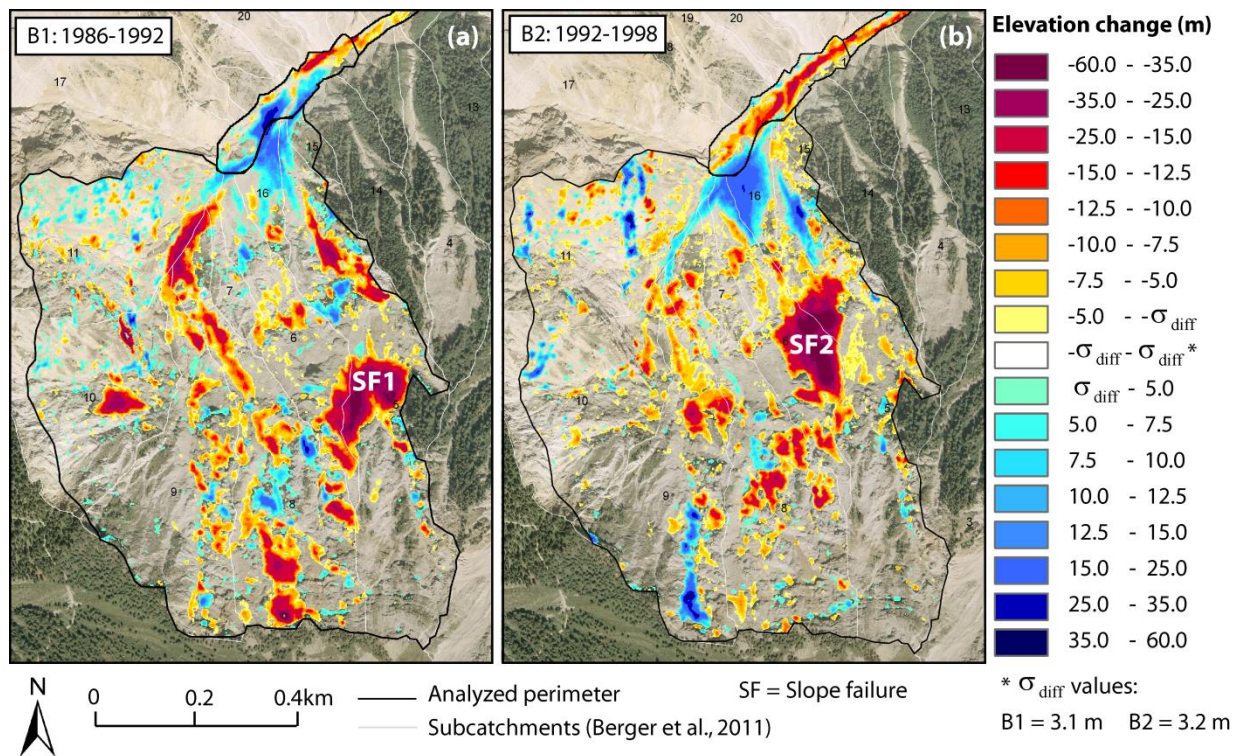


Figure 2.4 a,b – Spatial distribution of elevation change, including deposition, in the study slope and at the channel head for (a): sub-period B1 (1986-1992); (b) sub-period B2 (1992-1998), and location of the largest slope failures (SF1 and SF2). See also Appendix A.3.

2.3.3.3. Magnitude-Frequency analysis

There are two main ways in which to visualize and model slope failure MF with a power-law distribution in the tail. The first is to use the PDF:

$$p(x) = Cx^{-\beta} \quad (4)$$

where x is the quantity of interest (e.g. landslide area or volume), C is a normalization constant and β is the scaling exponent of the tail of the distribution ($\beta > 1$). This approach requires the binning of incremental magnitude values into bins of predefined width. Because the probability density diverges as $x \rightarrow 0$, there must be a lower bound, x_{\min} , to the power law behavior which is contained in the normalization constant, C .

The second is to use the complementary cumulative distribution function (CCDF), which is obtained by integrating Equation (4):

$$P(x) = P(X \geq x) = \left(\frac{x}{x_{\min}} \right)^{-\rho} \quad (5)$$

where $P(x)$ is the probability of a randomly picked failure volume exceeding x and ρ is the slope of the CCDF and is related to β by:

$$\rho = \beta - 1 \quad (6)$$

The use of the CCDF is thought to be preferable to the PDF in estimation of the scaling exponent as it avoids the ambiguities introduced by arbitrary selection of bin sizes or scale (e.g. Brardinoni and Church, 2004; Hungr et al., 2008). However, the rollover is more easily visualized in the PDF, making both useful in MF analysis.

We compiled a list of many studies that have reported MF distributions of both rockfalls and generic landslides using variations of the methods presented above (Table 2.4). This list omits many of the studies of landslides that are listed in a similar table in Van den Eeckhaut et al. (2007) but includes additional studies of rockfalls. Furthermore, we have cross-referenced estimates of β and ρ using equation (6) so as to aid comparison of these.

To make comparisons with many previously published landslide distributions, we plotted the empirical distributions of datasets (1) and (2) in PDF form in Figure 2.5a. We extracted the frequency of different slope failure volumes using a kernel density estimate, which is considered to be a more robust measure of frequency variations than the traditional histogram (Silverman, 1981). We applied a kernel density estimate using a box kernel with a width of 0.4 to the log-transformed volume data. We experimented with different kernel widths and found a width of 0.4 to best capture the frequency variations in the data and we normalized the frequency by the bin width (Malamud et al., 2004).

Table 2.4 - Next page – Comparison of values of the exponents of the power law tails (β and ρ) obtained for landslide and rockfall inventories, including this study, ordered from low to high β . R= Rockfall, L=Landslide, V= Volume, A=Area. H= Historical, E=Event-based. Values in bold are those reported in the studies.

Study	Slope failure type	Geological setting	Historical or event based	Time window	Attribute*	Range of power law fit**	Slope of PDF (β)	Slope of CDF ($\rho=\beta-1$)
Malamud et al., 2004	R	Mixed	H	Mixed	V	10^{-3} - 10^6 m ³ (9)	1.07	0.07
Guzzetti et al., 2003	R	Granitic cliffs	H	145 years	V	10^{-1} - 10^6 m ³ (7)	1.1	0.1
Dussauge-Peisser et al., 2002	R	Calcareous cliffs	H	60 years	V	10^1 - 10^6 m ³ (5)	1.41	0.41±0.11
Hungr et al., 1999	R	Massive felsic rock	H	30 years	V	10^{-2} - 10^4 m ³ (6)	1.43	0.43
Dussauge-Peisser et al., 2002	R	Metamorphic and sedimentary rocks	H	22 years	V	10^1 - 10^3 m ³ (2)	1.45	0.45±0.15
Dussauge-Peisser et al., 2002	R	Granitic cliffs	H	78 years	V	50 - 10^6 m ³ (6)	1.46	0.46±0.11
Dussauge-Peisser et al., 2003	R	Undifferentiated rock cliffs	H	10000 years	V	10^2 - 10^{10} m ³ (8)	1.52	0.52
Hungr et al., 1999	R	Jointed metamorphic rock	H	22 years	V	10^{-1} - 10^4 m ³ (5)	1.65	0.65
This study (Dataset (1))	L/R	Quartzitic rock and sediment	H	19 years	V	10^2 - 10^6 m ³ (4)	1.65	0.65
Gardner, 1970	R	Calcareous and quartzitic rock	H	2 summer periods	V	10^{-2} - 10 m ³ (5)	1.72	0.72
This study (Dataset (2))	L/R	Quartzitic rock and sediment	H	19 years	V	10^3 - 10^6 m ³ (3)	1.76	0.76
Lim et al., 2010	R	Sandstone + mudstone capped in glacial till	H	20 months	V	10^{-4} - 10^3 m ³ (7)	1.8	0.8
Malamud et al., 2004	L	Various	E	mixed	V (from A)	10^4 - 10^6 m ² (2)	1.93	0.93
Stark and Guzzetti, 2009	L	Sandstones, marls, limestones	H	17 years / 28 years	V (from A)	10^3 - 10^5 m ² (2)	2	1
Rousseau, 1999	R	Basaltic cliff	H	2 months	V	1.5 orders mag	2	1
Stark and Hovius, 2001	L	Vegetated slopes with thin regolith cover	H	2 years	A (eroded)	10^3 - 10^6 m ² (3)	2.11	1.11
Stark and Guzzetti, 2009	L	Clay and silt and clastic sediments.	H	17 / 28 years	A (dis)	10^3 - 10^5 m ² (2)	2.19	1.19
Malamud et al., 2004	L	Weakly cemented clastic sediment	E	few hours	A (dis)	10^3 - 10^5 m ² (2)	2.4	1.4
Malamud et al., 2004	L	Clay and silt and clastic sediments.	E	weeks	A (dis)	10^3 - 10^5 m ² (2)	2.4	1.4
Malamud et al., 2004	L	Soil, siltstone, volcanic rocks, phyllite and schist	E	2 months	A (dis)	10^3 - 10^5 m ² (2)	2.4	1.4
Stark and Hovius, 2001	L	Schists and gneisses with thin regolith cover	H	8 years	A (eroded)	$\sim 10^3$ - 10^6 m ² (3)	2.48	1.48

*Eroded area is that of the failure scar; disturbed (dis) area includes the scar and the runoff area; V (from A) are volumes calculated based on the empirical scaling relationship between area and volume, see text.

**Numbers in brackets are the orders of magnitude (mag) in the range of reported data.

We estimated the β of the power-law tail, which contains ~99% of the failure volume by three methods: (1) robust linear regression between the logarithmically transformed frequency (f) and the equivalent logarithmically transformed volumes; (2) maximum likelihood estimation of β and estimation of x_{\min} with fitting to the CCDF following Clauset et al. (2009) (Figure 2.6a,b); and (3) robust linear regression on the CCDF. Both methods (1) and (3) required the definition of the minimum volume at which power-law scaling of slope failure frequency starts (x_{\min}) and below which data were excluded from linear regression. This threshold was estimated from method (2), which allows an objective estimation of x_{\min} , β and the likelihood p that the tail is power-law distributed.

Whilst the PDF was useful to visualize the MF distribution, particularly the rollover, we find that the power law exponent estimated by linear regression from the PDF is biased and not recommendable. Other estimation methods such as the MLE or Hill's estimator are advisable (Hill, 1975; Clauset et al., 2009). A particular benefit of the procedure proposed by Clauset et al. (2009) is the estimation of the minimum magnitude for power law scaling and the fit to the power law tail (p -value), which are difficult to obtain from previous studies that have used PDF or indeed other methods of fitting to the CCDF.

2.3.3.4. Volume-Area and Depth-Gradient relations

To fit the empirical VA relationship to the data, the data were logarithmically transformed and fit using robust linear regression (Figure 2.7). The logarithmic transformation overcomes problems with fitting of data spanning multiple orders of magnitude. Guzzetti et al. (2009) showed that γ is not very sensitive to the exact fitting technique but suggested that robust linear regression is preferable as this reduces the effect of outliers.

Lastly, we explored where slope failures are likely to occur in space by looking at the relationship between mean failure depth and mean slope gradient of the pre-failure surface for failures of $V < x_{\min}$ and $V \geq x_{\min}$ (Figure 2.8).

2.4. Results

2.4.1. Erosion rates

The mean erosion rate increased from 0.24 ± 0.003 m yr⁻¹ in 1963 – 1986 (period A) to 0.39 ± 0.03 m yr⁻¹ in 1986 – 2005 (period B). Figure 2.3a shows that this increase in erosion rate is due to an increase in the mean depth of erosion from 7.5 m to 9.1 m and maximum depth of erosion from 38.7 m to 60 m in the two periods. Figure 2.3b shows the distribution of erosion depths in the 3 shorter periods of analysis (B1 – B3) within B. There is a higher probability of shallower erosion for each sub-period B1 – B3 compared to the entire period B due to the coalescence of slope failures and thus an increasing depth of erosion through time.

2.4.2. Magnitude-Frequency distributions

Delineation of slope failures described in section 3.3.2 produced two inventories. Procedure (1) produced an inventory of 2170 slope failures that affected 70% of the total slope area (dataset (1)). Procedure (2) produced a smaller inventory of 1475 slope failures that affected 48% of the slope area (dataset (2)). Both inventories span 6 orders of magnitude in area and 7 orders of magnitude in volume.

The empirical MF distributions of datasets (1) and (2) (Figure 2.5a) have a characteristic form with rollover and power-law tail. The rollover is located at the modal failure volume (rollover magnitude) of $\sim 50 \text{ m}^3$. We plotted the volumetric uncertainty around dataset (1). This uncertainty results in some uncertainty in the rollover magnitude ($\pm 20 \text{ m}^3$) but not in the form of the power-law tail.

Values of β we obtained using MLE and linear regression on the CCDF are consistently around 1 (or more) higher than those obtained by linear regression to the PDF (Table 2.5). This bias is real and has been shown numerically (Clauset et al., 2009). In fact, β estimated from the PDF for datasets (1) and (2) is less than 1, which is not feasible. The p -values of the power-law models estimated from the CCDF using MLE are all close to 1 and much higher than 0.1, meaning that the power law model gives a good fit to the data (Clauset et al., 2009). All our estimated values of β and x_{\min} for datasets (1) and (2) fall in between values reported for rockfall and landslides (Table 2.4).

Table 2.5 – Comparison of frequency-volume relationship using the methods of least squares fitting (LS) to the PDF and CCDF and maximum likelihood estimation (MLE) based on the method of Clauset et al. (2009). p -values over 0.1 indicate a good fit to the power law distribution. ‘Tail’ refers to the power law tail, i.e. where $x \geq x_{\min}$.

Attribute	Dataset (1)	Dataset (2)
LS (PDF) (β)	0.65	0.72
LS (CCDF) (β)	1.64	1.75
MLE (β)	1.65	1.76
p -value	0.76	0.93
$x_{\min} (\text{m}^3)$	233	1440
Equivalent $A (\text{m}^2)^*$	61	204
Number of failures (n)	497	205
Proportion of events in tail (%)	22.9	13.9
Volume of events in tail (m^3)	6.25×10^6	5.07×10^6
% of total volume	98.7	96.1

*Calculated based on $\gamma = 1.1$ in Equation (7) and reported in Table 2.7.

Although the empirical probability distributions of slope failures within period B (Figure 2.5b) all show heavy tails, there is some variability in the power law exponents. The problem of binning mentioned in Section 2 is particularly evident in this plot with many of the larger values contained within the same frequency bin. Table 2.6 gives the different estimates of the power-law exponent, which may indicate sampling variability or different slope failure triggering histories in the periods.

Several studies that have investigated the causes of temporal variability in the MF distribution for a particular slope have attributed this to externally induced changes in slope stability (e.g. Chen, 2009; Li et al., 2011; Schlögel et al., 2011). However, a recent study by Korup et al. (2012) suggests that this variability may arise from statistical noise and that MF distributions may be powerless to detect environmental variability. It was beyond the scope of this paper to investigate the causes of temporal variability in the MF distribution. These are investigated in an additional study of the climatic and seismic controls on hillslope erosion and channel sediment transfer in the Illgraben (Bennett et al., 2013).

Table 2.6 – Comparison of frequency-volume relationship using different methods for different periods within dataset (1) (B1 – B3). p – values over 0.1 indicate a good fit to the power law distribution. The p – value is not reported for B2 as the number of landslides is too small for an accurate estimation of β . ‘Tail’ refers to the power law tail, i.e. where $x \geq x_{\min}$.

Attribute	B1: 1986 - 1992	B2: 1992 - 1998	B3: 1998 - 2005
LS (PDF) (β)	0.56	0.71	0.63
LS (CCDF) (β)	1.59	2.04	1.68
MLE (β)	1.54	1.99	1.72
p-value	0.1		0.1
x_{\min} (m ³)	131	3975	59
Equivalent A (m ²)*	32	773	21
Number of failures (n)	220	32	424
Proportion of events in tail (%)	37	4	53
Volume of events in tail (m ³)	2.28x10 ⁶	1.38x10 ⁶	2.52x10 ⁶
% of total volume	99	91	99

*Calculated based on values of α and γ reported in Table 2.7 for area type A.

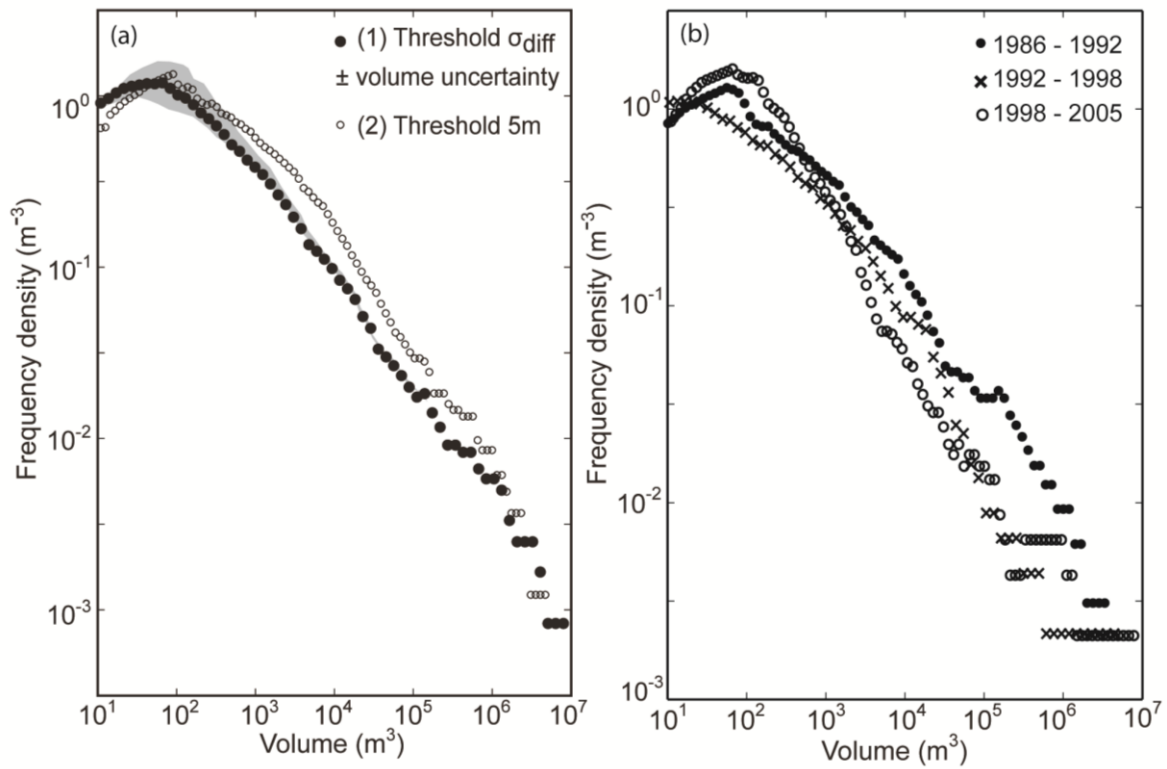


Figure 2.5 a,b – (a): Empirical frequency-volume distribution for logarithmically transformed datasets (1) and (2). Uncertainty in the volume of individual landslides is shown for dataset (1) as the grey range. The uncertainty is similar for dataset (2). (b): Distributions for temporal sub-periods B1-B3 within dataset (1).

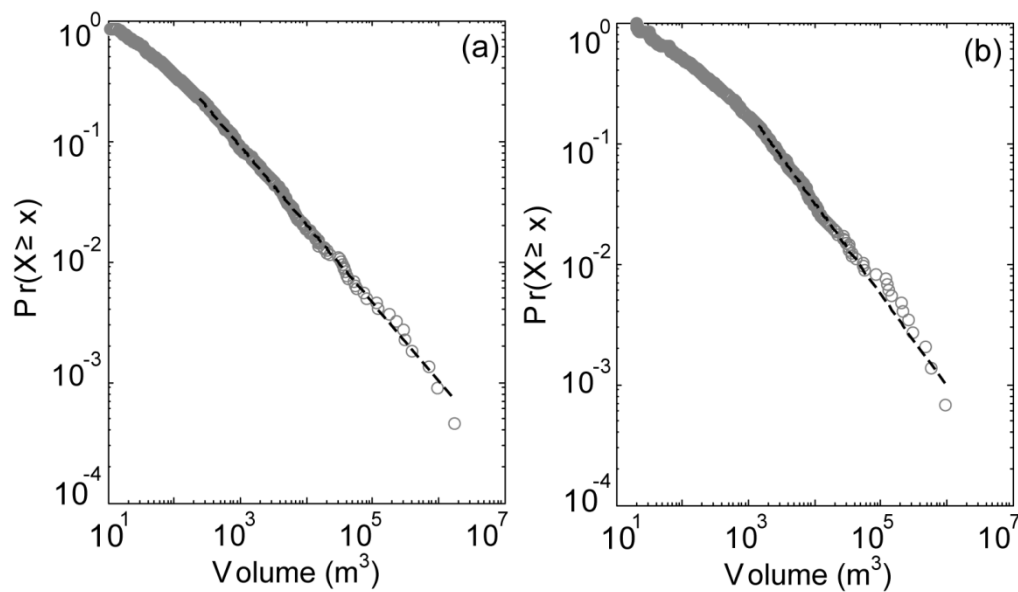


Figure 2.6 a,b – Complementary cumulative empirical distributions for (a) dataset (1) and (b) dataset (2), fit with theoretical power law model by the maximum likelihood method.

2.4.3. Volume-Area relation

We fitted the relationship between landslide volume and area of the form $V = \alpha A^\gamma$ to the data (Figure 2.7). For dataset (1) we obtained estimates of $\alpha=0.41$ and $\gamma=1.1$ (Table 2.7). The exponent γ is similar for dataset (2) indicating that it is insensitive to the extraction procedure. We thus performed further sensitivity analyses of γ only on dataset (1).

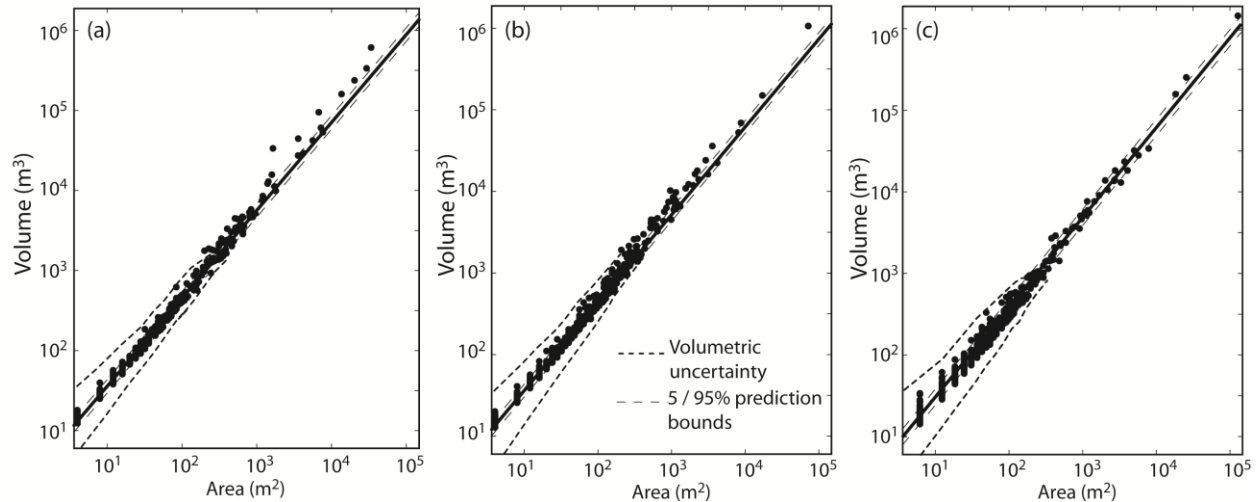


Figure 2.7 a-c – Volume-Area distribution of log transformed dataset (1) split into the three periods of analysis (a) B1: 1986-1992, (b) B2: 1992-1998, (c) B3: 1998-2005. Uncertainty in volumes is shown by the small dashed lines. Power-law fits are shown along with 95% prediction bounds. For model exponents see Table 2.7.

Table 2.7 – Comparison of volume-area relationship for projected and plan area and different periods using dataset (1). A is the projected area and A^* is the real surface area of the slope failure.

Area type	Attribute	Dataset (1)	B1: 1986 - 1992	B2: 1992 - 1998	B3: 1998 - 2005
A	α	0.41	0.46	0.48	0.32
	γ	1.1 ± 0.1	1.10	1.08	1.10
A^*	α	0.20	0.21	0.25	0.17
	γ	1.13 ± 0.1	1.09	1.07	1.06

Significantly, the exponent γ is practically constant between the different periods within dataset (1) (Table 2.7), showing that this relation is quite general for this geological setting. We also tested the sensitivity of the exponent to using real surface areas A^* , rather than projected areas A . Most studies report A (Malamud et al., 2004). However, on steep slopes such as those in our basin A may be significantly smaller than the actual surface area A^* . We calculated the mean gradient θ for each slope failure based on the surface prior to the failure and multiplied A by $1/\cos(\theta)$. For the steepest slope A^* was more than 7 times A but this does not affect the estimate of γ significantly, only the intercept α (Table 2.7). However,

volumetric uncertainty does propagate into uncertainty in γ . We estimated a range of exponents for the range of possible volumes of 1.02 – 1.31 for dataset (1).

The VA relation is dominated by the smallest failures ($< x_{\min}$) as these make up ~80% of the total number of failures in our inventory (Table 2.5). These have a small range of depths (Figure 2.8) such that larger failures are relatively thinner and thus smaller in volume relative to their area than small failures.

2.4.4. Pre-failure slope gradient of failures

The statistical distribution of slope failure volumes allows us to investigate detailed characteristics of the failures, such as mean failure depth as a function of pre-failure slope gradient in Figure 2.8. We found that failures of $V < x_{\min}$ (233 m^3 , Table 2.5) have a small range of mean depths ($\sim 2 - 6 \text{ m}$) but a wide range of pre-failure slope gradients ($\sim 15^\circ - 80^\circ$) and a mean gradient of $\sim 50^\circ$. Failures of $V \geq x_{\min}$ have a larger range of mean depths ($\sim 3 - 20 \text{ m}$) but narrower range of slope gradients and steeper mean gradient ($\sim 55^\circ$). The majority of failures of $V \geq x_{\min}$ occur on slopes above 45° in slope gradient.

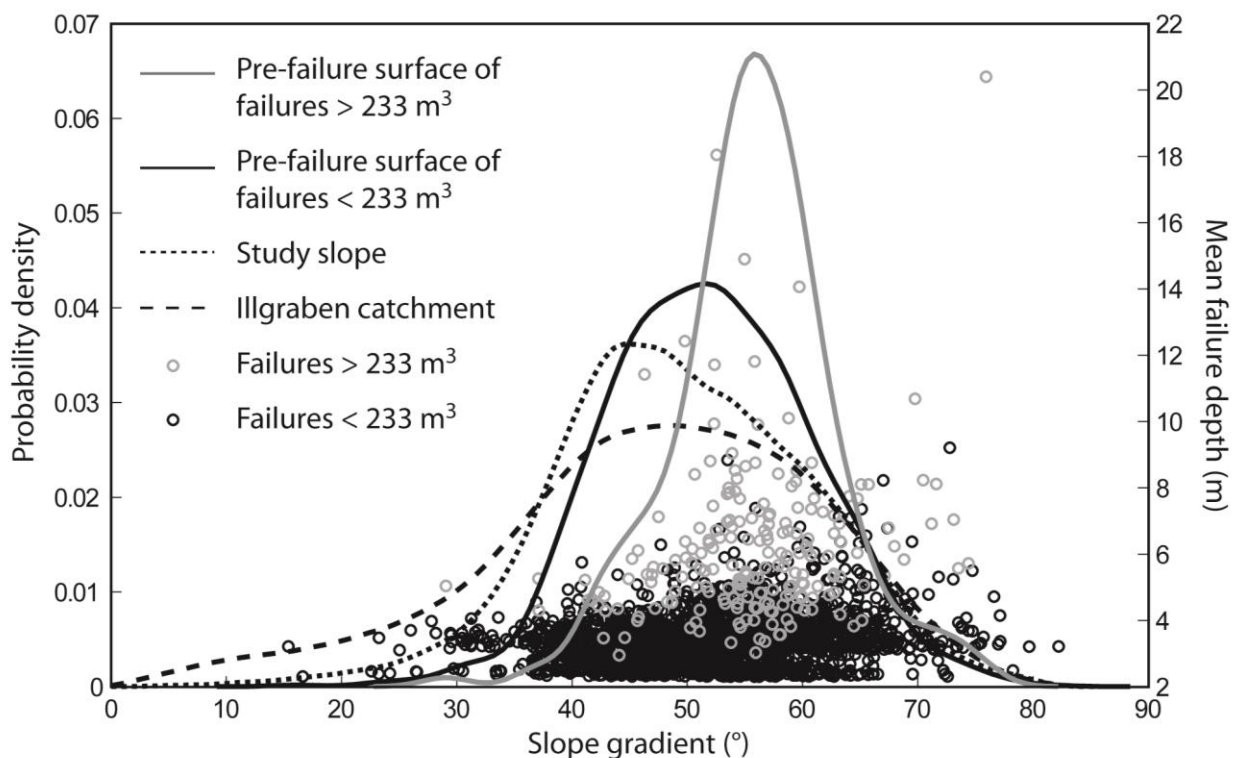


Figure 2.8 – Relationship between mean failure depth and slope gradient of the pre-failure surface for failures $> 233 \text{ m}^3$ (grey circles) and failures $< 233 \text{ m}^3$ (black circles) on the right-hand axes along with their probability distributions (grey and black lines respectively), plotted against the probability distributions of slope gradient of the study slope and Illgraben catchment (Figure 2.1).

2.5. Discussion

2.5.1. Methodological discussion

The main limitation of our analysis is the possibility that some of the slope failures in our inventory contain several individual failures that have coalesced over the 6-7 year time windows. Whilst coalescence is inherent to any historical inventory of slope failures (e.g. many in Table 2.4) it is particularly true for our inventory given the high erosion rate. In order to assess the possible degree of coalescence of slope failures within these periods we looked at repeated failures between periods B1, B2 and B3. For failed cells in any one period we calculated the likelihood that there was failure in the equivalent cell in one or both of the other periods. This analysis suggests that at most 28% of slope failures are affected by coalescence. The manual delineation of individual landslide scars within a failed area from inspection of the photo pairs was however not possible due to the lack of any sort of vegetation cover, and so any pattern of post-landslide vegetation re-growth, and the subtle contrast between the substrate and freshly eroded debris.

Whilst we cannot solve the problem of coalescence in our dataset, several points lead us to believe that the MF model is reliable. For instance (1) we modelled the sum of the failures in the different periods, so mimicking the coalescence over a single period, and obtained a similar exponent $\beta = 1.6$; (2) we repeatedly drew 2 samples from our power-law model and modelled their sums and consistently obtained the same exponent, although slightly larger x_{\min} ; and finally, (3) we modelled the landslides measured in the study slope by Berger et al. (2011b) on a seasonal basis between 2007 and 2009 where coalescence was not an issue, and observe that these also follow a power-law distribution with an exponent $\beta = 1.89$ and $x_{\min} = 300 \text{ m}^3$. Further confirmation of our MF model could be achieved by a higher temporal resolution study of slope failures over a period of multiple years.

The use of photogrammetry to produce high resolution (2 m) DEMs enabled us to capture small events within the MF distribution, which are sometimes undersampled, particularly in heavily forested terrain (e.g. Stark and Hovius, 2001, Brardinoni and Church, 2004). This may explain why we obtain a relatively small modal failure magnitude (peak of the rollover) of $\sim 50 \text{ m}^3$ and a small failure magnitude for the start of power law scaling at $x_{\min} = \sim 200 \text{ m}^3$ in comparison to other studies of landslides (Table 2.4). This is an upper estimate of the rollover magnitude as coalescence may have decreased the frequency of the smallest events, but despite some uncertainty in its magnitude we suggest that the rollover does have a physical explanation, as we discuss in Section 5.2.

A number of landslide studies have focused on modeling the whole MF distribution including the rollover (e.g. Stark and Hovius, 2001; Malamud et al., 2004). Malamud et al. (2004) fit several landslide inventories with a 3 parameter inverse Gamma distribution. Stark and Hovius (2001) fit their probability densities of landslides with a double Pareto distribution. Both of these distributions capture the rollover that characterizes landslide distributions for small

landslides and the power-law tail for medium and large landslides. Stark and Hovius (2001) justify their effort to model their entire distribution of landslides in Taiwan by the observation that only 25% of their data are in the tail of their distribution. In our datasets, even less of the data are in the tail, 5 – 22%, but these make up between 96 and 99% of the total failed volume (Table 2.5). This indicates the importance of this part of the distribution to the overall sediment budget at the Illgraben. We therefore focused on modeling this part of the distribution, rather than attempting to describe the entire distribution with more complex models. Such models are more appropriate for rockfall hazard assessments, in cases that small slope failure volumes pose a significant hazard.

2.5.2. Physical interpretation of our dataset

A distinction between the MF distribution of generic landslides and rockfalls is apparent in Table 2.4. Exponents β reported for landslides between 1.93 (Malamud et al., 2004) and 2.44 (Stark and Hovius, 2001) are consistently higher than those for rockfall of between 1.07 (Malamud et al., 2004, based on various datasets) and 2 (Rousseau, 1999). The power-law exponent in the MF relation that we obtained for dataset (1), $\beta = 1.65$, is in the upper end of values found for rockfall and lower end of values found for landslides. All the studies reported in Table 2.4 that have obtained smaller exponents have investigated rock slopes of stronger bedrock (mainly granites and metamorphic rocks). Conversely, all studies that have obtained larger exponents have investigated rock slopes either of weaker bedrock (e.g. Lim et al., 2010) or soil-mantled slopes in which deep and large failures are less common. Our exponent is similar to that obtained by Gardner (1970) who also studied failures in quartzitic rock slopes. Our study supports the hypothesis that the value of β increases, and thus that large events are less frequent, when slope strength, as determined by cohesion (C) and friction angle (ϕ), decreases (Dussauge-Peisser et al., 2002). This is also in accordance with the erosion model proposed by Densmore et al. (1998).

The VA relationship has been widely used to convert areas of landslides into volumes and to calculate erosion rates from these (Table 2.4). The accurate calculation of γ is thus pertinent to the calculation of erosion by landslides. Larsen et al. (2010) suggested that γ could be used to differentiate between soil and bedrock landslides on the basis that the former have a lower range of γ (1.1 – 1.3) than the latter (1.3 – 1.6) in their global study of landslides. Our range of γ (1 – 1.3) is similar to that found for soil-based landslides rather than bedrock-landslides, despite the bedrock nature of our slope. The low γ -value results from the small depth of failures relative to their areas, which we hypothesize is due to the granular and incohesive nature of the highly fractured quartzite bedrock, which fails at relatively shallow depths for a rock slope. Our result demonstrates the difficulty of generalizing at this first order level of complexity (soil or bedrock) and caution against the application of an exponent developed from one study area to another based simply on the nature of landsliding (soil or bedrock) (Larsen et al., 2010). This is particularly pertinent concerning the calculation of erosion rates for the reason that the erroneous selection of γ may result in making large errors in the landslide

volumes and erosion rates derived from these (Larsen et al., 2010). More studies like this one are needed that constrain γ for different geological settings.

On the basis of our analysis and observations of the slope we hypothesize that erosion of the study slope occurs by two failure processes (Figure 2.8), based on the hypothesis of Katz and Aharonov (2006).

Type (1) failures are smaller failures with $V < x_{\min}$ (rollover part of the MF distribution) with a narrow depth range and wide range of pre-failure slope gradients. We hypothesize that these are slumps and slides within loose sediment and highly fractured bedrock that make up a relatively homogenous top layer of the slope that is exposed to physical and chemical weathering. Figure 2.9 is an example of the environment of failure. It shows a fold at the surface, around which the rocks are heavily fractured and disintegrated, and a discontinuous cover of loose sediment. The depth of the failures is determined by sediment availability on the slopes or the depth of this weathered layer. This failure type corresponds with the small slumps and slides failures found to occur within the top 5 m of a slope by Katz and Aharonov (2006) in their experimental study. The fact that some of our failures are relatively deep (>5 m) suggests that the weathered layer is quite deep. This is plausible considering the highly fractured nature and permeability of the quartzites and thus susceptibility to chemical and physical weathering (e.g. Jaboyedoff et al., 2004). The narrow depth range results in a characteristic, or modal, size of around 50 m³ for type (1) failures, giving a physical explanation for the presence of the rollover in our distribution.



Figure 2.9 – Example of the environment of type (1) failures: the upper 5m of weathered rock and unconsolidated sediment. A = loose sediment cover; B= fold in the quartzites cropping out at the surface; C= imminent failure of ~5m depth.

Type (2) failures are larger failures with $V \geq x_{\min}$ (power-law tail of the MF distribution) with a wide depth range and narrow range of pre-failure slope gradients. We hypothesize that these are rockslides and rockfalls that occur within layered and fractured bedrock. These have a depth determined by the location of failure surfaces within the slope and are generated mostly on very steep slopes ($>45^\circ$) due to the forces needed to overcome the friction angle of the rock mass. Several factors may act to create potential failure surfaces in the study slope. The first is the presence of discontinuities between different geological units, which may behave as sliding surfaces (e.g. Dussauge-Peisser et al., 2003). One of the largest slope failures (SF1 in Figure 2.4a and Appendix A.3) occurred on the boundary between 2 rock types. Another large slope failure (SF2 in Figure 2.4b) occurred just above the thrust fault that cross cuts the bottom of the slope. A close up of SF2 is shown in Figure 2.10a-c. The downslope locus of the failure occurred along the thrust fault and geological discontinuity (Figure 2.10c). We observed water originating from this boundary (X in Figure 2.10c). It is known that water along discontinuities enhances the fracturing process (e.g. Pelletier et al., 1997). Another factor that may create potential failure surfaces is bedding plane strength variability (e.g. Pelletier et al., 1997). In the massive quartzites we found layers of crushed quartzite crystals, which may reduce slope stability along potential failure surfaces. Jaboyedoff et al. (2004) describe how the existence of joints containing layers of crushed and weathered ‘soil-like’ material, known as fault gouge, played a fundamental role in the destabilization of the 1991 Randa rockslide, for example. These hypothesized mechanisms could be investigated by a geomechanical study of the slope along with a higher resolution study of slope failure in the rock face. Regardless of the exact mechanisms by which these failures occur, we suggest that it is the heterogeneous nature of the fractured and bedded rock that produces a wide range of failure depths and thus deviations from the characteristic landslide size and the emergence of a power-law distribution for type (2) failures (Katz and Aharonov, 2006).

The combination of both failure types gives the characteristic MF distribution with rollover and power-law tail. This study therefore lends some empirical support to the hypothesis of Katz and Aharonov (2006) that the complex MF distribution of landslides is the combined effect of these two processes.

The distribution of type (1) and type (2) failures with slope gradient is significant in understanding the evolution of rock slopes. The fact that type (1) failures have a slope gradient distribution almost identical to the study area suggests that the slopes in the area are generally very close to the local friction angle. 95% of the large type (2) failures occur at slopes above 45° in gradient, suggesting that this is a threshold above which these failures degrade the steep slopes and limit the local relief. This provides a physical basis for the use of the concept of a threshold hillslope angle for slope failure in many landscape evolution models (e.g. Densmore et al., 1998).

Erosion rates of up to $\sim 350 \text{ mm yr}^{-1}$ (1986 – 2005) are much greater than previously reported rock-slope erosion rates (e.g. Moore et al., 2009). Averaged over the active part of the basin (4.6 km^2) this gives an annual erosion rate of about 61 mm. This is a lower estimate as it does

not take into account erosion elsewhere in the catchment. This is an order of magnitude greater than the maximum erosion rates reported for glaciated basins and volcanic rivers (Koppes and Montgomery, 2009). We propose that a high density and favorable orientation of fractures and geological discontinuities result in low rock mass strength that predisposes the slope to failure. However, the rate of erosion is ultimately controlled by environmental factors that control the processes that act to degrade the slopes (e.g. Moore et al., 2009) and which we investigate in an additional paper (Bennett et al., 2013).

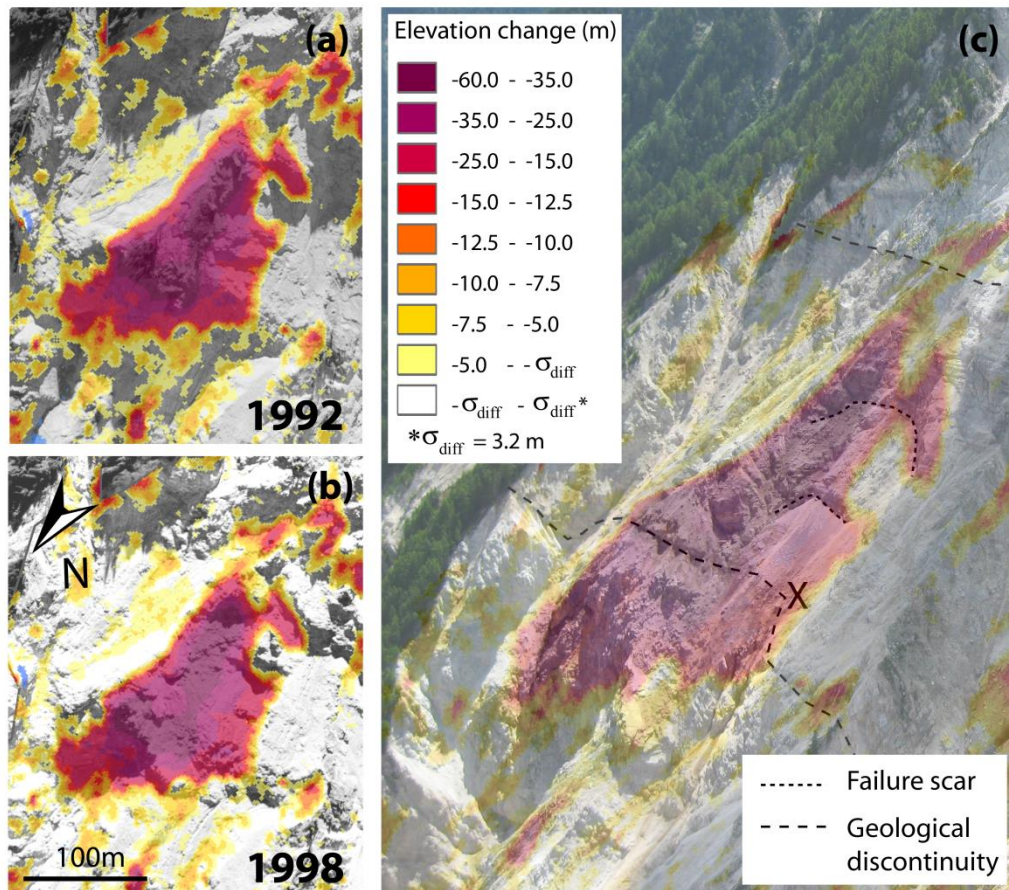


Figure 2.10 a-c – Example of a type (2) failure, SF2 in Figure 2.4b. (a): 1992 orthophoto overlaid with the 1992-1998 elevation change map. (b): 1998 orthophoto overlaid with the same elevation change map. (c): Oblique photograph taken in July 2011 overlaid with the elevation change map. The relation of SF2 to the thrust fault is clear. We observed water originating from this boundary at point X.

2.6. Conclusions

We used a digital photogrammetric processing procedure to produce a multi-temporal and high-resolution record of erosion of a steep rock slope at the head of the Illgraben catchment, Switzerland, spanning 42 years. The high erosion rate enabled us to extract a multi-temporal inventory of ~2500 slope failures that occurred in a period of particularly great erosion, 1986 – 2005. This was split in 3 sub-periods of 6/7 years. We characterized the slope failures based on their magnitude-frequency, volume-area and depth-slope gradient relations. We explored

variability in the characteristics of slope failures in the magnitude-frequency distribution and identified the relative importance of slope failures of different magnitudes as contributors to erosion and landforming agents.

The slope failures have a characteristic magnitude-frequency distribution with a rollover at $\sim 50 \text{ m}^3$ and a power-law tail between $\sim 200 \text{ m}^3$ and $1.6 \times 10^6 \text{ m}^3$ with a scaling exponent of 1.65. This exponent is at the upper end of values found for rockfalls within stronger bedrock and lower end of values found for landslides and rockfalls within weaker bedrock. This result supports the hypothesis that the value of the exponent increases, and thus that large events are less frequent, when slope strength, as determined by cohesion and friction angle, decreases.

The volume of the failures scales with area as a power law with a range of exponents $\gamma = 1 - 1.3$ resulting from volume uncertainty. These values are low for the bedrock nature of the slope, when comparing to a worldwide compilation of landslides. We hypothesize that this is due to the highly fractured and weathered state of the quartzitic bedrock, which fails at relatively shallow depths for bedrock.

Our analysis supports the hypothesis that the MF distribution is the result of two failure processes. Type (1) failures are frequent, small slides and slumps within an upper weathered layer of highly fractured rock and loose sediment. The depth of this layer limits the volume of the failures resulting in a modal failure volume, giving a physical explanation for the rollover. Type (2) failures are less frequent rockslides and falls within the internal bedded and fractured slope along pre-existing potential failure surfaces. The heterogeneous nature of the potential failure surfaces results in a wide range of failure depths, giving rise to the power law tail of the magnitude frequency distribution.

Rockslides and rockfalls of high magnitude and relatively low frequency are responsible for the high erosion rate of the study slope of $0.39 \pm 0.03 \text{ m yr}^{-1}$ as they make up $\sim 99\%$ of the total failure volume. They are also significant in the context of landscape evolution at the head of the catchment as they occur on slopes above 45° and limit the relief of the slope. This study therefore supports the concept of a threshold hillslope angle for slope failure in landscape evolution modeling.

Acknowledgements

This study was completed within the SedyMONT project, part of the ESF-funded TOPOEUROPE. Funding provided by the Swiss National Science Foundation Grant 20T021-120467 is acknowledged. Aerial photographs and 2005 Digital Elevation Model were provided by Swisstopo. Ground Control Points used in photogrammetric processing were provided by Catherine Berger. Many thanks to Rafael Caduff and James Glover for their geological insight and to Bettina Schaeppi for her help with the analysis.

3. Patterns and controls of sediment production, transfer and yield in the Illgraben

Abstract

*Quantification of the volumes of sediment removed by rock-slope failure and debris flows and identification of their coupling and controls are pertinent to understanding mountain basin sediment yield and landscape evolution. This study captures a multi-decadal period of hillslope erosion and channel change following an extreme rock avalanche in 1961 in the Illgraben, a catchment prone to debris flows in the Swiss Alps. We analyzed photogrammetrically-derived datasets of hillslope and channel erosion and deposition along with climatic and seismic variables for a 42 year period from 1963 – 2005. Based on these analyses we identify and discuss (1) patterns of hillslope production, channel transfer and catchment sediment yield, (2) their dominant interactions with climatic and seismic variables, and (3) the nature of hillslope-channel coupling and implications for sediment yield and landscape evolution in this mountain basin.

Our results show an increase in the mean hillslope erosion rate in the 1980s from $0.24 \pm 0.01 \text{ m yr}^{-1}$ to $0.42 \pm 0.03 \text{ m yr}^{-1}$ that coincided with a significant increase in air temperature and decrease in snow cover depth and duration, which we presume led to an increase in the exposure of the slopes to thermal weathering processes. The combination of highly fractured slopes close to the threshold angle for failure, and multiple potential triggering mechanisms, means that it is difficult to identify an individual control on slope failure. On the other hand, the rate of channel change was strongly related to variables influencing runoff. A period of particularly high channel erosion rate of $0.74 \pm 0.02 \text{ m yr}^{-1}$ (1992–1998) coincided with an increase in the frequency and magnitude of intense rainfall events.

Hillslope erosion exceeded channel erosion on average, indicative of a downslope-directed coupling relationship between hillslope and channel, and demonstrating the first order control of rock-slope failure on catchment sediment yield and landscape evolution.

**Bennett, G.L., Molnar, P., McArdell, B.W., Schlunegger, F., Burlando, P. 2013. Patterns and controls of sediment production, transfer and yield in the Illgraben. Geomorphology, 188, 68-82.*

3.1. Introduction

Rock-slope failures are a critical process in mountain basins. They are a key source of sediment, removing large portions of hillslopes and delivering substantial quantities of sediment to the heads of mountain channels (e.g. Hovius et al., 1997; 2000; Korup et al., 2004; Korup, 2006, 2010; Bennett et al., 2012). In many mountain basins, debris flows subsequently transport much of this sediment, and deliver it to the downstream fluvial system (e.g. Dietrich and Dunne, 1978; Haeberli et al., 1990; Zimmermann and Haeberli, 1992; Rebetez et al., 1997; Bovis and Jacob, 1999; Marchi et al., 2002; Hürlimann et al., 2003; Jomelli et al., 2004; Jakob et al., 2005; Berger et al., 2011a; Brardinoni et al., 2012). Debris flows are also important land-forming agents (Stock and Dietrich, 2006) and hazards (Jakob and Hungr, 2005). Quantification of the volumes of sediment removed by rock-slope failure and transferred by debris flows, and identification of their coupling and controls (Harvey, 2001; 2002; 2012) are pertinent to understanding landscape evolution in mountain basins and mountain basin sediment yield (Korup et al., 2010, Brardinoni et al., 2012).

Geomorphic hillslope-channel coupling, defined as the exchange of mass and energy between hillslopes and channels (Korup and Schlunegger, 2007), is important for identifying the factors that influence hillslope and channel erosion. The dominant view in geomorphology is that channel incision into bedrock in active mountain belts sets the base level for hillslope erosion (Burbank et al., 1996; Whipple, 2004). In this situation, frequent landsliding on threshold hillslopes is thought to rapidly adjust relief created by fluvial bedrock incision (Burbank et al., 1996) and may be referred to as a bottom-up process (Bishop, 2007). The direction of coupling is from channel to hillslope, in the upslope direction (Harvey, 2001; 2002; 2012). However, as Korup et al. (2010) point out, this concept is at odds with widespread landsliding that occurs independently of fluvial slope undercutting, apparently in response to environmental controls. There are many examples of large rock-slope failures aggrading and even blocking channels and consequently reducing or even preventing channel bedrock incision. Thus a downslope-directed coupling relation in which hillslope erosion controls landscape evolution and sediment yield may be more common than is currently thought (Schlunegger et al., in press). Studies that quantify relative rates of hillslope and channel erosion are needed to assess the prevalence of a downslope directed coupling relationship in the landscape.

Potential environmental controls on hillslope sediment production include rainfall (e.g. Crozier, 2010; Rossi et al., 2010) and seismic activity (e.g. Keefer, 1984; Korup, 2010). In addition, a link between an increase in air temperature and frequency of slope failures in high mountain regions is gaining support in the literature (e.g. Gruber et al., 2004; Fischer et al., 2012). Alpine permafrost has warmed by 0.5-0.8°C in the upper tens of meters during the last century (Harris et al., 2003), potentially reducing the stability of hillslopes by the melting of ice along potential failure surfaces (Haeberli et al., 1997). Conversely, higher mean temperatures may also increase slope stability and reduce the rate of sediment supply to debris flow channels by vegetation establishment on slopes and an increase in the length of the growing period (Schwab et al., 2009). Additionally, higher temperatures may decrease the occurrence of thermal weathering

by processes of freeze-thaw (e.g. Matsuoka and Sakai, 1999) and frost cracking/ ice-segregation (e.g. Hales and Roering, 2007). The combination of all of these effects means that in some settings it is difficult to detect an individual control on slope failure. For example, Allen et al. (2011) were not able to detect the dominance of any one particular factor of many possible influencing factors of slope failure in the Southern Alps of New Zealand, including climatic and tectonic factors. More research and good datasets are needed over longer timescales to decipher the environmental controls, particularly thermal controls, on slope failure.

Significant climatic change has been observed across the European Alps in the past century, with potential implications for sediment production and transfer in mountain basins. Air temperature has increased across the Alps, with a significant acceleration in the 1980s (e.g. Casty et al., 2005). An increase in precipitation and runoff has been observed in many mountain basins (e.g., Beniston et al., 1994; Rebetez et al., 1997; Frei and Schär, 2001; Birsan et al., 2005).

Changes in runoff are generally stronger than changes in precipitation, especially in the winter and spring, and they coincide with a significant warming in these seasons (Birsan et al., 2005). Several studies have noted an increase in debris-flow activity associated with both increasing temperatures and intense precipitation events (Haeberli et al., 1990; Zimmermann and Haeberli, 1992; Rebetez et al., 1997; Jomelli et al., 2004). Triggering of debris flows is most often linked to rainfall events of a certain intensity and duration (e.g. Caine, 1980; Rebetez et al., 1997; Jomelli et al., 2004; Badoux et al., 2009). Conversely, the impact of increasing temperature on debris-flow activity is less clear. Increasing temperatures are thought to increase debris-flow activity by increasing the sediment supply for debris-flow generation through permafrost degradation of contributing hillslopes (Zimmermann and Haeberli, 1992; Haeberli et al., 1990, 1993, 1997). In other catchments, sediment supply has often been identified as a limiting factor in debris flow occurrence (Zimmermann and Haeberli, 1992; Bovis and Jakob, 1999; Marchi et al., 2002; Jomelli et al., 2004; Jakob et al., 2005). Thus hillslope sediment production processes and their influencing factors need to be considered in order to fully understand debris-flow activity.

With an exceptional hillslope erosion rate by rock-slope failure of $0.39 \pm 0.03 \text{ m yr}^{-1}$ (Bennett et al., 2012) and a large and well-monitored annual sediment yield of about $100,000 \text{ m}^3 \text{ yr}^{-1}$ by debris flows (McArdell et al., 2007; McArdell and Graf., 2009, Schlunegger et al., 2009), the Illgraben in the Swiss Alps is an ideal mountain basin in which to study the combined impact of rock-slope failure and debris-flow dominated channel sediment-transfer on mountain basin sediment yield. We present an analysis of a dataset of sediment production, transfer and yield in the Illgraben spanning 1963–2005. The differentiation of sediment yield into hillslope and channel sources in different sub-periods enables the identification of their independent potential influencing factors and of hillslope-channel coupling on a decadal scale. In order to study the climatic and seismic controls on these hillslope and channel processes and ultimately on sediment yield, we conduct an analysis of precipitation, temperature, snow depth and seismic data for the study period. The ultimate objectives are to identify (1) patterns of hillslope sediment production, channel transfer and catchment sediment yield, (2) their dominant

interactions with climatic and seismic variables, and (3) the nature of hillslope-channel coupling and implications for landscape evolution in this mountain basin.

This study extends those of Schlunegger et al. (2009) and Berger et al. (2011b). Schlunegger et al. (2009) assessed rates of hillslope activity in the catchment and provided some initial estimates of hillslope erosion rates. Berger et al. (2011b) identified patterns of hillslope sediment production and channel transfer in the upper Illgraben catchment over a period of 2 years. They observed accumulation of sediment from slope failure in the upper channel in the spring and its removal during the summer.

3.2. Study site

Located in western Switzerland, the Illgraben contributes disproportionally more sediment than water into the Rhône River (Figure 3.1). The entire Illgraben basin is $\sim 9.5 \text{ km}^2$ in area, consisting of two tributary basins: the Illgraben ($\sim 4.6 \text{ km}^2$), which outputs several debris flows each year into the Rhône River, and the Illbach ($\sim 4.9 \text{ km}^2$), which contributes very little to sediment output due to the construction of the Illsee dam in 1923 (Berger, 2010). In this study we focus on the active Illgraben sub-catchment, referred to hereafter as the Illgraben.

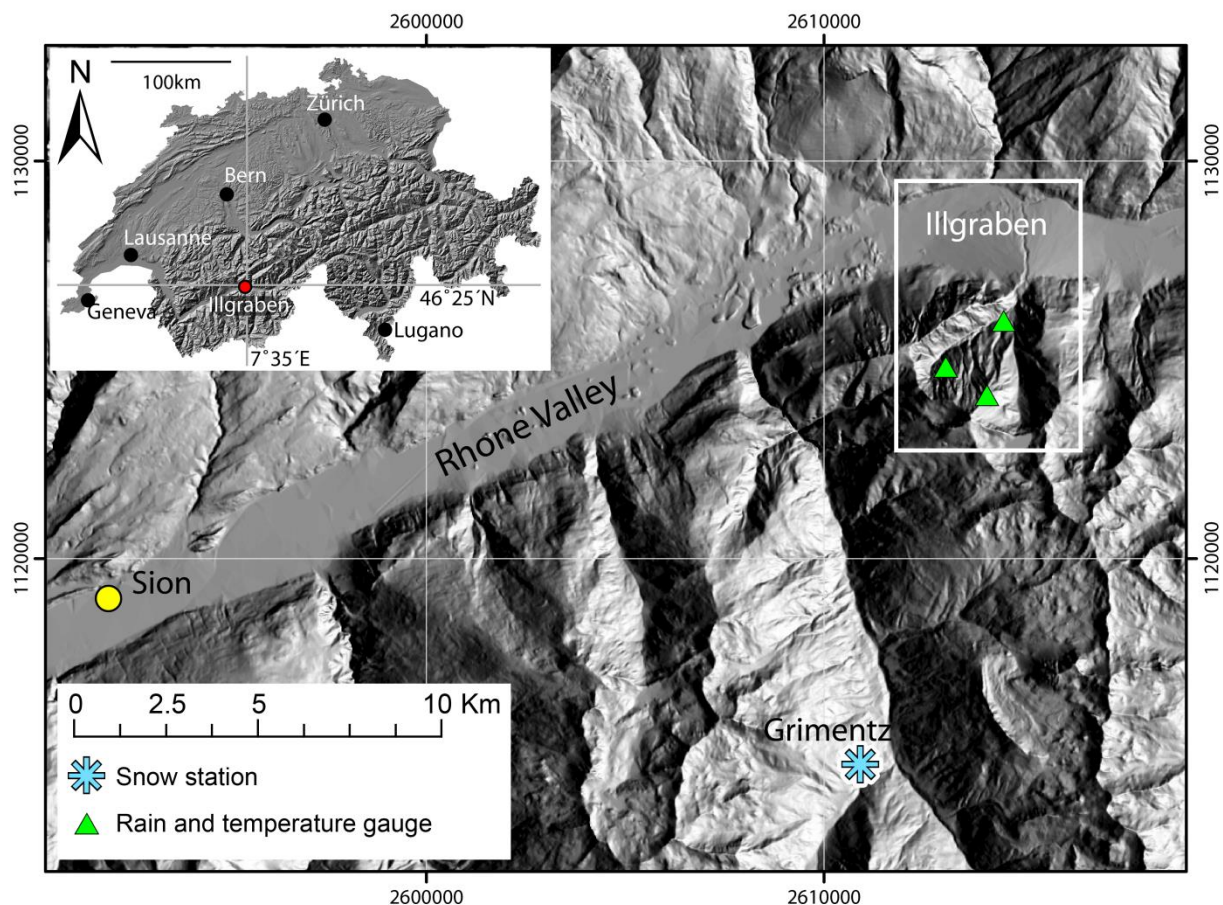


Figure 3.1 – Location map of the Illgraben in relation to the Rhône Valley and Switzerland (inset map). The locations of Sion and Grimentz, from which we obtained time series of temperature and snow depth are also shown. The study area delineated by the white box is shown in detail in Figure 3.2.

The Illgraben experiences a temperate-humid climate with a relatively low mean annual precipitation ranging from 700 mm in the lower part (610 m a.s.l) to 1700 mm at its summit (2716 m a.s.l). The rainfall occurs mainly during intense summer rainstorms in which rainfall intensity may reach more than 70 mm hr⁻¹ (Berger, 2010). Mean annual air temperature (MAT) is about 4°C based on temperature data at stations within the basin (Figure 3.1).

The Illgraben is underlain by Triassic metasedimentary rocks. The trunk channel follows a SW-NE striking fault that dissects the axial plane of a large anticline (Schlunegger et al., 2009). To the south and at the head of the channel and making up the study slope (Fig. 2), slopes expose highly fractured white and light-green sericitic quartzites with interbedded dolomites and schists, all of which dip steeply to the south-east. Slopes to the north of the channel are underlain by a succession of limestones and dolomites that also dip steeply to the south east. About 44% of the Illgraben is exposed bedrock and loose sediment cover, 42% is covered by forest and 14% by grassland (Schlunegger et al., 2009). The debris fan, with a radius of ~2 km, area of ~9 km² and volume of ~500x10⁶ m³ (Badoux et al., 2009), is large by Alpine standards and is indicative of past high rates of sediment output (Schürch, 2011).

Schlunegger et al. (2009) quantified hillslope erosion in the Illgraben and identified slopes within the study slope as the most actively eroding in the catchment between 1959 and 2004, with regions of up to 60 m of vertical erosion over the period. In contrast, the slopes to the north of the channel of predominantly dolomites experienced less than 10 m of erosion in the same period. Much of the slopes to the south of the main channel and northeast of the study slope are disconnected from the main channel due to dense vegetation cover (Schlunegger et al., 2009) and sediment supply to the main channel from these slopes is negligible. Berger et al. (2011b) made similar findings concerning catchment hillslope activity. They documented eight rockfall events and two landslides from aerial imagery in 2008 and 2009 ranging in volume from 300 to 4400 m³. All of these occurred from the study slope, apart from one landslide that occurred along a tributary channel of the main channel, located to the northeast of the study slope within the forested slopes. These studies both point to the study slope as being the most active in the Illgraben.

Bennett et al. (2012) conducted a more detailed investigation of the study slope and estimated an erosion rate of 0.39±0.03 m yr⁻¹ between 1986 and 2005 using digital photogrammetry. They found that the erosion of the study slope was achieved by ~2500 slope failures in 3 sub-periods between 1986 and 2005 that spanned 6 orders of magnitude in volume. They consider slope failure from the study slope to occur by two processes. Small, shallow slumps and slides (up to ~200 m³) remove the top, weathered layer of the slope and make up the majority of failures. Larger and deeper (>5 m) failures occur along failure surfaces within the internal part of the slope and make up almost 99% of the total failure volume.

Several extreme historical slope failures are documented in the 20th century. Major rock fall activity was reported for 1920, 1928, 1934 and 1961 by Gabus et al. (2008) and Lichtenhahn (1971). The rock avalanche of 1961 had a volume in the range of 3-5 x 10⁶ m³ and had an

initiation zone on the flank of the dolomite slopes to the north of the study slope and channel (Schürch, 2011). A large rock avalanche deposit with a volume of at least $6 \times 10^6 \text{ m}^3$ near to the fan apex has recently been dated at $3,080 \pm 410 \text{ yrs.}$ (Schürch, 2011).

The main channel has been affected by human intervention for the purposes of erosion control and monitoring. A 49 m-high check dam (CD), henceforth referred to as CD1 (Figure 3.2), was built in the upper channel between 1967 and 1969 in an attempt to retain sediment from the 1961 rock avalanche. An additional 28 smaller CDs were constructed along the channel between CD1 and the outlet (Fig. 2a) in the following decade to further stabilize the channel. Debris-flow activity has been monitored since 2000 by the Swiss Federal Research Institute WSL. A horizontal force plate together with fluid pressure sensors installed at CD29 by the outlet to the Rhône River, record total normal and shear forces and fluid pressure ratios, and geophones, laser and radar sensors are used to calculate front velocity and flow depth (McArdell et al., 2007).

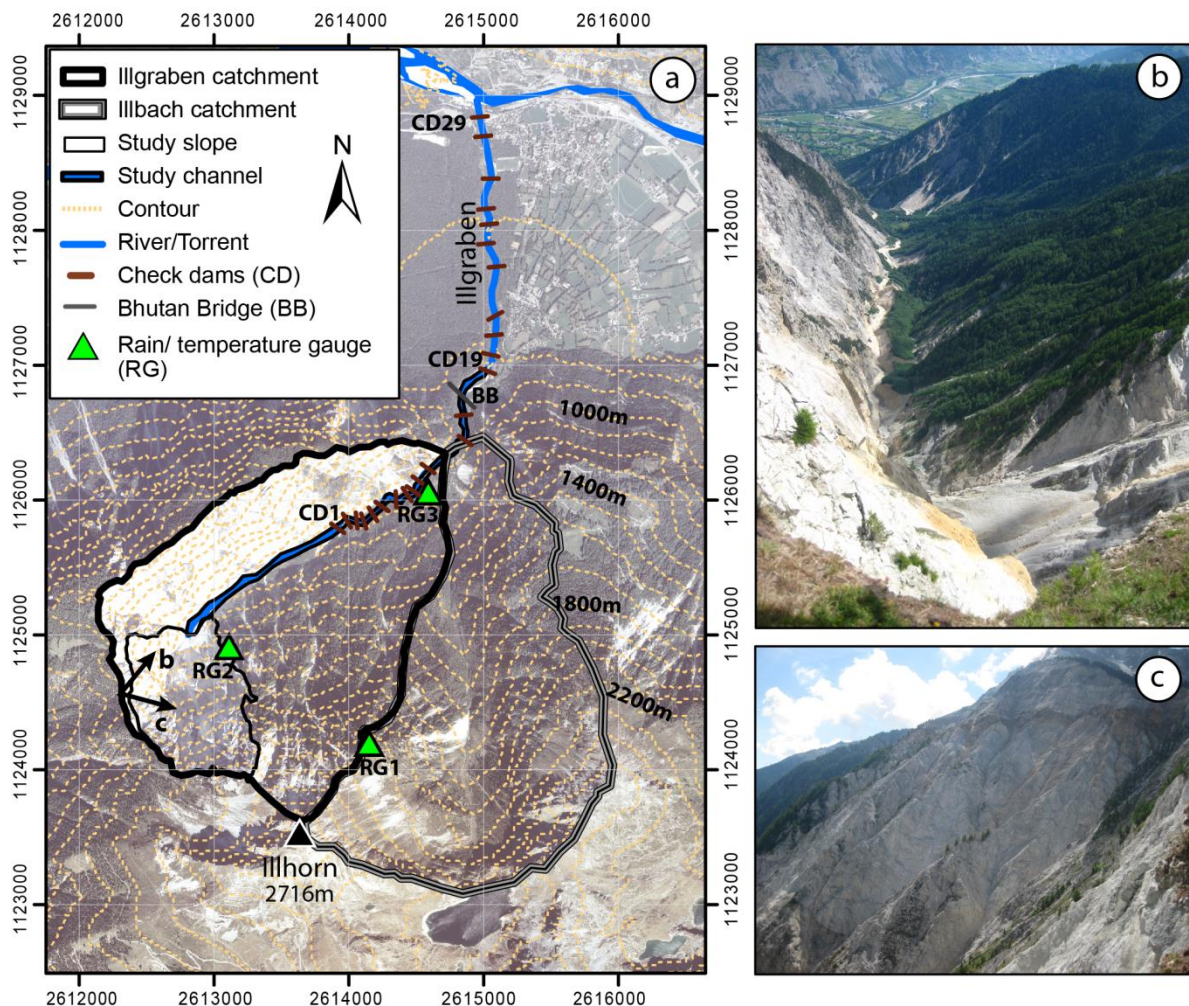


Figure 3.2 – The Illgraben and Illbach catchments and Illgraben channel; (a) map of the study slope and channel within the Illgraben catchment and channel and in relation to the surrounding topography and hydrogeography; (b) view of the base of the study slope and upper part of the study channel from the catchment crest; (c) view of the upper part of the study slope from the catchment crest. Viewing directions of photographs (b) and (c) are shown in panel (a) with black arrows.

Sediment discharge from the Illgraben into the Rhône River is dominated by debris flows. In between debris flows, low flow conditions and occasional floods transport suspended sediment along with small volumes of bedload. Usually, only sediment by debris flows and large floods can be estimated with accuracy. The volumes of sediment output by debris flows have been extraordinarily high by European standards, ranging between 60,000 and 180,000 m³ yr⁻¹ (McArdell et al., 2009; Berger et al., 2011b). In 2007 small floods were also recorded (Badoux et al., 2009), allowing an estimate of their contribution to total sediment output. There were 19 events in total in 2007; 3 of these were debris flows, contributing ~20,000 m³ of sediment, and 16 events were floods, contributing ~1,600 m³ of sediment, or 8% of that transported by debris flows. The large sediment output has resulted in a braided pattern extending over several kilometers downstream of the Illgraben in the otherwise channelized Rhône River (Schlunegger et al., 2009) and makes up between 5 and 15% of the sediment input to the entire Rhône basin (Schlunegger et al., in press).

3.3. Datasets

3.3.1. Sediment fluxes

In a previous study, we generated DEMs for 1963, 1986, 1992 and 1998 from aerial image stereopairs taken from Swisstopo (Bennett et al., 2012). These are of 2 m resolution, except for 1963, which has a resolution of 4 m. We used the 2005 Swisstopo DEM both to register the DEMs to a common reference plane and as an additional DEM in our analysis, giving four study periods (A, B1, B2 and B3). Elevation uncertainty ranges between 3.4 m for the first period of analysis (A, 1963–1986) and 2.3 m for the last period (B3, 1998–2005). The calculation of volumes of erosion and deposition from the DEMs within the study slope and channel involved several steps in ArcGIS (Bennett et al., 2012): (1) the generation of elevation change maps, (2) extraction of statistically significant changes beyond $\pm 1\sigma$ of error in elevation change maps, (3) calculation of volume changes in areas of significant change, and finally (4) estimation of volume uncertainty. We converted the resulting volumes and associated uncertainties into average rates of change and uncertainty for the different study periods (Table 3.1).

Debris-flow volumes have been calculated from flow depth and velocity data at CD29 since 2000 (McArdell et al., 2009, Appendix B.1). Prior to 2000, debris flows were recorded and their volumes estimated based on observations of deposits and witness accounts (unpublished WSL project reports, Appendix B.1). Figure 3.3 shows the annual debris-flow volume estimates. The pause in debris flows as a result of the construction of CD1 is apparent in this time series.

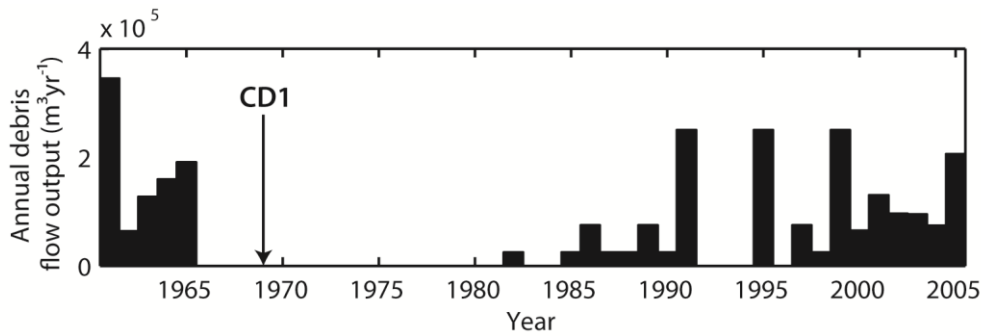


Figure 3.3 – Estimated annual average debris flow output constructed from unpublished WSL project reports (Appendix B.1). Where debris flow volume was unknown prior to 2000, an average volume of $\sim 30,000\text{m}^3$ per event was used. The black arrow indicates the construction date of CD1.

3.3.2. Climatic variables

To investigate climatic controls on sediment production and transfer, we analyzed precipitation and air temperature variables. Three rain gauges in the catchment record rainfall at a 10-minute resolution during the summer months since 2001 (RG, Figure 3.2). Only one of these gauges, RG 1, records rainfall reliably (Badoux et al., 2009). However, for this study we needed a long-term record of precipitation, which we extracted for 1961–2010 from the RhiresD dataset. RhiresD is a MeteoSwiss gridded data product that provides daily precipitation for Switzerland at kilometer grid spacing by interpolating daily rainfall measurements from stations across the country (Schiemann et al., 2010). We calculated the mean of the 12 grid cells covering the catchment and immediate vicinity so as to get a representative time-series of daily rainfall over the basin for the study period. We consider this record to be a better representation of long-term daily rainfall for the Illgraben than the nearby stations of Leuk and Sion alone. We compared the RhiresD-modeled rainfall with measured rainfall at RG 1 for the summer months of 2001–2007 using two measures: intermittency, defined as the percentage of days with no rainfall, and the mean daily rainfall depth. The intermittency is 52.7% for RG1 and 43.6% for the RhiresD. The latter is about 10% lower because of the increased probability of rainfall occurring within one of the 12 grid cells than at the single point of RG 1. The mean rainfall depth on wet days differs by only 0.04 mm (6.83 mm at RG 1 and 6.79 mm from RhiresD) justifying the use of the RhiresD dataset for the study period.

Three temperature gauges at the locations of the RGs record air temperature at 10-minute intervals since 2000. We obtained mean daily temperature data for Sion (482 m) (Figure 3.1) from MeteoSwiss for the period 1961–2005. This is the nearest station with a daily record of temperature spanning the study period. We estimated a mean monthly temperature lapse rate for the catchment from the Sion, RG 1 and RG 2 data for 2000–2010. The lapse rate ranges from $-0.21^\circ\text{C } 100\text{ m}^{-1}$ in January to $-0.64^\circ\text{C } 100\text{ m}^{-1}$ in April. Mean lapse rates and standard deviations of lapse rates are higher in the winter months due to the occurrence of frequent thermal inversions, during which temperatures in the basin may be very similar to or even slightly higher than those in the valley (Stull, 1988). We used the estimated mean monthly lapse rates

to adjust the temperature data from Sion to the mean elevation of the study slope for the whole study period.

There are no snow depth measurements for the Illgraben itself. Therefore, we obtained snow depth data for the study period from nearby Grimentz, 6 km to the southwest of the Illgraben (Figure 3.1). We use these data as an indication of the relative annual changes in snow cover. We chose this station from several surrounding stations due to its similar elevation to the study slope (1560 m) and for the length, reliability and completeness of the record (1953 to present). This station is maintained by the Institute of Snow and Avalanche Research (SLF) and we assume that the data are not significantly affected by snow redistribution.

3.3.3. Seismic activity

Switzerland is characterized by low to moderate seismicity (Edwards and Fähr, 2013). There are about 10 earthquakes that are felt by people each year on average, with damaging events predicted every 5 to 10 years based on long term statistics (Wiemer et al., 2009). Because of the weathered rock and very steep slopes, these events may also be significant for slope stability in the Illgraben. We used data from the ECOS-09 Earthquake Catalogue of Switzerland (Fähr et al., 2011) to investigate the possible influence of seismic activity on the erosion rate of the study slope. We consider earthquakes within 100 km of the study slope, of which there were 4840 of magnitude (Mw) 0.69–5.3.

3.4. Methods

Based on our knowledge of the Illgraben sediment sources (see Section 2) we schematized the sediment routing system as shown in Figure 3.4. We calculated rates of hillslope erosion (E_h) and sediment output (O_h), change in sediment storage for the channel reach above CD1 (c_1) (ΔS_{c1}) and between CD1 and CD19 (c_2) (ΔS_{c2}) and total catchment output (O_t) for each period. The mean annual sediment output rate for the hillslope and the mean annual change in storage for the channel reaches are calculated as the difference between erosion and deposition, normalized by the area (of the hillslope or channel reach) and duration of the period in years. For additional information regarding the photogrammetric processing and error analysis of the DEMs the reader is referred to Bennett et al. (2012). The inputs from the side slopes were not quantified in Bennett et al. (2012) and are thus not included in this analysis but are likely negligible compared to the input from the study slope, which was shown to be the most active slope in the catchment by Schlunegger et al. (2009) and Berger et al. (2011b).

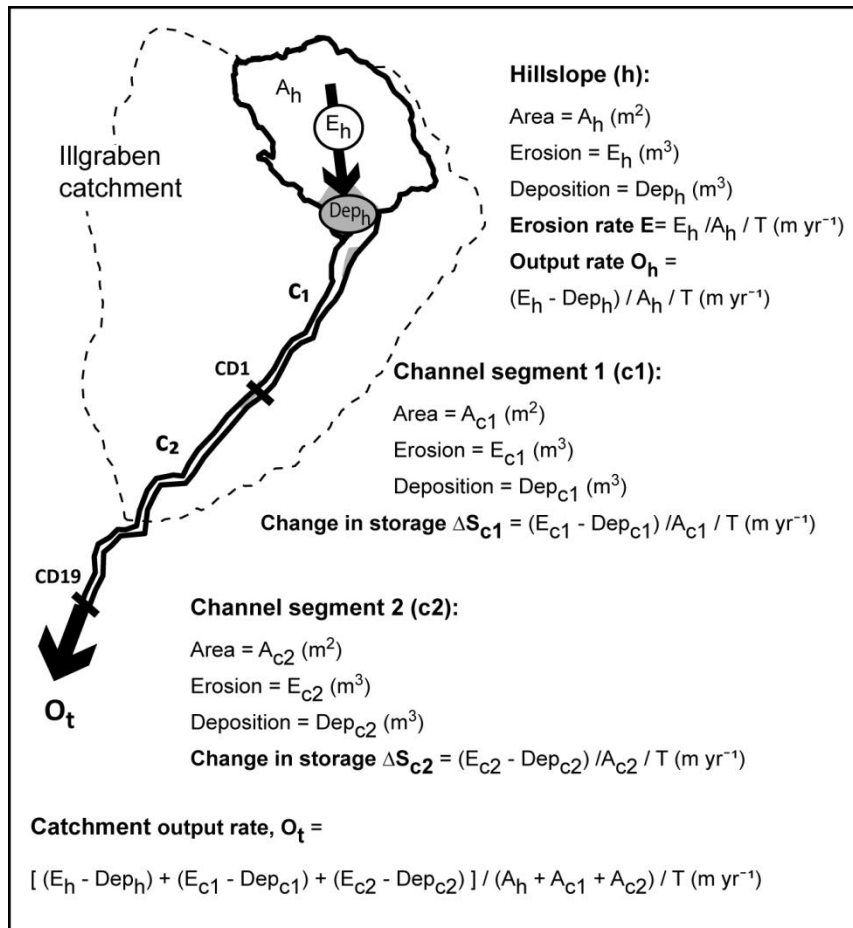


Figure 3.4 – Schematic of the sediment routing system with equations used to calculate rates of hillslope erosion, hillslope output, channel storage change and catchment output of sediment referred to in the text and displayed in Figure 3.5. T refers to the length of the period (years) between the relevant DEMs. Variables highlighted in bold are shown in Figure 3.5.

We calculated several precipitation statistics from the precipitation data including average daily precipitation and the number of days with precipitation accumulations over certain thresholds (0, 10, 20 and 30 mm). We also calculated multiple day (2, 3 and 4 day) rainfall event sums and their frequency (Table 3.2). We calculated these statistics over 3 different timescales: annual, as a measure of the total water budget (snow and rain); June and July, the months with the majority of debris flows; and snow-free periods of the year, as a measure of the potential impact of rainfall on the study slope.

We calculated several air temperature statistics: mean annual air temperature (MAT), mean April to October air temperature, the number of freezing days ($T < 0^\circ\text{C}$), the number of freezing days with no snow cover, the number of fluctuations around 0°C (freeze-thaw cycles) and the number of days within the window for ice-segregation of Hales and Roering (2007) ($3^\circ\text{C} \leq T \leq -8^\circ\text{C}$). We also inferred from the Grimentz data the average daily snow depth, maximum snow depth, and average snow cover duration for each period. We consider the maximum snow

depth for the season as an indication of snow melt at the end of the season as it determines the amount of water available in the snow pack.

We tested if the calculated climate statistics differed significantly between periods A (1963–1986) and B (1986–2005) using the Mann-Whitney U test at a significance level of 5%. We did not conduct a test of statistical significance on the seismic data due to changes in detection instrumentation over the study period. The sub-periods B1–B3 within period B are too short to conduct tests of statistical significance. In these periods we observed and qualitatively assessed whether the temporal pattern of change matches that of changes in E_h and changes in channel storage ΔS_c .

It has been shown that the initiation of slope failure may be determined by the seismic energy delivered to the slope, rather than the peak ground acceleration (PGA) (Kokusho et al., 2011). We thus calculated the seismic energy delivered to the study slope by earthquakes that occurred within a 100 km radius. Ground shaking at a location can be calculated as a function of earthquake magnitude, depth, distance and site conditions. We used a model for the Fourier velocity spectrum of an earthquake (Edwards et al., 2011) with standard parameter values calculated for Switzerland (Edwards et al., 2011; Poggi et al., 2011; Edwards and Fäh, 2013). The Fourier velocity spectrum is integrated to give seismic energy delivered to a square meter of the study slope, from which the total seismic energy delivered to the entire slope is calculated. As yet, no calibration of the threshold energy for slope failure has been developed (Kokusho and Ishizawa, 2007), but a threshold PGA for slope failure volume has been calibrated (Meunier et al., 2007). Thus, we also calculated the PGA of the earthquakes using the Swiss foreland stochastic ground motion model presented in Edwards and Fäh (2013) and Edwards et al. (2011) to establish which, if any, earthquakes were likely to have triggered slope failure. Finally, in order to identify the possible triggers of large rock-slope failures we investigated the climatic and seismic variables for the 2 weeks preceding the 1961 rock avalanche.

3.5. Results

3.5.1. Sediment production and transport

In terms of sediment budget, the first result is that the total sediment output rate from the Illgraben catchment (O_t) is greater than the estimated debris-flow volume (O_{df}) (Figure 3.5a). Importantly, this demonstrates that we are capturing the main sediment delivery area (Schlunegger et al., 2009; Berger et al., 2011b) and are not missing a large quantity of sediment input from tributaries and side slopes. In the period in which debris flows were accurately measured (1998–2005), the estimated catchment output is roughly twice that of debris flows. There are several reasons why O_{df} and O_t may not be equal. Firstly, our sediment output O_t includes fluvially transported material that is not included in O_{df} and is the subject of ongoing research (Appendix B.2). Based on estimates of sediment transported by small floods in 2007, fluvial transport may contribute an additional 8% of sediment to O_{df} (section 2).

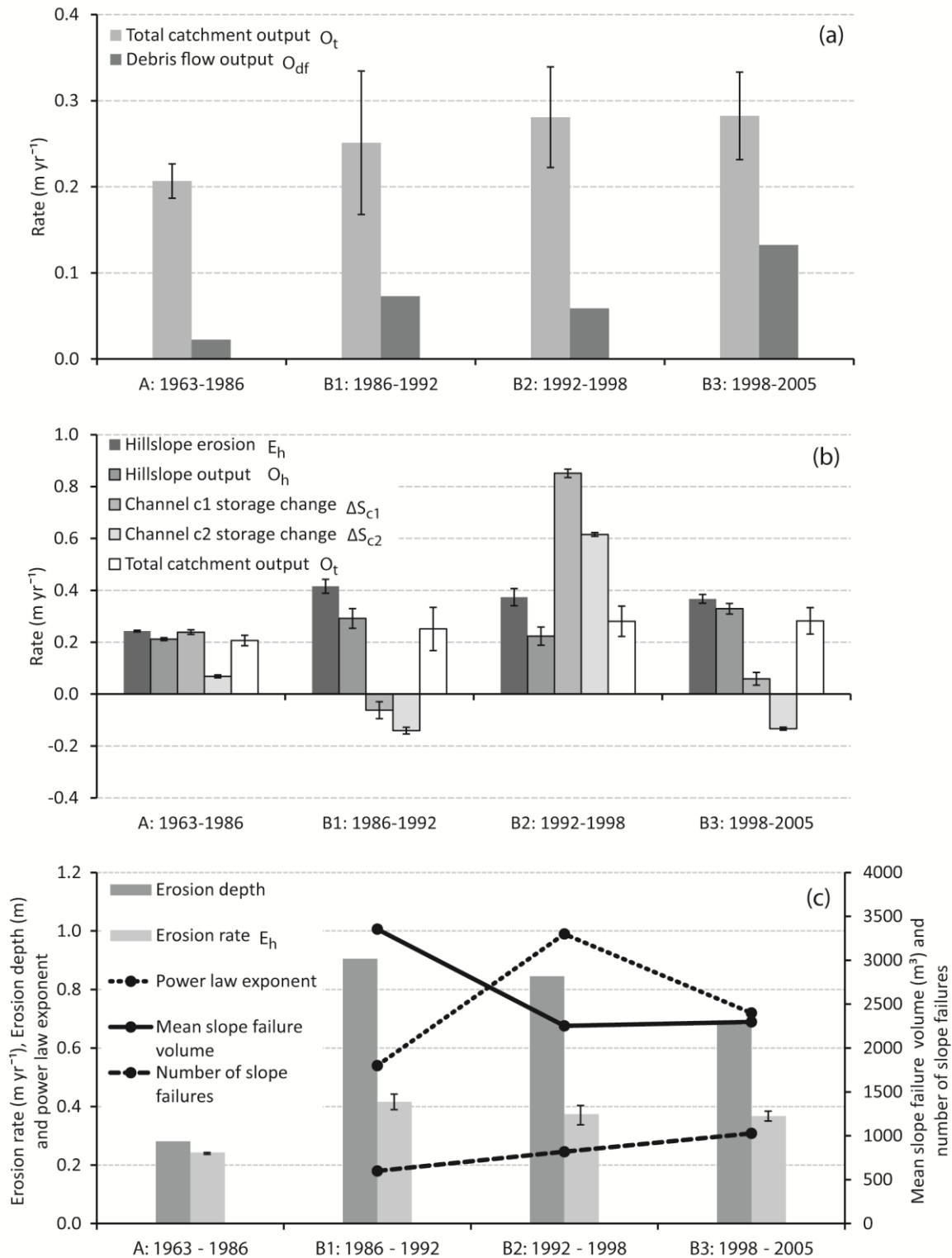


Figure 3.5 a-c – (a) Comparison of DEM-derived total catchment output rate with debris flow output rate. Output rate from debris flow data is obtained by normalizing the debris flow output, for 1963-2000 from unpublished WSL reports and for 2000-2005 from McArdeall et al. (2009), by the total study area. This is only a rough estimation for periods A, B1 and B2 due to the fact that the debris flow output was only roughly estimated until 2000. (b) DEM-derived rates of hillslope erosion and output (erosion – deposition), channel sediment storage change for c1 and c2 (see also Figure 3.7) and total catchment output with associated uncertainty bars. (c) DEM-derived rate and depth of hillslope erosion for periods A to B3 and statistics of slope failures from Bennett et al. (2012) for sub-periods B1-B3.

Secondly, the measurement locations of O_t and O_{df} are different; O_t is sediment output at the fan apex and thus does not include the change in the channel over the debris fan, while O_{df} is measured at CD29, at the catchment outlet. Redeposition of sediment on the fan would reduce O_t and decrease the discrepancy. We can estimate a likely percentage of redeposition over the fan from data published in Schürch et al. (2011b). They measured the volume changes over the fan (between CD10 and CD29) of 14 debris flows that occurred between 2007 and 2009. Eleven of these were depositional resulting in cumulative deposition of 10^5 m^3 over this period. This equates to redeposition of almost 30% of sediment over the fan. Finally, there are large uncertainties in the estimation of debris flow volumes. For example, in the 2 years 1998–2000, debris flow volumes are likely underestimated (unpublished WSL reports). Additionally, the volume calculation from measurements of velocity and frontal height as a function of time contains uncertainty (Schlunegger et al., 2009; Schürch et al., 2011b).

Figure 3.5b shows the temporal sequence in mean erosion rates and sediment output in the different periods (values are listed in Table 3.1). We find that two main changes occurred. Firstly, there was an increase in the mean hillslope erosion rate between periods A and B and a corresponding increase in hillslope output rate and total catchment output rate. Secondly, there was a dramatic increase in mean channel erosion in sub-period B2 compared to the sub-periods B1 and B3. In period B2 the channel was eroding rapidly, while in periods B1 and B3 the channel aggraded.

The increase in hillslope erosion rate after period A is related to an even greater increase in the mean depth of erosion (Figure 3.5c). The statistics of slope failures from Bennett et al. (2012) are superimposed on the erosion rate and depth of erosion in periods B1 to B3 in Figure 3.5c. While the number of slope failures increased from ~500 to ~1000 between periods B1 and B3, the mean failure volume and depth decreased, related to a decrease in erosion depth and rate. The power law exponent of failures in the tail of the magnitude frequency distribution also increased, indicating a decrease in frequency of the largest failures relative to the smaller ones (Bennett et al., 2012).

The boundary of the channel with the study slope is important with regard to the geomorphic coupling of the hillslope with the channel. Throughout the study period there was a zone of deposition at the base of the study slope (Figure 3.6). This zone of deposition is persistent throughout the study period, unlike any zones of deposition in the channel, which are usually eroded in subsequent periods (Figure 3.7). This hillslope zone of deposition results in lower O_h than E_h (Table 3.1). The amount of redeposition does not reflect the pattern of channel storage change and so would appear to have separate controls. For example, B2 was the period of most erosion of channel storage but also of most hillslope redeposition.

Table 3.1 – Rates of hillslope erosion (E_h) and output (O_h), channel storage change (ΔS_{c1} and ΔS_{c2}) and catchment output (O_t) and uncertainties. Positive ΔS_c means erosion.

Rate (myr^{-1})	A (63 -86)	B1 (86-92)	B2 (92-98)	B3 (98-05)
E_h	0.24 ± 0.01	0.42 ± 0.03	0.37 ± 0.03	0.37 ± 0.02
O_h	0.21 ± 0.01	0.29 ± 0.04	0.22 ± 0.04	0.32 ± 0.02
ΔS_{c1}	0.24 ± 0.01	-0.06 ± 0.03	0.85 ± 0.02	0.06 ± 0.03
ΔS_{c2}	0.07 ± 0.01	-0.14 ± 0.01	0.62 ± 0.01	-0.13 ± 0.01
O_t	0.21 ± 0.02	0.25 ± 0.08	0.28 ± 0.06	0.28 ± 0.05

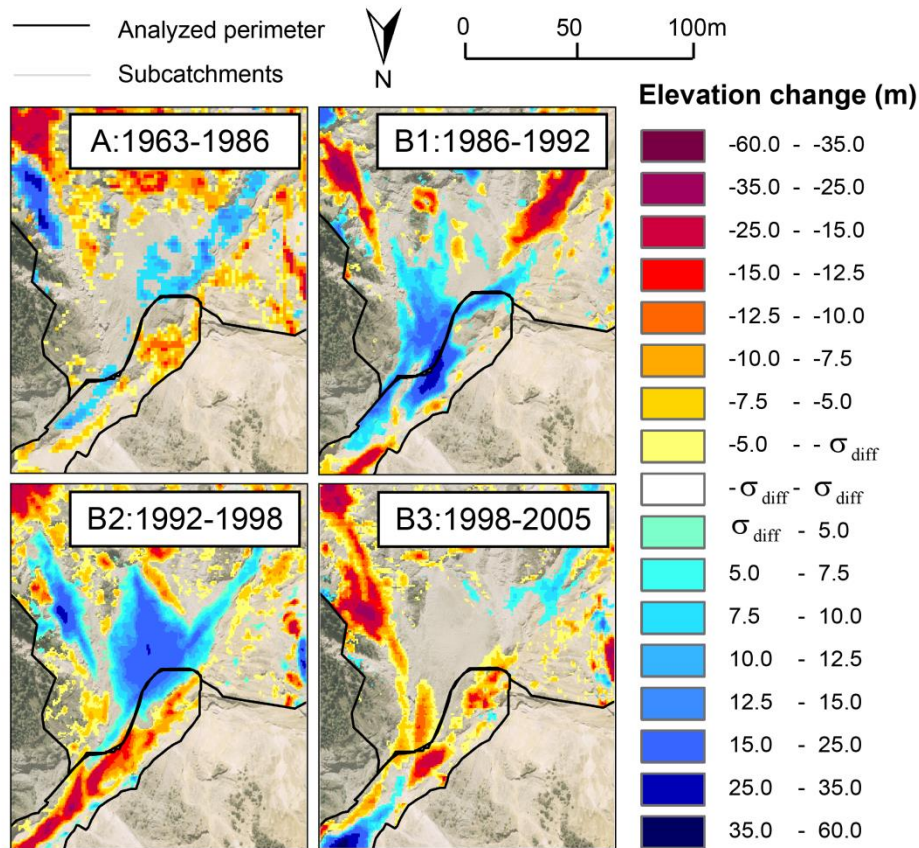


Figure 3.6 – Depositional zone at the base of the study slope and channel head. For values of σ_{diff} , see Figure 3.7. Data from Bennett et al. (2012).

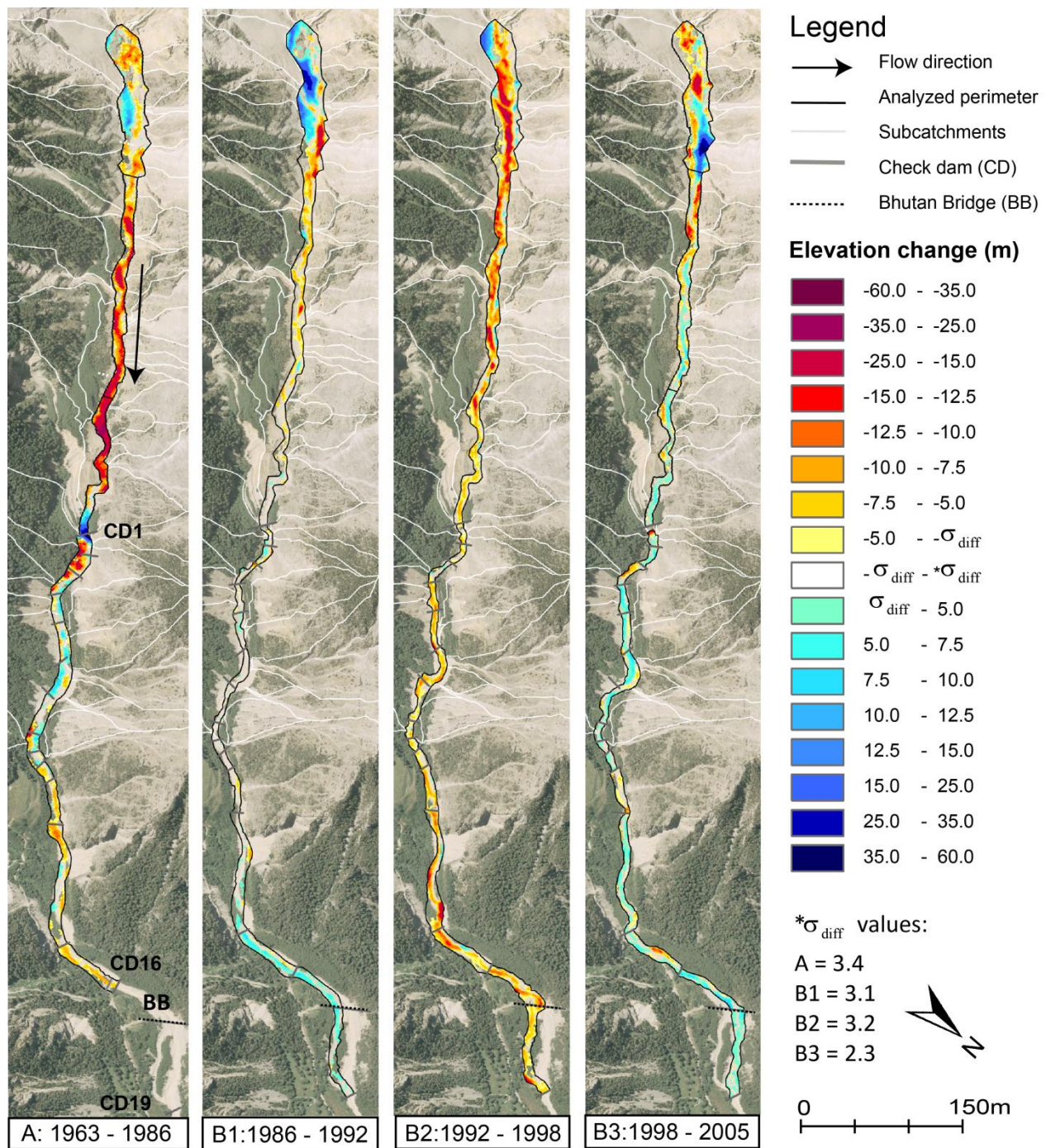


Figure 3.7 – Channel elevation change for periods A and B1–B3 (see also Figure 3.5). σ_{diff} values are the elevation uncertainties specific to each period. Only elevation changes above $\pm \sigma_{diff}$ are considered statistically significant (Bennett et al., 2012).

3.5.2. Relation of changes to climate and earthquakes

Annual precipitation did not differ significantly between periods A and B and is therefore not a significant explanatory variable for the changes in hillslope erosion (Figure 3.8a-b; Table 3.2). The number of days of rainfall of different magnitudes in June and July also did not show a statistically significant difference between periods A and B (Table 3.2). The only statistically significant differences between periods A and B that we can identify is that period B had generally fewer days of precipitation but higher 2-day event totals. There was also a significant increase in the number of days of rainfall in snow free periods of the year. However, the increase only occurred in period B2 and therefore does not explain the increase in hillslope erosion observed in period B1. Based on these results, we conclude that the increase in hillslope erosion between periods A and B cannot be confidently explained by changes in precipitation statistics in those periods.

Air temperature changed significantly between periods A and B. Mean annual air temperature increased by more than 1°C from 2.7 to 3.8°C. The shift is evident across the whole range of the statistical distribution (Figure 3.8c) and in the plot of mean monthly temperatures for periods A and B (Figure 3.9). The warming tendency was accompanied by statistically significant decreases in the number of freezing days, and all snow cover variables (mean and maximum snow depth, snow cover duration) (Figure 3.8d). There were also decreases in the number of frost-cracking days and the number of freeze-thaw cycles (Table 3.2). However, the number of freezing days per year with no snow cover increased significantly between periods A and B, with a particularly strong increase in period B1, which indicates a possible increase in thermal weathering of the slope related to its increased exposure to fluctuations in temperature. Based on these results, we conclude that temperature-related variables are much more likely to explain the increase in hillslope erosion between periods A and B.

In assessing the influence of seismic activity on the study slope, we must first consider the likely influence of individual events based on their PGAs. The largest earthquake in the study period occurred in 1964. It had the greatest magnitude ($M_w=5.3$), delivered the most energy to the slope (74 J m^{-1}) and resulted in the greatest PGA (0.05 m/s^2), although it had one of the longest hypocentral distances from the slope (86 km). The PGA of this event is two orders of magnitude below the threshold of 1 m/s^2 for slope failure found by Meunier et al. (2007) for earthquakes in Taiwan and California, suggesting that it and all other, smaller events are unlikely to have triggered a slope failure. However, the threshold PGA for failure may be lower for the highly fractured and steep slopes of the Illgraben.

Regardless of the significance of seismic events with such low PGAs to the study slope, seismic energy is not correlated with hillslope erosion rate. Average annual seismic energy was several times greater in period A than in period B although the number of earthquakes was higher in B. Period B1 of the highest hillslope erosion rate was in fact the period with the least seismic energy. It is therefore very unlikely that seismic activity was a cause of the observed increase in hillslope erosion.

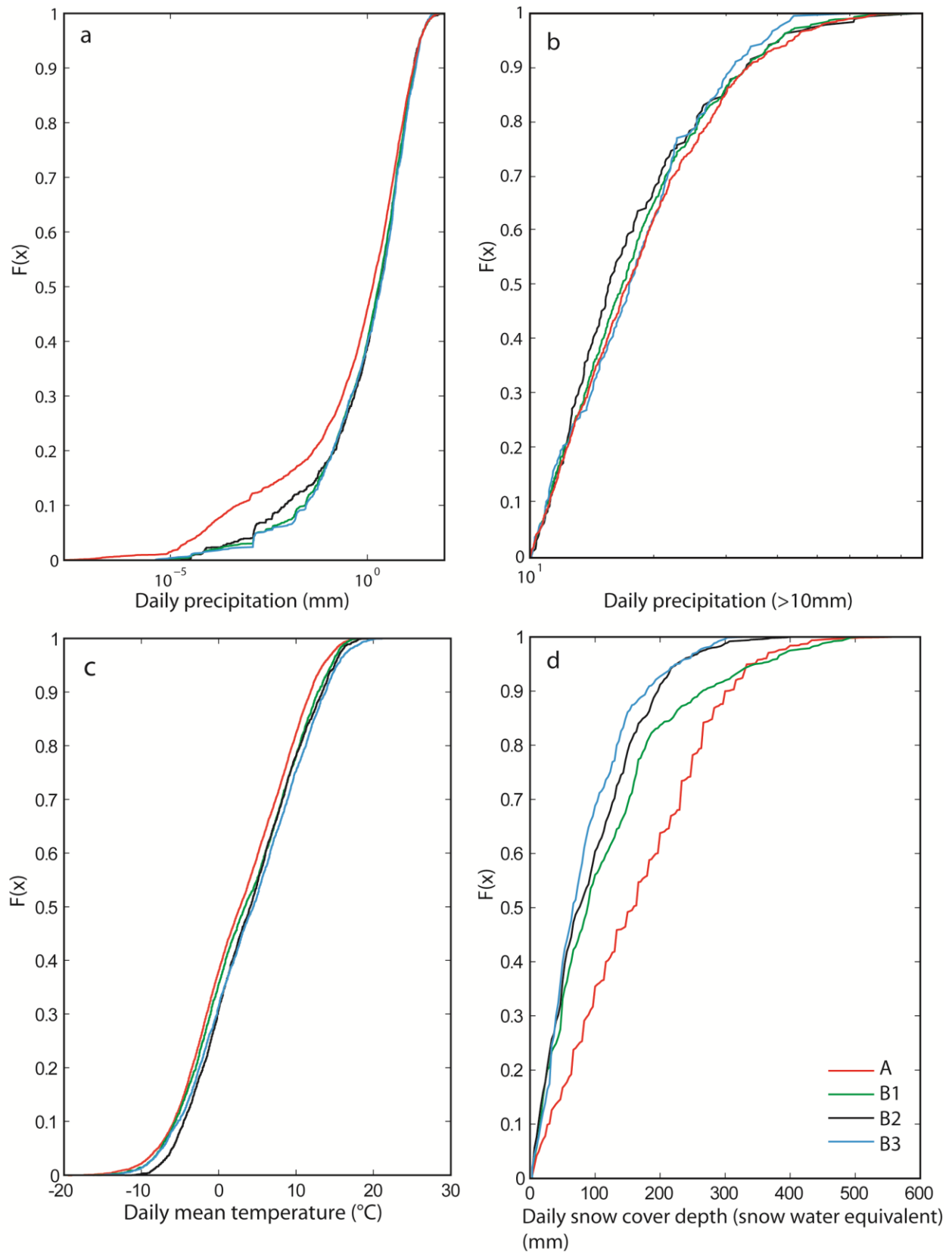


Figure 3.8 a-d – Empirical cumulative distribution functions of the main climatic variables in Table 3.2 for the different study periods.

Table 3.2 – Analysis of climatic variables for sub-periods within 1963-2005. Statistically significant changes in statistics are marked X. All p-values for statistically significant changes in variables marked in Table 3.2 are less than 0.04.

Variable	A 1963- 1986	B 1986- 2005		B1 1986- 1992	B2 1992- 1998	B3 1998- 2005
Precipitation in Jan – Dec (12 months)						
Mean annual rainfall	985	1007		963	1061	997
Days yr ⁻¹ >0mm	199.9	187.5	X	178.3	190.5	192.7
Days yr ⁻¹ >10mm	31.5	32.8		31.7	35.7	31.4
Days yr ⁻¹ >20mm	11.9	11.5		10.3	13.5	10.7
Days yr ⁻¹ >30mm	4.7	4.5		4.5	4.2	4.7
Rainfall in June – July (2 months)						
Days yr ⁻¹ >0mm	62.2	59.5		55.5	62.3	60.8
Days yr ⁻¹ >10mm	9.4	10.4		9.1	11.2	10.8
Days yr ⁻¹ >20mm	3.9	3.4		2.3	3.8	4
Days yr ⁻¹ >30mm	1.5	1.1		0.6	1	1.6
Rainfall in snow-free period						
Days yr ⁻¹ >0mm	118.7	127.7	X	107.3	129.2	143.9
Days yr ⁻¹ >10mm	18.1	21.4	X	18.3	23.3	22.3
Days yr ⁻¹ >20mm	7.3	7.3		5.8	8.8	7.3
Days yr ⁻¹ >30mm	2.7	2.7		2.5	2.7	3
Multiple day rainfall events						
Number of 2 day events	12.1	13.2		12.7	12.6	14
Mean event total (mm)	18.1	21.5	X	17.4	23	23.1
Number of 3 day events	4.9	5.4		5.2	4.4	6.1
Mean event total (mm)	28.5	34		23.4	35.7	39.1
Temperature						
Mean annual air temp. (°C)	2.7	3.8	X	3.4	4	4.1
Mean Apr-Oct air temp (°C)	7.8	8.1	X	8.7	8.8	7.1
Frost cracking days (-3 - -8°C)	62.5	55.7		59	50.8	57
Freezing days (<0°C)	138.3	124.3	X	129.3	111.8	130.6
Freeze thaw events	14.3	15.1		15.2	16.3	13.9
Snow at Grimentz						
Snow cover duration (days)	155.1	133.2	X	128.3	126.7	142.9
Mean snow cover (cm)	149.4	89.7	X	77.3	107.5	85.7
Max snow height (cm)	501	453	X	294	453	360
Days with T<0°C and no snow cover	17.6	22.7	X	31	21.8	17

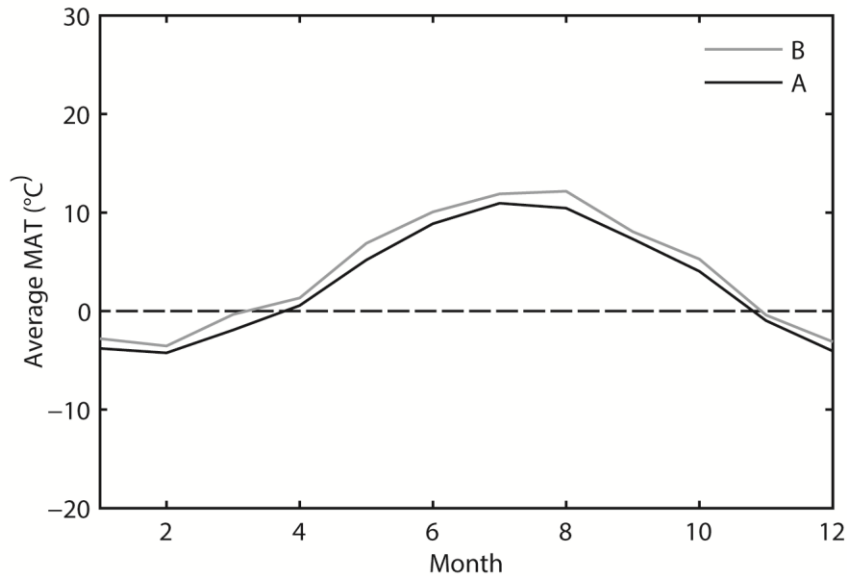


Figure 3.9 – Mean monthly temperatures for periods A and B adjusted for the mean elevation of the study slope.

The dramatic erosion of channel storage in both reaches in period B2 (compared to periods B1 and B3) corresponded to a general increase in rainfall intensity in this period, especially in the summer (June-July) and in the snow-free period of the year. Higher rainfall was accompanied by the highest mean snow depth and, by inference, meltwater runoff in period B2 (Table 3.2). The result is that the pattern of channel sediment storage change between periods B1 and B3 qualitatively corresponds to rainfall variability and meltwater availability, suggesting that runoff generated in the channel is driving channel erosion, by fluvial transport and debris flow generation.

3.5.3. Triggering of the 1961 rock avalanche

We looked at the conditions for the 2 weeks preceding the rock avalanche on 26 March 1961 to assess possible triggering factors of this failure and to enhance understanding of the factors influencing slope failure in our study period.

There was a series of four earthquakes of $M_w=3.1$ in the 2 weeks prior to the rock avalanche (Figure 3.10). Three of these occurred within 15 km of the slope that failed and delivered substantial seismic energy to the slope. The closest of these (within 2.5 km of the failure slope) delivered 2×10^6 J to the study slope on 18 March and was a rare event in the 0.4th percentile compared to all events within a 100 km radius from 1960 to 2005, although it had a PGA of 0.01 m/s^2 , 2 orders of magnitude below the suggested threshold for slope failure of Meunier et al. (2007). One week prior to the rock avalanche there was a rainfall event of 10 mm. In the following 4 days the air temperature dropped by 7.4°C to below 0°C (Figure 3.10) and remained below 0°C for several days. The rock avalanche occurred on the first day air temperature rose above 0°C. The meteorological conditions following the earthquake were very uncommon over

the study period. For instance a temperature drop $\geq 7.4^{\circ}\text{C}$ in 4 days has a probability of occurrence of $<1\%$. An equivalent temperature drop that was preceded by a rainfall event of $\geq 10\text{mm}$ was an even rarer event.

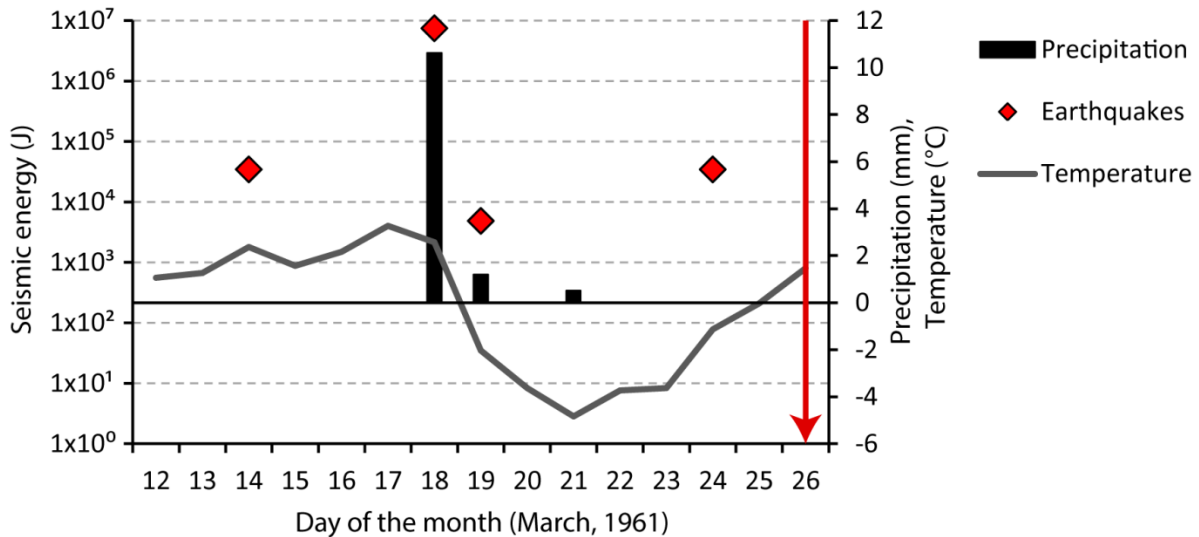


Figure 3.10 – Seismic activity and meteorological conditions leading up to the rock avalanche on 26th March (red arrow).

This example illustrates the difficulty of identifying the triggers of slope failures. Several factors may have contributed to the failure, and it is practically impossible to conclusively separate the factors into those that may have predisposed the slope to failure from those that acted as triggers.

3.6. Discussion

3.6.1. Patterns and influences of hillslope erosion

The increase in E_h after period A was related to increases in the depth of erosion and mean slope failure volume (Figure 3.5c). The statistics of individual failures are not known for period A as the longer duration of the period and coalescence of failures prohibited the extraction of individual failures (Bennett et al., 2012). However, due to the shallower depth of erosion we suggest that there was an absence of large, deep-seated bedrock failures in period A and that these occurred mostly in period B. This leads to the question of the possible causes of the increase in this type of slope failure process in period B.

Potential influencing factors for deep-seated slope failures include seismic activity, thermal variations in the rock, availability of erodible bedrock and the supply of water from rainfall, snowmelt, or thawing permafrost. Our results suggest that neither total rainfall amount nor seismic activity influenced the increase in hillslope erosion as B1 was the sub-period in the study period with the least rainfall and seismic activity. In the following discussion we propose

two hypotheses to explain the increase in hillslope erosion through deep-seated bedrock failures.

The first hypothesis to explain the observed increase in hillslope erosion in period B1 is an increase in thermal weathering of the slope surface, related to an increase in the exposure of the slope to variations in air temperature, in turn related to the significant decrease in snow cover depth and duration, a feedback that has been suggested in the literature (Jomelli et al., 2004). An increase in thermal weathering is suggested by a near doubling in the number of days with no snow cover and air temperature below 0°C between periods A and B1. Air temperature fluctuations may also affect the slope during times of low snow cover. Keller and Gubler (1993) determined a critical snow height of 0.8 m for thermal insulation of the ground. Rödder and Kneisel (2012) found that the depth of penetration of the winter cold wave can be twice as deep in winters with a snow depth <0.8 m. The mean annual snow depth during B1 was just below this critical snow depth suggesting that thermal weathering during the snow-covered periods may also have played a role. Cycles of expansion and contraction in the shallow subsurface have been shown to create stress changes at greater depths and induce failure along discontinuities that are already close to failure (Gischig et al., 2011). Thus variations at the surface may be responsible for the observed increase in the depth of erosion and related increase in erosion rate in period B1.

The second hypothesis to explain the increase in E_h is the lagged permafrost degradation at depth in the slope associated with the increase in MAT (e.g. Gruber et al., 2004; Fischer et al., 2012). Although the MAT at the altitude of our study slope remained above 0°C throughout the study period, the north facing exposure of the study slope and the complex topographic variations mean that MAT may be very spatially variable and possibly below 0°C locally. Furthermore, it is possible that permafrost may persist at depth even if surface air temperatures would not indicate it (Noetzli et al., 2007). There is still some localized permafrost on the upper slopes of the Illhorn (above 2200m) according to the Swiss map of permafrost (BAFU, 2006).

In support of a thermal influence on the increase in hillslope erosion, either by an increase in weathering or the thawing of permafrost, the temporal pattern of E_h of the study slope corresponds to the temporal pattern of rock-slope failures related to air temperature documented by Fischer et al. (2012) for the whole of Switzerland over more than a century. Fischer et al. (2012) note that the periods with little or no slope failure in the past century (1910 – 1930 and 1960 – 1980) correspond to steady or even slightly decreasing atmospheric temperature, whereas periods with increased slope failure activity (1940 – 1960 and 1990 onwards) correspond to time periods of atmospheric warming. The timing of the increase in hillslope erosion of our study slope, through an increase in deep-seated, large-volume failures, corresponds with an increase in rock-slope failures in the Swiss Alps and neighboring areas since 1990 (Fischer et al., 2012). Similar temporal patterns were also observed in the Mont Blanc Massif (Ravanel and Deline, 2011).

While thermal processes appear to have been the most important factor influencing slope failure in period B1, we lack evidence for a clear trigger of slope failure that can explain the temporal pattern of hillslope erosion and the occurrence of the 1961 rock avalanche. The 1961 event was preceded by both extreme meteorological conditions and seismic activity, making it difficult to identify its trigger. We suggest that it is difficult to distinguish triggers of slope failure in the Illgraben, given that the hillslopes are highly fractured and close to threshold conditions for incipient failure (Bennett et al., 2012) and given multiple potential triggers of failure, such as thermal weathering, permafrost degradation, seismic events and large storms. This questions the general anticipation that there has to be an environmental trigger of slope failure. Instead, slope failure can be considered as a progressive phenomenon occurring in a self-organized fashion (Rosser et al., 2007). Rosser et al. (2007) hypothesize that a slope accumulates damage from small failures and eventually reaches a threshold condition for large failure, which thus may have no apparent environmental trigger.

3.6.2. Patterns and influences of channel sediment transfer

An important factor to consider in understanding the patterns of channel sediment storage change over the study period is the influence of the construction of CD1 and of a series of smaller check dams along the length of the channel during the late 1960s and 1970s on channel sediment transfer. The 1961 rock avalanche filled the channel with $3.5 \times 10^6 \text{ m}^3$ of sediment (Gabus et al., 2008). The authorities thus constructed CD1 (Figure 3.2), 1.5 km from the head of the channel in the late 1960s to halt the increase in debris-flow activity that occurred following this event. The apparent absence of debris flows reaching the catchment outlet until the early-1980s (Figure 3.3) indicates that the check dams indeed reduced sediment output during this time. Without the construction of CD1 the high rate of debris-flow activity that immediately followed the 1961 rock avalanche would have undoubtedly continued, resulting in a more rapid release of the rockfall deposit and a higher rate of erosion of sediment stored in the channel in period A. As it was, the average erosion rate of the two channel reaches, ΔS , was only $0.15 \pm 0.01 \text{ m yr}^{-1}$ compared to $0.20 \pm 0.02 \text{ m yr}^{-1}$ in period B.

However, the effect of the dams on channel sediment transfer was neutralized by their being filled by the mid-1980s, when debris flows resumed (Figure 3.3). Indeed, the debris flows in 1991, 1995 and 1999 were the largest recently reported with an upper estimate of their volume of $2.5 \times 10^5 \text{ m}^3$ (unpublished WSL reports). During period B2 of rapid channel erosion the channel incised into sediment stored behind the check dams, demonstrating that they cannot entirely prevent channel incision. The channel also later changed its path to a previously occupied channel just below the Bhutan Bridge for a length of 100 m (Figure 3.7). Thus, although the check dams have reduced the gradient of the channel and may have some effect in modulating debris flow severity, we consider the pattern of ΔS of the two channel reaches post-1986 not to be significantly disturbed by damming.

There are two main processes by which the increase in intense rainfall events may have resulted in the high rate of erosion of channel storage in period B2. Firstly, by an increase in

extreme streamflow events during which sediment was entrained and debris flows initiated (Badoux et al., 2009). Alternatively, the increase in water supply may have increased debris flow frequency by the mobilization of landslides into debris flows (Costa, 1984; Bovis and Jakob, 1999; Marchi et al., 2002; Guzzetti et al., 2004). The relation between rapid channel storage erosion and rainfall intensity agrees with findings in several other catchments at this time. For example, Rebetez et al. (1997) found that an increase in debris-flow activity in the Ritigraben catchment was related to an increase in three-day event magnitude in August and September.

In contrast to B2, B1 was a period of deposition in both channel sections. This indicates dominantly transport-limited conditions in this period, in which hillslope erosion and supply (output) exceeded the capacity of the channel to transfer sediment (e.g. Schlunegger et al., 2009), which is in agreement with the analysis of the precipitation variables that showed that this was the driest period. B2 therefore represents a lagged response of the channel system to the increase in hillslope erosion and supply in B1. Significantly more sediment was removed from the channel in B2 than the sediment supplied by the hillslope in period B1, emphasizing the importance of entrainment by debris flows (Berger et al., 2011b).

3.6.3. Hillslope-channel coupling and implications for landscape evolution and sediment yield

A key concept in geomorphology is that channel incision into bedrock in active mountain belts sets the base level for hillslope erosion (Burbank et al., 1996; Whipple, 2004), which implies an upslope-directed coupling relationship (Harvey, 2001; 2002; 2012). In this case, the rate of channel incision controls the rate of hillslope erosion and catchment sediment yield. Several factors are inconsistent with such a coupling relationship in the Illgraben. Firstly, hillslope erosion rate exceeded channel erosion rate over the study period, indicating that hillslopes eroded independently of channel incision. E_h ($0.35 \pm 0.02 \text{ m yr}^{-1}$) exceeded the sediment eroded from channels ($0.18 \pm 0.01 \text{ m yr}^{-1}$) by a factor of almost 2 over the study period 1963-2005. Additionally, the detachment locations of slope failures within the study slope are inconsistent with an upslope-directed coupling relationship in which landslides typically occur at the over-steepened toes of the hillslopes directly adjacent to the incising channel (Korup and Schlunegger, 2007). Instead, many slope failures within the study slope occurred several hundred meters above the channel head (Bennett et al., 2012). While an effect of check dams is to prevent channel incision and in turn reduce basal hillslope failures, the high E_h in B1 indicates that channel stabilization did not stabilize the hillslopes as would be expected in the case of an upslope-directed coupling relationship.

Furthermore, the state of connectivity of the study slope with the channel is at odds with an upslope-directed coupling relationship. Throughout the study period there is a zone of deposition at the base of the study slope (Figure 3.6). This zone of deposition buffered the channel from the hillslope such that not all sediment eroded from the hillslopes was immediately output into the channel. Moreover, this zone would have buffered the hillslope from the channel, such that channel incision in B2 did not result in an increase in hillslope

erosion in B3. On the basis of this evidence, we suggest that this study demonstrates a downslope-directed coupling relationship in which hillslopes erode independently of channel incision at a rate influenced by environmental factors as discussed in section 3.6.2.

Hillslope erosion rate was the first order control on the total sediment output over the study period. For example, O_t increased in period B1 in response to the increased hillslope erosion rate. However, much of the sediment eroded from the study slope was stored in the channel and not released until period B2. Indeed O_t was slightly higher than in B1 demonstrating a lagged response of the catchment to the increase in hillslope erosion. This demonstrates the importance of the channel in regulating catchment output O_t , although it plays a secondary role to hillslopes in controlling catchment sediment yield.

Undoubtedly the check dams have a role to play in the future evolution of the catchment by preventing removal of the sediment cover and thus bedrock incision. It remains to be seen if hillslope erosion will maintain the rapid rate witnessed over the study period. One possibility is that hillslope erosion will reduce as the slopes attain more stable gradients. Alternatively, given the availability of fractured rock and sufficient water from rainfall and snowmelt, rock-slope failure may continue to erode the slopes of the Illhorn and continue providing high sediment yields into the Rhône.

3.7. Conclusions

We analyzed a photogrammetrically derived dataset of hillslope production, channel transfer and catchment output of sediment in the Illgraben, a highly active debris flow catchment in the Swiss Alps, along with climatic and seismic data for the period 1963 to 2005. We aimed to identify (1) patterns of hillslope sediment production, channel transfer and catchment sediment yield, (2) their dominant interactions with climatic and seismic variables, and (3) the nature of hillslope-channel coupling and implications for sediment yield and landscape evolution in this mountain basin. The study captures a multi-decadal period of channel erosion in response to an extreme rock avalanche in 1961 that was punctuated by shorter cut-and-fill cycles that occurred in response to the construction of check dams, changes in hillslope sediment supply and changes in transport capacity.

There were two main results from the analysis of patterns of sediment production and transfer. Firstly, there was an increase in mean hillslope erosion rate between periods A (1963 – 1986) and B (1986 – 2005) from $0.24 \pm 0.01 \text{ m yr}^{-1}$ to $0.39 \pm 0.03 \text{ m yr}^{-1}$. This corresponded with an increase in the depth of slope erosion. Secondly B2 (1992 – 1998) was a period of rapid channel erosion of up to $0.74 \pm 0.02 \text{ m yr}^{-1}$, which was preceded and followed by periods of channel aggradation.

Analysis of climatic variables revealed a picture of a warming climate. Mean annual air temperature increased between A and B from 2.7°C to 3.8°C . Related to this were significant

decreases in snow depth and duration and the number of freezing days, as well as in the number of frost cracking and freeze thaw days.

We demonstrate that changes in precipitation are unlikely to be responsible for the observed increase in hillslope erosion rate after period A. Seismic energy delivered to the slope is likely too small to be an obvious influence on hillslope erosion rate. Possible hypotheses for the increase in hillslope erosion rate in the 1980s are therefore related to the significant increase in air temperature: (1) longer exposure of the slope to weathering associated with the significant increase in air temperature and decrease in snow cover depth and duration, and (2) thermally induced degradation of permafrost still present at depth in the slope. These hypotheses are supported by the coincidence in time of the increase in hillslope erosion in the Illgraben with an increase in slope failure observed across the Alps by several other researchers and also associated with the accelerated increase in air temperature. While thermal processes appear able to have preconditioned the slope for failure, the actual triggering mechanisms remain unclear, as highlighted by the example of the 1961 rock avalanche.

On the other hand, the particularly high channel erosion rate in period B2 of 0.74 myr^{-1} coincided with an increase in the frequency and magnitude of extreme rainfall events, strongly suggesting their influence on channel sediment transfer by fluvial processes and debris flows.

Hillslope erosion exceeded channel erosion on average, indicative of a downslope-coupling relationship between hillslope and channel, and demonstrating the first order control of slope failure on catchment sediment yield. This study exemplifies the importance of understanding the factors that influence hillslope sediment supply in order to fully understand patterns of channel sediment transfer and catchment sediment yield.

Acknowledgements

This study was completed within the SedyMONT project, part of the ESF-funded TOPOEUROPE. Funding provided by the Swiss National Science Foundation Grant 20T021-120467 is acknowledged. Data for this research were provided by Swisstopo (2005 DEM and aerial photographs), MeteoSwiss (rainfall and temperature), the Institute of Snow and Avalanche Research (SLF) (snow depth), and The Swiss Seismological Service (SED). Ben Edwards (SED) provided the model for the calculation of seismic energy. Thanks to Bettina Schaeppi for her help throughout the analysis, Athanasios Paschalis for his help with handling the RhiresD dataset, Ben Edwards for his help with the seismic data and Peter Schürch for his comments on an earlier version of the manuscript. The comments of Professor Michael Church, Tim Davies and an anonymous reviewer also helped to improve the manuscript.

4. A probabilistic sediment cascade model of sediment transfer in the Illgraben

Abstract

*We present a probabilistic sediment cascade model to simulate sediment discharge in a mountain basin (Illgraben, Switzerland) where sediment is produced by hillslope landslides and exported out of the basin by debris flows and floods. The model conceptualizes the fluvial system as a spatially lumped cascade of connected reservoirs representing hillslope and channel storages where sediment goes through multiple cycles of storage and remobilization by surface runoff. The model includes all relevant hydrological processes that lead to runoff in an Alpine basin. Although the model describes the processes of sediment transfer and debris flow generation in a simplified manner it produces remarkably complex sediment discharge behaviour, which is driven by the availability of sediment and the triggering potential (system memory and climate). The model reproduces the observed statistical distribution, characteristics, and seasonal and daily timing of debris flows in the Illgraben as well as the measured residence time of sediment in the channel, suggesting that it captures the essential physics of the system at this scale. We show that it is the runoff regime that is the most important control on sediment transfer in the Illgraben, which includes in particular processes such as snow cover accumulation, snowmelt and soil water storage. Stochasticity of sediment input is important in reproducing sediment storage and discharge dynamics, but the triggering mechanism of landslides cannot be confidently detected in the sediment discharge output. We show the impact of sediment availability on simulated sediment discharge events in general, and quantify their division into transport and supply-limited debris flows, debris floods and debris flows. Finally we show an advantage of this modeling approach over rainfall intensity thresholds used commonly for debris flow initiation.

**Bennett, G.L., Molnar, P., McArdeell, B.W., Burlando, P. A probabilistic sediment cascade model of sediment transfer in the Illgraben. Submitted to Water Resources Research.*

4.1. Introduction

Mountain basin sediment discharge is inherently non-linear and stochastic in its relationship to climatic forcing and sediment production. This leads to difficulties in the prediction of sediment discharge and making inferences about environmental change from sediment yield data alone (e.g., Jerolmack and Paola, 2010; Van de Wiel and Coulthard, 2010). The non-linearity in sediment discharge may arise from several sources, of which storage effects and geomorphic thresholds are generally thought to be the most important (e.g., Phillips, 2003, 2006). Transient sediment storage in various landscape compartments determines the availability of sediment for transport and as a result sediment discharge may be transport or supply-limited (e.g., Bovis and Jakob, 1999; Lisle and Church, 2002). Geomorphic thresholds are tipping points in the system at which events take place or the system behavior changes (Schumm, 1979). Intrinsic thresholds are reached by gradual adjustment of internal system properties (e.g. sediment storage) to a point when even a small forcing triggers a significant event. External thresholds are reached when an external driving force (e.g. rainfall) exceeds a critical limit and often results in a large magnitude event.

This paper aims to implement geomorphic thresholds and storage effects in a model of sediment transfer with which to explain the non-linearity and stochasticity in sediment discharge in the case of a mountain basin, where sediment is produced by hillslope landslides and exported out of the basin by floods and debris flows. The model is based on the notion of a sediment cascade, which conceptualizes the fluvial system as a cascade of connected reservoirs representing different compartments (e.g. hillslopes and channels) where sediment goes through multiple cycles of storage and remobilization before being discharged from the basin (Burt and Allison, 2010 and references therein). A similar setup was used by Lu et al (2005, 2006) to explain the sediment delivery ratio in the Murray Darling River Basin looking at peak response only. In our study we apply the sediment cascade continuously in time to simulate daily water and sediment dynamics. The transfer of sediment in the cascade is driven by fluvial processes and sediment storage, while the triggering of events supplying sediment may be stochastic or related to climatic variables. This conceptualization is founded on observations which have shown debris flows to be triggered by rainfall and conditioned on basin wetness (e.g., Badoux et al., 2009) yet at the same time limited by the availability of sediment (e.g., Bovis and Jakob, 1999; Jakob et al., 2005).

Numerical modeling is a useful tool for understanding and developing hypotheses about mountain basin sediment transfer because it allows for full control over initial conditions and parameters, which is difficult to achieve in either field or laboratory studies (Van de Wiel et al., 2011). Further benefits of numerical modeling are the repeatability of experiments and the possibility of analyzing scenarios. Sediment transfer modeling approaches range from simple empirical models to complex physically-based models that attempt to represent the processes of sediment transfer in as much detail as possible. Landscape evolution (long-term) and soil erosion (short-term) models, based on the 1D or 2D application of equations of motion for water and sediment fall into this group. While they can be used for detailed simulations in

space and time of the transfer of sediment through the drainage basin (e.g. Coulthard et al., 2000; Tucker et al., 2001; Molnar et al., 2006; Coulthard and Van De Wiel, 2007; Van De Wiel and Coulthard, 2010), they assume sediment transport laws and are heavily data-dependent. As such they are subject to uncertainties that are difficult to evaluate, leading to an over-parameterized problem where observed data are sometimes not sufficient to justify the model complexity.

Conceptual models that attempt to identify a set of rules that captures the ‘essential physics’ behind a phenomenon (Brasington and Richards, 2007) may be more suitable alternatives for the study of sediment transfer. The sediment cascade model in this paper belongs to this group. The aim of our model is to incorporate the minimum process representation required to reproduce first-order properties of sediment transfer in our mountain basin, such as sediment storage residence time, sediment discharge volumes and seasonal timing, and the statistical properties of their dynamics, such as the frequency of supply-limiting conditions and the probability distribution of sediment discharge events. Furthermore, we use the model in a probabilistic framework, allowing for stochasticity in landslide triggering and studying the resulting probability distributions of sediment discharge by floods and debris flows. This allows us to include the inherent uncertainty in the timing and volume of sediment input and their effects on sediment discharge which would not be possible with deterministic models. Some other examples of this approach in geomorphology can be found in Benda and Dunne (1997b), Fuller et al. (2003), Tipper (2007), Van De Wiel et al. (2011), among others. We propose that the value of our modeling approach comes from it being used in conjunction with observations, both to explain these and to develop testable hypotheses.

In the development of the sediment cascade model in this paper we specifically have a landslide and debris flow catchment in mind, although the concepts are generally applicable to any basin that can be schematized into a cascade. We apply the model to the Illgraben in Switzerland, where a unique continuous 10-year record of debris flows (e.g. Badoux et al., 2009) provides the opportunity to calibrate it. In addition to the record of sediment discharge, the probability distribution of landslide volumes for the catchment has been estimated (Bennett et al., 2012), and there are measurements of erosion and storage of sediment on the hillslopes and in the channel (Bennett et al., 2013), as well as all necessary climate data. Importantly, previous studies in the catchment enable the independent estimation of the majority of model parameters such that calibration of the model does not involve extensive fine-tuning.

We have three main objectives in this paper: (1) We develop and apply the sediment cascade model to the Illgraben and investigate the conditions that lead to the transformation of the probability distribution of slope failures into that of debris flows in terms of the triggering and transport mechanisms in the basin. (2) We investigate the impact of sediment storage in the Illgraben cascade on simulated sediment discharge events in general, and their division into transport and supply limited, floods, debris floods and debris flows. (3) Our premise is that the availability of sediment and triggering potential (system memory and climate) drive sediment

discharge behaviour. On this basis we investigate the rainfall that leads to debris flows in the model in order to understand and quantify the limitations of rainfall intensity thresholds for debris flow initiation.

4.2. Slope failures and debris flows in the Illgraben

The Illgraben is a small (4.6 km²), NE facing catchment discharging into the Rhône Valley in southwest Switzerland (Figure 4.1), formed within highly fractured Triassic metasedimentary rocks, predominantly quartzites, limestones and dolomites (Schlunegger et al., 2009). It is of great research interest because of its large sediment output into the Rhône River of ~60,000–180,000 m³ yr⁻¹ mostly in the form of debris flows (McArdell et al., 2009; Berger et al., 2011b). As a result, the Rhône River downstream of the Illgraben has developed a braided morphology over a reach more than 6 km in length.

Large debris flows have been measured at the bottom of the fan since 2000 by the WSL. We utilize part of this record from 2000 through 2009, containing 36 debris flows of volumes between 2900 m³ and 107,000 m³ with a known bulk density, assumed to be constant for the entire flow (e.g. McArdell et al., 2007; Schlunegger et al., 2009), to calibrate parts of our model (Table B.2, Appendix B.1). Larger debris flows have occurred in the past according to observations (unpublished WSL reports, Table 1, Appendix B.1). The largest documented event with a total volume of several hundred thousand cubic meters occurred on 6 June 1961, causing considerable damage on the debris flow fan. The sediment discharge regime is also characterized by floods and smaller debris flows, but these are minor contributions to the sediment budget. In 2007 when more detailed measurements were made, 16 of 19 events were floods contributing ~1600 m³ of sediment, or 8% of the 20,000 m³ of sediment transported by the 3 large debris flow events. Instrumentation is removed from the channel at the end of October and reinstalled at the beginning of May. Therefore sediment discharge is only recorded from May through October.

Several studies have investigated the production and transfer of sediment through the Illgraben. In a previous study we used digital photogrammetry to produce a record of erosion and deposition in the upper catchment between 1963 and 2005 (Bennett et al., 2012; 2013). More than 2000 landslides occurred between 1986 and 2005 from the most active slope in the catchment, spanning 6 orders of magnitude in volume and producing a mean erosion rate of the slope of 0.39 ± 0.03 m yr⁻¹ (Bennett et al., 2012). Their probability distribution, with roll-over below 233 m³ and power-law tail above this volume, is attributed to two types of slope failure – shallow slumps and slides making up the roll-over and deep-seated bedrock failures making up the power law tail. The latter are the most significant for the sediment budget, accounting for more than 98% of the total sediment supply. Large slope failures are also documented earlier in the 20th century, in 1920, 1928, 1934 and 1961 (Gabus et al., 2008; Lichtenhahn, 1971). The largest rock avalanche was on 26 March 1961 with a volume in the

range of $3\text{--}5 \times 10^6 \text{ m}^3$. The sediment generated by this event presumably led to the largest recorded debris flow later in the year.

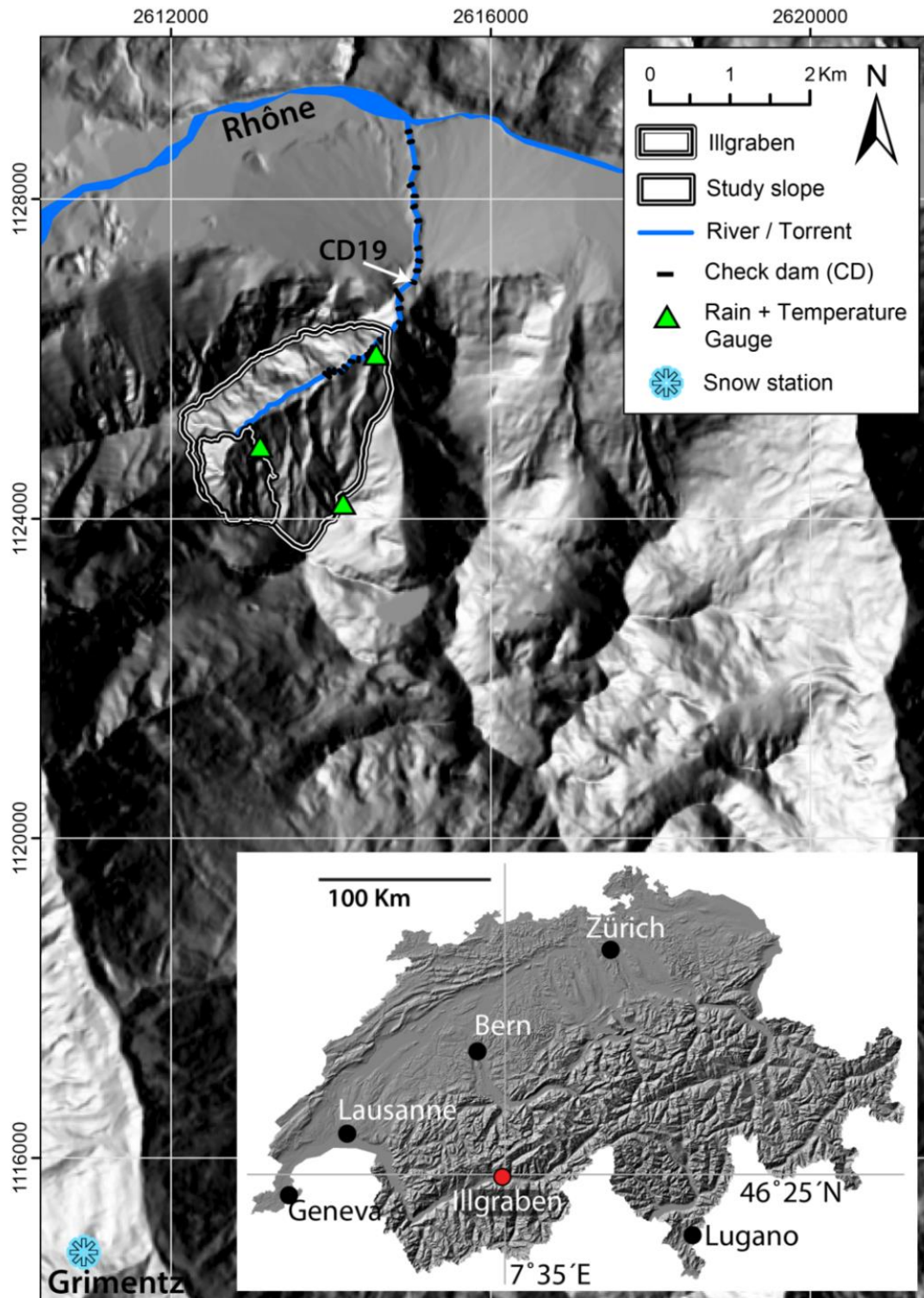


Figure 4.1 - Location of the Illgraben in the Rhone Valley and Switzerland.

The controls on the hillslope erosion rate are ambiguous but a thermal control seems present. Bennett et al. (2013) showed that an increase in the mean rate of hillslope erosion in the 1980s

in the Illgraben is most likely explained by the increased exposure of the hillslope to thermal weathering due to a significant reduction in snow cover induced by an increase in air temperature. Berger et al. (2011b) illustrated the occurrence of channel filling during the winter and spring seasons by slope failures between 2007 and 2009, supporting the hypothesis that thermal weathering is the most important control on slope failure. Another important finding is that hillslopes are eroding independently of channel incision (Bennett et al., 2013) meaning that feedback from channels to hillslopes need not be considered in the model at this timescale.

There are several possible triggering mechanisms of debris flows in the Illgraben (Badoux et al., 2009). The largest debris flows, such as the one documented in 1961, are probably associated with failures of landslide dams (Badoux et al., 2009). A recent study has shown the propagation of a landslide into a debris flow at the end of the summer (Burtin et al., 2012). However, the most frequent mechanism of debris flow generation is thought to be by entrainment of sediment stored in the channel during runoff events that are predominantly generated by summer rainstorms (Bennett et al., 2013). Snowmelt can play an important role in conditioning or even triggering debris flows in the late spring and early summer (Badoux et al., 2009). Therefore our sediment cascade should also contain a hydrological model, which on a continuous basis simulates precipitation, snow accumulation and melt, evapotranspiration and runoff generation, which together determine conditions for floods and debris flows.

4.3. Model structure and calibration

The sediment cascade model SedCas is a conceptual water and sediment transfer model which is spatially lumped at the basin scale. It consists of two parts: a hydrological and a sediment model. The hydrological model simulates the water balance for the basin including all relevant hydrological processes that lead to surface runoff generation. The sediment model simulates the cascade of sediment from landslides to hillslopes and into channels, and together with the runoff simulated by the hydrological model determines sediment discharge events in the form of sediment-poor floods, termed floods, sediment-laden floods, termed debris floods, and debris flows. The time step of both models is daily (Figure 4.2).

The hydrological model is a lumped model based on the linear reservoir concept (e.g., Eriksson, 1971; Kirchner, 2009). The water storage reservoir is fed by rainfall and snowmelt and depleted by evapotranspiration and runoff. Daily precipitation is derived from the MeteoSwiss RhiresD gridded product as detailed in Bennett et al. (2013). Daily air temperature is measured at Sion and interpolated to mean basin altitude with a constant lapse rate. Daily solar radiation and cloud cover data are also measured at Sion. Precipitation is separated into solid and liquid phase by a temperature threshold and a degree-day model is used to estimate snowmelt. Details of the hydrological model and its calibration are in Section 3.1.

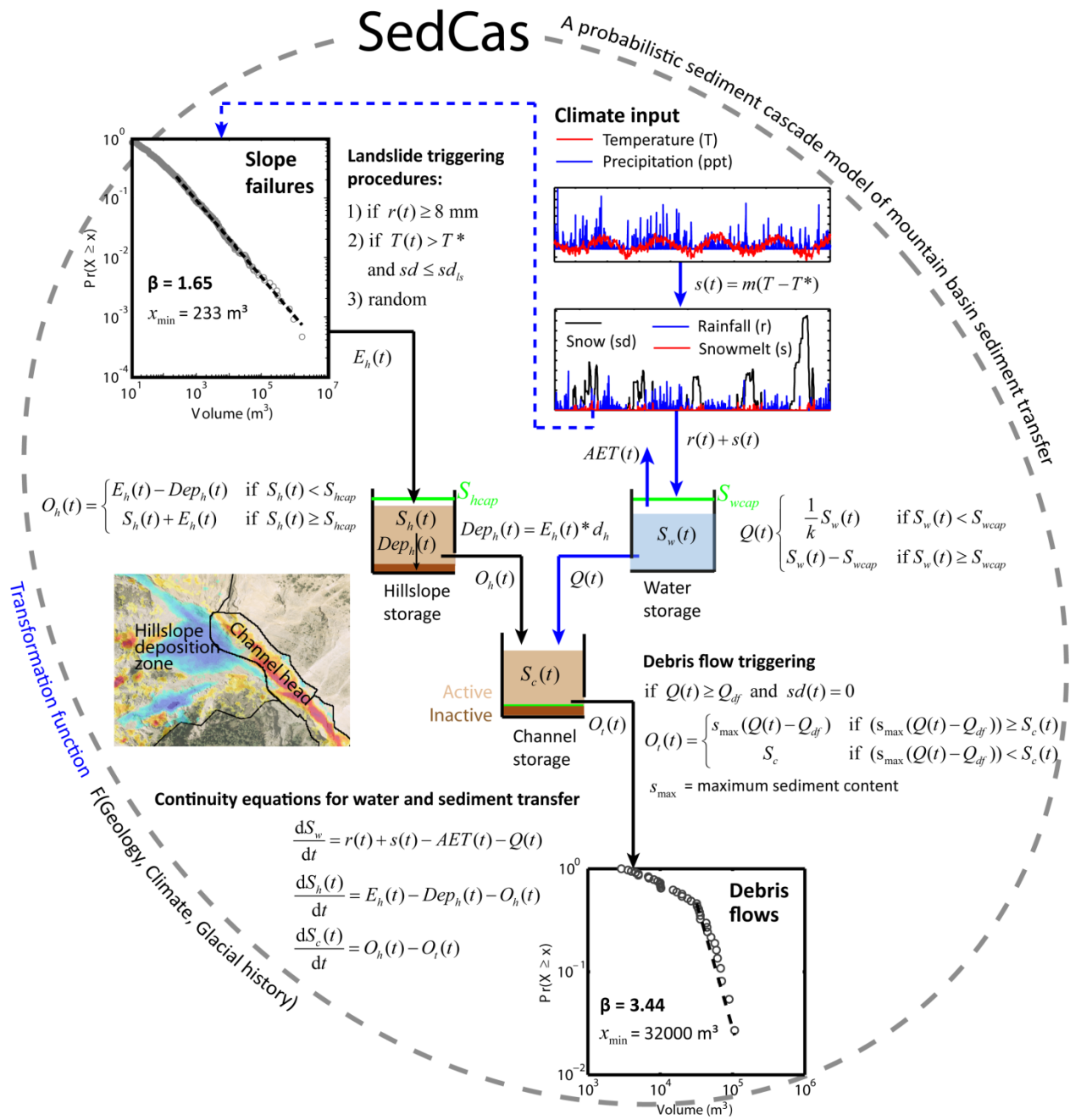


Figure 4.2 - SedCas model structure. The probability distribution of slope failures is from Bennett et al. (2012a). The distribution of sediment discharge events (debris flows) are those measured at the catchment outlet from 2000 through 2009.

The sediment model is a lumped model of the sediment cascade and consists of two sediment storage reservoirs, one for the hillslope and the other for the channel components. The hillslope reservoir represents the storage of sediment on hillslopes ready for transport into the channel system. Physically it represents the areas of deposition at the base of the hillslopes studied by Bennett et al. (2012; 2013) (Figure 4.2), and shown to be the most active in the basin (Schlunegger et al., 2009; Berger et al., 2011b). The channel reservoir represents the channel between the base of the hillslope area and the fan apex (near to CD19 in Figure 4.1) studied by Bennett et al. (2013). Sediment is supplied stochastically into the hillslope reservoir by slope

failures derived from the probability distribution of landslides established by Bennett et al. (2013). Details of the sediment model and its calibration are in Section 4.3.2.

Table 4.1 - Model parameters. Parameters estimated independently are indicated with *x*.

Parameter	Description	Value	
T^*	Threshold temperature for snow accumulation, melt, and melt of water frozen in the ground	0°C	
m	Snowpack melt rate factor	2.2 mm day ⁻¹	
δ_{sum}	Albedo (summer)	0.3	x
δ_{win}	Albedo (winter)	0.8	x
α	Parameter in the calculation of evaporation efficiency γ	0.2 mm ⁻¹	
S_{wcap}	Basin-wide water storage capacity	21 mm	x
k	Residence time of water in the storage reservoir	2 days	
x_{min}	Minimum landslide volume from the power law tail	233 m ³	x
β	Power law scaling exponent in landslide distribution	1.65	x
μ	Mean of the log-normal distribution of landslides $< x_{\text{min}}$	3.36 m ³	x
σ	Standard deviation of log-normal distribution of landslides $< x_{\text{min}}$	1.18 m ³	x
d_h	Hillslope redeposition rate	0.012	x
S_{hcap}	Hillslope storage volume threshold	7.5 10 ⁴ m ³	
sd_{ls}	Threshold snow depth for landslides triggered by thermal weathering (procedure 1) (in SWE)	12 mm	x
r_{ls}	Threshold rainfall for landslides triggered by rainfall (procedure 2)	8 mm day ⁻¹	x
Q_{df}	Critical discharge to generate a sediment discharge event	0.4 m ³ s ⁻¹	x
ρ_{df}	Mean wet bulk density of debris flows	1800 kg m ⁻³	x
ρ_h	Dry bulk density of hillslope sediment in the model	1400 kg m ⁻³	x
S_{max}	Maximum potential ratio of sediment to water in the flow, which equates to a maximum sediment concentration of 0.48.	0.92	x

4.3.1. Hydrological model

4.3.1.1. Snow

The hydrological model uses a simple description of the snow accumulation and melting to predict snow depth as a function of elevation, temperature, precipitation and a constant melt factor (e.g., Perona et al., 2007; Molini et al., 2011). Accumulation of the snow pack occurs through cumulated precipitation events when temperature is below a threshold T^* . When temperature exceeds T^* the snowpack melts at a rate proportional to temperature, $s(t) = m(T - T^*)$ where s is snowmelt and m is the melt-rate factor. Snowmelt feeds the water reservoir together with rainfall. The model may be driven by observations of daily precipitation and temperature or stochastic simulations thereof.

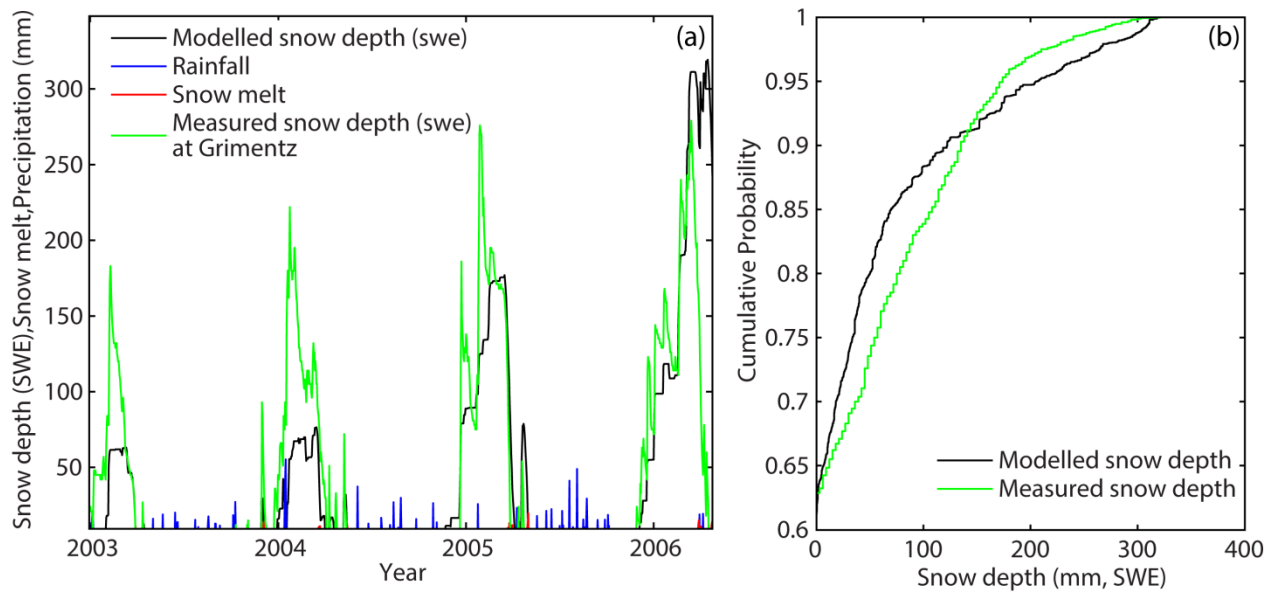


Figure 4.3 - (a) Example of time series of modeled daily snow depth, rainfall, snowmelt and measured snow depth (in SWE) at Grimentz. (b) Cumulative distribution of modeled and measured daily snow depth for the period 2000-2009.

For the calibration of the snow module we used snow depth data from the Grimentz station 6 km to the southwest of the Illgraben (Figure 4.1), chosen from several surrounding stations due to its similar elevation to the study area. We converted snow depth into snow water equivalent (SWE) using a density of 0.3 g cm^{-3} , which was an average of fresh and old snow measurements taken at the nearby Arolla glacier (Carenzo et al., 2009) assuming an equal contribution of old and new snow to the snow pack. We calibrated T^* and m based on the duration of snow cover and snow depth for the period 2000 through 2009. We found that having the same threshold temperature $T^* = 0^\circ\text{C}$ for accumulation and ablation and $m = 2.2 \text{ mm } ^\circ\text{C}^{-1} \text{ day}^{-1}$ produced the best results ($\text{RMSE} = 1.5 \text{ mm day}^{-1}$). Figure 4.3a shows an example of the time series of modeled snow depth (SWE) compared to the observed snow depth at Grimentz, along with modeled snowmelt and rainfall. It is important in our model to capture snow cover duration well since snow insulates the ground from freeze-thaw processes. The model simulates snow cover 37% of the time compared to 40% for measured snow cover, which together with a good representation of the probability distribution of snow depth is considered satisfactory (Figure 4.3b).

4.3.1.2. Water balance

The water balance in the hydrological model is solved with a linear reservoir model at the daily time scale. The water storage reservoir represents the capacity of the soil (weathered bedrock) in the basin to store and discharge water. It is fed by snowmelt and rainfall and depleted by evapotranspiration and runoff:

$$\frac{dS_w}{dt} = r(t) + s(t) - AET(t) - Q(t) \quad (7)$$

where S_w is water storage in the reservoir, r is rainfall, s is snowmelt, AET is evapotranspiration and Q is runoff. All of these are basin-averaged values.

Actual evapotranspiration is modeled as a fraction of daily potential evapotranspiration (PET) which is computed with the Priestley-Taylor method (Priestley and Taylor, 1972). This requires time series of mean daily temperature, solar radiation, cloud cover and values for albedo and elevation. We obtained the time series from the MeteoSwiss weather station in Sion and took the mean elevation of the study site. Albedo was $\delta_{sum} = 0.3$ for the summer and $\delta_{win} = 0.8$ for the winter, which are average values for bare ground and snow respectively. AET is computed as a fraction of PET ,

$$AET = \gamma PET \quad (8)$$

where γ is an efficiency parameter which is determined as a function of catchment water storage following Tuttle and Salvucci (2012),

$$\gamma = \left[1 - e^{(-\alpha S_w)} \right] \quad (9)$$

where α is a parameter which determines how water availability in the subsurface limits evapotranspiration at the potential rate. The parameter $\alpha = 0.2 \text{ mm}^{-1}$ was calibrated to reproduce the mean annual AET for the study region (Hydrological Atlas of Switzerland).

Runoff from the water storage reservoir takes place under two conditions. When the water storage capacity S_{wcap} is not reached, outflow is computed as a function of the stored amount assuming a linear reservoir relation. When the capacity is exceeded, then all excess water generated by rain and/or snowmelt is discharged into the channel system and out of the basin:

$$Q(t) = \begin{cases} \frac{1}{k} S_w(t) & \text{if } S_w(t) < S_{wcap} \\ S_w(t) - S_{wcap} & \text{if } S_w(t) \geq S_{wcap} \end{cases} \quad (10)$$

The residence time k represents the attenuation of runoff through subsurface flow paths. Based on our observations in the Illgraben we allow the discharge in the first case from the subsurface reservoir only when $T > T^*$. During the winter months, water in the subsurface reservoir is assumed to be frozen. Only when the temperature rises above T^* draining of water from the frozen soil is initiated. We do not have independent observations of runoff to calibrate the model, but because runoff is responsible for triggering debris flows and the rate of draining of storage influences runoff events, we calibrated k to get the best possible timing of debris flows.

The water storage capacity S_{wcap} was independently estimated from the difference in observed runoff and basin-integrated rainfall for several flood and debris flow events in the catchment in 2005 and 2006 (Nydegger, 2008). For rainfall events without snowmelt we argue that the maximum observed difference represents the catchment storage capacity in this period. Averaged over the catchment this results in $S_{wcap} = 21 \text{ mm}$ (Table C.1, Appendix C.1). This is a

lower estimate because it is based on only two years of data and assumes that the soil was completely dry at the beginning of the events.

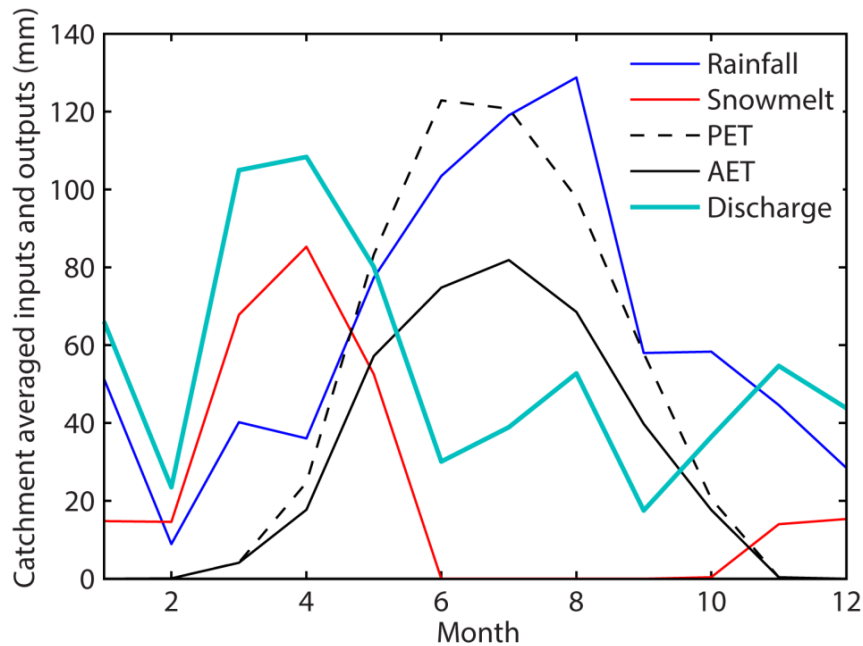


Figure 4.4 - Seasonal distribution of modeled hydrological variables. Plotted are the monthly means over the simulation period 2000-2009.

Figure 4.4 shows the seasonal distributions of modeled hydrological variables for the period 2000-2009. Rainfall peaks during the summer months, but *AET* removes a large fraction of the water during this time, reducing discharge. Discharge is highest in the spring as a result of large inputs of snowmelt and low values of *AET*. Mean annual values of rainfall, *AET* and discharge after calibration are 1018 mm, 362 mm and 657 mm, respectively. These agree with values reported for the region in the Hydrological Atlas of Switzerland. We have no other means of calibrating the hydrological outputs in more detail without continuous discharge measurements at the catchment outlet.

4.3.2. Sediment model

4.3.2.1. Sediment supply by slope failure

The SedCas model schematic in Figure 4.2 shows that sediment is delivered into the hillslope storage reservoir by slope failures at an average annual hillslope erosion rate $E_h(t)$. Bennett et al. (2012) presented the probability distribution of more than 2000 slope failures from the study slope in the period 1986–2005, ranging over 6 orders of magnitude in volume. The tail of the distribution followed a power law above a minimum landslide volume ($x_{min} = 233 \text{ m}^3$) with an exponent $\beta = 1.65$ (Bennett et al., 2012). We used this distribution along with the observed average annual number of slope failures (25 per year) to randomly draw slope failure volumes in the model. Additionally, we imposed an upper slope failure volume of $3 \times 10^6 \text{ m}^3$, which is the volume of the largest known slope failure in the catchment in 1961 (Bennett et al., 2013) because we know that a larger event did not occur in the study period.

To study the significance of different possible triggering mechanisms and thus timing of slope failures on sediment discharge, we experimented with 5 different sediment input procedures. Each procedure is calibrated to reproduce the observed mean annual number of failures and mean annual erosion rate. Because of the random selection of slope failure volumes, the annual erosion rate of each simulation run is variable. However, the average annual erosion rate of 1000 runs used in the simulation is equal to the observed mean $E_h(t) = 0.39 \text{ m yr}^{-1}$ (Bennett et al., 2012) in all sediment input procedures.

The first 3 sediment input procedures differ in the conditions for the triggering of large slope failures ($x > x_{min}$) from the inverse power law distribution. In procedure (1) large failures are triggered on days with air temperature $T \leq 0^\circ\text{C}$ and snow depth $sd < 12 \text{ mm}$ (SWE). This procedure is based on the argument that freezing conditions without an insulating layer of snow on the ground are conducive to thermal weathering and slope failure (Bennett et al., 2013). The calibrated snow depth corresponds to about 40-80 mm of snow on the ground which is much less than what is required to insulate the ground from air temperature variations (e.g., Keller and Gubler, 1993; Rödder and Kneisel, 2012). Procedure (2) is a test of rainfall as a trigger of slope failure. Large failures are triggered by daily rainfall $r_{ls} > 8 \text{ mm day}^{-1}$, which is calibrated to reproduce the observed average annual number of failures. Finally in procedure (3) large failures have no relation to climatic forcing and are generated randomly in time from the power law distribution. In all of the first 3 procedures we also generate small failures from a log-normal probability distribution which we fit to the observed small failures ($x < x_{min}$) with a mean $\mu = 3.36 \text{ m}^3$ and standard deviation $\sigma = 1.18 \text{ m}^3$.

The last 2 procedures do not directly utilize the observed probability distribution of slope failures. Procedure (4) mimics the case of a large slope avalanche filling the hillslope and channel storages at the beginning of the period, the storages are then gradually emptied by debris flows during the following years. The volume of sediment entered into the channel reservoir corresponds to about 10 years' worth of sediment ($\sim 3 \times 10^6 \text{ m}^3$) in a single failure. In procedure (5) there is a constant daily sediment supply of $800 \text{ m}^3 \text{ day}^{-1}$ by slope failures into the channel system. These two procedures also preserve the mean annual hillslope erosion rates. They are used as a reference against which the first three realistic sediment delivery procedures are compared.

4.3.2.2. Sediment storage accounting

The sediment cascade model consists of two sediment reservoirs: hillslopes and channels. Volume and mass continuity is ensured in each of the reservoirs:

$$\begin{aligned} \frac{dS_h(t)}{dt} &= E_h(t) - O_h(t) \\ \frac{dS_c(t)}{dt} &= O_h(t) - O_t(t) \end{aligned} \tag{11}$$

where $S_h(t)$ is hillslope storage, $E_h(t)$ is hillslope erosion by slope failure, $Dep_h(t)$ is redeposition of sediment in the hillslope storage reservoir, $O_h(t)$ is hillslope sediment output, $S_c(t)$ is channel storage and $O_c(t)$ is catchment output.

We allow for the possibility of longer term storage in the hillslope reservoir, accounting for the fact that not all sediment generated by landslides passes directly into the channel system. The deposition rate is a constant fraction of eroded sediment on a given date $Dep_h(t) = d_h E_h(t)$. The hillslope redeposition parameter $d_h = 0.12$ was estimated from the observed storage on hillslopes and hillslope erosion estimated by DEM differencing (Bennett et al., 2012; 2013). We impose a critical storage S_{hcap} above which the hillslope reservoir cannot store sediment anymore and releases it into the channel in a single landslide. This threshold represents the condition when the hillslope debris fans have reached a critical angle of repose at which they fail. S_{hcap} was estimated as the maximum observed hillslope deposition in the analysis period of Bennett et al. (2012; 2013) and verified with independent hillslope residence time estimates. The hillslope sediment output into the channel reservoir is the remainder of the landslide sediment after redeposition:

$$O_h(t) = \begin{cases} E_h(t) - Dep_h(t) & \text{if } S_h(t) < S_{hcap} \\ S_h(t) + E_h(t) & \text{if } S_h(t) \geq S_{hcap} \end{cases} \quad (12)$$

The initial condition for the hillslope storage reservoir $S_h(0) = 2.5 \times 10^4 \text{ m}^3$ was estimated from the time series of DEMs described in Bennett et al. (2013).

The channel reservoir receives sediment from the hillslopes and releases it periodically in the form of debris flows and floods. It is conceptualized to consist of two components: active and inactive storage (Figure 4.2). This conceptualization reflects different residence times and an inaccessibility of sediment for mobilization, e.g. in floodplains (Nakamura and Kikuchi, 1996) or base of debris flow deposits (Lancaster and Casebeer, 2007). In the case of the Illgraben however, this stratification of storage in the channel is induced by human intervention. Inactive storage represents the sediment stored behind a series of 19 check dams along the channel in the upper catchment (Figure 4.1). Inactive storage is treated as inaccessible to debris flows. It was estimated to be $3 \times 10^6 \text{ m}^3$ from the 1963 DEM and an earlier topographic map. The active channel storage $S_c(t)$ is any sediment stored above this amount. It is a key component of the SedCas model because the actual sediment discharge concentration and volume is dependent on the availability of sediment in active storage at the time of the event.

The initial condition for the active channel storage for each model run $S_c(0)$ is set to close to empty based on our data which show that the channel was eroded to almost base level only two years earlier in 1998. We also observed that there were only relatively few and small debris flows in 2000 and 2001, which we interpret as further evidence of a lack of sediment in the channel at this time.

4.3.2.3. Debris flow generation

Sediment discharge events are generated in the model by hydrological forcing, i.e. by runoff in the channel system (Figure 4.2). When the water storage capacity S_{wcap} is reached, any excess snowmelt or rainfall generates surface runoff $Q(t)$ according to Equation (4). For triggering large sediment discharge events we introduce the critical discharge Q_{df} . Physically speaking, Q_{df} is a discharge that corresponds to a critical bed shear stress needed to entrain sufficient sediment along the channel system in order to generate an event, shear stress being a function of discharge for a given channel geometry. We call these “events” debris flows for now, but we will show later that they are in fact a spectrum of sediment discharge events ranging from floods to debris flows limited and unlimited by sediment supply. The sediment discharge volume $O(t)$ is computed as:

$$O(t) = \begin{cases} \frac{\rho_h}{\rho_{df}} s_{\max} [Q(t) - Q_{df}] & \text{if } \frac{\rho_h}{\rho_{df}} s_{\max} [Q(t) - Q_{df}] < S_c(t) \\ S_c(t) & \text{if } \frac{\rho_h}{\rho_{df}} s_{\max} [Q(t) - Q_{df}] \geq S_c(t) \end{cases} \quad (13)$$

where ρ_{df} is the mean wet bulk density observed in debris flows, ρ_h is the dry bulk density of hillslope sediment stored in the channel, and s_{\max} is a maximum ratio of sediment to water in the flow for an event unlimited by sediment supply. In our model we hypothesize that flows below Q_{df} do transport fine sediment in suspension, however they do not qualify as large sediment discharge events, and contribute insignificantly to the total sediment budget.

We make an independent estimate of Q_{df} from the rainfall intensity-duration curve developed for the Illgraben from observed debris flows and floods in 2007 (Badoux et al., 2009; Figure C.1, Appendix C.1). The daily rainfall depth needed to trigger an event, converted into discharge assuming uniform rainfall and a fully saturated basin, is $Q_{df} = 0.4 \text{ m}^3 \text{ s}^{-1}$. When Q_{df} is exceeded, the excess discharge is able to entrain sediment at a rate specified by s_{\max} and sediment availability. We use the mean observed debris flow wet bulk density $\rho_{df} = 1800 \text{ kg m}^{-3}$ to estimate the largest sediment concentration that we can get on a mean daily basis. Assuming that the porosity of hillslope and debris flow material are equal, we estimate it from ρ_{df} as $p = 0.52$, and get a dry bulk density of hillslope sediment $\rho_h = 1400 \text{ kg m}^{-3}$ and $s_{\max} = 0.92$, which equates to a volumetric sediment concentration $c_{\max} = 0.48$ of the average observed debris flow event. This is a maximum possible concentration in the model, because the actual sediment concentration of a discharge event c is dependent on sediment availability in channel storage and may be much less than c_{\max} (Equation 7).

Similarly to the treatment of the water reservoir, we assume that the channel reservoir output is reduced in the winter because of snow accumulation in the channel system and frozen sediment in storage. Although the debris flow monitoring system is turned off in the winter,

from occasional on-site observations we know that runoff and sediment discharging events, including debris flows, are rare. We therefore include an additional condition for debris flow generation in the model that is the absence of snow cover. This is based on the hypothesis that snow accumulations in the channel block debris flows as has been suggested for example for the Ritigraben by Stoffel et al. (2008).

The calibration of the SedCas model components was performed as much as possible by independent estimation of individual model parameters and without fine-tuning of the model output (examples are the estimation of c_{\max} and Q_{df} ; see Table 4.1). Other parameters were calibrated on the 36 observed debris flows over the calibration period and on an independent estimate of sediment residence time in the channel, based on data from DEM analyses (Bennett et al., 2012; 2013). Residence time was estimated as the volume of the channel reservoir (i.e. sediment storage) divided by the flux through it (Eriksson, 1971), assuming that all sediment in the reservoir has an equal probability of evacuation (e.g., Benda and Dunne, 1997a; Lisle and Church, 2002; Malmon et al., 2003). We calculated sediment storage for each period (1986-1992; 1992-1998; 1998-2005) above the 1998 channel surface, the lowest of the DEMs, and calculated the flux through the channel as the sum of the input from the hillslopes and channel storage change for that period. We obtained an average sediment residence time of 450 days (Table C.2, Appendix C.2), which is in general agreement with a residence time of 1 year estimated by Berger et al. (2011b).

4.4. Results

4.4.1. Probability distribution of debris flows

The observed and simulated probability distributions of debris flows for the 10-year period 2000-2009 are shown in Figure 4.5. The simulated distribution gives the mean and 5% and 95% percentiles from 1000 realizations simulated with the landslide triggering procedure (1) after Bennett et al. (2013). Since the Illgraben monitoring station only records events which exceed 2900 m³, only these large events are shown in the figure. The hypothetical potential distribution of debris flows with maximum sediment concentration c_{\max} is also shown. These are debris flows that would have occurred if sediment supply in Equation (7) was not limiting. The result shows a remarkable fit to the observed probability distribution of debris flows, even though the model was not explicitly fine-tuned to achieve this. Our first objective in the paper was to investigate the conditions that lead to the transformation of the probability distribution of slope failures into that of debris flows and our results show the following.

First, the general shape of the distribution of debris flow volumes with a sharp drop-off and steep tail is very different from the distribution of the input landslide volumes which has a less steep and much more consistent power law behavior over a much greater range (see also schematic in Figure 4.2 or data in Bennett et al. (2012)). We see in Figure 4.5 that the simulated potential distribution of debris flows not limited by sediment supply also has this sharp drop-off, so we conclude that it is the hydrology, i.e. the runoff regime in our model that generates this feature and not sediment supply.

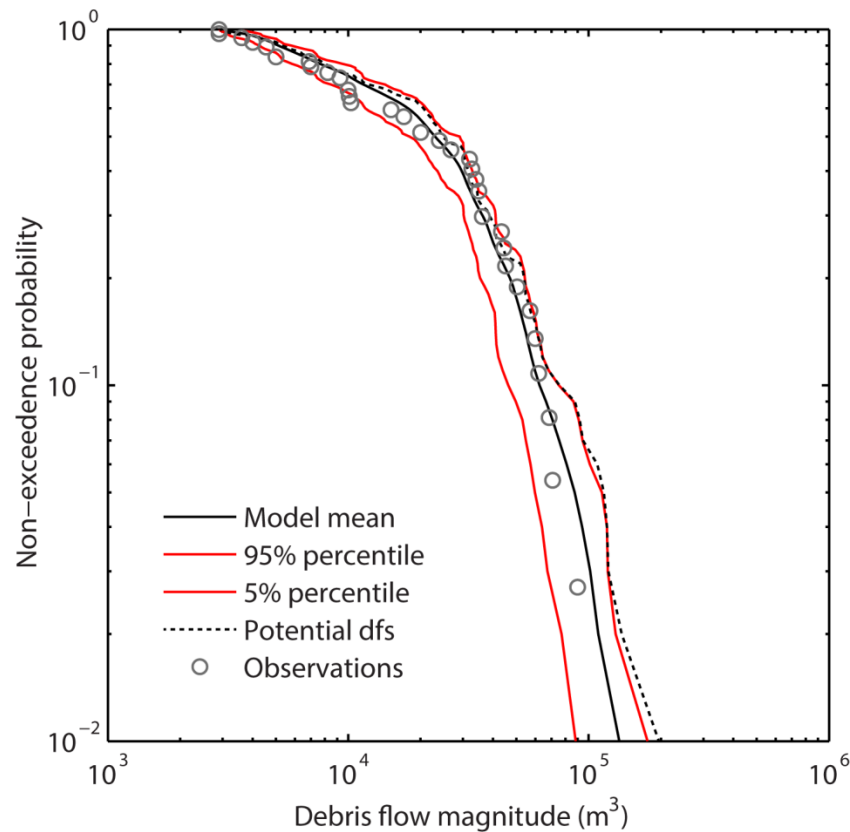


Figure 4.5 - Non-exceedence probability distribution of modeled debris flows, potential debris flows and observed debris flows, based on model runs with sediment input procedure (1). The black line is the mean of 1000 runs of the model and the red lines are the 5% and 95% percentiles. Potential debris flows are events with the maximum potential sediment concentration c_{max} in the hypothetical case of an abundant sediment supply.

Second, we found that the first three landslide input procedures all fit the observed debris flow data reasonably well. The drop-off point x_{min} , the slope of the power law tail β , and mean number and volume of debris flows for all procedures are listed in Table 4.2. In terms of debris flow characteristics, the first 3 procedures which utilized the distribution of slope failures produced the best results. The last two procedures are physically unrealistic and do in fact depart most from the observed debris flow statistics. For example the constant supply of sediment (procedure 5) leads to an over-estimation of the number of debris flows, an underestimation of their average volume, and as a result a mean residence time that is half that observed. The opposite is true for procedure 4. However, the first three realistic sediment input procedures gave very similar and good results and it is difficult to objectively judge which one is better (Table 4.2). This means that the sediment cascade, the runoff regime and debris flow generation, filter out many of the differences in the sediment input procedures to the point that they are not evident anymore in the sediment discharge.

Table 4.2 - Results of 1000 model runs for different sediment input procedures compared to observations (df = debris flow; * indicates the procedures that were closest to the observation for each measure). The percentage of supply-limited events is calculated as the % of potential events with lower than maximum sediment concentration. The percentage of supply-prohibited events is calculated as the % of potential events that did not occur due to the absence of any stored sediment along the channel. The same statistics are given for all events ($>0 \text{ m}^3$).

Measure	Sediment input scenario (1000 runs)				
	Observations	Drawn from the probability distribution			Reference procedures
		(1)	(2)	(3)	(4) (5)
Mean # dfs ($>2900 \text{ m}^3$)	36	73*	79	72*	74 99
Mean df vol (10^3 m^3)	30.4	30.5*	25.2	26.9	36.3 24.6
Mean β of df	3.44	3.6	3.18	3.5*	3.6 3.02
Mean x_{\min} of df (10^3 m^3)	3.2	3.6	2.9	3.3*	5.1 2.7
Mean residence time (days)	450	718	472*	568	1102 197
Mean % supply limited events		7	18	12	1 21
Mean % supply prohibited events		34	31	37	36 14
Mean % supply limited events (all)		22	41	35	1 24
Mean % supply prohibited events (all)		20	9	22	36 11
(1) Large landslides triggered by freezing events when snow height < 12 mm					
(2) Landslides triggered by rainfall events >8 mm rainfall/day					
(3) Large landslides drawn randomly from power law					
(4) Single $3 \times 10^6 \text{ m}^3$ rock avalanche at the beginning of the time series					
(5) Constant daily sediment supply (800 m^3 per day)					

4.4.2. Transport and sediment supply limitations

To investigate the impact of sediment storage on simulated sediment discharge events and their division into transport and supply limited we first looked at the reduction of the actual debris flow volumes from their potential size in the model. This is shown in Figure 4.6 where the mean actual debris flow volumes are plotted against their potential volumes for the sediment input procedure (1).

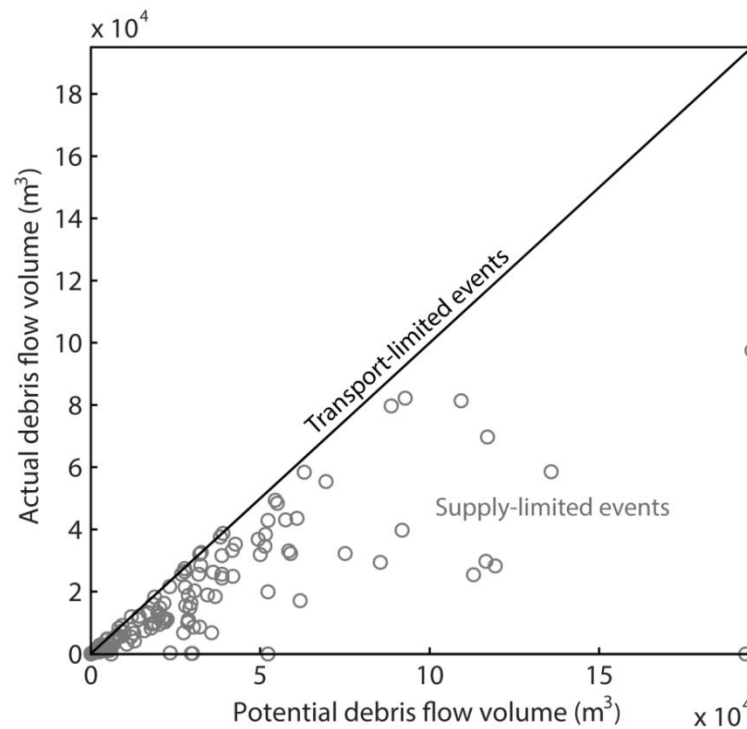


Figure 4.6 - Mean actual debris flow volumes of 1000 runs versus potential debris flow. The black line is the one-to-one line in the case of an abundant sediment supply, i.e. represents transport limited events. The model was run with sediment input procedure (1) and the event data are binned to compute the mean.

There is clearly a large variability in simulated debris flow volumes as a function of the availability of sediment. While small debris flows tend not to be limited by sediment availability, the large ones definitely are. Overall, sediment supply limited 22-41% of the debris flows in the first three sediment input procedures, and in fact in 9-22% cases the lack of sediment completely prohibited a debris flow from occurring in our model (Table 4.2). Of course we cannot verify these results with data, but they do indicate that sediment supply is likely to be a key ingredient in debris flow formation even in this erosive catchment.

To explore the connection between runoff and sediment supply limitations in more detail it is helpful to look at the results on a daily event basis. The runoff regime in our model determines the timing and magnitude of sediment discharge. Figure 4.7 shows the relationship between simulated water and sediment discharge in the model according to Equation (7). We arbitrarily

chose a sediment concentration $c = 0.05$ to distinguish between floods and debris flows as this is the lowest sediment concentration that was observed in our debris flow dataset. The monitoring system captures large events greater than 2900 m^3 which in our model consist mostly of simulated debris flows and some debris floods. However it is also evident that the model generates many low sediment concentration floods which is what we would expect in reality as well.

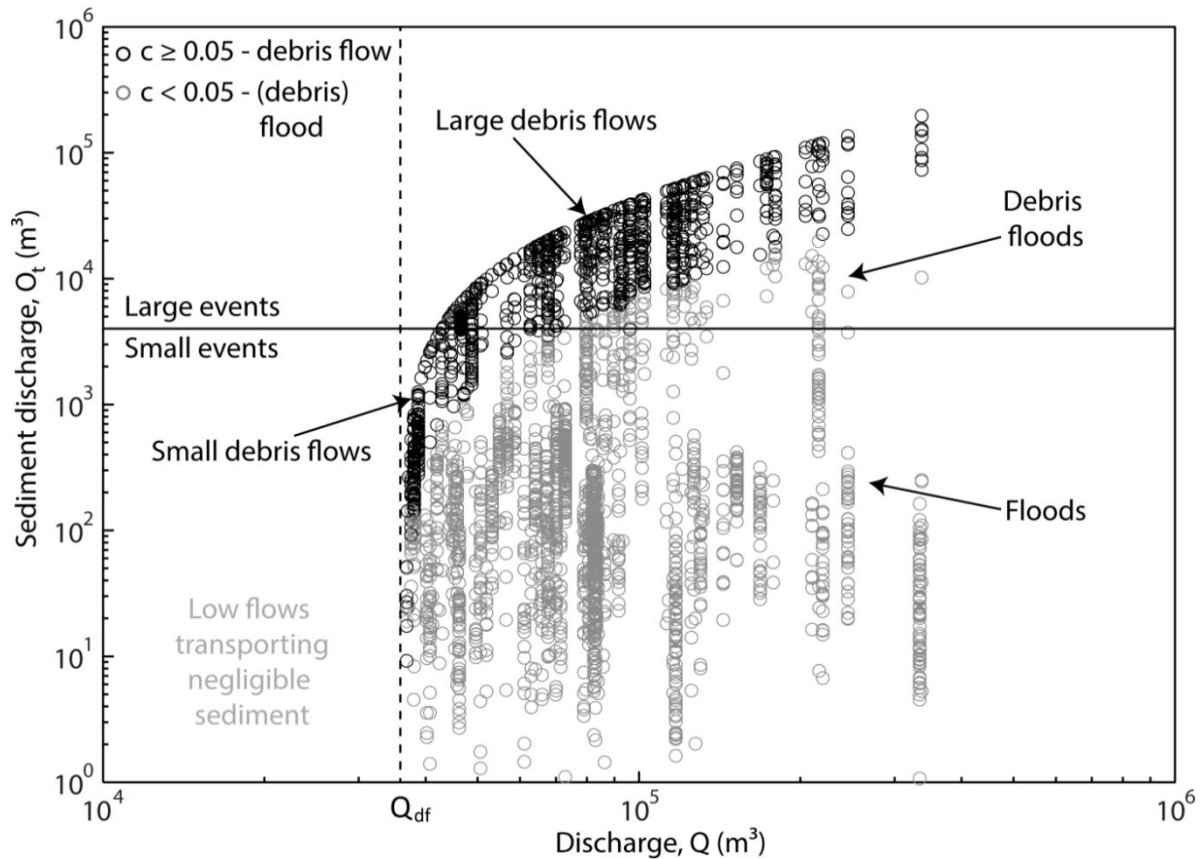


Figure 4.7 - Relationship between sediment discharge and water discharge according to Equation (7). Sediment concentration c is calculated as the volume of sediment in the total volume of water and sediment in an event, assuming a material porosity $p = 0.52$, and where water is the excess discharge $Q - Q_{df}$. The Illgraben monitoring system only records “large events” (horizontal line in figure) which exceed a sediment discharge of 2900 m^3 .

A consequence of sediment supply limitations is that the actual sediment concentration of individual events varies. We plot the simulated probability distribution of event sediment concentrations in Figure 4.8, where it varies between 0.1 and $c_{\max} = 0.48$. The simulated median sediment concentration of over 1000 runs for sediment input procedure (1) was about $c = 0.3$.

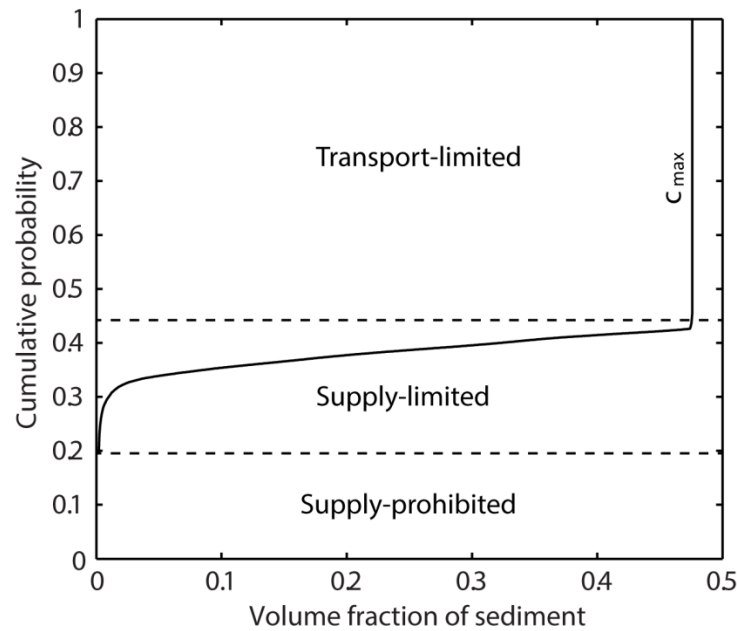


Figure 4.8 – Cumulative distribution of the actual volumetric sediment concentration c of modeled debris flows, shown for procedure (1).

4.4.3. Timing of debris flows

In addition to the sediment supply limitations explored above it is also necessary to investigate the actual triggering of debris flows, i.e. the rainfall and runoff conditions that generate debris flows in the model and their timing with regard to observations. Figure 4.9a shows an example of a time series of modeled sediment discharge events, split into supply unlimited ($c = c_{\max}$) and limited ($c < c_{\max}$), superimposed on observed debris flows, along with modeled discharge events and debris-flow-limiting snow cover. Figure 4.9b shows the concordant channel sediment storage for this model run.

A first aspect of event timing is to capture general seasonality. The main debris flow season between May and October is captured very well in terms of magnitude and timing of debris flow occurrence by SedCas (Figure 4.10). The model also predicts some sediment discharge in other months of the year, apart from February when a permanent snow cover inhibits debris flows, which we cannot verify because data are not collected in these months. Although the monthly mean discharge is highest between March and May, most of this discharge occurs gradually through the process of snowmelt and therefore there are relatively few runoff events that exceed Q_{df} . Additionally, snow cover during the spring inhibits many potential debris flows. Figure 4.10b shows the accumulation of sediment during the winter and spring and evacuation during the summer and autumn, in agreement with the observations of Berger et al. (2011b).

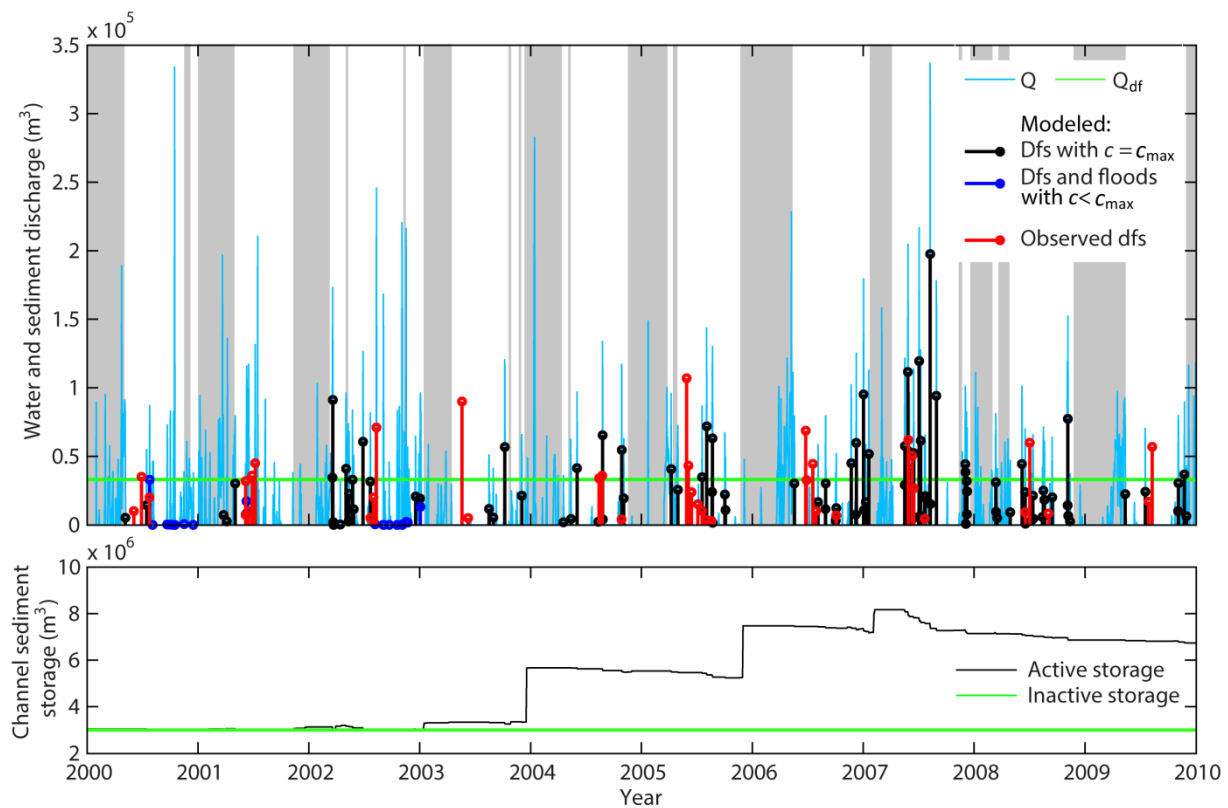


Figure 4.9 - (a) Time series of water discharge Q , modeled debris flows and supply limited debris flows and floods, and observed debris flows. Grey bars denote snow cover. (b) Evolution of channel sediment storage during one example model run, shown for procedure (1).

A second aspect is the timing of actual debris flows, which was investigated by computing the sensitivity and specificity of the model predictions. Sensitivity is the fraction of all observed debris flows correctly predicted, specificity is the fraction of all non-debris flow days correctly predicted. These skills are also combined into an overall likelihood ratio (e.g., Begueria, 2006) and reported in Table 4.3. Almost a third of the debris flows are modeled on the correct day and this increases to almost half if we consider a window of 3 days around the observed debris flow. Equally as important as the prediction of events is the prediction of non-events. The likelihood ratio captures both skills and allows us to show the accuracy of the different sediment input procedures. Table 4.3 shows that in terms of the timing of debris flows events, procedure (2) in which failures are triggered by rainfall events outperforms procedures (1) and (3) especially because it has a high sensitivity. Procedures (4) and (5) underperform because they lead to fewer supply-limited sediment discharge events. It has to be stressed that perfect event timing cannot be expected, because although the timing of simulated debris flows is driven by climate (runoff) and so should be close to observations; it is also determined by sediment availability which in the simulations is stochastic.

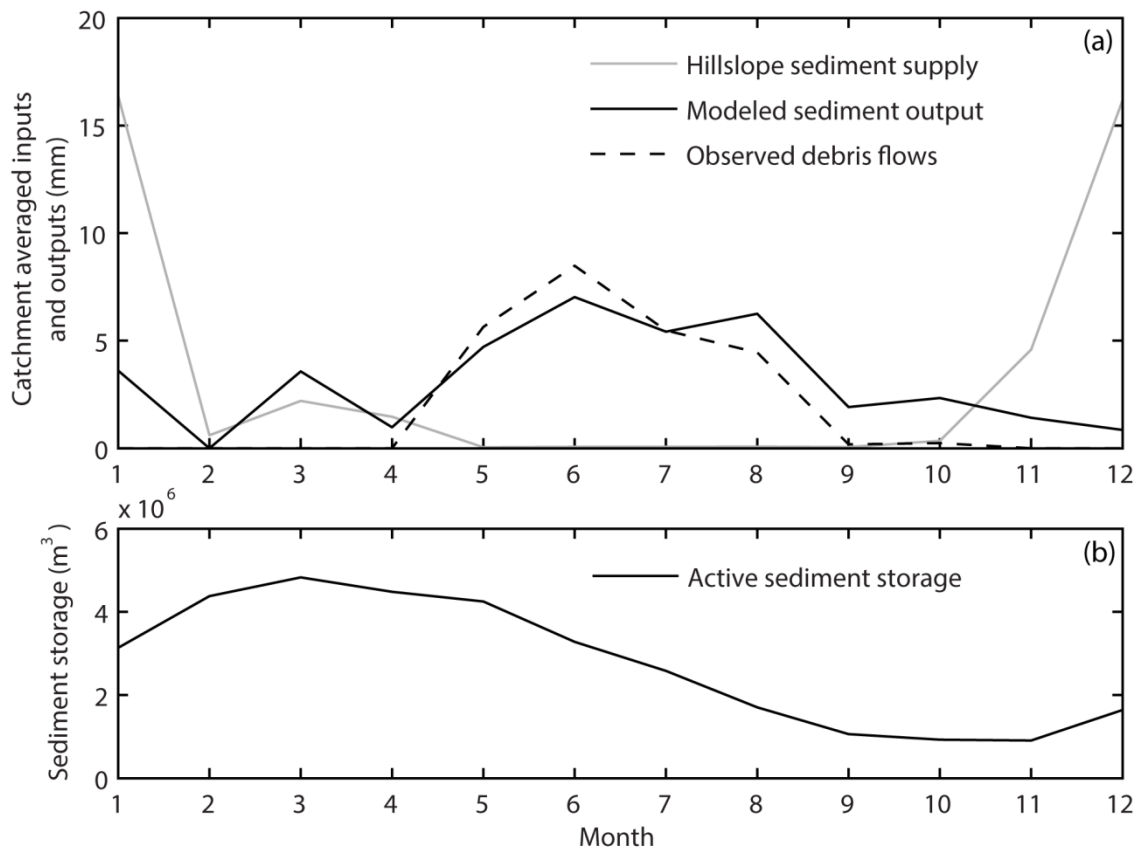


Figure 4.10 - (a) Seasonal distribution of mean sediment input and output depth in (mm) (modeled and observed); and (b) active sediment storage, both shown for procedure (1).

Finally, we can use the same statistics to compare the predictive skill of SedCas with a rainfall intensity curve which predicts debris flows to occur whenever rainfall exceeds a critical intensity, here 8 mm day^{-1} taken from Badoux et al. (2009). Table 4.3 shows that although the rainfall intensity model would have a much higher sensitivity, it would also have many Type II errors (false positive predictions) and so a low specificity, which finally leads to a lower likelihood ratio than any of our tested sediment input procedures.

The main advantage of our model however lies in the fact that it predicts that debris flow events occur for a range of rainfall intensities, and therefore it inherently quantifies the uncertainty in using a rainfall threshold as an independent variable. For instance, Figure 4.11 shows the daily rainfall intensities for which debris flows in the model were produced with the sediment input procedure (1). The comparison with actual observed rainfall intensity on debris flow days is extraordinary and testifies to the good performance of the hydrological model. Overall we conclude that our model performs much better than a simple precipitation threshold in predicting the occurrence and timing of debris flows.

Table 4.3 - Comparison of the predictive skill of variations of our model with variations of a more simple precipitation exceedance model based on accuracy statistics. We consider the prediction of all debris flows ($> 0 \text{ m}^3$) in the analysis.

Model Result	Sensitivity	Specificity	Likelihood ratio
Triggering by precipitation			
Rainfall $> 8 \text{ mm}$	0.694	0.923	9.013
SedCas (different sediment input scenarios)			
1	0.231	0.982	12.81
2	0.272*	0.981	14.24*
3	0.228	0.982*	12.92
4	0.194	0.982	10.50
5	0.250*	0.975	10.05

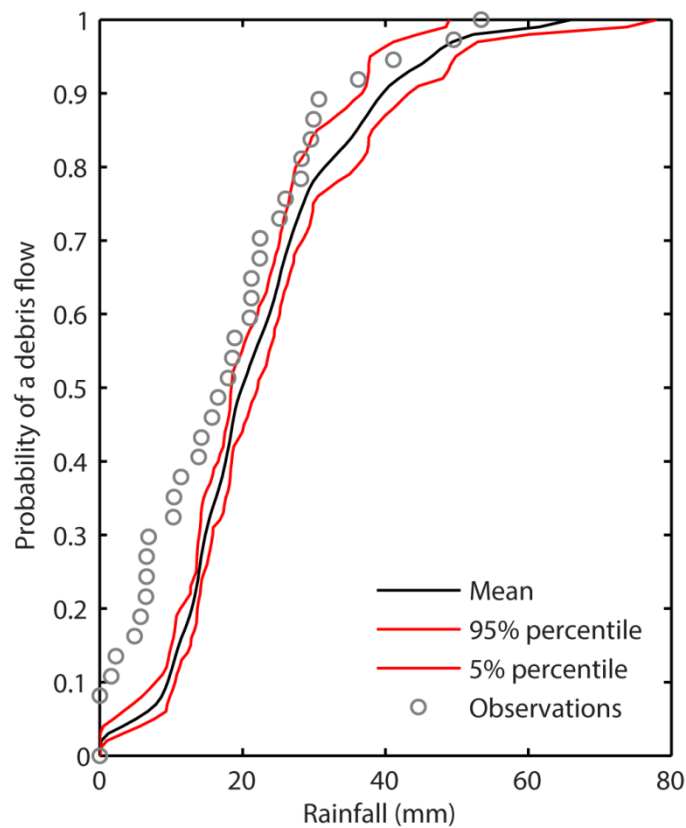


Figure 4.11 - Modeled and observed (36 events) probability of debris flow occurrence as a function of daily rainfall intensity. Simulations are for sediment input procedure (1).

4.5. Discussion

We present a sediment transfer model based on the sediment cascade concept with the overall aim of modeling and explaining the non-linearity and stochasticity of sediment discharge from a mountain basin. Processes and interactions of sediment and water production and transfer are simplified and conceptualized in the model, yet they combine to produce remarkably complex and realistic behavior and result in highly non-linear and stochastic sediment discharge. The model successfully reproduces the first-order properties of the sediment transfer system, including the probability distribution, seasonal statistics and timing of observed debris flows in the Illgraben over the studied 10-year period and the residence time of sediment in the channel. This is despite the fact that most parameters were independently estimated and not fine-tuned to best reproduce debris flows. The added value of our approach is that we can attempt an attribution of causes to the observed sediment discharge characteristics and quantify the role of supply limitations in an explicit way.

Based on model results we can attribute the sediment discharge properties to a combination of stochasticity of sediment supply and the hydrological forcing. Hydrological forcing, through the processes that generate runoff, play the most important role in reproducing the magnitude and frequency of debris flows as indicated by the resemblance of the probability distribution of debris flows to that of hypothetical supply-unlimited debris flows driven solely by runoff events (Figure 4.5). Given an unrealistic sediment supply, as in the case of sediment input procedures 4 and 5, debris flow properties were not realistically reproduced. This is because both procedures result in unrealistic sediment storage dynamics, indicated by a too long or short residence time of sediment in the channel and less frequent supply-limiting conditions by which debris flows are limited in size or even prohibited (Table 4.2).

A stochastic sediment supply is needed to reproduce realistic sediment storage, supply-limiting conditions, and ultimately sediment discharge properties. However, an important finding is that the actual triggering mechanism and thus timing of slope failures drawn from the probability distribution of slope failures (procedures 1-3) has a rather small influence on the shape of the debris flow distribution. The influence of the sediment input is filtered out by the sediment cascade, runoff regime and debris flow generation procedure. This shows why the reconstruction of sediment input characteristics from yield data alone may be problematic in some basins (e.g., Jerolmack and Paola, 2010).

The occasional supply-limited condition in the channel (22-41% of the events were supply-limited, 9-22% were prohibited from occurring altogether) results in highly non-linear sediment discharge. The variety of simulated sediment discharge events that can be classified into floods and debris flows based on their sediment concentration are illustrated in Figure 4.7. The implication is that it is difficult to attribute any individual sediment discharge event, for example in the sedimentary record, to a particular runoff discharge event. However, because the distribution of sediment discharge events does reflect the distribution of runoff events, we suggest that changes in the magnitude and frequency of discharge and factors controlling

discharge may be inferred from records of sediment discharge. This would not be the case if the distribution of sediment discharge only reflected the internal sediment storage dynamics of the system (e.g. Van de Wiel and Coulthard, 2011). We hypothesize that changes in climate may be reflected in the sediment discharge via changes in runoff magnitude and frequency, which could be evaluated in future work by simulation under different climate and sediment supply scenarios.

The primary objective of this paper was to develop a model to explain statistical distribution of debris flows, rather than to accurately predict their timing. The fact that the model predicts the timing of almost 30% of debris flows on the day and 50% of debris flows within 1 day of the observed event is a validation of the hydrological model considering that the stochastic sediment supply cannot reproduce the exact sediment storage dynamics over the calibration period. The fact that the model is able to capture the entire range of possible rainfall depth associated with observed debris flows (Figure 4.11) is further validation of the hydrological model. However, the daily resolution means that debris flows triggered by high intensity rainfall events of a duration much shorter than 1 day cannot be captured, which explains the lower probability of debris flows at low daily rainfall magnitudes compared to observations in Figure 4.11. These limitations explain the relatively low sensitivity of 30% of the model compared to a rainfall intensity-duration threshold of Badoux et al. (2009) that predicts many more of the events in the period on which it was calibrated. Our modeling approach illustrates the importance of considering hydrological and sediment storage dynamics for debris flow prediction and in-so-doing demonstrates the limitations of rainfall intensity thresholds for debris flow initiation.

The model results in transport-limited behavior about 55% of the time (Figure 8), in line with descriptions of the Illgraben as a transport-limited system (Schlunegger et al., 2009; Bennett et al., 2013). However, the model clearly demonstrates the fluctuation between transport and supply limiting conditions as a function of both the hydrological forcing and stochastic sediment input and that it is therefore overly simplistic to consider the Illgraben as a purely transport-limited system when trying to understand and predict debris flow occurrence.

4.6. Conclusions

We developed a probabilistic sediment cascade model with the overall aim of explaining the non-linear and stochastic sediment discharge from a mountain basin. We based this model on the Illgraben, a debris-flow prone catchment in the Swiss Alps, for which measurements of slope failures and debris flows spanning several years are available. The model consists of two sediment storage reservoirs representing hillslopes and channels and one water reservoir for the basin hydrology, and water and sediment are transferred between the reservoirs based on simple but physically meaningful rules. There are few parameters, most of which are estimated independently, and not fine-tuned to model output. Our main conclusions are as follows:

(1) The model successfully reproduces the probability distribution, characteristics and timing of 36 observed debris flows from 2000 through 2009. The residence time of sediment in the channel is also reproduced by the model, all of which suggest that it captures the essential dynamics of the system at this scale.

(2) The model results suggest that the main control on the shape of the probability distribution of debris flows is the distribution of runoff events and therefore the hydrological dynamics, which include snow cover and soil water storage dynamics, and are driven by observed climate data. Our results suggest that the stochastic element of sediment input is important to reproduce realistic sediment storage, occasional supply-limiting conditions (22-41% of the events were supply-limited and 9-22% were prevented from occurring altogether) and ultimately the distribution of sediment discharge. However, the triggering mechanism of slope failures cannot be detected in the distribution of sediment discharge events. This corroborates the hypothesis of Jerolmack and Paola (2010) that the reconstruction of sediment input characteristics from yield data or stratigraphic records alone may be problematic in some basins.

(3) Supply-limiting conditions produce a range of sediment concentrations for a discharge event of a given magnitude and sediment discharge events can be classified accordingly into floods, debris floods and debris flows. Additionally, the model generates debris flows for a wide range of rainfall magnitudes as a function of antecedent moisture. For the reason that it includes sediment and water storage (system memory), the model is an advancement over rainfall intensity-duration threshold curves for debris flow initiation, indicated by its higher predictive skill than a prediction based on the exceedence of a rainfall threshold at a daily resolution.

In summary, although the approach presented here describes the processes of sediment transfer and debris flow generation in a simplified manner, it produces remarkably complex sediment discharge behaviour, which can be explained only by considering jointly the availability of sediment and the triggering potential, quantifying the role of history (system memory) and climate (triggering events) on sediment discharge dynamics in the Illgraben. Although this application was developed for the Illgraben we believe the findings have general implications for fluvial systems that can be schematized into sediment cascades and where the supply of sediment and triggering of events is largely stochastic.

Acknowledgements

This study was completed within the SedyMONT project, part of the ESF-funded TOPOEUROPE. Funding provided by the Swiss National Science Foundation Grant 20T021-120467 is acknowledged. Climatic input data were provided by MeteoSwiss (rainfall and temperature) and the Institute of Snow and Avalanche Research (SLF) (snow depth). Thanks to Bettina Schaeppi for her help with the model code.

5. Conclusions and outlook

This chapter is divided into several sections. More general conclusions in the context of the research aims and hypotheses identified in section 1.4 are given in section 5.1. Specific details related to the Illgraben are given in section 5.2 and section 5.3 gives an outlook for further research.

5.1. Conclusions

In this thesis I have quantified and modeled sediment production, transfer and yield in a mountain basin prone to rock-slope failure and debris flows on a temporal scale of decades. Data were obtained using digital photogrammetry, analyzed in relation to climate and seismic activity, and used in a new model of sediment transfer.

Understanding *mountain basin sediment transfer* requires data on sediment production, transport and yield. This is a significant challenge due to the difficulty of observing processes particularly of sediment production and transport over long enough time periods to capture their magnitude-frequency relations. This study is one of the first to have quantified these processes over periods of decades. Rates of sediment production, transfer and yield in the Illgraben were quantified for the period 1963 – 2005 in 4 sub-periods. This was achieved this using a sophisticated photogrammetric procedure involving software that is specialized for extracting digital elevation models (DEMs) in steep and challenging terrain, which otherwise proves to be difficult using standard commercial software. This study can therefore provide a reference for other studies attempting to use digital photogrammetry to quantify change in steep mountainous terrain.

From the time series of DEMs, I extracted the largest *historical inventory of slope failures* for a single slope that I am aware of (more than 2000 failures), possible due to the extremely high erosion rate of the study slope ($0.39 \pm 0.03 \text{ m yr}^{-1}$) and the relatively long observation window afforded by the aerial photographs used to produce the DEMs. Based on this inventory I have provided the first empirical evidence that the characteristic landslide magnitude-frequency distribution with roll-over and power law tail may indeed be the result of two different slope failure processes: shallow slumps and slides and deep-seated rock falls and slides, as was previously hypothesized by Katz and Aharanov (2006) based on their experimental study. Additionally, I have demonstrated that it is preferable to fit a *power-law model* to the tail of the magnitude-frequency distribution using a maximum likelihood approach, rather than linear regression, although this is not a new statistical revelation (Clauset et al., 2009). The reason for this is that linear regression tends to underestimate the power law scaling exponent significantly.

Landslide volumes are more difficult to measure than area and are thus often inferred from landslide areas using an empirical scaling relationship. The selection of the scaling exponent in this relationship has a significant effect on the estimated landslide volumes and on erosion rates that may be calculated from these. The landslides we measured from the bedrock study slope had a scaling exponent in the range suggested for soil-covered slopes by Larsen et al. (2010), which I suggest is due to the highly fractured and weathered nature of the bedrock. This result demonstrates the importance of constraining the empirical relationship between landslide volume and area for different geological settings. This is an important finding concerning the calculation of erosion rates from landslide areas.

The most significant process of hillslope erosion from the study slope is large deep-seated failure, which makes up the power-law tail of the magnitude-frequency distribution and contributes ~99% of the total sediment supply. Unlike small failures making up the roll-over of the distribution, which occur across a range of slope gradients, these failures generally occur on slopes steeper than 45°, providing important empirical support for the concept of *threshold hillslopes* used in landscape evolution models.

Temporal patterns of rates of sediment production, transfer and yield over the study period were analyzed with respect to each other and climatic and seismic variables. The interaction or *coupling between hillslopes and channels* is important concerning our understanding of landscape evolution and sediment yield. I have demonstrated the operation of a downslope-directed coupling relationship in the Illgraben in which hillslopes erode more rapidly and independently of channel incision and are the first order control on sediment yield and landscape evolution. This is contrary to the more commonly described upslope-directed coupling relationship in which channel incision is the first order control on hillslope erosion and sediment yield and supports the assertion that a downslope-directed coupling relationship may be more common in the landscape than previously thought (Schlunegger et al., in press). It also means that the environmental controls of hillslope erosion must be considered.

If we are to predict the impact of climate change on future rates of earth surface processes, we must first understand their present day interactions with climate. This study demonstrates the difficulty of identifying a dominating climatic *control on hillslope erosion*, as has been noted by other studies. An increase in the erosion rate of the study slope in the 1980s coincided with a significant regional increase in air temperature at this time. In the absence of an increase in either precipitation or seismic activity, and considering the increase in hillslope activity observed across the Alps at this time, a thermal control on the increase in hillslope erosion is the most likely. However, when looking at the event timescale, an individual control/trigger is difficult to identify and suggests that the triggering of slope failures is stochastic and occurs by multiple triggering mechanisms.

The study also demonstrates the different sensitivities of hillslope and channel erosion to climate variables. While hillslope erosion is more likely controlled by thermal processes and is therefore more sensitive to changes in air temperature, channel erosion is controlled by the frequency and magnitude of runoff events and is therefore more sensitive to changes in precipitation. This study therefore suggests the difficulty in the prediction of the effects of climate change on sediment yield.

However, numerical modeling can help to understand the interaction of sediment production, transport and storage with each other and with climate and can aid prediction of future sediment yields under a changing climate. The main contribution of this thesis is a novel *probabilistic sediment cascade model* of sediment transfer that explains the observed non-linear sediment discharge under present climate and therefore may be used in the future to predict future sediment yield under a changing climate (Section 5.3). While the model is applied to the Illgraben in this thesis, it is more generally applicable to any basin that can be schematized into a cascade and that is dominated by stochastic processes of sediment production and transfer. The model is based on the sediment cascade concept in the sense that sediment and water are routed through a spatial chain of storage reservoirs, yet it also extends the concept to an investigation of thresholds and feedbacks within the system.

The model integrates data and understanding generated in the thesis on rates, interactions and controls of sediment production, transfer and yield together with data from previous studies in the catchment. It is fed with slope failures from the probability distribution of slope failures developed in this thesis and by climate data and routes sediment and water through the storage reservoirs based on simple but physically meaningful rules.

Despite its simplicity, the model successfully reproduces the distribution, statistics and timing of the observed debris flows over the calibration period, 2000-2009, and can thus be said to capture the essential physics of the system. Although the hydrological regime is shown to be the most important control on sediment discharge, an experiment involving different procedures of generating sediment input with the model shows the importance of a stochastic sediment supply in reproducing realistic sediment storage dynamics and hence sediment output. It also demonstrates that the triggering mechanism of slope failures has little influence on the sediment output. This corroborates the hypothesis of Jerolmack and Paola (2010) that the reconstruction of sediment input characteristics from yield data or stratigraphic record alone may be problematic in some basins.

Several studies have defined channels as either transport or supply limited. The model demonstrates the fluctuation of a mountain channel between these two states and the importance of this behavior in the reproduction of observed debris flow properties. The model performs better at predicting debris flows than a simple rainfall threshold demonstrating the

importance of considering hydrological and sediment storage variability in the prediction of the timing of debris flows. This highlights the limitations of using rainfall intensity-duration thresholds to predict debris flows.

5.2. Findings relevant to the Illgraben

The Illgraben was already known to have high rates of erosion and a sediment yield that exceeds Alpine standards by two orders of magnitude (Schlunegger et al., 2009). However, using digital photogrammetry, I quantified even higher erosion rates and sediment yield and their temporal variability between 1963 and 2005. We measured mean erosion rates of between $0.24 \pm 0.01 \text{ m yr}^{-1}$ (1963 – 1986) and $0.42 \pm 0.03 \text{ m yr}^{-1}$ (1986 – 1992). These high erosion rates ultimately give rise to high annual sediment yields with an average of $2.3 \times 10^5 \text{ m}^3$ for the study period. These sediment yields are higher than previously estimated from measurements of debris flows captured by an in-channel monitoring system from 2000 onwards (McArdell et al., 2007; 2009). We suggest that the main reason for the discrepancy is that debris flow activity from November through April is not monitored. Our model of sediment transfer suggests that debris flows do occur during the winter months. Additionally, small debris flows and floods are usually not measured, but may transport significant material. Finally, suspended sediment transport during base flow conditions may transport up to 15% of the total load (Section 5.3) (Appendix B.2).

Periods of channel aggradation and degradation are related both to changes in hillslope sediment supply and the magnitude and frequency of rainfall events. The channel aggraded in response to the increase in hillslope erosion in 1986-1992. It subsequently rapidly degraded at a rate of $0.74 \pm 0.02 \text{ m yr}^{-1}$ in 1992-1998 related to an increase in the frequency of intense rainfall events. These results support the description of the Illgraben as a dominantly transport limited system (Schlunegger et al., 2009) and also suggest that the most important mechanism of debris flow generation is by entrainment of sediment stored along the channel during runoff events.

The sediment transfer model developed in this thesis indicates that *hydrological dynamics* play the most important role in determining the observed magnitude-frequency distribution of debris flows in the Illgraben, in line with the suggestion that the Illgraben is predominantly a transport limited system. However, the model demonstrates the fluctuation of the catchment between transport and supply limited conditions (Section 5.1). Supply limiting conditions limit the volumes of 22-41% of debris flows and prohibit about 9-22% of debris flows from occurring at all. Supply limiting conditions are important in accurately reproducing the statistics and distribution of observed debris flows. Significantly, they are also important to consider in the prediction of debris flow events from the catchment.

5.3. Outlook

My analysis encountered the following main problems that may be investigated in further research and which may be of general interest for the scientific community.

Identifying change from DEMs

Due to the inevitable coalescence of slope failures in our dataset over the multiannual periods of analysis, we encountered the problem of indentifying individual/discrete slope failures. Although we concluded that this does not affect the power-law scaling exponent of the distribution of slope failures presented in Chapter 2, it raises the question of whether slope failure should be regarded as a discrete or progressive/gradual phenomenon as also recognized by Lim et al. (2010). This ultimately depends on the time window of observation. Repeat terrestrial laser scanning is a viable technique to measure surface change over shorter timescales, as done in the channel in the Illgraben (Schürch, 2011), that could be applied to monitor slope failure in the Illgraben (e.g. Lim et al., 2010). Radar interferometry is a promising technique to monitor progressive failure that has already been used by Caduff et al. (in review) in the Illgraben to measure rates of 3 mm a day for a failure at the head of our study slope. A more detailed assessment of slope failures at the Illgraben using such techniques would help to test our hypothesis of two processes of slope failure operating on the slope, how these failures occur in time and in relation to each other.

Temperature effects on erosion

Concerning controls on hillslope erosion in the Illgraben, I identified a potential link between increasing temperatures and an increase in the depth and rate of hillslope erosion in the 1980s (Chapter 3). The hypothesis that this link is due to a thawing of permafrost at depth in the slope at this time would be difficult to test in the Illgraben because if true then it would already be thawed out, not to mention the difficulty of investigating changes that happen at meters of depth in the slope. The alternative hypothesis that a decrease in snow cover and increase in the exposure of the slope to thermal weathering processes may have increased slope failure depth and frequency would be possible to test by monitoring rock temperature with temperature probes along with slope failure frequency using repeat laser scanning, for example, throughout the year. As exemplified by the analysis of the 1961 rock avalanche, seismic activity cannot be ruled out as an influencing factor on slope failure. Therefore seismic activity could also be monitored, potentially in conjunction with the use of seismic sensors to detect landslide triggered debris flows (Burtin et al., 2012).

The reason for the extreme rates of hillslope erosion and thus sediment yield in the Illgraben compared to other basins in the Alps and worldwide is unclear. It may be that the Illgraben has a unique tectonic and geological setting that may explain its rapid erosion. Further investigation of processes of slope failure will help to answer this question along with detailed data from other debris flow catchments in the Alps and elsewhere with which to compare with the Illgraben.

Debris flow triggering and prediction

There are still open questions concerning debris-flow triggering in the Illgraben. The model of sediment transfer developed in this thesis (Chapter 4) only included the mechanism of entrainment of sediment in the channel by runoff events. While this mechanism appears to explain the first-order properties and seasonal timing of debris flow events, the model is unable to reproduce the daily timing of all observed debris flows and a possible explanation may be that there are other triggering mechanisms that produce debris flows in the Illgraben. Initial results from the installation of seismometers around the catchment show the triggering of a debris flow by a landslide (Burtin et al., 2011). This technique shows promise in identifying the relative frequency of landslide triggered debris flows.

The model is not intended to be used to predict debris flow hazard and indeed only predicts 30% of observed debris flows on the day. However, the results may be used to inform the intensity-duration approach to predicting debris flow events (e.g. Badoux et al., 2009). For example, the model results show the importance of considering channel sediment storage to understand debris flow occurrence. Channel sediment storage shows a seasonal distribution, declining over the summer months due to exhaustion by debris flows. Therefore, it would be interesting to produce intensity-duration curves applicable for different months of the year in which sediment storage plays varying roles of importance. Similarly, concerning water storage, water is stored as snow and frozen into the soil over the winter months, therefore melting in the spring produces some of the biggest debris flows. The threshold intensity and duration of rainfall to trigger a debris flow may therefore be lowered in the spring. This is another reason for developing monthly or seasonal rainfall intensity-duration curves for debris flow prediction.

Suspended sediment transport between debris flows

One possible reason for the discrepancy between our estimate of sediment yield and the estimate from debris flow monitoring in the Illgraben is that sediment transport events under the threshold volume of $\sim 2500 \text{ m}^3$ are not monitored by the current monitoring system. I conducted a preliminary study of suspended sediment transport in the Illgraben to determine the contribution of suspended sediment transport to the total sediment yield (Appendix B.2). I roughly estimate a 15% contribution of suspended sediment transport to total sediment yield. This accounts for part of the discrepancy between sediment yield measured in this study and that measured by the monitoring system. A large part of the discrepancy may be attributed to the fact that debris flows are not monitored and therefore measured during the winter, whereas the model suggests that they occur in every month, apart from February due to complete snow cover in this month.

From the preliminary study of suspended sediment transport, I observed that sediment concentration was higher shortly after a debris flow compared to a sample taken during a similar discharge but not following a debris flow. While this may be due to measurement error, it is not unreasonable to expect higher suspended sediment concentration in the flow following a disturbance of the channel bed by a debris flow. There are few studies of suspended

sediment transport following debris flows. Therefore a more detailed study of suspended sediment transport immediately following a debris flow would be a valuable addition to debris flow research. This could either be achieved by taking manual 'grab' samples for intervals after a debris flow, or using a robust automatic sampler.

The model of sediment transfer developed in this thesis may be used in further research for the following applications:

Analysis of the impact of climate change on sediment yield

The model has been calibrated based on 10 years of debris flow measurements in the Illgraben utilizing observed climate data as the climatic input and has helped to understand the climatic controls on sediment yield. The model may therefore be used to predict future sediment yield under a changing climate. Climate data could be generated using a weather generator, adjusted according to climate change scenarios, and the model run based on this data for hundreds of years. This would enable the testing of the hypothesis generated in Chapter 4 that it may be possible to detect changes in the magnitude-frequency distribution of precipitation in the magnitude-frequency distribution of sediment discharge events.

Modeling uncertainty in short-term erosion rates

Quantifying the rate at which rock erodes and sediment is produced is fundamental to understanding landscape evolution. Modern rates of erosion spanning 10^0 to 10^1 years are typically inferred from estimates of sediment yield, either measured as a flux of sediment past a gauging station or determined by measuring the accumulation of sediment in a reservoir. Cosmogenic nuclides in river sediment record erosion rates over a timescale ($10^2 - 10^4$ years) that is sufficiently long to be insensitive to very short-term variability in sediment transport and that is meaningful for timescales of rock weathering and rock uplift (von Blanckenburg, 2005). Importantly, the measured erosion rates are independent of the present-day sediment flux.

Several studies have presented comparisons between modern day erosion rates measured from sediment discharge or reservoirs and long term erosion rates measured using cosmogenic nuclides. Conflicting relationships exist between modern and long term rates in these studies. Modern day erosion rates were found to be lower than long term rates in Idaho (Kirchner et al. 2001), the Regen, Neckar, Loire and Meuse catchments (Schaller et al., 2001), the European Alps (Wittmann et al., 2007), and in the Nepal Himalaya (Gabet et al., 2008). In contrast, higher modern day erosion rates were found in Sri Lanka (Hewawasam et al., 2003) and in an arid mountain basin in southern Israel (Clapp et al. 2000). Modern day erosion rates were found to be in equilibrium with long-term rates in the Nepal Himalaya (Gabet et al., 2008; Andermann et al., 2011). Some studies attribute the apparent change or lack of change in erosion rates to real causes. For example, Hewawasam et al. (2003) suggest that higher modern day erosion rates in Sri Lanka are the result of the increased agricultural land use. Gabet et al. (2008) suggest that the approximately steady state erosion in the Khudi catchment is representative of southern, landslide-dominated watersheds in the Nepal.

However, modern day erosion rates are blighted by uncertainty resulting from the episodic nature of sediment discharge and the inability to capture the long term behavior of the system in a relatively short term sampling window (e.g. Fuller et al., 2003). This uncertainty makes it difficult to identify if the observed changes in erosion rates are real (Kirchner et al., 2001; Schaller et al., 2001; Wittmann et al., 2007) and is therefore important to quantify. The model of sediment transfer developed in this thesis may be used to quantify this uncertainty by sampling from the time series of modeled sediment discharge and calculating the spread of possible erosion rates (e.g. Fuller et al. 2003).

Bibliography

- Allen, S., Cox, S., and Owens, I., 2011, Rock avalanches and other landslides in the central Southern Alps of New Zealand: a regional study considering possible climate change impacts: *Landslides*, v. 8, no. 1, p. 33-48.
- Andermann, C., Crave, A., Gloaguen, R., Davy, P., and Bonnet, S., 2012, Connecting source and transport: Suspended sediments in the Nepal Himalayas: *Earth and Planetary Science Letters*, v. 351–352, p. 158-170.
- Andermann, C., Gloaguen, R., Bonnet, S., Crave, A., and Merchel, S., 2011, Erosion patterns in the Nepal Himalayas from river gauging, cosmogenic nuclides and precipitation data, *Geophysical Research Abstracts Vol. 13 EGU2011-2525-12011*.
- Badoux, A., Graf, C., Rhyner, J., Kuntner, R., and McArdell, B., 2009, A debris-flow alarm system for the Alpine Illgraben catchment: design and performance: *Natural Hazards*, v. 49, no. 3, p. 517-539.
- Bagnold, R., 1966, An approach to the sediment transport problem from general physics: *US Geol. Surv. Prof. Paper*, v. 422, p. 231-291.
- Ballantyne, C. K., 2002, Paraglacial geomorphology: *Quaternary Science Reviews*, v. 21, no. 18-19, p. 1935-2017.
- Bardou, E., and Delaloye, R., 2004, Effects of ground freezing and snow avalanche deposits on debris flows in alpine environments: *Natural Hazards and Earth Systems Science*, v. 4, no. 4, p. 519-530.
- Beguería, S., 2006, Validation and Evaluation of Predictive Models in Hazard Assessment and Risk Management: *Natural Hazards*, v. 37, no. 3, p. 315-329.
- Benda, L., 1990, The influence of debris flows on channels and valley floors in the Oregon Coast Range, U.S.A: *Earth Surface Processes and Landforms*, v. 15, no. 5, p. 457-466.
- Benda, L., and Dunne, T., 1997a, Stochastic Forcing of Sediment Supply to Channel Networks from Landsliding and Debris Flow: *Water Resources Research*, v. 33, p. 2849–2863.
- Benda, L., and Dunne, T., 1997b, Stochastic Forcing of Sediment Routing and Storage in Channel Networks: *Water Resources Research*, v. 33, p. 2865-2880.
- Beniston, M., Rebetez, M., Giorgi, F., and Marinucci, M. R., 1994, An analysis of regional climate change in Switzerland: *Theoretical and Applied Climatology*, v. 49, no. 3, p. 135-159.
- Bennett, G. L., and Evans, D. J. A., 2012, Glacier retreat and landform production on an overdeepened glacier foreland: the debris-charged glacial landsystem at Kvíárjökull, Iceland: *Earth Surface Processes and Landforms*, v. 37, no. 15, p. 1584-1602.
- Bennett, G. L., Molnar, P., Eisenbeiss, H., and McArdell, B. W., 2012, Erosional power in the Swiss Alps: characterization of slope failure in the Illgraben: *Earth Surface Processes and Landforms*, v. 37, no. 15, p. 1627-1640.
- Bennett, G. L., Molnar, P., McArdell, B. W., Schlunegger, F., and Burlando, P., 2013, Patterns and controls of sediment production, transfer and yield in the Illgraben: *Geomorphology*, v. 188, p. 68-82.
- Berger, C., 2010, Debris flow entrainment and sediment transfer processes at the Illgraben catchment, Switzerland. PhD thesis: University of Bern, 158 p.
- Berger, C., McArdell, B. W., and Schlunegger, F., 2011a, Direct measurement of channel erosion by debris flows, Illgraben, Switzerland: *Journal of Geophysical Research*, v. 116, no. F1, p. F01002.
- Berger, C., McArdell, B. W., and Schlunegger, F., 2011b, Sediment transfer patterns at the Illgraben catchment, Switzerland: Implications for the time scales of debris flow activities: *Geomorphology*, v. 125, no. 3, p. 421-432.

- Betts, H. D., Trustrum, N. A., and Rose, R. C. D., 2003, Geomorphic changes in a complex gully system measured from sequential digital elevation models, and implications for management: *Earth Surface Processes and Landforms*, v. 28, no. 10, p. 1043-1058.
- Birsan, M. V., Molnar, P., Burlando, P., and Pfaundler, M., 2005, Streamflow trends in Switzerland: *Journal of Hydrology*, v. 314, no. 1-4, p. 312-329.
- Bishop, P., 2007, Long-term landscape evolution: linking tectonics and surface processes: *Earth Surface Processes and Landforms*, v. 32, no. 3, p. 329-365.
- Bolin, B., and Rodhe, H., 1973, A note on the concepts of age distribution and transit time in natural reservoirs: *Tellus*, v. 25, p. 58-62.
- Bovis, M. J., and Dagg, B.R., 1992, Debris flow triggering by impulsive loading: mechanical modelling and case studies: *Canadian Geotechnical Journal*, v. 29, p. 345-352.
- Bovis, M. J., and Jakob, M., 1999, The role of debris supply conditions in predicting debris flow activity: *Earth Surface Processes and Landforms*, v. 24, no. 11, p. 1039-1054.
- Brardinoni, F., Church, M., Simoni, A., and Macconi, P., 2012, Lithologic and glacially conditioned controls on regional debris-flow sediment dynamics: *Geology*, v. 40, no. 5, p. 455-458.
- Brardinoni, F., Slaymaker, O., and Hassan, M. A., 2003, Landslide inventory in a rugged forested watershed: a comparison between air-photo and field survey data: *Geomorphology*, v. 54, no. 3-4, p. 179-196.
- Brasington, J., and Richards, K., 2007, Reduced-complexity, physically-based geomorphological modelling for catchment and river management: *Geomorphology*, v. 90, no. 3-4, p. 171-177.
- Brasington, J., Rumsby, B.T., and McVey, R.A., 2000, Monitoring and modelling morphological change in a braided gravel-bed river using high resolution GPS-based survey: *Earth Surface Processes and Landforms*, v. 25, no. 973-990.
- Brierley, G., Fryirs, K., and Jain, V., 2006, Landscape connectivity: the geographic basis of geomorphic applications: *Area*, v. 38, no. 2, p. 165-174.
- Burbank, D. W., Leland, J., Fielding, E., Anderson, R. S., Brozovic, N., Reid, M. R., and Duncan, C., 1996, Bedrock incision, rock uplift and threshold hillslopes in the northwestern Himalayas: *Nature*, v. 379, no. 6565, p. 505-510.
- Burt, T., Allison, R., 2010, Sediment cascades in the environment: an integrated approach, *Sediment Cascades, An Integrated Approach*, Wiley-Blackwell, p. 1-16.
- Burtin, A., Hovius, N., Turowski, J., McArdell, B., and Vergne, J., 2012, High-resolution seismic monitoring of geomorphic activity in a catchment, *Geophysical Research Abstracts Vol. 14*, EGU2012-11263.
- Caduff, R., Schlunegger, F., Kos, A., McArdell, B.W., and Weismann, A., Terrestrial radar interferometric measurements of slope deformation in a steep alpine debris-flow headwater area: *Geophysical Research Letters*, in review.
- Caine, N., 1980, The Rainfall Intensity: Duration Control of Shallow Landslides and Debris Flows: *Geografiska Annaler. Series A, Physical Geography*, v. 62, no. 1/2, p. 23-27.
- Cannon, S. H., 2001, Debris-flow generation from recently burned watersheds: *Environmental & Engineering Geoscience*, v. 7, no. 4, p. 321-341.
- Cannon, S. H., and Reneau, S. L., 2000, Conditions for generation of fire-related debris flows, Capulin Canyon, New Mexico: *Earth Surface Processes and Landforms*, v. 25, no. 10, p. 1103-1121.
- Carenzo, M., Pellicciotti, F., Rimkus, S., and Burlando, P., 2009, Assessing the transferability and robustness of an enhanced temperature-index glacier-melt model: *Journal of Glaciology*, v. 55, no. 190, p. 258-274.

- Casty, C., Wanner, H., Luterbacher, J., Esper, J., and Böhm, R., 2005, Temperature and precipitation variability in the European Alps since 1500: *International Journal of Climatology*, v. 25, no. 14, p. 1855-1880.
- Chen, C., 2009, Sedimentary impacts from landslides in the Tachia River basin, Taiwan, 2010–2099: *Geomorphology*, v. 133, no. 143-151.
- Clapp, E. M., Bierman, P. R., Schick, A. P., Lekach, J., Enzel, Y., and Caffee, M., 2000, Sediment yield exceeds sediment production in arid region drainage basins: *Geology*, v. 28, no. 11, p. 995-998.
- Clauset, A., Shalizi, C.R., Newman, M.E.J., 2009, Power-law distributions in empirical data: *SIAM Review*, v. 51, no. 4, p. 661-703.
- Coe, J. A., Kinner, D. A., and Godt, J. W., 2008, Initiation conditions for debris flows generated by runoff at Chalk Cliffs, central Colorado: *Geomorphology*, v. 96, no. 3-4, p. 270-297.
- Costa, J. E., 1984, *Physical Geomorphology of Debris Flows*. Berlin and New York, Springer-Verlag, *Developments and Applications of Geomorphology*.
- Coulthard, T. J., Kirkby, M. J., and Macklin, M. G., 2000, Modelling geomorphic response to environmental change in an upland catchment: *Hydrological Processes*, v. 14, no. 11-12, p. 2031-2045.
- Coulthard, T. J., and Van De Wiel, M. J., 2007, Quantifying fluvial non linearity and finding self organized criticality? Insights from simulations of river basin evolution: *Geomorphology*, v. 91, no. 3–4, p. 216-235.
- Crozier, M. J., 2010, Deciphering the effect of climate change on landslide activity: A review: *Geomorphology*, v. 124, no. 3-4, p. 260-267.
- Cruden, D. M., and Varnes, D. J., 1996, Landslide types and processes, *in* Turner, A. K. a. S., R.L., ed., *Landslides Investigation and Mitigation*, National Research Council, Transportation Research Board, Special Report 247, p. 36-75.
- Davies, T. R. H., and Korup, O., 2010, *Sediment Cascades in Active Landscapes*, Sediment Cascades, John Wiley & Sons, Ltd, p. 89-115.
- Densmore, A. L., Ellis, M. A., and Anderson, R. S., 1998, Landsliding and the evolution of normal-fault-bounded mountains: *Journal of Geophysical Research*, v. 103, no. B7, p. 15203-15219.
- Dietrich, W. E., and Dunne, T., 1978, Sediment budget for a small catchment in mountainous terrain: *Zeitschrift für Geomorphologie*, v. 29, p. 191-206.
- Dussauge-Peisser, C., Grasso, J.-R., and Helmstetter, A., 2003, Statistical analysis of rock fall volume distributions: Implications for rock fall dynamics: *Journal of Geophysical Research*, v. 108, no. B6.
- Dussauge-Peisser, C., Helmstetter, A., Grasso, J.-R., Hantz, D., Jeannin, M., and Giraud, A., 2002, Probabilistic approach to rock fall hazard assessment: potential of historical data analysis: *Natural Hazards and Earth Systems Science*, v. 2, p. 15-26.
- Edwards, B., and Fäh, D., 2013, A Stochastic Ground-Motion Model for Switzerland: *Bulletin of the Seismological Society of America*, v. 103, no. 1, p. 78-98.
- Edwards, B., Fäh, D., and Giardini, D., 2011, Attenuation of seismic shear wave energy in Switzerland: *Geophysical Journal International*, v. 185, no. 2, p. 967-984.
- Eriksson, E., 1971, Compartment Models and Reservoir Theory: *Annual Review of Ecology and Systematics*, v. 2, no. 1, p. 67-84.
- Fäh, D., Giardini, D., Kästli, P., Deichmann, N., Gisler, M., Schwarz-Zanetti, G., Alvarez-Rubio, S., Sellami, S., Edwards, B., Allmann, B., Bethmann, F., Wössner, J., Gassner-Stamm, G., Fritsche, S., Eberhard, D., 2011, ECOS-09 Earthquake Catalogue of Switzerland Release

- 2011 Report and Database. Public catalogue, 17. 4. 2011: Swiss Seismological Service ETH Zurich, Report SED/RISK/R/001/20110417.
- Fischer, L., Eisenbeiss, H., Kääb, A., Huggel, C., and Haeberli, W., 2011, Monitoring topographic changes in a periglacial high-mountain face using high-resolution DTMs, Monte Rosa East Face, Italian Alps: *Permafrost and Periglacial Processes*, v. 22, no. 2, 140-152.
- Fischer, L., Purves, R. S., Huggel, C., Noetzli, J., and Haeberli, W., 2012, On the influence of topographic, geological and cryospheric factors on rock avalanches and rockfalls in high-mountain areas: *Natural Hazards and Earth System Science*, v. 12, p. 241-254.
- Frei, C., and Schar, C., 2001, Detection probability of trends in rare events: Theory and application to heavy precipitation in the Alpine region: *Journal of Climate*, v. 14, no. 7, p. 1568-1584.
- Fryirs, K., 2013, (Dis)Connectivity in catchment sediment cascades: a fresh look at the sediment delivery problem: *Earth Surface Processes and Landforms*, v. 38, no. 1, p. 30-46.
- Fryirs, K., and Brierley, G. J., 2001, Variability in sediment delivery and storage along river courses in Bega catchment, NSW, Australia: implications for geomorphic river recovery: *Geomorphology*, v. 38, no. 3-4, p. 237-265.
- Gabet, E. J., 2000, Gopher bioturbation: field evidence for non-linear hillslope diffusion: *Earth Surface Processes and Landforms*, v. 25, no. 13, p. 1419-1428.
- Gabet, E. J., 2007, A theoretical model coupling chemical weathering and physical erosion in landslide-dominated landscapes: *Earth and Planetary Science Letters*, v. 264, no. 1-2, p. 259-265.
- Gabet, E. J., Burbank, D.W., Pratt-Sitaula, B., Putkonen, J., and Bookhagen, B., 2008, Modern erosion rates in the High Himalayas of Nepal: *Earth and Planetary Science Letters*, v. 237, no. 3-4, p. 482-494.
- Gabus, J. H., Weidmann, M., Bugnon, P.-C., Burri, M., Sartori, M., Marthaler, M., 2008, Feuille 1287 Sierre. - Atlas géol. Suisse 1:25 000, Notice expl. 111.
- Gardner, J., 1970, Rockfall: a geomorphic process in high mountain terrain. *The Albertan Geographer*, v.6, p. 15-20.
- Gischig, V. S., Moore, J. R., Evans, K. F., Amann, F., and Loew, S., 2011, Thermomechanical forcing of deep rock slope deformation: 2. The Randa rock slope instability: *Journal of Geophysical Research*, v. 116, no. F4, p. F04011.
- Gray, J. R., 2008, Suspended-Sediment Transport Measurement, *Encyclopedia of Water Science*, Second Edition, Volume I-II, Taylor & Francis Group, p. 1204-1208.
- Gray, J. R., Laronne, J.B., and Marr, J.D.G., 2010, Bedload-Surrogate Monitoring Technologies, *USGS Scientific Investigations Report 2010-5091*.
- Gruber, S., Hoelzle, M., and Haeberli, W., 2004, Permafrost thaw and destabilization of Alpine rock walls in the hot summer of 2003: *Geophysical Research Letters*, v. 31, no. 13, p. L13504.
- Gruen, A., and Akca, D., 2005, Least squares 3D surface and curve matching: *ISPRS Journal of Photogrammetry and Remote Sensing*, v. 31, no. 3B, p. 151-174.
- Gutenberg, B. and Richter, C. F., 1949, *Seismicity of the earth and associated phenomena*: Princeton University Press, Princeton, 303 p.
- Guzzetti, F., Carrara, A., Cardinali, M., Reichenbach P., 1999, Landslide hazard evaluation: a review of current techniques and their application in a multi-scale study, Central Italy. *Geomorphology*, v. 31, p. 181-216.
- Guzzetti, F., Ardizzone, F., Cardinali, M., Rossi, M., and Valigi, D., 2009, Landslide volumes and landslide mobilization rates in Umbria, central Italy: *Earth and Planetary Science Letters*, v. 279, no. 3-4, p. 222-229.

- Guzzetti, F., Reichenbach, P., Wieczorek, G. F., 2003, Rockfall hazard and risk assessment in the Yosemite Valley, California, USA. *Natural Hazards and Earth Systems Science*, v. 3, p. 491-503.
- Guzzetti, F., Malamud, B.D., Turcote, D.L., and Reichenbach, P., 2002, Power-law correlations of landslide areas in Central Italy: *Earth and Planetary Science Letters*, v. 195, p. 169-183.
- Guzzetti, F., Peruccacci, S., Rossi, M., and Stark, C., 2008, The rainfall intensity–duration control of shallow landslides and debris flows: an update: *Landslides*, v. 5, no. 1, p. 3-17.
- Haeberli, W., Guodong, C., Gorbunov, A. P., and Harris, S. A., 1993, Mountain permafrost and climatic change: *Permafrost and Periglacial Processes*, v. 4, no. 2, p. 165-174.
- Haeberli, W., Rickenmann, D., Zimmermann, M., and Rössli, U., 1990, Investigation of 1987 Debris Flows in the Swiss Alps: General Concept and Geophysical Soundings: IAHS Publication, v. 194, p. 303-310.
- Haeberli, W., Wegmann, M., and Vonder Mühll, D., 1997, Slope stability problems related to glacier shrinkage and permafrost degradation in the Alps.: *Ecologiae Geologicae Helvetiae*, v. 90, p. 407-414.
- Hales, T. C., and Roering, J. J., 2007, Climatic controls on frost cracking and implications for the evolution of bedrock landscapes: *J. Geophys. Res.*, v. 112, no. F2, p. F02033.
- Hantz, D., Vengeon, J.M., and Dussauge-Peisser, C., 2003, An historical, geomechanical and probabilistic approach to rock-fall hazard assessment: *Natural Hazards and Earth Systems Science*, v. 3, p. 693-701.
- Harris, C., Vonder Mühll, D., Isaksen, K., Haeberli, W., Sollid, J. L., King, L., Holmlund, P., Dramis, F., Guglielmin, M., and Palacios, D., 2003, Warming permafrost in European mountains: *Global and Planetary Change*, v. 39, no. 3–4, p. 215-225.
- Harrison, S., 2001, On Reductionism and Emergence in Geomorphology: *Transactions of the Institute of British Geographers*, v. 26, no. 3, p. 327-339.
- Harvey, A. M., 2001, Coupling between hillslopes and channels in upland fluvial systems: implications for landscape sensitivity, illustrated from the Howgill Fells, northwest England: *Catena*, v. 42, no. 2-4, p. 225-250.
- Harvey, A. M., 2002, Effective timescales of coupling within fluvial systems: *Geomorphology*, v. 44, no. 3-4, p. 175-201.
- Harvey, A.M., 2012, The coupling status of alluvial fans and debris cones: a review and synthesis: *Earth Surface Processes and Landforms*, v. 37, no. 1, p. 64-76.
- Hergarten, S., 2002, Landslides, sandpiles, and self-organized criticality: *Natural Hazards and Earth Systems Science*, v. 3, p. 505-514.
- Hewawasam, T., von Blanckenburg, F., Schaller, M., and Kubik, P., 2003, Increase of human over natural erosion rates in tropical highlands constrained by cosmogenic nuclides: *Geology*, v. 31, no. 7, p. 597-600.
- Hill, B. M., 1975, *Annals of Statistics*, v. 3, 1163p..
- Hovius, N., Stark, C. P., and Allen, P. A., 1997, Sediment flux from a mountain belt derived by landslide mapping: *Geology*, v. 25, no. 3, p. 231-234.
- Hovius N, Stark CP, Hao-Tsu C, Jiun-Chuan L. 2000. Supply and removal of sediment in a landslide-dominated mountain belt: central range, Taiwan. *Journal of Geology* 108: 73–89.
- Howard, A. D., 1994, A detachment-limited model of drainage basin evolution: *Water Resources Research*, v. 30, no. 7, p. 2261-2285.
- Hungr, O., Evans, S.G., and Hazzard, J., 1999, Magnitude and frequency of rock falls along the main transportation corridors of southwestern British Columbia: *Canadian Geotechnical Journal*, v. 36, p. 224-238.

- Hungr, O., McDougall, S., Wise, M., and Cullen, M., 2008, Magnitude–frequency relationships of debris flows and debris avalanches in relation to slope relief: *Geomorphology*, v. 96, no. 3-4, p. 355-365.
- Hürlimann, M., Rickenmann, D., and Graf, C., 2003, Field and monitoring data of debris-flow events in the Swiss Alps: *Canadian Geotechnical Journal*, v. 40, p. 161-175.
- Istanbulluoglu, E., and Bras, R. L., 2005, Vegetation-modulated landscape evolution: Effects of vegetation on landscape processes, drainage density, and topography: *Journal of Geophysical Research*, v. 110, no. F2, p. F02012.
- Iverson, R., Reid, M., and Lahusen, R., 1997, Debris flow mobilization from Landslides: *Annual Review of Earth and Planetary Sciences*, v. 25, no. 1, p. 85-138.
- Jaboyedoff, M., Baillifard, F., Bardou, E., and Girod, F., 2004, The effect of weathering on Alpine rock instability: *Quarterly Journal of Engineering Geology and Hydrogeology*, v. 37, no. 2, p. 95-103.
- Jakob, M., Bovis, M., and Oden, M., 2005, The significance of channel recharge rates for estimating debris-flow magnitude and frequency: *Earth Surface Processes and Landforms*, v. 30, no. 6, p. 755-766.
- Jakob, M., and Hungr, O., 2005, *Debris-flow hazards and related phenomena*, Berlin, New York, Springer, 170 p.
- Jerolmack, D. J., and Paola, C., 2010, Shredding of environmental signals by sediment transport: *Geophys. Res. Lett.*, v. 37, no. 19, p. L19401.
- Jomelli, V., Pech, V., Chochillon, C., and Brunstein, D., 2004, Geomorphic Variations of Debris Flows and Recent Climatic Change in the French Alps: *Climatic Change*, v. 64, no. 1, p. 77-102.
- Katz, O., and Aharonov, E., 2006, Landslides in vibrating sand box: What controls types of slope failure and frequency magnitude relations?: *Earth and Planetary Science Letters*, v. 247, no. 3-4, p. 280-294.
- Keefer, D., K., 1984, Landslides caused by earthquakes: *Geological Society of America Bulletin*, v. 95, no. 4, p. 406-421.
- Keller, F., and Gubler, H.U., Interaction between snow cover and high mountain permafrost, Murtèl-Corvatsch, Swiss Alps. , *in* *Proceedings VI. International Conference on Permafrost*, Beijing, 1993, South China University of Technology Press.
- Kirchner, J. W., 2006, Getting the right answers for the right reasons: Linking measurements, analyses, and models to advance the science of hydrology: *Water Resources Research*, v. 42, no. 3, p. W03S04.
- Kirchner, J.W., 2009, Catchments as simple dynamical systems: Catchment characterization, rainfall-runoff modeling, and doing hydrology backward: *Water Resources Research*, v. 45, no. 2, p. W02429.
- Kirchner, J. W., Finkel, R. C., Riebe, C. S., Granger, D. E., Clayton, J. L., King, J. G., and Megahan, W. F., 2001, Mountain erosion over 10 yr, 10 k.y., and 10 m.y. time scales: *Geology*, v. 29, no. 7, p. 591-594.
- Kokusho, T., and Ishizawa, T., 2007, Energy Approach to Earthquake-Induced Slope Failures and Its Implications: *Journal of Geotechnical and Geoenvironmental Engineering*, v. 133, no. 7, p. 828-840.
- Kokusho, T., Ishizawa, T., and Koizumi, K., 2011, Energy approach to seismically induced slope failure and its application to case histories: *Engineering Geology*, v. 122, no. 1–2, p. 115-128.
- Koppes, M. N., and Montgomery, D. R., 2009, The relative efficacy of fluvial and glacial erosion over modern to orogenic timescales: *Nature Geoscience*, v. 2, no. 9, p. 644-647.

- Korup, O., 2006, Rock-slope failure and the river long profile: *Geology*, v. 34, no. 1, p. 45-48.
- Korup, O., 2010, Earthquake-triggered landslides- Spatial patterns and impacts: CCES: Coupled Seismogenic Geohazards in Alpine Regions (COGEAR), v. Module 1a- Report.
- Korup, O., Schlunegger, F., 2007. Bedrock landsliding, river incision, and transience of geomorphic hillslope-channel coupling: evidence from inner gorges in the Swiss Alps. *Journal of Geophysical Research* 112, F03027.
- Korup, O., Densmore, A. L., and Schlunegger, F., 2010, The role of landslides in mountain range evolution: *Geomorphology*, v. 120, no. 1-2, p. 77-90.
- Korup, O., Görüm, T., and Hayakawa, Y., 2012, Without power? Landslide inventories in the face of climate change: *Earth Surface Processes and Landforms*, v. 37, no. 1, p. 92-99.
- Korup, O., McSaveney, M. J., and Davies, T. R. H., 2004, Sediment generation and delivery from large historic landslides in the Southern Alps, New Zealand: *Geomorphology*, v. 61, no. 1-2, p. 189-207.
- Lancaster, S. T., and Casebeer, N. E., 2007, Sediment storage and evacuation in headwater valleys at the transition between debris-flow and fluvial processes: *Geology*, v. 35, no. 11, p. 1027-1030.
- Lane, S. N., Westaway, R. M., and Murray H. D., 2003, Estimation of erosion and deposition volumes in a large, gravel-bed, braided river using synoptic remote sensing: *Earth Surface Processes and Landforms*, v. 28, no. 3, p. 249-271.
- Larsen, I. J., Montgomery, D. R., and Korup, O., 2010, Landslide erosion controlled by hillslope material: *Nature Geoscience*, v. 3, no. 4, p. 247-251.
- Larsen, I. J., Pederson, J. L., and Schmidt, J. C., 2006, Geologic versus wildfire controls on hillslope processes and debris flow initiation in the Green River canyons of Dinosaur National Monument: *Geomorphology*, v. 81, no. 1, p. 114-127.
- Li, C., Ma, T., Zhu, X., and Li, W., 2011, The power-law relationship between landslide occurrence and rainfall level: *Geomorphology*, v. 130, no. 3-4, p. 221-229.
- Lichtenhahn, C., 1971, Zwei Betonmauern: Die Geschieberückhaltesperre am Illgraben (Wallis) und die Staumauer des Hochwasserschutzbeckens an der Orlegna im Bergell (Graubünden). *International Symposium Interpraevent*. Volume 3, p. 451-456.
- Lim, M., Rosser, N. J., Allison, R. J., and Petley, D. N., 2010, Erosional processes in the hard rock coastal cliffs at Staithes, North Yorkshire: *Geomorphology*, v. 114, no. 1-2, p. 12-21.
- Lisle, T. E., and Church, M., 2002, Sediment transport-storage relations for degrading, gravel bed channels: *Water Resources Research*, v. 38, no. 11, 1219.
- Lu, H., Moran, C. J., and Prosser, I. P., 2006, Modelling sediment delivery ratio over the Murray Darling Basin: *Environmental Modelling & Software*, v. 21, no. 9, p. 1297-1308.
- Lu, H., Moran, C. J., and Sivapalan, M., 2005, A theoretical exploration of catchment-scale sediment delivery: *Water Resources Research*, v. 41, no. 9.
- Malamud, B. D., Turcotte, D. L., Guzzetti, F., and Reichenbach, P., 2004, Landslide inventories and their statistical properties: *Earth Surface Processes and Landforms*, v. 29, no. 6, p. 687-711.
- Malet, J.-P., van Asch, Th. W. J., van Beek, R., and Maquaire, O., 2005, Forecasting the behaviour of complex landslides with a spatially distributed hydrological model: *Natural Hazards and Earth Systems Science*, v. 5, p. 71-85.
- Malmon, D. V., Dunne, T., and Reneau, S.L., 2003, Stochastic Theory of Particle Trajectories through Alluvial Valley Floors: *The Journal of Geology*, v. 111, no. 5, p. 525-542.
- Marchi, L., Arattano, M., and Deganutti, A. M., 2002, Ten years of debris-flow monitoring in the Moscardo Torrent (Italian Alps): *Geomorphology*, v. 46, no. 1-2, p. 1-17.

- Matsuoka, N., and Sakai, H., 1999, Rockfall activity from an alpine cliff during thawing periods: *Geomorphology*, v. 28, no. 3–4, p. 309-328.
- McArdell, B. W., Bartelt, P., and Kowalski, J., 2007, Field observations of basal forces and fluid pore pressure in a debris flow: *Geophysical Research Letters*, v. 34, no. 7, p. L07406.
- McArdell, B. W., Berger, C., Schlunegger, F., 2009, Sediment transfer processes in a debris-flow dominated catchment in the Swiss Alps: *EOS Transactions, AGU*, v. 90(52), Abstract EP54A-03.
- McArdell, B. W., and Graf, C., 2009, Field observations of debris flow properties at the Illgraben catchment, Switzerland., *in* *Proceedings Geological Society of America Annual Meeting 2009*, p. 240-243.
- Meunier, P., Hovius, N., and Haines, A. J., 2007, Regional patterns of earthquake-triggered landslides and their relation to ground motion: *Geophysical Research Letters*, v. 34, no. 20, p. L20408.
- Molini, A., Katul, G. G., and Porporato, A., 2011, Maximum discharge from snowmelt in a changing climate: *Geophysical Research Letters*, v. 38, no. 5, p. L05402.
- Molnar, P., Burlando, P., Kirsch, J. and Hinz, E., 2006, Model investigations of the effects of land-use changes and forest damages on erosion in mountainous environments: *IAHS Publications*, v. 306, p. 589-600.
- Moore, J. R., Sanders, J. W., Dietrich, W. E., and Glaser, S. D., 2009, Influence of rock mass strength on the erosion rate of alpine cliffs: *Earth Surface Processes and Landforms*, v. 34, no. 10, p. 1339-1352.
- Nakamura, F., and Kikuchi, S.I., 1996, Some methodological developments in the analysis of sediment transport processes using age distribution of floodplain deposits: *Geomorphology*, v. 16, no. 2, p. 139-145.
- Noetzli, J., Gruber, S., Kohl, T., Salzmänn, N., and Haeberli, W., 2007, Three-dimensional distribution and evolution of permafrost temperatures in idealized high-mountain topography: *Journal of Geophysical Research*, v. 112, no. F2, p. F02S13.
- Nydegger, C., 2008, Fluvial system dynamics in steep headwater basins: A study on the Illgraben catchment (VS), Masters thesis: ETH Zurich, 96 p.
- Pelletier, J. D., Malamud, B. D., Blodgett, T., and Turcotte, D. L., 1997, Scale-invariance of soil moisture variability and its implications for the frequency-size distribution of landslides: *Engineering Geology*, v. 48, no. 3-4, p. 255-268.
- Perona, P., Porporato, A., and Ridolfi, L., 2007, A stochastic process for the interannual snow storage and melting dynamics: *Journal of Geophysical Research*, v. 112, no. D8, p. D08107.
- Phillips, J., 2003, Alluvial storage and the long-term stability of sediment yields: *Basin Research*, v. 15, no. 2, p. 153-163.
- Phillips, J. D., 2006, Evolutionary geomorphology: thresholds and nonlinearity in landform response to environmental change: *Hydrology and Earth System Sciences*, v. 10, no. 5, p. 731-742.
- Poggi, V., Edwards, B., and Fäh, D., 2011, Derivation of a Reference Shear-Wave Velocity Model from Empirical Site Amplification: *Bulletin of the Seismological Society of America*, v. 101, no. 1, p. 258-274.
- Priestley, C. H. B., Taylor, R. J., 1972, On the assessment of surface heat flux and evaporation using large-scale parameters: *Monthly Weather Review*, v. 100, p. 81-92.
- Ravanel, L., and Deline, P., 2011, Climate influence on rockfalls in high-Alpine steep rockwalls: The north side of the Aiguilles de Chamonix (Mont Blanc massif) since the end of the 'Little Ice Age': *The Holocene*, v. 21, no. 2, p. 357-365.

- Rebetez, M., Lugon, R., Baeriswyl, P.-A., 1997, Climatic change and debris flows in high mountain regions: The case study of the Ritigraben Torrent (Swiss Alps): *Climatic Change*, v. 36, p. 371-389.
- Rhyner, J., McArdell, B.W., Badoux, A., Kuntner, R., Teyssie, P., 2005, Technischer Bericht Notfallkonzept Illgraben: Technical Report, WSL and Teyssie & Candolfi.
- Rödder, T., and Kneisel, C., 2012, Influence of snow cover and grain size on the ground thermal regime in the discontinuous permafrost zone, Swiss Alps: *Geomorphology*, v. 175–176, p. 176-189.
- Roering, J. J., Kirchner, J. W., and Dietrich, W. E., 1999, Evidence for Nonlinear, Diffusive Sediment Transport on hillslopes and Implications For Landscape Morphology: *Water Resources Research*, v. 35, no. 3, p. 853-870.
- Rousseau N. 1999. Study of seismic signals associated with rockfalls at 2 sites on the Reunion island (Mahavel Cascade and Souffrière cavity). IPG: Paris.
- Rosser, N., Lim, M., Petley, D., Dunning, S., and Allison, R., 2007, Patterns of precursory rockfall prior to slope failure: *Journal of Geophysical Research*, v. 112, no. F4, p. F04014.
- Rosser, N. J., 2010, Landslides and Rockfalls, *in* Burt, T., Allison, R., ed., *Sediment Cascades, An Integrated Approach*, Wiley-Blackwell, p. 55-88.
- Rossi, M., Witt, A., Guzzetti, F., Malamud, B. D., and Peruccacci, S., 2010, Analysis of historical landslide time series in the Emilia-Romagna region, northern Italy: *Earth Surface Processes and Landforms*, v. 35, no. 10, p. 1123-1137.
- Schaller, M., von Blanckenburg, F., Hovius, N., and Kubik, P. W., 2001, Large-scale erosion rates from in situ-produced cosmogenic nuclides in European river sediments: *Earth and Planetary Science Letters*, v. 188, no. 3-4, p. 441-458.
- Scherrer, S. C., Appenzeller, C., and Laternser, M., 2004, Trends in Swiss Alpine snow days: The role of local- and large-scale climate variability: *Geophysical Research Letters*, v. 31, no. 13, p. L13215.
- Schlögel, R., Torgoev, I., De Marneffe, C., and Havenith, H.-B., 2011, Evidence of a changing size–frequency distribution of landslides in the Kyrgyz Tien Shan, Central Asia: *Earth Surface Processes and Landforms*, v. 36, no. 12, p. 1658-1669.
- Schlunegger, F., Badoux, A., McArdell, B. W., Gwerder, C., Schnydrig, D., Rieke-Zapp, D., and Molnar, P., 2009, Limits of sediment transfer in an alpine debris-flow catchment, Illgraben, Switzerland: *Quaternary Science Reviews*, v. 28, no. 11-12, p. 1097-1105.
- Schlunegger, F., Norton, K., Caduff, R., *in press*, Hillslope processes in temperate environments, *in* Marston, R., Stoffel, M. , ed., *Treatise in Geomorphology*, Vol. 3: Mountain and Hillslope Geomorphology: London, Elsevier.
- Schumm, S. A., 1979, Geomorphic Thresholds: The Concept and Its Applications: *Transactions of the Institute of British Geographers*, v. 4, no. 4, p. 485-515.
- Schürch, P., 2011, Debris-flow erosion and deposition dynamics. Doctoral thesis, Durham University. Available at Durham E-Theses Online: <http://etheses.dur.ac.uk/3395/>
- Schürch, P., Densmore, A. L., Rosser, N. J., Lim, M., and McArdell, B. W., 2011, Detection of surface change in complex topography using terrestrial laser scanning: application to the Illgraben debris-flow channel: *Earth Surface Processes and Landforms*, v. 36, no. 14, p. 1847-1859.
- Schürch, P., Densmore, A. L., Rosser, N. J., and McArdell, B. W., 2011, Dynamic controls on erosion and deposition on debris-flow fans: *Geology*, v. 39, no. 9, p. 827-830.
- Schwab, M., Rieke-Zapp, D., Schneider, H., Liniger, M., and Schlunegger, F., 2008, Landsliding and sediment flux in the Central Swiss Alps: A photogrammetric study of the Schimbrig landslide, Entlebuch: *Geomorphology*, v. 97, no. 3-4, p. 392-406.

- Schwab, M., Schlunegger, F., Schneider, H., Stöckli, G., Rieke-Zapp, D., 2009, Contrasting sediment flux in Val Lumnezia, (Graubünden, Eastern Swiss Alps) and implications for landscape development.: *Swiss Journal of Geoscience*, v. 102, p. 211-222.
- Silverman, B. W., 1981, Using Kernel Density Estimates to Investigate Multimodality: *Journal of the Royal Statistical Society. Series B (Methodological)*, v. 43, no. 1, p. 97-99.
- Simonett, D. S., 1967, Landslide distribution and earthquakes in the Bewani and Torricelli Mountains, New Guinea., *in* Jennings, J. N., Mabbutt, J.A., ed., *Landform Studies from Australia and New Guinea*: Cambridge, Cambridge University Press, p. 64-84.
- Slaymaker, O., 1991, Mountain geomorphology: A theoretical framework for measurement programmes: *Catena*, v. 18, no. 5, p. 427-437.
- Stark, C. P., and Guzzetti, F., 2009, Landslide rupture and the probability distribution of mobilized debris volumes: *Journal of Geophysical Research*, v. 114, F00A02.
- Stark, C. P., and Hovius, N., 2001, The characterization of landslide size distributions: *Geophysical Research Letters*, v. 28, no. 6, p. 1091-1094.
- Stedinger, J. R., Vogel, R.M., and Foufoula-Georgiou, E., 1993, Frequency analysis of extreme events, *in* Maidment, D., ed., *Handbook of Applied Hydrology*: New York, McGraw Hill, p. 18.11-18.65.
- Stock, J. D., and Dietrich, W. E., 2006, Erosion of steepland valleys by debris flows: *Geological Society of America Bulletin*, v. 118, no. 9-10, p. 1125-1148.
- Stoffel, M., 2010, Magnitude–frequency relationships of debris flows — A case study based on field surveys and tree-ring records: *Geomorphology*, v. 116, no. 1–2, p. 67-76.
- Stoffel, M., Conus, D., Grichting, M. A., Lièvre, I., and Maître, G., 2008, Unraveling the patterns of late Holocene debris-flow activity on a cone in the Swiss Alps: Chronology, environment and implications for the future: *Global and Planetary Change*, v. 60, no. 3–4, p. 222-234.
- Stull, R. B., 1988, *An Introduction to Boundary Layer Meteorology*, Dordrecht, Kluwer Academic Publishers, 666 p.
- Sugai, T., Ohmori, H., and Hirano, M., 1994, Rock control on magnitude–frequency distribution of landslides: *Transactions of the Japanese Geomorphological Union*, v. 15, p. 233-351.
- Syvitski, J. P. M., Kettner, A. J., Overeem, I., Hutton, E. W. H., Hannon, M. T., Brakenridge, G. R., Day, J., Vorosmarty, C., Saito, Y., Giosan, L., and Nicholls, R. J., 2009, Sinking deltas due to human activities: *Nature Geoscience*, v. 2, no. 10, p. 681-686.
- Syvitski, J. P. M., Vörösmarty, C. J., Kettner, A. J., and Green, P., 2005, Impact of Humans on the Flux of Terrestrial Sediment to the Global Coastal Ocean: *Science*, v. 308, no. 5720, p. 376-380.
- Taylor, J. R., 1997, *An Introduction to Error Analysis: the Study of Uncertainties in Physical Measurements*, Sausalito, California, University Science Books.
- Tipper, J. C., 2007, The 'stochastic river': The use of budget-capacity modelling as a basis for predicting long-term properties of stratigraphic successions: *Sedimentary Geology*, v. 202, no. 1-2, p. 269-280.
- Tucker, G. L. S., Gasparini N., and Bras R., 2001, The Channel-Hillslope Integrated Landscape Development model (CHILD), *in* Harmon, R., Doe III, WW, ed., *Landscape Erosion and Evolution Modeling*.: New York, Kluwer Academic Publishers.
- Tucker, G. E., and Hancock, G. R., 2010, Modelling landscape evolution: *Earth Surface Processes and Landforms*, v. 35, no. 1, p. 28-50.
- Turowski, J. M., Rickenmann, D., and Dadson, S. J., 2010, The partitioning of the total sediment load of a river into suspended load and bedload: a review of empirical data: *Sedimentology*, v. 57, no. 4, p. 1126-1146.

- Van De Wiel, M. J., and Coulthard, T. J., 2010, Self-organized criticality in river basins: Challenging sedimentary records of environmental change: *Geology*, v. 38, no. 1, p. 87-90.
- Van De Wiel, M. J., Coulthard, T. J., Macklin, M. G., and Lewin, J., 2011, Modelling the response of river systems to environmental change: Progress, problems and prospects for palaeo-environmental reconstructions: *Earth-Science Reviews*, v. 104, no. 1–3, p. 167-185.
- Van Den Eeckhaut, M., Poesen, J., Govers, G., Verstraeten, G., and Demoulin, A., 2007, Characteristics of the size distribution of recent and historical landslides in a populated hilly region: *Earth and Planetary Science Letters*, v. 256, no. 3–4, p. 588-603.
- von Blanckenburg, F., 2005, The control mechanisms of erosion and weathering at basin scale from cosmogenic nuclides in river sediment: *Earth and Planetary Science Letters*, v. 237, no. 3-4, p. 462-479.
- Waugh, D., 2000, *Geography: An Integrated Approach*, Nelson Thornes, 655 p.:
- Whipple, K. X., 2004, Bedrock rivers and the geomorphology of active orogens: *Annual Review of Earth and Planetary Sciences*, v. 32, p. 151-185.
- Whipple, K. X., and Tucker, G. E., 1999, Dynamics of the stream-power river incision model: Implications for height limits of mountain ranges, landscape response timescales, and research needs: *Journal of Geophysical Research*, v. 104, no. B8, p. 17661-17674.
- Wieczorek, G., and Glade, T., 2005, Climatic factors influencing occurrence of debris flows, *Debris-flow Hazards and Related Phenomena*, Springer Berlin Heidelberg, p. 325-362.
- Wiemer, S., Giardini, D., Fäh, D., Deichmann, N., and Sellami, S., 2009, Probabilistic seismic hazard assessment of Switzerland: best estimates and uncertainties: *Journal of Seismology*, v. 13, no. 4, p. 449-478.
- Wittmann, H., von Blanckenburg, F., Kruesmann, T., Norton, K. P., and Kubik, P. W., 2007, Relation between rock uplift and denudation from cosmogenic nuclides in river sediment in the Central Alps of Switzerland: *Journal of Geophysical Research*, v. 112, no. F4, F04010.
- Zhang, L., 2005, Automatic digital surface model (DSM) generation from linear array images, Report no 88, Institute of Geodesy and Photogrammetry, ETH Zurich, Switzerland.
- Zhang L, and Gruen. A., 2006, Multi-image matching for DSM generation from IKONOS imagery.: *ISPRS Journal of Photogrammetry and Remote Sensing*, v. 60, no. 3, p. 195-211.
- Zimmermann, M., Haeberli, W., 1992, 'Climatic Change and Debris Flow Activity in High-Mountain Areas – A Case Study in the Swiss Alps', *Greenhouse-Impact on Cold-Climate Ecosystems and Landscapes: Catena Supplement*, v. 22, p. 59-72.

Appendix A

Supplementary material for Chapter 2

A.1. Aerial photographs and camera calibration certificates

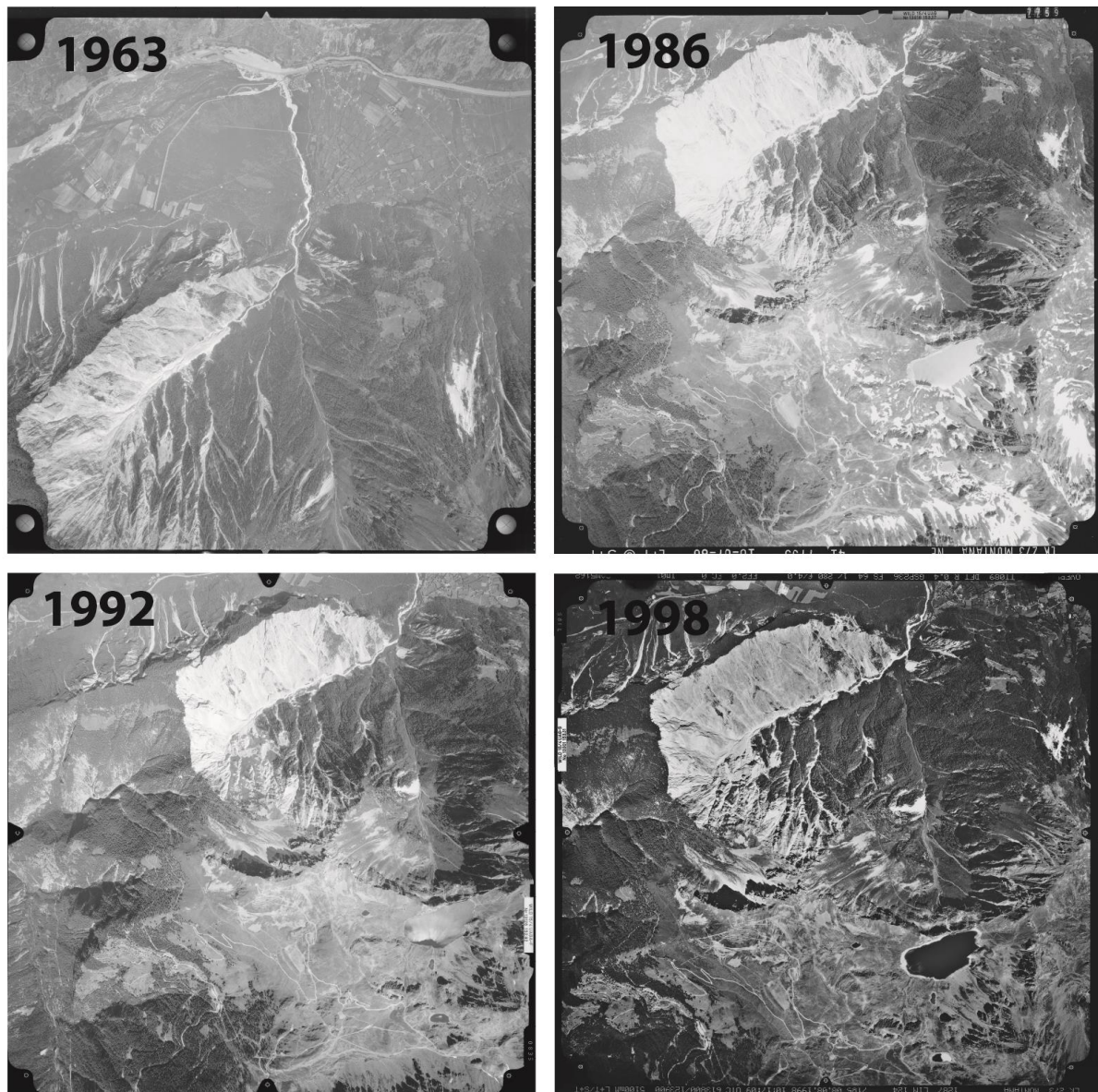


Figure A.1 – One of each aerial photograph stereopair used in the photogrammetric procedure to extract DEMs as detailed in Chapter 2.

Figure A.2– Next 17 pages – The 4 camera calibration certificates for cameras used to acquire the photographs in Figure A.1.



Calibration Certificate

Wild Camera No. 11.5 Ag. 29
Lens No. 29

**Lens Cone**

Type: **RC5**
 No.: **11.5 Ag. 29**
 Size: **18 x 18 cm**

Lens Calibration date: 26.2.63

Type: **Aviagon**
 No.: **29**
 f = **115 mm**
 max. aperture: **f:5.6**

Resolving Power (Lines per millimetre)

High contrast and max. aperture **f:5.6**

Film: **Agfa Isopan IFF 13 Planfilm**

Glass plate:

	0°	5°	10°	15°	20°	25°	30°	35°	40°	45°	50°	55°	60°
rad.	70	70	69	67	65	51	54	64	38	28			
tang.	70	70	67	65	62	64	58	52	37	28			

rad.													
tang.													

Distortion in millimetres

The given distortion is the arithmetic mean between the four half-diagonals. Distortion positive away from centre. **Goniometer measurements made without filter.**

Calibrated focal length: **115.29 mm**

Radius	20	40	60	80	90	100	110	114
Distortion	+0.007	+0.008	+0.003	-0.004	-0.008	-0.006	+0.001	+0.004

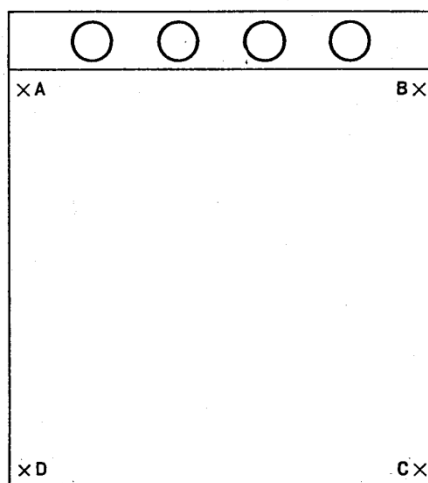
The displacement of the principal point of autocollimation from the intersection of the diagonals is within **0.02 mm**.

Date of Dispatch: **4.3.63**

WILD

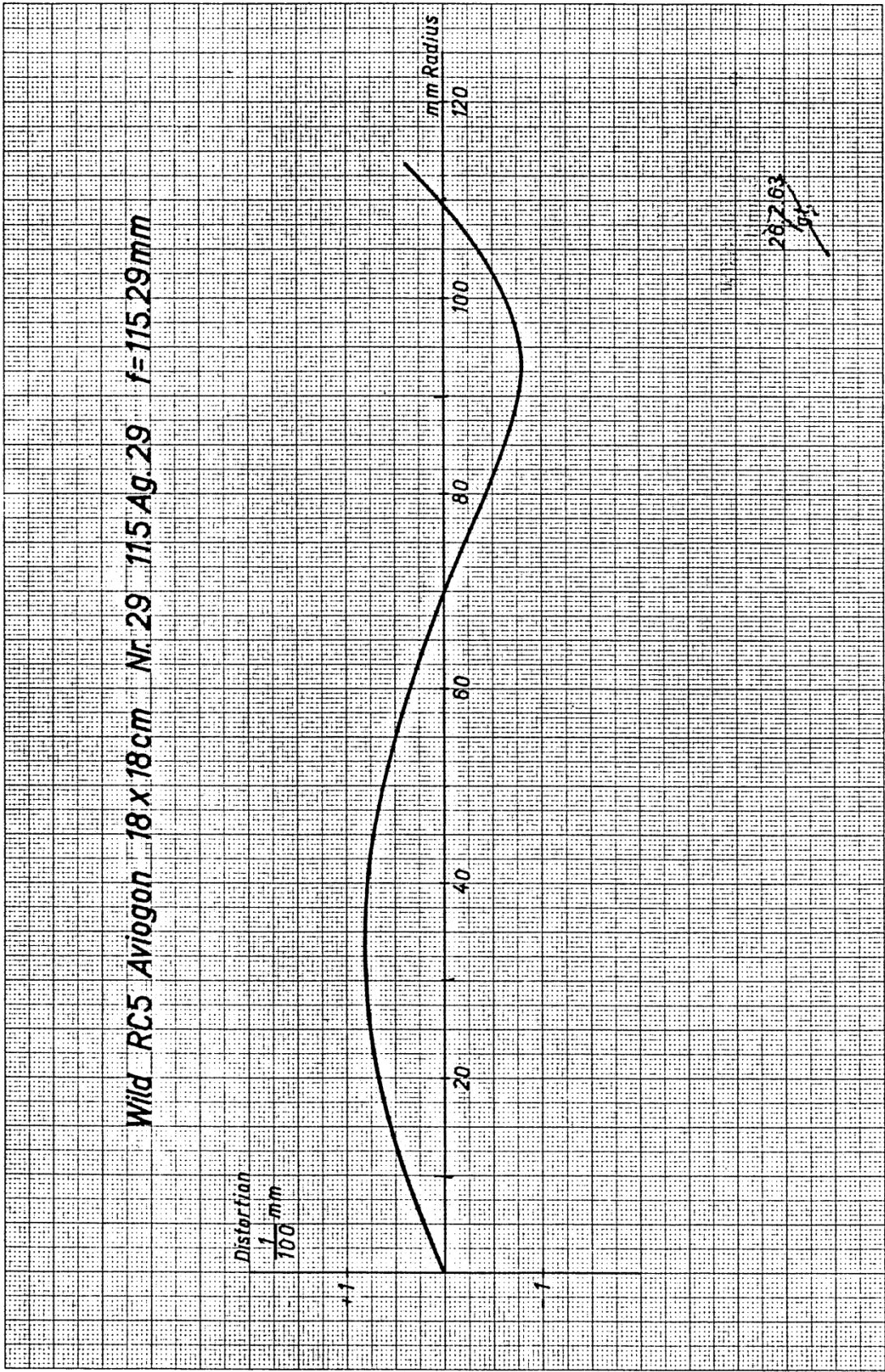
LENS CONE**LENS****CALIBRATION DATE: 26.2.63**Type: **RC5**Type: **Aviagon**No.: **11.5 Ag. 29**No.: **29**Size: **18 x 18 cm**f = **115 mm**

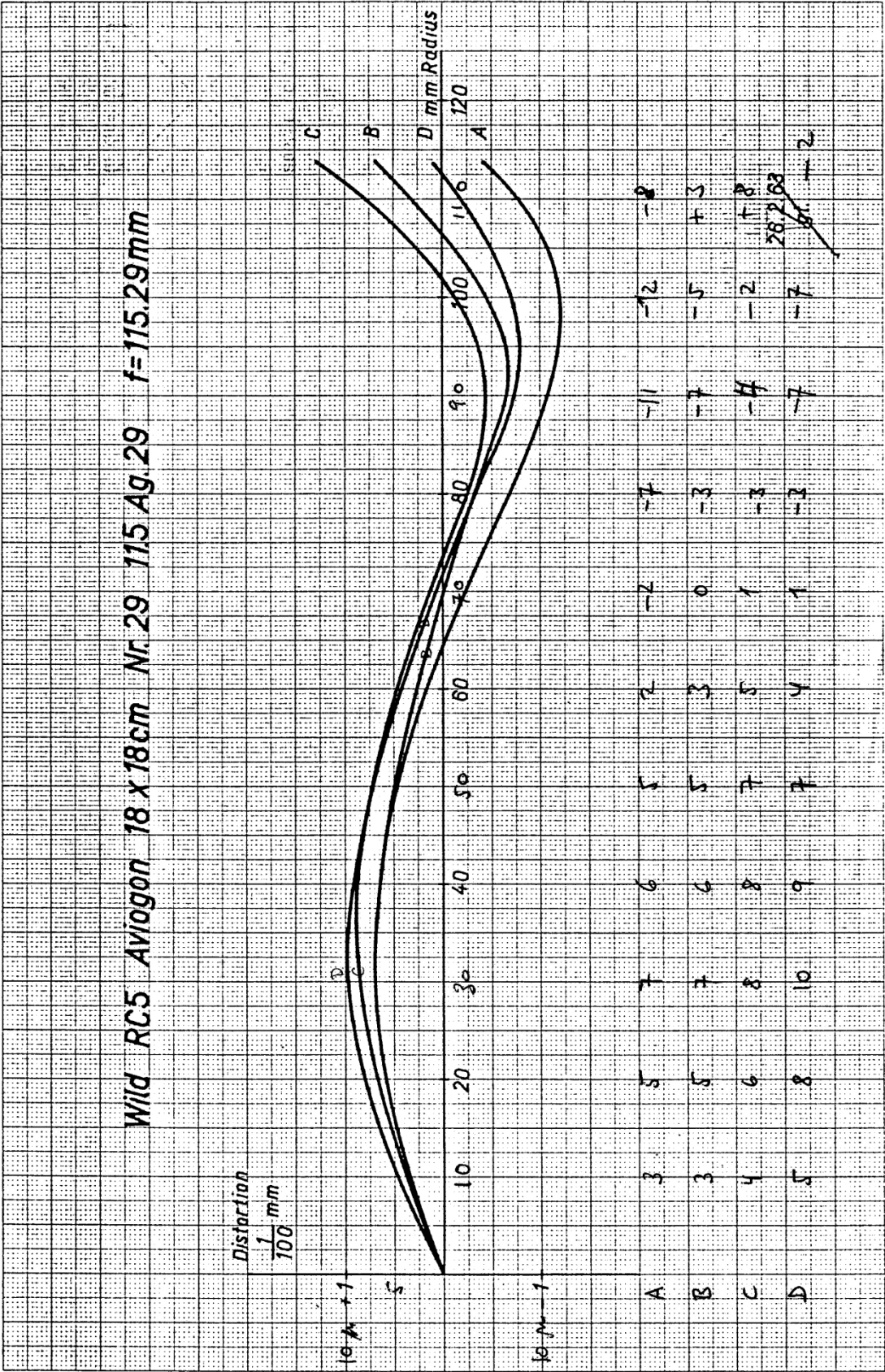
Seen on camera from top



A	—	B	=	163.993
B	—	C	=	163.997
C	—	D	=	163.992
D	—	A	=	163.998
A	—	C	=	231.929
B	—	D	=	231.917

 WILD HEINRICH
 LENS





CAMERA CALIBRATION CERTIFICATE

CAMERA TYPE : RC10

LENS TYPE : 15/4 UAG

LENS NO. : 13018

CALIBRATION DATE : 14.05.85

WILD HEERBRUGG LTD



CAMERA CALIBRATION

CAMERA: RC10 LENS: 15/4 UAG NO.: 13018 CALIBRATION DATE: 14.05.85

APERTURE : F / 4.0
 FILTER ON GONIOMETER : VIS (400 - 700 NM)
 FILTER ON CAMERA : --
 CALIBRATED FOCAL LENGTH : 153.37 MM

RADIAL DISTORTION (MICROMETERS)

REFERRED TO PRINCIPAL POINT OF SYMMETRY (PPS)
 (POSITIVE VALUES DENOTE IMAGE DISPLACEMENT AWAY FROM CENTER)

RADIUS μm	SEMI - DIAGONALS				MEAN
	1	3	2	4	
10	1.3	0.1	0.6	0.1	0.5
20	1.6	0.0	1.3	0.6	0.8
30	1.0	0.5	1.1	0.5	0.7
40	1.2	0.8	1.3	1.0	1.0
50	1.6	0.3	1.4	0.7	1.0
60	1.0	0.7	1.8	0.7	1.0
70	1.1	1.0	1.1	1.3	1.1
80	0.7	1.5	1.1	1.6	1.2
90	1.5	1.7	1.0	2.0	1.5
100	0.2	1.5	1.1	2.1	1.2
110	-0.1	1.3	0.6	2.4	1.0
120	-1.0	-0.3	-0.7	1.4	-0.1
130	-1.8	-1.5	-0.9	-0.1	-1.0
140	-3.1	-3.3	-1.2	-2.6	-2.5
148	-2.6	-4.9	-0.3	-3.4	-2.8

PHOTOGRAPHIC RESOLUTION (LINE PAIRS PER MILLIMETER)

INTERNATIONAL 3-LINE TEST-CHART, CONTRAST (LOG) : 2.0

APERTURE : 4.0

FILTER : 450 NM

FILM : AGFAPAN 25 PROFESSIONAL (ASA SPEED: 25)

DEVELOPER : AGFA-GEVAERT STUDIOAL LIQUID 1:15 6 MIN

ANGLE:	0	5	10	15	20	25	30	35	40	45
(DEGREES)										
RAD.	67	67	83	81	79	76	73	77	57	38
TANG.	67	67	65	62	59	69	63	71	55	33

AWAR (AREA WEIGHTED AVERAGE RESOLUTION) IN LP/MM : 68

CAMERA CALIBRATION

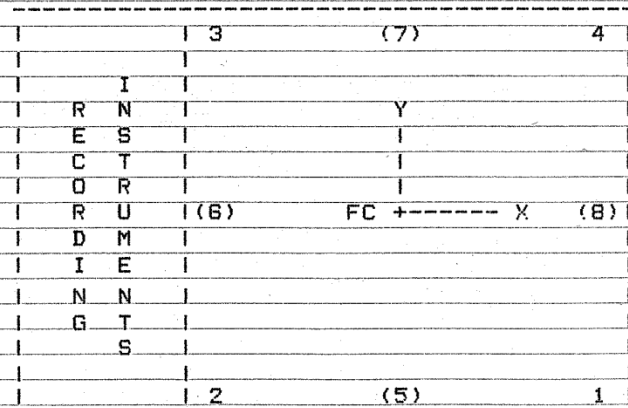
CAMERA: RC10 LENS: 15/4 UAG NO.: 13018 CALIBRATION DATE: 14.05.85

PRINCIPAL POINT OF AUTOCOLLIMATION (PPA) AND
PRINCIPAL POINT OF SYMMETRY (PPS)-----
REFERRED TO FC, SEE DIAGRAM

	X (MM)	Y (MM)
PPA	0.008	0.000
S	0.002	-0.002

FUCIAL MARKS, REFERRED TO FC

	X (MM)	Y (MM)
1	106.001	-105.999
2	-106.003	-106.001
3	-106.004	106.003
4	106.001	105.999

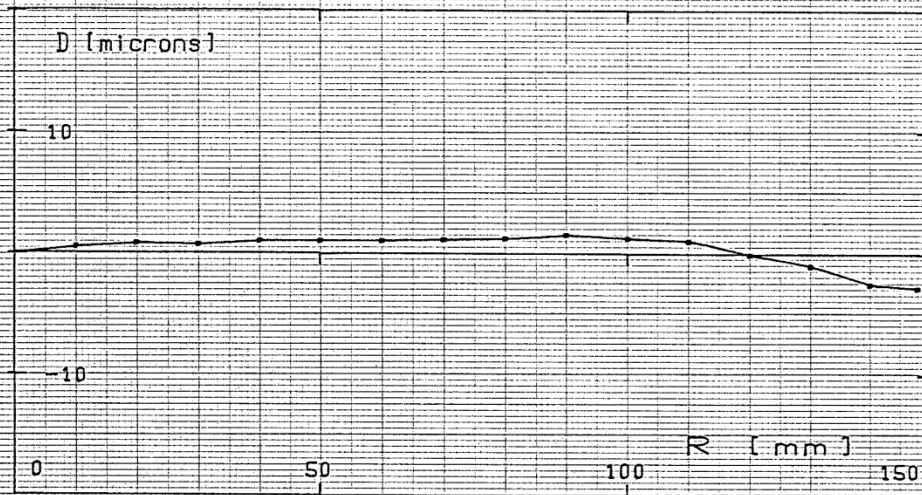


AS SEEN ON FOCAL PLANE FRAME

RC10 1574 UAG NO. 13018

14.05.85

APERTURE : F / 4.0
FILTER ON GONIOMETER : UIS (400 - 700 NM)
FILTER ON CAMERA : --
C.F.L. : 153.37 MM



MEAN RADIAL DISTORTION CURVE

RADIAL DISTORTION FOR SEMI-DIAGONALS
REFERRED TO PPS

CAMERA CALIBRATION CERTIFICATE

CAMERA TYPE : RC20
LENS TYPE : 15/4 UAGA-F
LENS NO. : 13126

CALIBRATION DATE : 21.02.91

WILD LEITZ LTD



Leica Heerbrugg Ltd
CH-825 Heerbrugg
Calibration Department
Supervisor



CAMERA CALIBRATION

*CAMERA: RC20 LENS: 15/4 UAGA-F NO.: 13126 CALIBRATION DATE: 21.02.9

APERTURE : F / 4.0
 FILTER ON GONIOMETER : VIS (400 - 700 NM)
 FILTER ON CAMERA : --
 CALIBRATED FOCAL LENGTH : 152.92 MM

RADIAL DISTORTION (MICROMETERS)

 REFERRED TO PRINCIPAL POINT OF SYMMETRY (PPS)
 (POSITIVE VALUES DENOTE IMAGE DISPLACEMENT AWAY FROM CENTER)

RADIUS MM	SEMI - DIAGONALS				MEAN
	1	3	2	4	
10	0.5	-0.3	0.2	-0.1	0.0
20	0.3	-0.6	0.4	-0.2	0.0
30	0.2	-0.5	0.4	-0.9	-0.2
40	-0.1	-0.4	-0.2	-0.8	-0.3
50	-0.2	-1.0	-0.2	-1.2	-0.6
60	-1.2	-0.6	-0.5	-1.5	-0.9
70	-1.1	-0.8	-1.1	-1.2	-1.0
80	-0.9	-0.5	-0.4	-0.6	-0.6
90	-0.2	0.1	-0.4	-0.2	-0.1
100	-0.7	-0.3	0.5	0.2	0.0
110	0.3	0.6	1.2	1.9	1.0
120	-0.1	0.3	0.8	1.9	0.7
130	-1.1	-0.3	1.3	1.4	0.3
140	-1.4	-0.5	2.1	1.4	0.4
148	0.6	-2.0	1.1	0.9	0.1

PHOTOGRAPHIC RESOLUTION (LINE PAIRS PER MILLIMETER)

 INTERNATIONAL 3-LINE TEST-CHART, CONTRAST (LOG) : 2.0
 APERTURE : 4.0
 FILTER : 450 NM
 FILM : AGFAPAN 25 PROFESSIONAL (ASA SPEED: 25)
 DEVELOPER : KODAK HC110 PREPARATION 2 SOLUTION C

ANGLE: (DEGREES)	0	5	10	15	20	25	30	35	40	45
RAD.	106	119	104	81	56	54	73	69	57	42
TANG.	106	94	103	79	74	78	71	71	55	33

AWAR (AREA WEIGHTED AVERAGE RESOLUTION) IN LP/MM : 69

210

CAMERA CALIBRATION

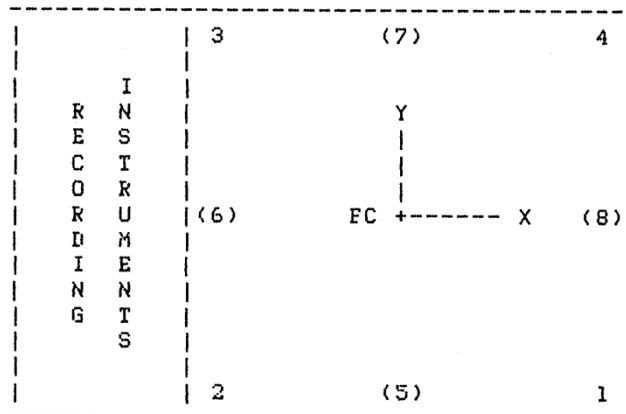
CAMERA: RC20 LENS: 15/4 UAGA-F NO.: 13126 CALIBRATION DATE: 21.02.91

PRINCIPAL POINT OF AUTOCOLLIMATION (PPA) AND
PRINCIPAL POINT OF SYMMETRY (PPS)-----
REFERRED TO FC, SEE DIAGRAM

	X (MM)	Y (MM)
PPA	0.004	0.013
S	0.003	0.013

TRUDICIAL MARKS, REFERRED TO FC

	X (MM)	Y (MM)		X (MM)	Y (MM)
1	105.998	-105.996	5	-0.004	-110.000
2	-106.000	-106.002	6	-110.004	0.005
3	-106.004	106.002	7	-0.001	110.007
4	106.001	106.002	8	110.004	0.003

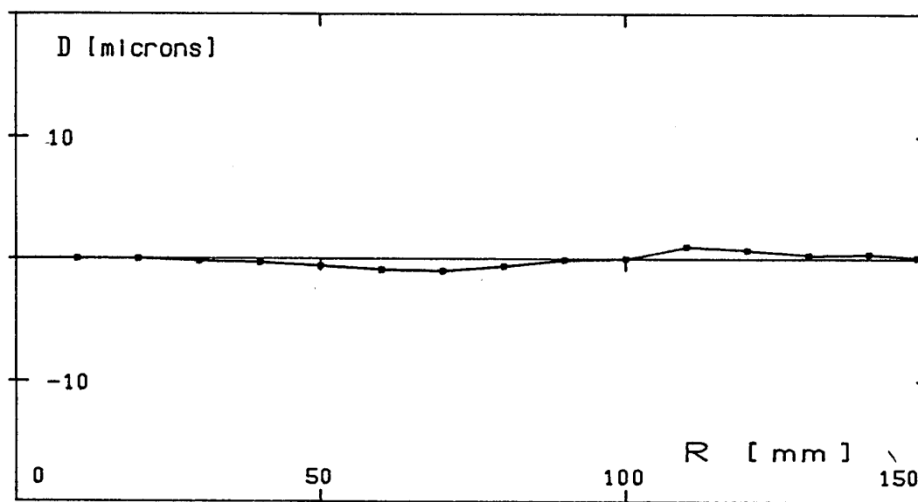


AS SEEN ON FOCAL PLANE FRAME

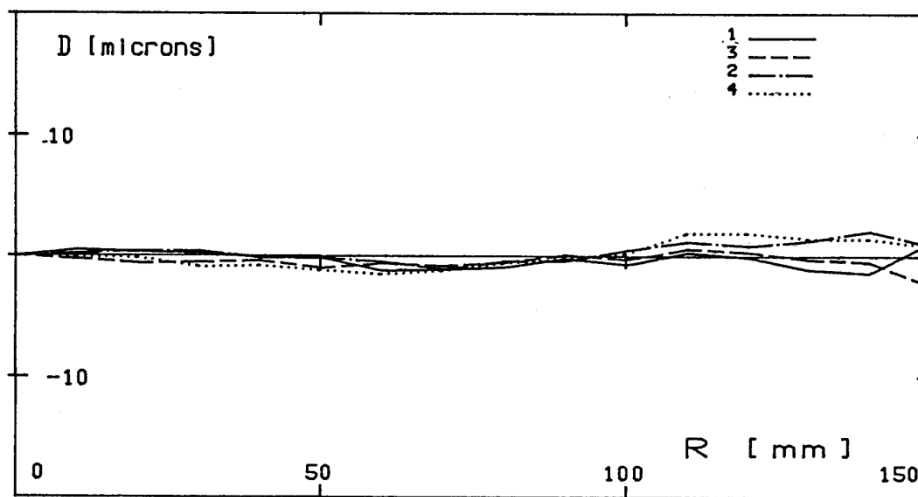


RC20 15/4 UAGA-F NO. 13126 21.02.91

APERTURE : F / 4.0
FILTER ON GONIOMETER : VIS (400 - 700 NM)
FILTER ON CAMERA : --
C.F.L. : 152.92 MM



MEAN RADIAL DISTORTION CURVE



RADIAL DISTORTION FOR SEMI-DIAGONALS
REFERRED TO PPS

152.92

ca 1330197

(VD)

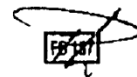
CAMERA CALIBRATION CERTIFICATE

CAMERA TYPE : RC30
LENS TYPE : 15/4 UAG-S
LENS NO. : 13301

Calibration date: 10.11.1997

SwissOptic AG, Heerbrugg

 **swissoptic**
SwissOptic AG
Heinrich-Wild-Strasse
CH-8435 Heerbrugg
Schweiz



22. 10. 98 a.g.

RC30

15/4 UAG-S

No. 13301

10.11.1997

Aperture: 4.0
 Filter on goniometer: VIS (400 - 700 NM)
 Filter on camera: —
 C.F.L.: 153.503 mm

Radial distortion (micrometers) referred to principal point of symmetry (PPS)
 (Positive values denote image displacement away from center)

Radius mm	Half - Sides				Mean
	1	3	2	4	
10	-0.5	-1.0	-0.8	-0.8	-0.7
20	-1.0	-2.0	-1.4	-1.5	-1.4
30	-1.5	-2.4	-1.6	-2.0	-1.8
40	-1.2	-2.0	-1.9	-1.7	-1.7
50	-0.7	-2.0	-1.8	-1.2	-1.4
60	-0.6	-1.8	-1.3	-0.9	-1.1
70	0.6	-1.4	-1.3	-0.3	-0.6
80	0.6	-0.6	-0.9	0.5	-0.1
90	1.9	-0.3	-0.7	0.6	0.3
100	1.7	-0.1	1.1	0.9	0.9
110	1.7	0.3	1.5	1.5	1.2
120	1.6	1.3	0.6	1.3	1.2
130	0.8	1.0	1.6	0.7	1.0
140	-1.3	1.0	0.4	-0.3	0.0
148	-2.6	0.2	-0.4	-0.7	-0.8

Photographic resolution (line pairs per millimeter)

International 3-line test-chart, contrast (log): 2.0

Aperture: 4.0
 Filter: 450 NM
 Film: KODAK PANATOMIC X 2412
 Developer: KODAK HC110

Angle (deg)	0	5	10	15	20	25	30	35	40	45
Radial:	117	117	115	101	98	119	114	108	90	83
Tangential:	117	116	114	109	103	108	111	111	87	52

AWAR (Area weighted average resolution) in lp/mm: 108



RC30

15/4 UAG-S

No. 13301

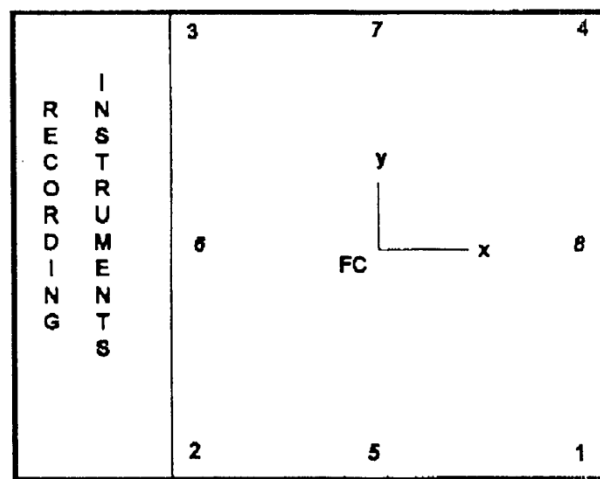
10.11.1997

Principal point of autocollimation (PPA) and
principal point of symmetry (PPS)
referred to central cross (FC), see diagram

	x (mm)	y (mm)
PPA	0.004	0.011
PPS	0.009	0.002

Fiducial marks, referred to central cross (FC)

	x (mm)	y (mm)		x (mm)	y (mm)
1	105.996	-105.995	5	-0.001	-111.992
2	-106.001	-105.999	6	-112.000	0.003
3	-106.002	105.998	7	0.001	111.988
4	106.001	105.999	8	112.002	0.000



as seen on focal plane frame

RC30

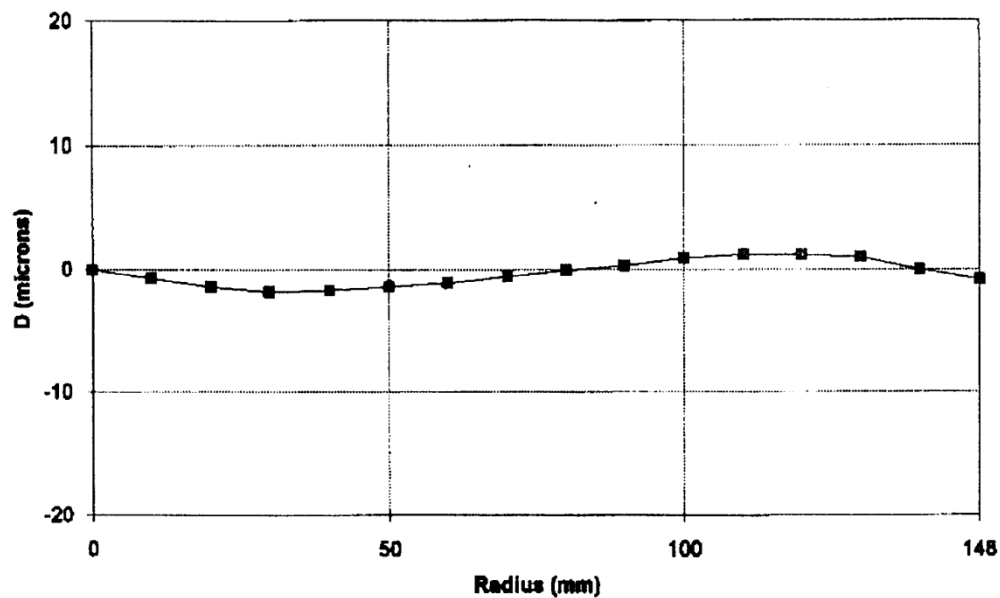
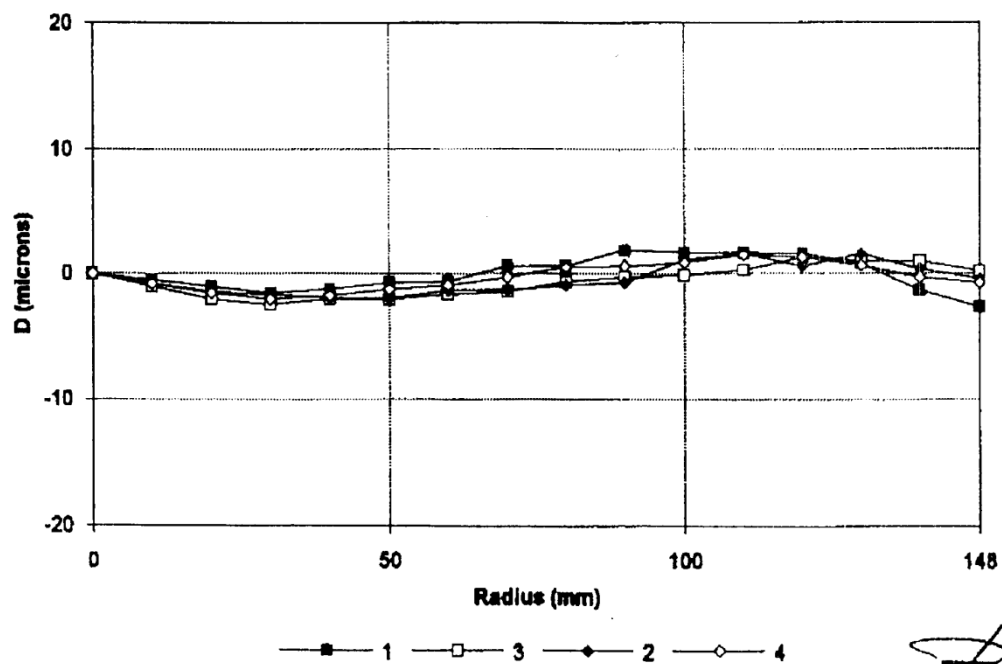
RC30

15/4 UAG-S

No. 13301

10.11.1997

Aperture: 4.0
Filter on goniometer: VIS (400 - 700 NM)
Filter on camera: —
C.F.L.: 153.503 mm

Mean radial distortion**Radial distortion for semi-diagonals referred to PPS**

A.2. Details of Ground Control Points used in the photogrammetric procedure

Table A.1 – Ground Control Points (GCPs) used for each set of aerial photographs. For GCPs from Berger et al. (2010) please see Appendix in Berger (2010). GCPs from the University of Bern (Uni Bern) were collected by MSc students during a field course and are given in more detail in figures below.

GCP	Years used	Source	x (m)	y (m)	z (m)
pm_u_081007_02	1963, 1992	Berger, 2010	2611840	1124873	1935.39
flw_u_081007_02	1986, 1992, 1998	Berger, 2010	2612639	1123980	2152.95
flw_o_081007_02	1986, 1992, 1998	Berger, 2010	2613343	1123838	2397.1
gu_sh_07	1986	Berger, 2010	2614606	1126077	941.15
uia_s_081001_02	1963, 1986, 1992, 1998	Berger, 2010	2614875	1124088	1817.69
uia_n_081001_02	1963, 1992, 1998	Berger, 2010	2614919	1124163	1792.76
om_st_081001_01	1963, 1992	Berger, 2010	2615619	1125630	1663.91
gcp_35	1963, 1998	Uni Bern	2612632	1123004	2275.067
gcp_30	1963, 1998	Uni Bern	2613274	1122499	2304.525
gcp_31	1986	Uni Bern	2613520	1122294	2344.783

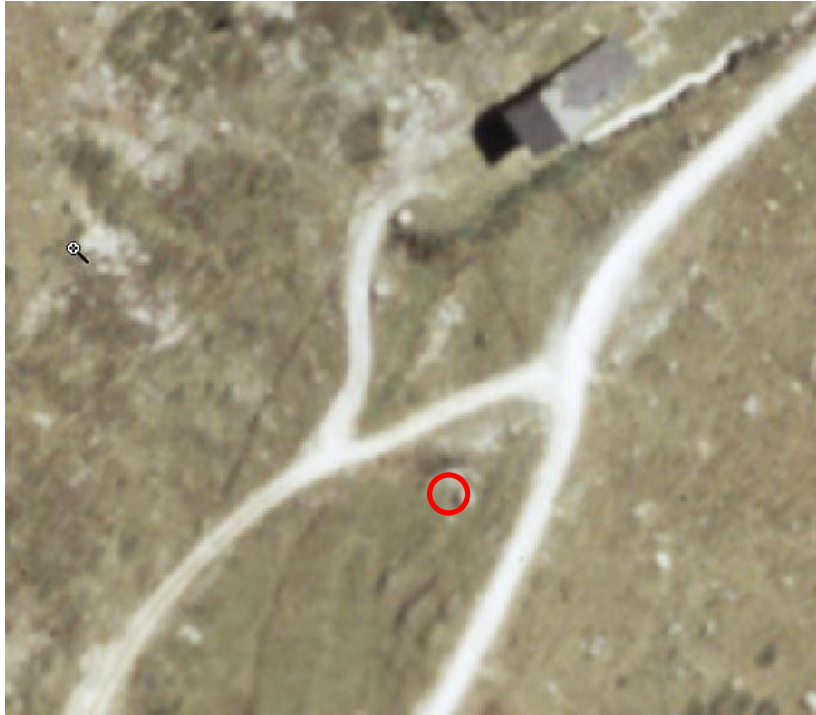


Figure A.3 – GCP 30 – taken from documentation by MSc students of the University of Bern



Figure A.4 – GCP 31 – taken from documentation by MSc students of the University of Bern

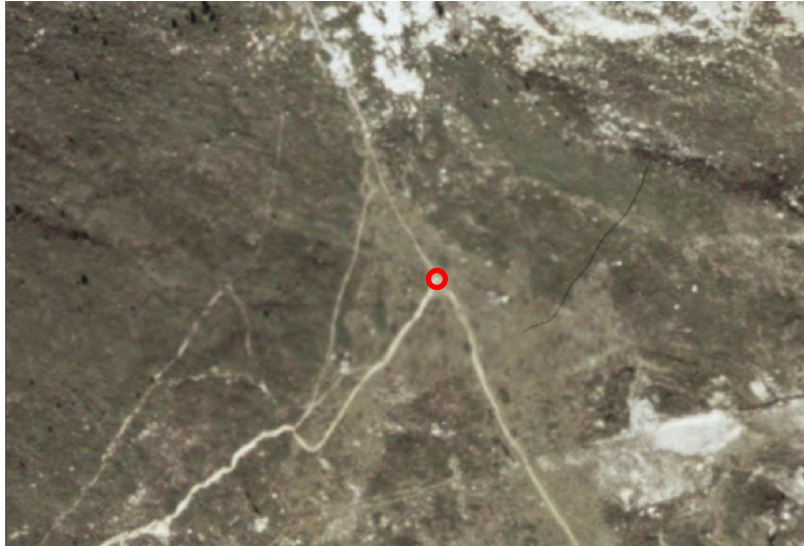


Figure A.5 – GCP 35 – taken from documentation by MSc student of the University of Bern



Figure A.6 – Collection of GCP 35 by a MSc student of the University of Bern. Photo taken by an MSc student of the University of Bern.

A.3. Additional figures of slope change

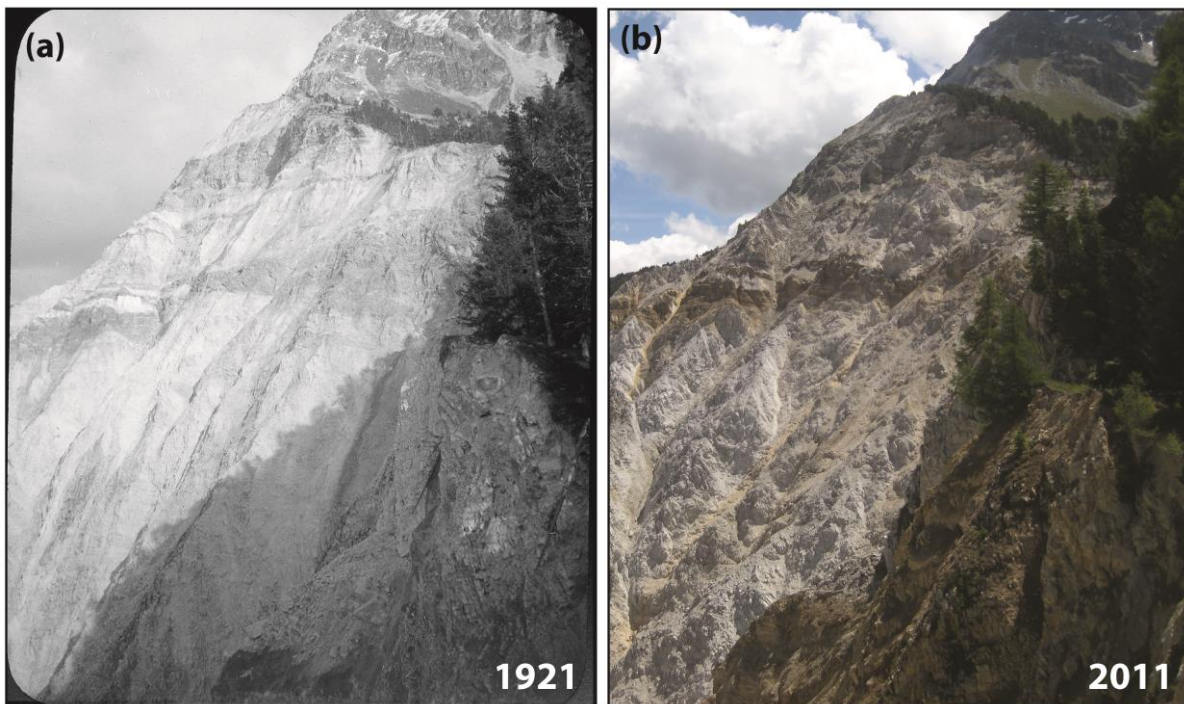


Figure A.7 – Part of the study slope, the South face of the Illhorn in 1921 and from roughly the same location 90 years on in 2011. Significant erosion is evident from comparison of the two photos.

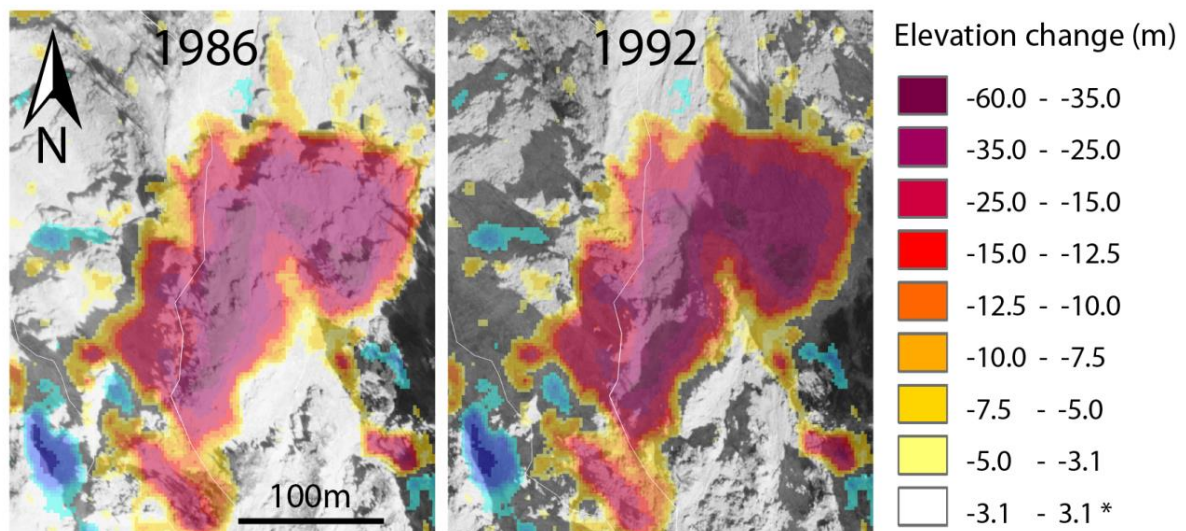


Figure A.8 – Slope failure (SF) 1 in Figure 2.4 shown by the 1986-1992 elevation change overlaid on the orthophotos from these periods. The removal of the cliff between 1986 and 1992 by slope failure is clear from comparison of the orthophotos, providing some validation of the elevation change calculated from the DEMs. * The value of 3.1 is calculated from uncertainty analysis presented in Chapter 2.

Appendix B

Supplementary material for Chapter 3

B.1. Recorded debris flow volumes

Table B.1 – Sediment volumes of observed debris flow events in the Illgraben in the period of 1963 to 1999 (modified after Rhyner et al., 2005)

Date	Volume	Comments
08.06.1963		
18.06.1963		
28.06.1963		
12.08.1963		
20.05.1964		
30.05.1964		
02.06.1964		
14.06.1964		
17.06.1964		
04.05.1965		
07.06.1965		
08.06.1965		
18.06.1965		
04.07.1965		
25.07.1965		
31.07.1982	<25000	
06.06.1985	<25000	
06.07.1986	25000-75000	data doubtful
07.06.1987	<25000	
29.08.1988	<25000	
16.08.1989	25000-75000	data doubtful
13.08.1990	<25000	
12.07.1991	75000-250000	
03.10.1995	75000-250000	data doubtful
21.08.1997	25000-75000	data doubtful
30.10.1998	<25000	
16.08.1999	75000-250000	

Table B.2 – Debris flow volumes from 2000 through 2009 (McArdell et al., 2009a). Debris flows from 2000 through 2005 were used along with debris flows from 1998 and 1999 shown in Table B.1 to calculate the annual sediment yield in period B3 shown in Figure 3.5a

Date	Max Discharge [m ³ /s]	Max Flow Height [m]	Max Velocity [m/s]	Roughly Estimated Volume WSL [m ³ /s]
03 Jun 00, 17:21	47	2.50	2.66	10000
28 Jun 00, 14:19	87	2.90	4.07	35000
24 Jul 00, 07:50	10	1.42	1.14	20000
05 Jun 01, 21:30	43	1.93	3.40	32000
08 Jun 01, 16:30	15	0.99	3.00	7000
15 Jun 01, 18:30	18	0.96	3.80	10000
27 Jun 01, 14:30	52	1.58	6.30	36000
07 Jul 01, 07:30	114	2.65	6.10	45000
31 Jul 02, 10:30	62	2.57	3.10	20000
10 Aug 02, 07:30	99	1.78	10.00	71000
19 Mai 03, 14:00	94	3.26	3.50	90000
12 Aug 04, 17:10	29	1.53	3.00	34000
23 Aug 04, 23:30	16	1.28	2.30	36000
25 Okt 04, 22:50	5	0.88	3.20	4000
28 Mai 05, 16:00	154	2.21	9.19	107000
03 Jun 05, 19:20	20	1.25	2.51	43257
13 Jun 05, 09:10	37	1.04	5.86	23907
04 Jul 05, 12:40	15	1.08	2.31	15101
18 Jul 05, 11:10	25	1.57	2.34	10244
01 Aug 05, 17:10	9	1.05	1.44	3600
18 Aug 05, 13:10	4	0.91	0.70	2900
24 Jun 06, 15:50	149	2.80	6.01	68626
27 Jun 06, 22:40	79	2.52	3.85	32566
18 Jul 06, 18:00	96	2.49	4.82	44500
28 Jul 06, 11:50	20	1.50	1.94	10100
03 Okt 06, 14:30	16	1.39	1.65	6856
28 Mai 07, 02:43	67	1.50	6.62	62000
10 Jun 07, 21:55	36	1.35	4.40	50500
15 Jun 07, 13:04	32	1.74	2.51	26750
21 Jul 07, 19:17	1	0.85	0.30	4560
16 Jun 08, 20:35	15	1.13	2.37	9237
01 Jul 08, 19:23	86	2.35	5.32	60000
31 Aug 08, 20:20	18	1.39	1.89	8200
28 Jul 09, 23:38	5	0.99	2.21	17000
09 Aug 09, 19:49	127	2.56	5.90	57000

Velocity – Generally calculated using the travel time between CD27 and CD29

Depth – Generally taken from the laser at the highway bridge; before 2004 this was measured from radar

Discharge – Calculated as the product of front velocity and wetted area under the bridge.

Volume – See Schlunegger et al. (2009) for a brief description. Basically the discharge is integrated through time using a Strickler friction approach with the ks value calibrated for the front of the flow. It is then possible to calculate the sediment content of the flow assuming hydrostatic pressure, a density of quartz etc.

B.2. Suspended sediment sampling

In Chapter 3 I identified a discrepancy between the sediment yield that I measured from the DEMs and the sediment yield measured from the recorded debris flows in period B3 (1998-2005), with the former being a factor of 1.8 larger than the latter. Whilst this discrepancy may be partially explained by a lack of measurements of debris flows over the winter months, some of the missing sediment must be discharged as suspended sediment in fluvial transport, which is not captured by instruments designed to extreme events. There are no measurements of suspended sediment transport in the Illgraben that we know of. Therefore over the summer of 2011 I conducted a sampling campaign to determine the potential contribution of suspended sediment to the total sediment load.

I used a low-cost, manual sampling procedure, which involved taking grab samples from the channel at times of low flow in 0.5 l bottles. Samples were taken in the channel at CD28, close to the catchment outlet. I dried the samples in the oven, weighed them and calculated the concentration of sediment as the percentage by weight of sediment in the sample. The sediment concentration of the samples is given in Table B.3.

The discharge for each sample was calculated using the Francis equation $q = 3.33(b - 0.2h)h^{3/2}$ where q = flow rate (m^3/s), h = head on the weir (m), b = width of the weir (m). In recognition that the channel cross section is not a perfect rectangular weir, I reduced the values of the width and depth to roughly 2/3rds of the maximum values for the cross section to give a more realistic approximation of the discharge.

The initial results suggest a linear relationship between sediment concentration and discharge (Figure B.1). The sample on 03/07/2012 was taken about 1 day after a debris flow, which may explain its high concentration. We hypothesize that suspended sediment concentration is higher following debris flows due to the disturbance of the channel bed and availability of loose sediment for fluvial transport. Further samples are needed to test this hypothesis and to make the rating curve more robust.

We can make a rough estimate of the contribution of suspended sediment transport to total sediment load based on the average sediment concentration of the samples and discharge at the time of sampling (Table B.3) and the assumption that there is stream flow and therefore suspended sediment transport for half of the year. This results in an annual suspended sediment load of $\sim 1.3 \times 10^5 \text{ m}^3$, which equates to 17% of the debris flow load or 15% of the total load. When added to the sediment load from debris flows for 1998-2005, this reduces the discrepancy with the DEM measured flux in this period to about a factor of 1.5. This suggests that there must be additional sources of missing sediment, such as that exported during the winter as debris flows and floods that are not recorded by the debris flow monitoring system (Chapter 4).

Table B.3 – Details of the Illgraben suspended sediment samples

Date	Time	Location	Discharge $\text{m}^3 \text{s}^{-1}$	Discharge l s^{-1}	Sediment concentration %
12.04.2012	10am	CD 28	0.001	1	0.01
26.06.2012	11.50am	CD28	0.0115	11.5	0.12
26.06.2012	13.50pm	Gas pipe	0.02	20	0.26
03.07.2012*	1.40pm	Gas pipe	0.014	14	0.28
06.07.2012	9.40am	Gas pipe	0.0056	5.6	0.09
06.07.2012	10.10am	CD 28	0.0079	7.9	0.09
17.07.2012	9.45am	Gas pipe	0.0052	5.2	0.04

*~24 hours after a debris flow

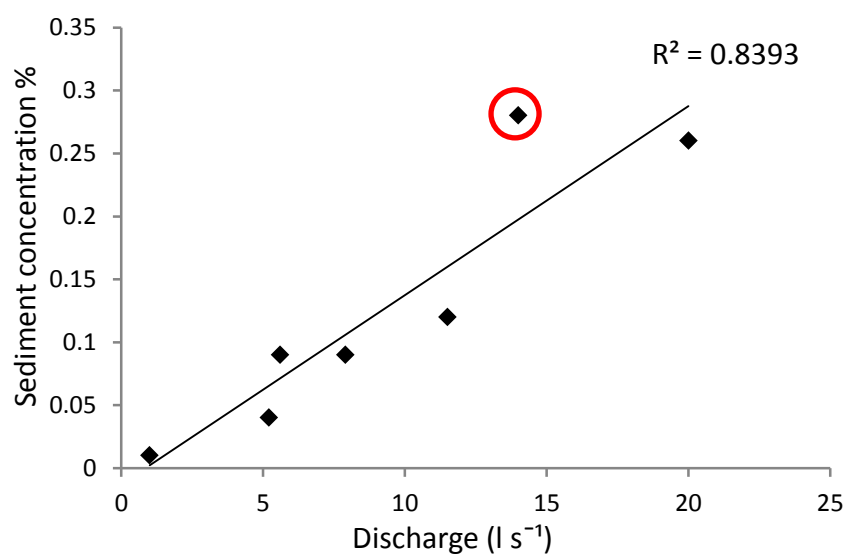


Figure B.1 – Preliminary sediment rating curve for suspended sediment transport in the Illgraben. The sample point highlighted by the red circle was taken about 1 day following a debris flow and is starred in Table B.3.

Appendix C

Supplementary material for Chapter 4

C.1. Independent calibration of hydrological model parameters

Table C.1 – Table modified from Nydegger (2008) showing the calibration of catchment water storage (S_{wcap}). The first 5 columns are values reported in Nydegger (2008) for the analyzed events and last 2 columns are my calculations of catchment water storage. The value highlighted in bold is a minimum estimate of catchment water storage based on the greatest difference between rainfall and runoff of the analyzed events. This reasoning is explained in more detail in Chapter 4.

Type	Date	Duration [h]	Runoff [m3]	Rainfall [m3]	Runoff coefficient [%]	Rainfall-runoff [m3]	Catchment averaged Storage mm
DF	04.07.2005	01:10:00	11522.0	76040.7	15.2	64518.7	6.2
DF	02.08.2005	00:21:00	1456.5	95035.4	1.5	93578.9	9.0
Flood	20.08.2005	10:40:00	10033.0	188527.9	5.3	178494.9	17.2
Flood	21.08.2005	08:30:00	6126.2	118776.2	5.2	112650.0	10.8
DF	18.05.2006	04:30:00	32435.4	140418.1	23.1	107982.7	10.4
DF	24.06.2006	00:44:00	29918.4	183738.6	16.3	153820.2	14.8
DF	27.06.2006	00:39:00	29469.4	103072.9	28.6	73603.4	7.1
DF	18.07.2006	00:59:00	19496.1	236021.9	8.3	216525.8	20.8
DF	28.07.2006	00:51:00	2959.0	98591.4	3.0	95632.4	9.2
DF	03.10.2006	00:23:00	2290.4	119504.8	1.9	117214.4	11.3

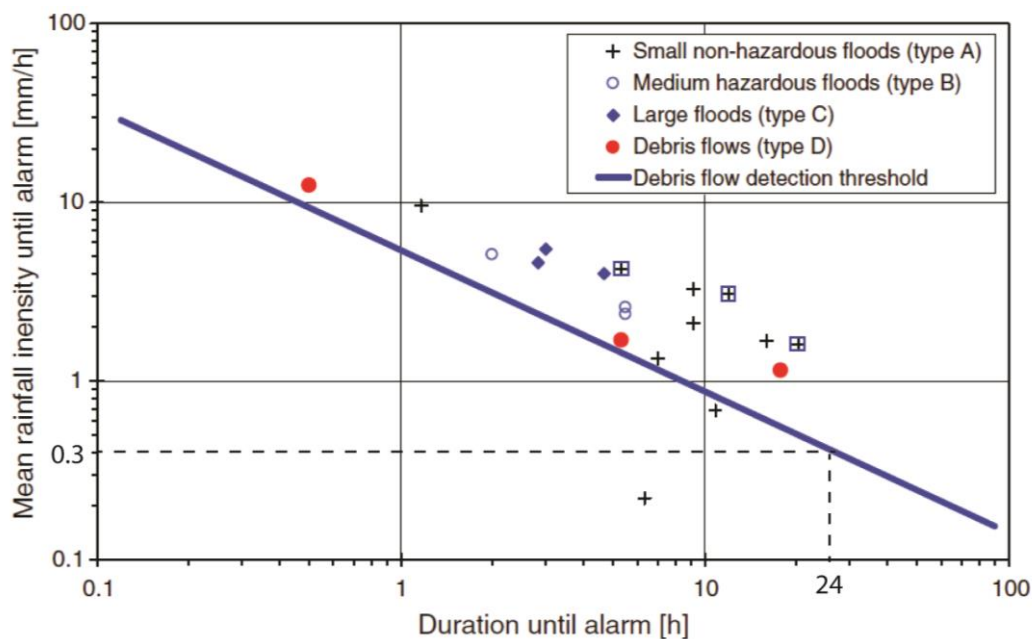


Figure C.1 – Modified from Figure 7 in Badoux et al. (2009) showing the selection of the critical discharge for debris flow generation (Q_{df}) in the model in Chapter 4.

C.2. Estimation of channel sediment residence time

Table C.2 – Calculation of residence time of sediment in channel storage.

Channel above CD1							
Period	Storage* (m ³)	Channel storage change (m ³)	Hillslope flux (m ³)	Flux** (m ³)	Annual flux (m ³)	Residence time (years)	Residence time (days)
1986-1992	256180	-55547	1433961	1122234	187039	1.4	500
1992-1998	249949	454361	1097798	1302210	217035	1.2	420
1998-2005	0	NA	NA	NA	NA	0	0
1986-2005 average						0.8	307
Channel below CD1							
Period	Storage (m ³)	Channel storage change (m ³)	Upstream flux (m ³)	Flux** (m ³)	Annual flux (m ³)	Residence time (years)	Residence time (days)
1986-1992	132159	-55547	1122234	934529	155755	2.5	910
1992-1998	157899	179989	1302210	1324299	220717	1.9	700
1998-2005	0	NA	NA	NA	NA	0	0
1986-2005 average						1.5	537
						1.2	422

*Storage calculated as the sediment between the 1998 DEM channel surface, which is the deepest erosion depth over the study period into the sediment stored in between the checkdams, and the DEM at the start of the period of analysis

**Flux through the channel section calculated as the hillslope flux - storage +/- the channel storage change.

Appendix D

Photo documentation



Figure D.1 – Rain/Temperature gauge 1, 2200m, from which I obtained time series of rainfall with which to validate Rhires-D modeled precipitation and time series of temperature with which to calculate a thermal lapse rate from Sion in Chapter 3.



Figure D.2 – Rafael Caduff and a masters student observing the study slope in summer 2011.



Figure D.3 – Brian McArdell (left) and Peter Molnar at CD29 in Spring 2012.



Figure D.4 – Me (Georgie Bennett) in the channel just below CD28 collecting a suspended sediment sample.



Figure D.5 – Rockfall in the Illgraben in December 2012.



Figure D.6 – Suspended sediment transport and deposition of boulders along the channel, February 2013.

Curriculum Vitae

Georgina Lucy Bennett

Jungstrasse 14, 8050 Zürich, Switzerland

Born 29 June 1986

British citizen

Education and Academic experience

Oct 2009 – Mar 2013	PhD in the Hydrology and Water Resources Management group, Institute of Environmental Engineering, ETH Zürich, Switzerland.
Oct 2008 – Sept 2009	MSc (by research) in Geography, Durham University, UK. Thesis: <i>'Assessing glacier retreat and landform production at the 'debris-charged' snout of Kviárjökull, Iceland'</i> .
Aug 2008 – Oct 2008	Research Assistant, Geography Department, Durham University, UK. Production of a report for the Forestry Commission, Scotland: <i>'Evaluation of optical satellite imagery for forest grant schemes'</i> .
Sept 2005 – June 2008	BSc Geography, First class, Durham University, UK. Dissertation: <i>'Paraglacial slope adjustment, landform succession and landscape evolution following recent glacier retreat, Sandfellsjökull, Iceland'</i> .
Sept 2002 – June 2004	A-Levels (4 As), Putney High School: Geography, Biology, Chemistry, Art.
Sept 1997 – June 2002	GCSEs (9: 8 A*, 1 A), Putney High School.

Selected work experience

Oct 2008 – June 2009	Durham University: Teaching assistant on undergraduate courses.
Oct 2005 – June 2007	Officer Cadet in Northumbrian Universities Officer Training Corps (Newcastle). Completion of Military Training Qualifications 1 and 2.
Apr 2005 – May 2005	Volunteer for the charity Moving Mountains. Assisted on a hydroelectric project, in a Himalayan village, Nepal.

Publications

Bennett, G.L., Molnar, P., Schlunegger, F., McArdell, B.W., Burlando, P. (2013) Patterns of and controls on sediment production, transfer and yield in the Illgraben, Switzerland. *Geomorphology*, Vol. 188, p. 68-82.

Bennett, G.L., Molnar, P., Eisenbeiss, H., McArdell, B.W. (2012) Erosional power in the Swiss Alps: Characterizing slope failure at the head of the Illgraben. *Earth Surface Processes and Landforms*, Vol. 37, 1627-1640.

Bennett, G.L. and Evans, D.J.A. (2012) Glacier retreat and landform production on an overdeepened glacier foreland: the debris-charged glacial landsystem at Kvíárjökull, Iceland. *Earth Surface Processes and Landforms*, Vol. 37, 1584-1602.

Bennett, G.L., Evans, D. J. A., Carbonneau, P. and Twigg, D. R. (2010) Evolution of a debris-charged glacier landsystem, Kvíárjökull, Iceland., *Journal of Maps*, v2010, 40-67. 10.4113/jom.2010.1114.

Bennett, G.L., Evans, D. J. A., Carbonneau, P. and Twigg, D. R. (2010) Published Map. In Bennett, G.L., Evans, D. J. A., Carbonneau, P. and Twigg, D. R. (2010) Evolution of a debris-charged glacier landsystem, Kvíárjökull, Iceland., *Journal of Maps*, v2010, 40-67. 10.4113/jom.2010.1114.

Selected conference presentations

Bennett, G.L., Molnar, P., McArdell, B.W., Burlando, P. (2013) Modeling a mountain basin sediment cascade, Geophysical Research Abstracts, Vol. 15, EGU2013-8629.

Bennett, G.L., Molnar, P., McArdell, B.W., Schlunegger, F., Burlando, P. (2013) Unraveling the Illgraben sediment cascade, Geophysical Research Abstracts, Vol. 15, EGU2013-8758.

Bennett, G.L., Molnar, P., Eisenbeiss, H., McArdell, B.W. (2012) Photogrammetric analysis of slope failures feeding the head of the Illgraben debris flow channel. Geophysical research abstracts, Vol. 14, EGU2012-10393-1.

Bennett, G.L., Molnar, P., McArdell, B.W., Eisenbeiss, H., and Burlando, P. (2011) Sediment transfer and landscape evolution by rock-slope failure and debris flows at the head of the Illgraben, Switzerland, 1963-2005, AGU Abstracts, EP31B-0812, San Francisco, USA.

Bennett, G.L., Evans, D.J.A., Carbonneau, P. and Twigg, D.R. (2011) The debris-charged glacier landsystem, a new landsystem model, based on Kvíárjökull, Iceland, INQUA, July 2011, Bern, Switzerland.

Bennett, G.L., Molnar, P., Korup, O., Burlando, P. (2011) Modeling uncertainty in short-term erosion rates. Geophysical research abstracts, Vol. 13 EGU2011-8368, EGU 2011.

Bennett, G.L., Molnar, P., Korup, O., McArdell, B. (2010) Modeling sediment transfer through mountain basins. Proceedings of Landscapes into Rock, Sept 2010, BGS, London, pp. 68-69.

Bennett, G.L., Evans, D.J.A., Carbonneau, P. and Twigg, D.R. (2009) Assessing glacier retreat and morphometric change at Kvíárjökull, Iceland. Proceedings of Remote Sensing and Photogrammetry Society Annual Conference 2009, September 8-11, Leicester, United Kingdom, pp. 740-745.